Towards A 4-D Spatial and Temporal Model of Human Enamel Biomineralisation

Mohammed Al-Mosawi

(BSc, MSc)

Supervisors:
Dr Maisoon Al-Jawad
Prof. Graham Roy Davis

A thesis submitted to the University of London for the degree of Doctor of Philosophy
2018

Dental Physical Sciences Unit
Institute of Dentistry
Barts and the London School of Medicine and Dentistry
Queen Mary, University of London

Statement of originality

I declare that the research included within this thesis is my own work or that where it has been carried out in collaboration with, or supported by others, that this is duly acknowledged below, and my contribution indicated. Previously published material is also acknowledged below.

I attest that I have exercised reasonable care to ensure that the work is original and does not to the best of my knowledge break any UK law, infringe any third party's copyright or other Intellectual Property Right, or contain any confidential material. I accept that the College has the right to use plagiarism detection software to check the electronic version of the thesis.

I confirm that this thesis has not been previously submitted for the award of a degree by this or any other university.

Name: Mohammed Al-Mosawi

Course: Doctor of Philosophy

Title of work submitted: Towards a 4-D Spatial and Temporal Model of Human Enamel Biomineralisation.

Examination: A thesis submitted for the degree of Doctor of Philosophy, University of London.

Signature: Mohammed Al-Mosawi

Date: 06/02/2018

Barts and The London
School of Medicine and Dentistry

Conference presentations

The annual Diamond SR User Meeting – Oxfordshire, UK (03/09/14 – 04/09/14)
A four-dimensional spatial and temporal model of human incisor enamel biomineralisation using X-ray techniques
Al-Mosawi, M., Davis, G.R. and Al-Jawad, M. (Poster presentation)

IADR/PER Congress – Dubrovnik, Croatia (10/09/14 – 13/09/14)
Spatial and temporal progression of human incisor labial enamel biomineralisation
Al-Mosawi, M., Davis, G.R. and Al-Jawad, M. (Oral and poster presentations)

ESRF User Meeting – Grenoble, France (09/02/15 – 11/02/15)
Towards a 4-D spatial and temporal model of human incisor enamel biomineralisation using X-ray techniques
Al-Mosawi, M., Davis, G.R. and Al-Jawad, M. (Poster presentation)

BSODR Annual General Meeting – Cardiff, UK (14/09/15 – 16/09/15)
Towards a 4-D spatial and temporal model of human incisor enamel biomineralisation using X-ray techniques
Al-Mosawi, M., Davis, G.R. and Al-Jawad, M. (Oral presentation)

XMaS User Meeting – Coventry, UK (25/05/16)
Towards a 4D spatial and temporal model of human dental enamel biomineralisation using X-ray diffraction at XMaS
Al-Mosawi, M., Davis, G.R. and Al-Jawad, M. (Oral presentation)

Gordon Research Conference: Biomineralization – Girona, Spain (14/08/16 – 19/08/16)
Towards a 4-D spatial and temporal model of human dental enamel biomineralisation using X-ray techniques
Al-Mosawi, M., Davis, G.R. and Al-Jawad, M. (Poster presentation)

Enamel 9 Symposium – Harrogate, UK (30/10/16 – 03/11/16)
Towards a 4-D model of human dental enamel biomineralisation
Al-Mosawi, M., Davis, G.R. and Al-Jawad, M. (Oral and poster presentations)

Society of Electron Microscope Technology Meeting – London, UK (14/12/16)
Spatial and temporal progression of human incisal enamel biomineralisation
Al-Mosawi, M., Davis, G.R. Bushby, A. and Al-Jawad, M. (Oral presentation)

Publications

Submitted papers

Al-Mosawi, M., Davis, G.R., Bushby, A., Montgomery, J., Beaumont, J. and Al-Jawad, M. “Crystallographic texture and mineral concentration quantification of developing and mature human incisal enamel”. Submitted to Scientific Reports on 29/11/2017.

Papers in preparation

Al-Mosawi, M., Davis, A., Montgomery, J., Beaumont, J. and Al-Jawad, M., “Using Synchrotron X-ray diffraction to investigate the distribution of enamel crystallites texture through entire permanent central incisal crowns at various developmental stages”.

Al-Mosawi, M., Davis, G.R., Addison, O., Hendriksz, C. and Al-Jawad, M. “Novel insights into the structure of hard tissues affected by inherited metabolic disorders”.

Al-Mosawi, M., Davis, G.R., Bikondoa, O., Schulli, T., Chahine, G., Chamard, V. and Al-Jawad, M. “Structural mapping of human dental enamel using advanced X-ray nano-diffraction”.

Acknowledgments

I would like to express my gratitude to my teachers and supervisors Dr Maisoon Al-Jawad, Senior Lecturer in Dental Physical Sciences, Institute of Dentistry, Queen Mary, University of London and Prof. Graham Roy Davis, Professor of 3D X-ray Imaging, Institute of Dentistry, Queen Mary, University of London for their valuable guidance and sympathetic encouragement at the different stages of this research program.

I am also grateful to Dr David Mills, X-Ray Microtomography Facilities Manager, Institute of Dentistry, Queen Mary, University of London who guided and assisted me in the reconstruction of the X-ray microtomography images and Dr Andy Bushby, Reader in Materials, School of Engineering and Materials Science, Queen Mary, University of London, who helped me with the quantitative backscattered electrons imaging experiments.

My gratitude is also due to Dr Janet Montgomery, Reader in Archaeological Science, Department of Archaeology, Durham University and Dr Julia Beaumont, Lecturer in Biological Anthropology, School of Archaeological Sciences, University of Bradford for providing the samples necessary to complete this thesis.

Finally, my heartiest thanks go to my family, my role-model and father, Ibrahim Al-Mosawi, my loving mother, Tilbah Saleh Al-Mosawi, my dear wife and son, Abraham, and my supportive siblings, Khawla, Raed, Esraa and Hamed.

Abstract

Precise timings and spatial progression of human enamel biomineralisation are still largely unknown due to scarcity of developing human enamel specimens available for investigation. This information is crucial for optimising emerging biomimetic regenerative and reparative dentistry routes.

Five developing permanent incisors were obtained from an archaeological source and used alongside mature contemporary teeth for comparison. X-ray microtomography (XMT), synchrotron X-ray diffraction (S-XRD) and quantitative back-scattered electrons (qBSE) imaging were used to investigate the mineral density distribution, the crystallites texture magnitude and orientation and the nanostructure of dental enamel at various developmental stages, respectively.

XMT revealed that there was a bi-directional mineralisation "front" that starts at the cusp tip and at the enamel-dentine junction (EDJ) travelling cervically and peripherally until the relative mineral density is uniform in the fully mature tooth (2.75 $g/cm^3 \pm$ 0.01 g/cm^3). S-XRD revealed that within one probed region, two populations of crystallite orientations exist simultaneously with an angular separation of 20-50°, with one population being more dominant than the other by a factor of approximately 3:7. Furthermore, one population displayed a higher degree of crystallite texture than the other. These phenomena were observed in all stages of tooth development. The crystallites in both populations were oriented approximately perpendicular to the EDJ regardless of development stage, indicating initial preferred directions of crystallites persist from early through to full maturation. The direction and magnitude of organisation within two distinct populations of crystallites within the developing and mature enamel has not been quantified previously. qBSE analyses suggested that the two observed populations are most likely due to prism decussation and revealed that mineralisation of prism cores precedes that of prism boundaries.

These results provide new insights towards building a quantitative spatio-temporal model of human enamel biomineralisation in order to inform emerging biomimetic reparative/regenerative dental technologies.

Table of contents

List of figures

List of tables

List of abbreviations

2-D	Two dimensional
3-D	Three dimensional
4-D	Four dimensional
ACP	Amorphous calcium phosphate
AI	Amelogenesis imperfecta
ALP	Alkaline phosphatase
BM	Bending magnet
BS	Back-scattered
BSE	Back-scattered electrons
BW	Bandwidth
c-HAp	Carbonated hydroxyapatite
C-terminal	Carboxy-terminal
CCD	Charge coupled device
CEJ	Cementum-enamel junction
CsI	Columnar caesium iodide
CT	Computed tomography
DC	Direct current
DCM	Double crystal monochromator
DCPD	Dicalcium phosphate dihydrate (brushite)
DLS	Diamond Light Source
DMM	Double multilayer monochromator
EBIC	Electron beam induced current

EBSD	Electron backscatter diffraction
EBSP	Electron backscattering pattern
EDJ	Enamel-dentine junction
EDTA	Ethylenediaminetetraacetic acid
EDX	Energy dispersive X-ray spectroscopy
ER	Endoplasmic reticulum
ESRF	European Synchrotron Radiation Facility
FAp	Fluorapatite
FEG	Field emission gun
FTIR	Fourier transform infra-red spectroscopy
FWHM	Full width at half maximum
GAG	Glycosaminoglycan
GIS-XRD	Grazing incidence synchrotron X-ray diffraction
^{1}H-NMR	Proton nuclear magnetic resonance
HAp	Hydroxyapatite
HSb	Hunter-Schreger band
ID	Insertion device
IEE	Inner enamel epithelium
IR	Infra-red
JE	Dental junctional epithelium
KLK-4	Kallikrein related peptidase 4
LaB_6	Lanthanum hexaboride
LAC	Linear attenuation coefficient

LA-ICPMS	Laser-ablation inductively coupled mass spectroscopy
LCD	Liquid crystalline displays
LINAC	Linear accelerator
LRAP	Leucine-rich amelogenin polypeptide
MAC	Mass attenuation coefficient
MMP-20	Metalloproteinase-20
MPS	Mucopolysaccharidosis
mRNA	Messenger ribonucleic acid
N-terminal	Amino-terminal
NSLS	National Synchrotron Light Source
OCP	Octacalcium phosphate
OCT	Optical coherent tomography
ODAM	Odontogenic ameloblast-associated proteins
OEE	Outer enamel epithelium
PDL	Periodontal ligament
PLM	Polarised light microscopy
qBSE	Quantitative back-scattered electrons imaging
QMUL	Queen Mary, University of London
RIXS	Resonant inelastic X-ray scattering
RNA	Ribonucleic acid
SAXS	Small-angle X-ray scattering
S-XRD	Synchrotron X-ray diffraction
SE	Secondary electrons

SEM	Scanning electron microscopy
SNR	Signal to noise ratio
SR	Synchrotron radiation
SRS	Synchrotron Radiation Source
TCP	Tricalcium phosphate
TDI	Time delay integration
TEM	Transmission electron microscopy
TMR	Transverse micro-radiography
TRAP	Tyrosine-rich amelogenin polypeptide
WAXS	Wide-angle X-ray scattering
wt.%	Weight percentage
XMaS	X-ray Magnetic Scattering
XMT	X-ray microtomography
XRD	X-ray diffraction
XRF	X-ray fluorescence spectroscopy

Chapter 1 - Introduction

1.1. Thesis structure

This thesis has been organised such that the structure and general aims and objectives have been outlined in Chapter 1. Chapter 2 provides a comprehensive outline of human dental enamel microstructure and development, reviewing the relevant literature and providing a rationale for the research approach adopted.

Chapter 3 provides a theoretical background into the X-ray absorption and scattering methods used to conduct this study and reviews the relevant X-ray microtomography (XMT) and X-ray diffraction (XRD) studies to date investigating human dental enamel. Furthermore, Chapter 3 gives a description of electron scanning microscopy and its applications in human dental enamel investigation.

Chapter 4 describes the sample preparation, experimental setup and data treatment for the techniques used to satisfy the objectives of this work. Chapters 5 and 6 give a detailed description of the experimental results and a comprehensive discussion of the findings are introduced. The final chapter concludes the analyses by linking all the studies, discussing the shortcomings and highlighting future areas for investigation.

1.2. General aims and objectives

The main aim of this thesis was to analyse and understand the biomineralisation progression of dental enamel in human incisors using X-ray absorption, X-ray scattering, and scanning electron microscopy techniques. This present project is a step forward toward achieving an understanding about the precise timing and spatial progression of human enamel biomineralisation. The goals of this study were to characterise the crystallography, microstructure and relative mineral density in the enamel of the single cusp dentition at different developmental stages using archaeological sources of immature enamel. Ultimately, this work aims to produce the data and understanding needed to put towards a 4-D spatio-temporal biomineralisation model of human enamel and to inform emerging regenerative dentistry technologies.

The specific objectives were:

- To track the progression of mineral densities of human dental enamel as a function of developmental stages using X-ray microtomography (XMT).
- To quantify and compare the crystallites texture magnitude and orientations of human dental enamel at different developmental stages using synchrotron X-ray diffraction (S-XRD).
- To investigate the developmental of the microstructure of enamel as a function of developmental stages using scanning electron microscopy (SEM).
- To collate the information collected from the XMT, S-XRD and SEM techniques in order to identify key changes during human dental enamel development.
- To use data gathered from X-ray techniques and SEM to map the process of biomineralisation in human dental enamel.

Chapter 2 - Enamel formation and structure

"We use them every day, clean them religiously and rely on them for eating, communication and physical appearance. We spend millions on educating and training people specifically to maintain them." (Tucker and Sharpe, 2004).

2.1. Introduction

The human tooth consists of three parts, a crown, a neck and one or more roots. The crown is the functional, visible part of the tooth. The neck is the area between the crown and the root. The root is embedded in the gum, fixing the tooth into the alveolar bone via a connective tissue structure called the periodontal membrane (also called the periodontal ligament (PDL)).

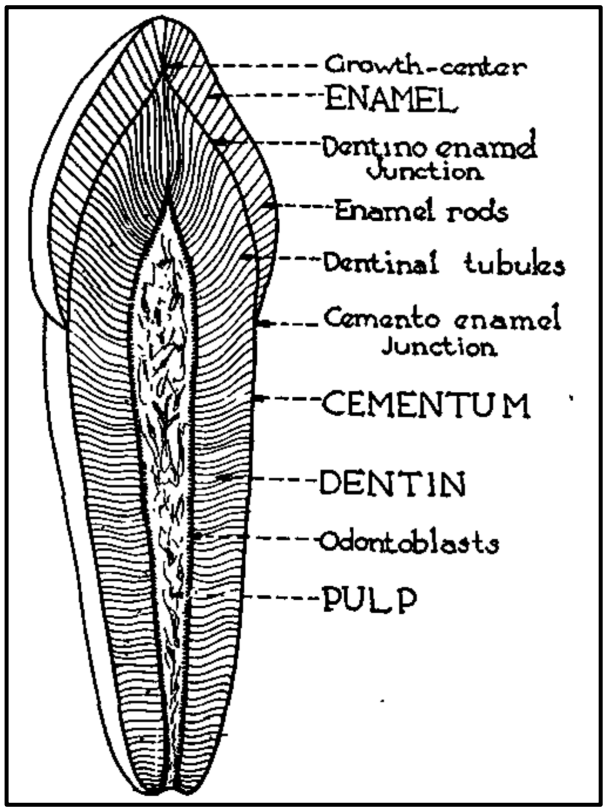

Figure 2.1: Schematic illustrating the structure of the human tooth **(Reproduced with permission of the rights holder, Elsevier, from Schour and Massler (1940b)**.

Teeth comprise of three types of mineralised tissues namely enamel, dentine and cementum, whose combination ensures that the tooth as a system can function for a time

span of approximately 70 years **(Figure 2.1)**. The innermost portion of the tooth, termed the dental pulp or the endodontic system, is made up of un-mineralised oral tissue. It contains blood vessels, fibroblasts, lymphatic and nervous elements and is responsible for regenerating/supplying the dental cellular components (Avery and Chiego, 2006, Nanci, 2012). Humans have two sets of teeth, with a deciduous dentition of 20 teeth and a permanent dentition of 32 teeth (Lacruz et al., 2017).

Dental enamel is the visible part of the tooth covering and protecting the underlying dentine **(Figure 2.1)**. Mature dental enamel is generally regarded as a composite material, comprising of approximately 96 $wt.\%$ mineral, 2-4 $wt.\%$ water and 1-2 $wt.\%$ organic matrix (LeFevre and Manly, 1938, Deakins and Volker, 1941, Robinson et al., 1971, Simmer and Fincham, 1995, Schmitz et al., 2014). By volume, mature enamel is approximately 86% mineral, 12% water and 2% organic material (Crabb and Darling, 1960, Stack, 1967). The organic matrix in dental enamel consists of proteins, peptides, and citric acid and is believed to fill the micro-pores between the crystallites and holding them together (Stack, 1967). The mineral phase contains a non-stoichiometric, impure hydroxyapatite (HAp) crystallites **(See Section 2.2.3)** with similar density, refractive index and birefringence to that of pure HAp **(Figure 2.9)** (Boyde, 1989).

The HAp in enamel was reported to incorporate sodium, magnesium, fluoride, hydrogen, phosphate and carbonate in its lattice (Trautz et al., 1953, Elliott, 1994, Elliott, 1997, Robinson et al., 2000, Elliott et al., 2005, Moradian-Oldak and Paine, 2008), with the principal impurity being 2-5 $wt.\%$ carbonate (Elliott, 1994). Throughout this thesis, the term carbonated hydroxyapatite (c-HAp) will be used to

refer to enamel apatite since the major impurity is the carbonate ions (Elliott, 1964). The organic to mineral ratio vary depending on tooth morphology (Robinson et al., 2000). Having less organic matter compared to other mineralised tissues, dental enamel emerges as the most highly mineralised and hardest biological tissue in the human body (Robinson et al., 1995b, Fincham et al., 1999).

In developing enamel, the early crystallites have been reported to appear as long plates (Rönnholm, 1962a) or ribbons (Rönnholm, 1962a, Kerebel et al., 1979). Initial crystallites are suggested to be 1.5nm thick (Rönnholm, 1962a, Kerebel et al., 1979, Beniash et al., 2009) and 15nm wide (Kerebel et al., 1979). It is believed that these initial structures are crystalline octacalcium phosphates (OCP) (Brown et al., 1987, Dowker et al., 1999), however, more recently, various workers proposed that they are most likely amorphous calcium phosphates (ACP) that eventually transform into c-HAp (Beniash et al., 2009, Simmer et al., 2012). In mature enamel the c-HAp crystallites assume more irregular profiles, where the majority have a roughly flattened hexagonal appearance (Frazier, 1968, Jongebloed et al., 1975, Kerebel et al., 1979) and measuring at approximately 26.3 nm in thickness, 68.3 nm in width (Kerebel et al., 1979, Daculsi et al., 1984) and with lengths that, in some cases, span the entire thickness of enamel (Boyde, 1989, Shore et al., 1995b). It is important to mention that there are large variations in the reported crystallites sizes in literature which may be due to various imaging limitations (Palmer et al., 2008).

Enamel formation is a protein mediated biomineralisation process during which controlled fluxes of mineral-forming ions and non-collagenous matrix proteins are secreted into the extracellular space by specialised epithelial cells called ameloblasts

(Moreno and Aoba, 1987, Heinz, 1989, Carter, 1990, Fincham et al., 1999, Moradian-Oldak, 2012, Cao et al., 2015). The available literature suggest that enamel matrix proteins aggregate (Eastoe, 1979) into nanometre sized quasi-spheres (Fincham et al., 1995, Moradian-Oldak et al., 1998, Fincham et al., 1999, Moradian-Oldak et al., 2000, Wallwork et al., 2001, Robinson et al., 2004) or nanoribbons (He et al., 2011, Martinez-Avila et al., 2012, Sanii et al., 2014, Carneiro et al., 2016, Lacruz et al., 2017) and are believed to play a role in the nucleation, orientation, and growth of enamel crystallites (Moradian-Oldak et al., 2000). There is still a large gap in our understanding of the mechanism by which these protein aggregates control the c-HAp crystallites growth leading directly to one of the main unsolved problems of biomineralisation (Elliott, 1994, Moradian-Oldak and Paine, 2008).

Until the 1960s, investigators were divided into two groups regarding the progression of enamel biomineralisation. One group of scholars postulated that enamel matrix formation and mineralisation occur simultaneously (Allan, 1959, Rönnholm, 1962a). The other group held the view that matrix formation and maturation are two distinct phases, where matrix formation precedes maturation (Diamond and Weinmann, 1940, Applebaum, 1943, Engfeldt and Hammarlund-Essler, 1956). With the development of electron microscopy the latter view became less substantiated since it was shown that the organic matrix and the apatite mineral are deposited concurrently (Angmar-Månsson, 1971).

In contrast to other mineralised tissues, dental enamel is acellular and hence does not undergo remodelling, has no collagen in its matrix and has an epithelial origin (Robinson et al., 2000). Nevertheless, it is sufficiently porous permitting diffusion and

chemical reactions to occur within its structure. Furthermore, it is a selectively permeable membrane, allowing water and ions to pass via osmosis. (Dorozhkin, 2007). On the mesoscale level, the literature appears to validate the view that c-HAp crystallites are tightly packed in an organised pattern into bundles, called prisms, approximately 2-8 μm in diameter and span the entire thickness of enamel unbroken (Robinson et al., 1995a, Dorozhkin, 2007, Reyes-Gasga et al., 2013).

It is a widely held view that prisms run more or less perpendicular to the enamel-dentine junction (EDJ) and the enamel surface **(Figure 2.1)** (Boyde, 1964). According to Boyde (1997), perpendicularity to enamel surface, allows for a more efficient packing of crystallites, maximises their strength and flexibility and enhances their wear resistance capabilities. Each prism is believed to comprise of approximately one thousand (Uskoković, 2013) to several thousand (Simmer et al., 2012) c-HAp crystallites arranged in parallel arrays with their crystallographic c-axes co-aligned and, according to Glas (1962), Kerebel et al. (1979) and Elliott (1994), are predominantly oriented parallel to the long axis of the prism. In human enamel the majority of prisms are arc-shaped and have a "keyhole pattern" in transverse section with a head and a tail region **(Figure 2.8)** (Boyde, 1964).

A prism head or sometimes referred to in the literature as prism core or prismatic enamel is considered to be the product of a single ameloblast cell (Robinson et al., 1995b, Fincham et al., 1999). However, the crystallites at the prism tails tend to have increased inter-crystalline space and have slightly different orientation compared to those at the prism heads, giving rise to interfaces separating adjacent prisms. A prism tail is believed to be the product of multiple neighbouring ameloblasts (Robinson et al.,

1995b). Hence, the main difference between prisms heads and tails crystallites is their orientation in relation to one another with an angle range of 20-50^0 between the two (Robinson et al., 1995b, Fincham et al., 1999). Dental enamel is formed by amelogenesis, a physiological process that begins *in utero* and requires several years to complete through a series of successive stages of proliferation, differentiation, secretion and maturation.

2.2. Enamel development and structure

"Tooth enamel is the hardest mammalian tissue, and, as such, in some ways the hardest to study" (Boyde, 1986).

2.2.1. Amelogenesis

It is widely accepted that the positioning of dental hard tissue-forming components precede the actual formation and development of dental hard tissues (Baeuerlein, 2004). Odontogenesis is the process by which embryonic cells differentiate into enamel-producing ameloblasts, dentine-producing odontoblasts and cementum-producing cementoblasts to form a specific number of teeth of varying sizes and shapes at specific locations in the mandible and maxilla (Tucker and Sharpe, 2004).

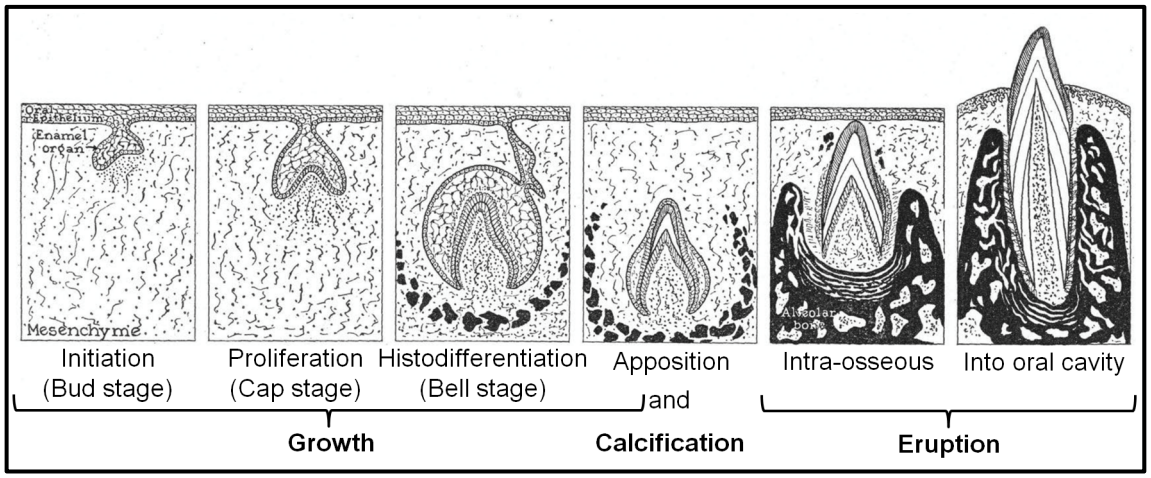

Figure 2.2: Stages of tooth development **(Reproduced with permission of the rights holder, Elsevier, from Schour and Massler (1940a)**

The principal stages of odontogenesis include the initial development of the dental lamina that folds to form the dental placode, followed by the bud, cap and bell stages **(Figure 2.2)**. In humans, this process starts 28-40 days post-ovulation (Baeuerlein, 2004) and involves up to 300 genes that are expressed by signal molecules regulating the epithelium and the underlying mesenchymal tissues interactions (Tucker and Sharpe, 2004). It is beyond the scope of this thesis to discuss the morphogenesis and histology of mammalian tooth formation, however, the reader is directed to a number of publications that cover all these topics (Schour and Massler, 1940a, Berkovitz et al., 2002, Tucker and Sharpe, 2004, Avery and Chiego, 2006, Nanci, 2012).

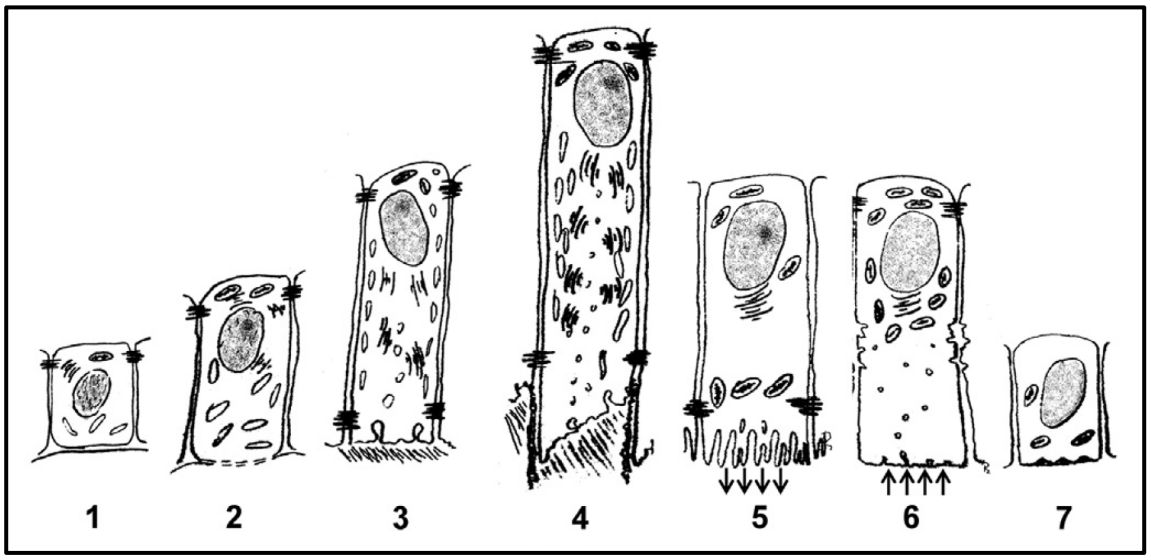

Figure 2.3: The various functional stages in the life cycle of human ameloblasts. **(1)** Morphogenetic stage; **(2)** histodifferentiation stage; **(3)** initial secretory stage (without Tomes' process) creating aprismatic enamel; **(4)** secretory stage (with Tomes' process) creating prismatic enamel; **(5)** ruffle-ended ameloblast of the maturation stage; **(6)** smooth-ended ameloblast of the maturation stage; **(7)** protective stage **(Reproduced with permission of the rights holder, Elsevier, from Varga et al. (2015)).**

Dentine formation (dentinogenesis) and enamel formation (amelogenesis) occur at about 20-24 weeks *in utero* with the deposition of dentine and enamel proteins and the beginning of calcification. Amelogenesis is a dynamic and a highly regulated physiological process that involves a series of successive stages of proliferation and

differentiation of cells as well as secretion, assembly and mineralisation of enamel matrix proteins (Mishra et al., 2009).

Amelogenesis begins *in utero* and progresses under precise genetic control and involves protein-protein interactions, protein-mineral interactions, and interactions involving the cell membrane (Palmer et al., 2008). Enamel development requires several years to complete and has been divided into a number of consecutive stages based on the tissue structure, histology and chemistry. It is reported that enamel secretion starts on the dentine horn and proceeds peripherally and cervically as a function of time. When the full thickness of the tissue has been laid down, the maturation stage begins **(See Section 2.2.1.4)**, where over 90% the enamel matrix is lost, while the crystallites expand in width and thickness, occupying most of the tissue volume (Avery, 1962, Smith and Nanci, 1995, Goldberg et al., 1995, Aoba, 1996, Rozzi, 1998, Nanci, 2012).

2.2.1.1. *Pre-secretory stage*

The pre-secretory stage involves the differentiation of the pre-ameloblasts, the formation of the basal lamina which separates the epithelial cells from the subjacent mesenchyme, and the subsequent resorption of the basal lamina by metallo-enzymes. At the early bell stage, the cuboidal cells of the inner enamel epithelium complete division and start to differentiate into pre-ameloblasts **(Figure 2.3 (1))**. During differentiation, these cells elongate and become columnar; they increase in cell height (up to 90 μm) and sagittal width (2-3 μm) within the region between the nucleus and the basement membrane.

The differentiating ameloblasts then reverse their secretory polarity through the proximal movement of their nuclei toward the stratum intermedium end of the cell, and

through the formation of inter-cellular organelles associated with protein synthesis (endoplasmic reticulum (ER) and Golgi apparatus) at the opposite distal end of the cell adjacent to the dental papilla **(Figure 2.3 (2))**. The pre-ameloblasts trigger the differentiation of the dental papilla into odontoblasts, which then secrete the first-formed dentine called mantle dentine. Prior to dentine mineralisation, pre-ameloblasts enzymes catalyse the breakdown of the basement membrane (future EDJ region) separating the pre-ameloblasts and the adjacent dental papilla. At this stage, the ameloblasts are aligned with one another by junctional complexes termed desmosomes. These desmosomes maintain ameloblast alignment, holding them together and controlling the passage of molecules into and out of the enamel matrix (Smith and Nanci, 1995, Berkovitz et al., 2002, Nanci, 2012, Berkovitz et al., 2010).

2.2.1.2. *Secretory stage*

It was previously reported that neighbouring ameloblasts have hexagonal packing **(Figure 2.4a)** with their cell membranes lying parallel to each other and with straight lateral cell margins **(Figure 2.4b)** (Boyde, 1964). Strands of tight junctions indicate the presence of a sealed permeability barrier that inhibits material from passing between secretory ameloblasts (compartmentalised microenvironment) (Goldberg et al., 1995).

Messenger RNAs (mRNAs) are translated by ribosomes on the rough ER forming enamel matrix proteins, most notably, amelogenin, ameloblastin and enamelin (Smith, 1998). The synthesised proteins are then transported by vesicles to the Golgi apparatus, where in certain cases they undergo post-translational modification. These vesicles are then packaged into electron dense secretory granules in order to be transported to the distal pole of the ameloblast to be exocytosed into the extracellular space (Berkovitz et al., 2002, Berkovitz et al., 2010). Initially, a secretory ameloblast comprises of a flat

secretory distal pole commonly known as proximal Tomes' process. According to Boyde (1987) these secretory surfaces can hardly be called processes because they do not project, however, the term proximal Tomes' process will be used throughout this thesis for clarity.

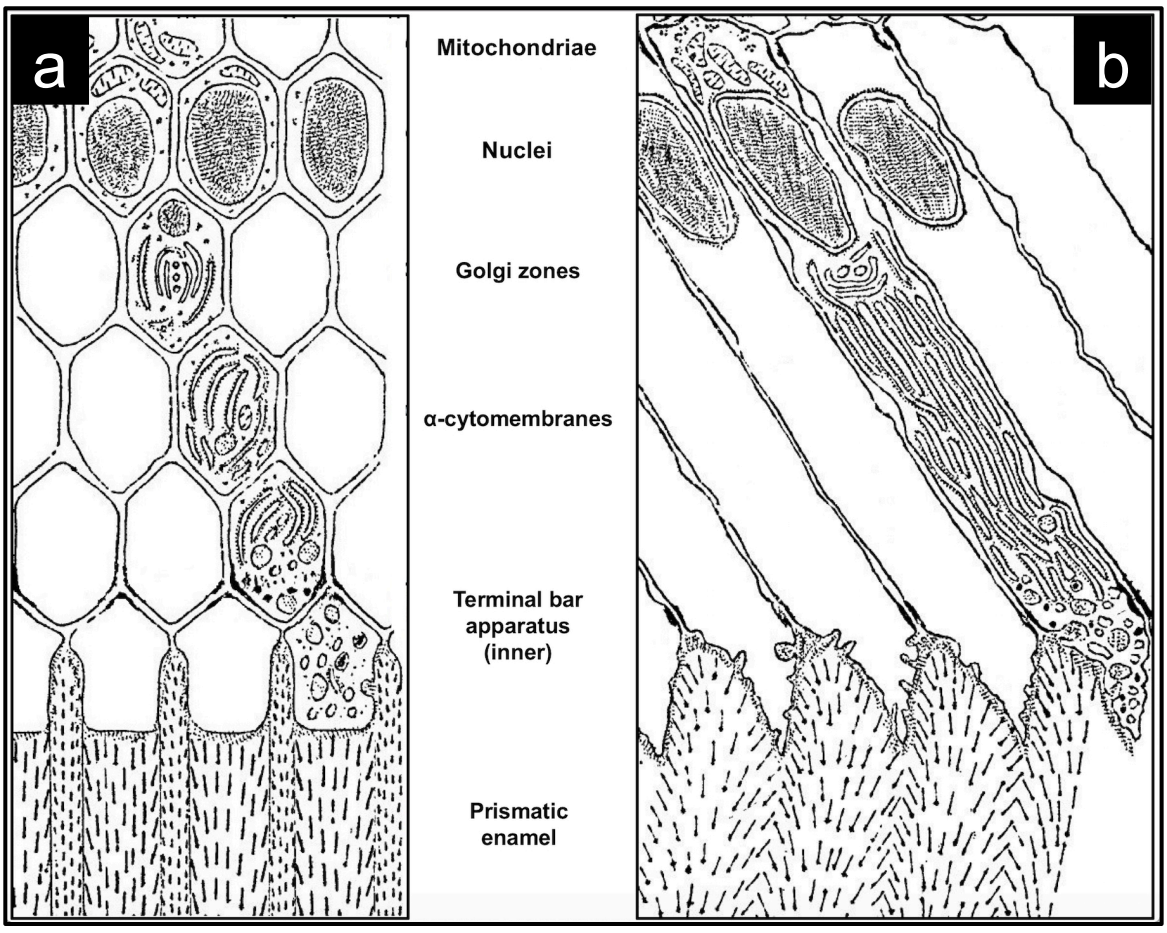

Figure 2.4: Developing enamel and its ameloblasts with their **a)** hexagonal packing in a section where prisms cut longitudinally and **b)** parallel cell membranes in a section along their long axis **(Reproduced with permission of the rights holder, Prof. Alan Boyde, from Boyde (1964))**.

More recently, it has become obvious that the ameloblasts secrete small amounts of matrix proteins that either diffuse into the basal lamina separating the ameloblasts from the dental papilla or accumulate in the developing dentine mantle **(Figure 2.3 (3))** (Smith and Nanci, 1995, Nanci, 2012, Berkovitz et al., 2010). Subsequently, the ameloblasts start to secrete large quantities of enamel matrix and mineral forming ions against the newly mineralised mantle dentine at the proximal Tomes' process surface

(Goldberg et al., 1995, Stavrianos et al., 2010). Various workers suggested that the mineral forming ions diffuse across the papillary layer from circulation. These ions are then transported actively (Josephsen and Fejerskov, 1977, Lacruz et al., 2013a) and passively (Smith, 1979, Nanci, 2012) into the polarised ameloblasts, to be subsequently secreted into the enamel matrix (Wang et al., 2014).

It is suggested that the matrix proteins play an important role in enamel biomineralisation, allowing it to take place in mild physiological conditions compared to the high temperatures and pressures required to form the same minerals *in vitro* (Gower, 2008). According to a definition provided by Boskey (1998), biomineralisation is the process by which mineral crystals are deposited in an organised fashion in the matrix of living organisms. A further definition is given by Mann (2001) who describes biomineralisation as the process that involves the selective extraction and uptake of elements from the local environment and their incorporation into functional structures under strict biological control. The key elements for biomineralisation include, an organic matrix (usually proteinaceous) within which the mineral forms, a system that control ionic composition of the media surrounding the forming mineral, and elements that regulate the precipitation kinetics (Mura-Galelli et al., 1992).

One theory regarding initial dental enamel biomineralisation suggests that the earliest enamel crystallites originate from mineralised collagen fibrils at the EDJ, possibly from dentine crystallites entering enamel. (Landis et al., 1988, Lin et al., 1993). However, the current accepted model for dental enamel biomineralisation indicates that the initiation, nucleation, orientation and growth of c-HAp crystallites occur within an intricate,

extracellular organic scaffold laid by ameloblasts (Fincham et al., 1995, Diekwisch et al., 1995).

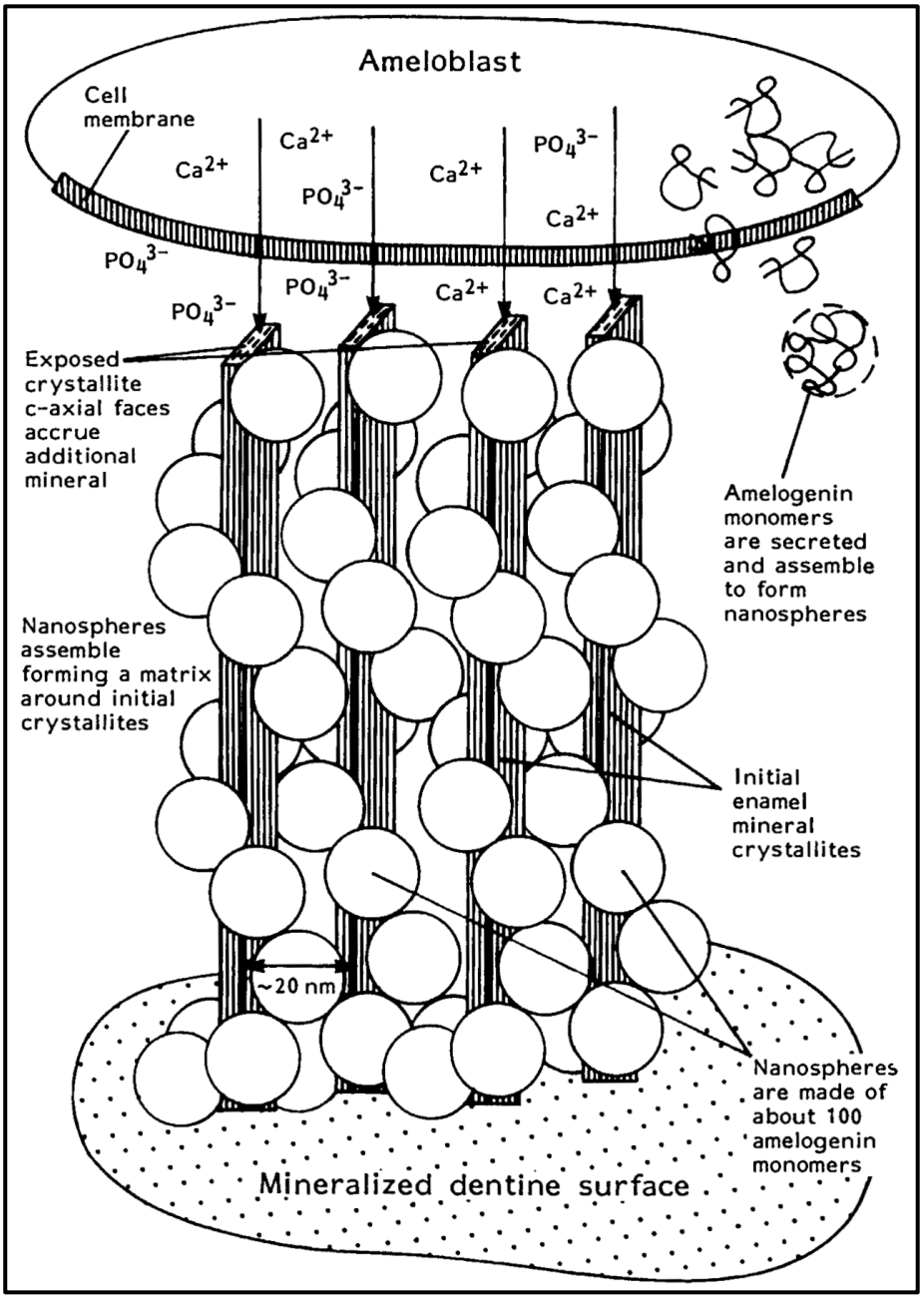

Figure 2.5: A schematic diagram of the nanosphere model showing: the secretion of ameloblasts and enamel forming ions, the self-assembly of amelogenin proteins into nanospheres, the stabilisation of mineral forming ions, the alignment of the nanospheres into chain like structures, the transformation of mineral forming ions into c-HAp crystallites **(Reproduced with permission of the rights holder, John Wiley and Sons, from Fincham and Simmer (1997)**.

The available evidence from recombinant mouse amelogenin (M179) seems to suggest that the amelogenins self-assemble into globular aggregates (Fincham et al., 1994,

Moradian-Oldak et al., 1994) about 5-100 nm in diameter (Fincham et al., 1994, Moradian-Oldak et al., 1998, Moradian-Oldak, 2001) termed "nanospheres" (Fincham et al., 1995) **(Figure 2.5).** It is suggested that these nanospheres are formed by externalising the hydrophilic C-terminus of amelogenins and shielding the hydrophobic residues from the surrounding water (Fincham and Simmer, 1997). Amelogenin-amelogenin interactions were found to occur between the 42-residue domain in the N-terminal region ("A" domain) and the 17-residue domain in the C-terminal region ("B" domain) of the protein (Paine and Snead, 1997). Furthermore, it was reported that nanospheres formation is both temperature and pH dependent (Moradian-Oldak et al., 1998).

Successively, the ameloblasts transport mineral forming ions such as calcium and phosphate at a concentration sufficient for precipitation into the extracellular matrix scaffold (Aoba, 1996, Fincham et al., 1999). Moreover, it was observed that the nanospheres aggregate further, forming a network of 10 to 15 linearly linked nanospheres (Du et al., 2005). However, other workers observed that the nanospheres lose stability (Martinez-Avila et al., 2012) and completely disappear (Fang et al., 2011) when calcium and phosphate ions are added *in vitro*. When these mineralising ions are present, recombinant human full length amelogenins (rH174) and its cleavage product, rH146, were found to aggregate over a period of days into nanoribbons **(Figure 2.6)**, nearly 16.7 nm ± 1 nm wide, with approximately 5-20 nm space between them (Martinez-Avila et al., 2012, He et al., 2011). Nanoribbons assembly is believed to be triggered by the formation of ion bridges with calcium and phosphate ions across amelogenin dimers.

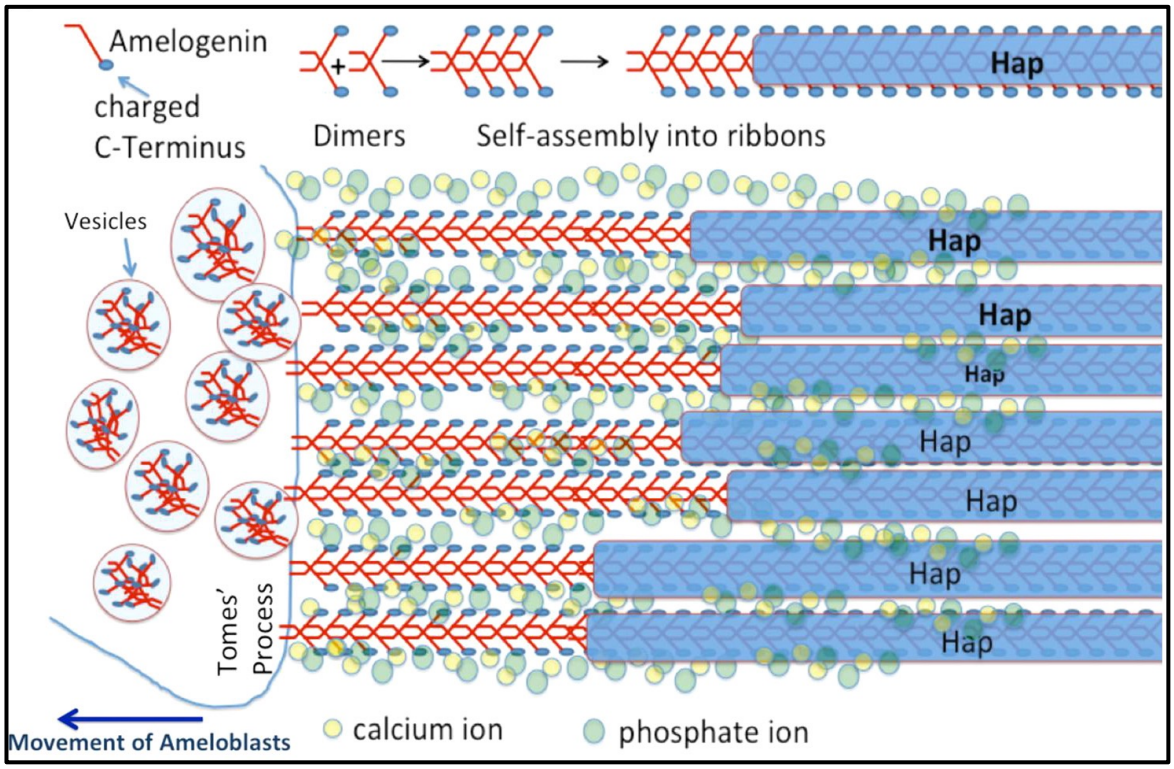

Figure 2.6: A schematic diagram of the nanoribbon model showing: amelogenin dimers secretion from vesicles, nanoribbon assembly and elongation, and the formation of c-HAp crystallites **(Reproduced from Lacruz et al. (2017) – Permission of the rights holder, The American Physiological Society, was not required).**

Nanoribbons elongate by the addition of newly secreted amelogenin dimers to the existing ribbons (Lacruz et al., 2017). These nanoribbons gradually assemble over a period of 1-3 weeks into bundles up to 100 μm in length resembling the appearance of apatite fibrils in an enamel prism (Martinez-Avila et al., 2011, Martinez-Avila et al., 2012, Carneiro et al., 2016). Furthermore, according to Fourier transform infra-red spectroscopy (FTIR) analyses, it was reported that, unlike the random-coil structure of amelogenin aggregates observed in nanospheres, amelogenins displayed β-sheet motif comparable to amyloid fibres when assembled into nanoribbons (Sanii et al., 2014).

It has been reported that enamel crystallites precipitation takes place simultaneously with the secretion of the matrix proteins (Aoba, 1996). For crystallites to nucleate, two conditions must be present, a supersaturated solution and a nucleating event (Diekwisch

et al., 1995). It has been shown that divalent anions such as hydrogen phosphite (HO_3P^{-2}) act as bridges between the matrix proteins and the crystallites (Zou et al., 2010). Initial enamel crystallites **(Figure 2.3 (3))** were described to be relatively thin (Goldberg et al., 1995, Stavrianos et al., 2010), short, randomly orientated and have Ca/P ratios (approximately 1.26 *in vitro* and 1.5-1.53 *in vivo*) characteristic of ACP, OCP and tricalcium phosphate (TCP) (Diekwisch et al., 1995). Older crystallites Ca/P molar ratio was reported to be close to 1.6 (Aoba and Moreno, 1990) and sometimes exceeding 1.67 (Diekwisch et al., 1995), indicating c-HAp formation. Other workers ruled out the possibility of ACP being a c-HAp precursor, due to its amorphous nature (Brown et al., 1987, Dowker et al., 1999). This claim was later refuted by a number of researchers, proposing that these structures are most likely ACP that eventually transform into c-HAp via solid-state transition (Beniash et al., 2009, Simmer et al., 2012).

It was proposed that amelogenins control crystallite elongation (Fincham et al., 1995) by binding to and inhibiting the growth of apatite crystallites at the (1 0 0) face and promoting the crystallites growth at the (0 0 1) face (Friddle et al., 2011). Furthermore, protein aggregates are believed to play a role in inhibiting early crystallite-crystallite lateral fusion by spacing the crystallites at approximately 20nm distances (Fincham et al., 1995). Early crystallites grow in the c-axis direction and appear as thin ribbon with hexagonal cross section representing the a and b planes. The crystallites grow into elongated prisms whose morphology and orientation are believed to be defined by the matrix organisation **(Figure 2.9)** (Fincham et al., 1995, Moradian-Oldak et al., 1998, Fincham et al., 1999, Veis, 2003).

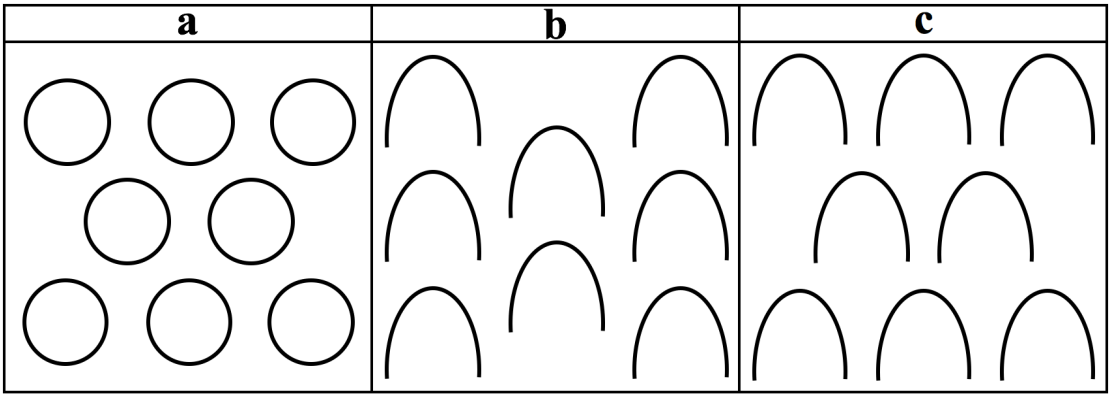

Figure 2.7: Enamel prism patterns **a)** 1, **b)** 2 and **c)** 3. Each pattern has a specific prism spatial organisation and morphology **(Adapted from Dumont (1995))**.

Initially, ameloblasts secret a layer of aprismatic enamel known as the initial enamel. As the initial layer forms, the secretory ameloblasts retreat centrifugally away from the EDJ. Osborn (1970) hypothesised that the outward movement of ameloblasts can be the result of various factors such as the high hydrostatic pressure generated by the secretory product and the secretory force produced by the ameloblast. As the ameloblast travels further away from the EDJ, a cytoplasmic cone-shaped secretory projection termed distal Tomes' process gradually develop at its distal end giving an ameloblast monolayer a "picket-fence" appearance if viewed on a histological section **(Figure 2.4b)** (Kallenbach, 1973, Fincham et al., 1999, Cao et al., 2015, Habelitz, 2015, Carneiro et al., 2016). The distal and proximal Tomes' processes of an ameloblast have different secretory surface angles and are believed to give rise to prismatic enamel (Sasaki and Higashi, 1983, Habelitz, 2015, Cao et al., 2015).

Prismatic enamel can be divided into three categories depending on the prism shape and the packing pattern **(Figure 2.7)**. In Pattern 1 enamel the prism boundary discontinuities form closed cylinders, which may sometimes exist in human teeth at cuspal enamel and in areas where prisms decussate **(Figure 2.7a)** (Boyde, 1964, Habelitz, 2015). Pattern 2 occurs in human enamel and Rhesus monkey and is also the primary pattern in rodent

incisor enamel. Here, enamel prisms have a “horseshoe” shaped profile and rows of prisms are separated by continuous inter-row sheets of inter-prismatic enamel **(Figure 2.7b)**. Pattern 3 is the pattern most commonly found in human enamel, in which prisms are arc-shaped and have a “keyhole pattern” in transverse sections **(Figure 2.7c and Figure 2.8)** (Boyde, 1964, Warshawsky et al., 1981, Dumont, 1995, Mishra et al., 2009, Stavrianos et al., 2010, Habelitz, 2015).

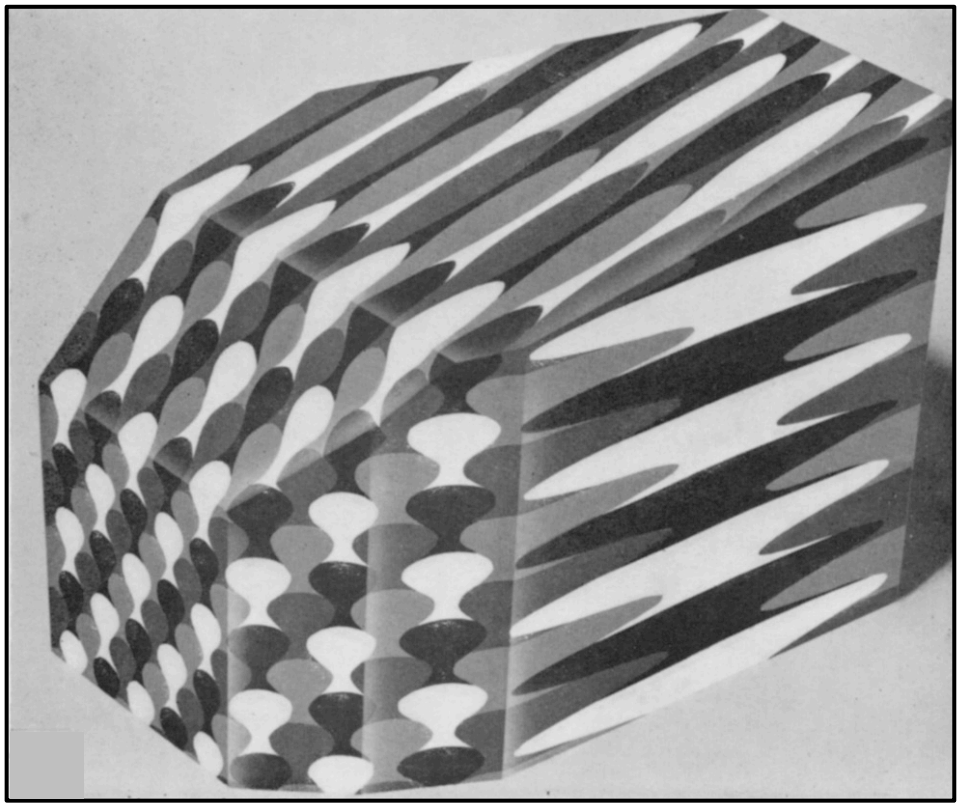

Figure 2.8: Model of enamel prisms with the keyhole cross-section prepared by injection moulding of coloured polystyrene **(Reproduced with permission of the rights holder, Elsevier, from Meckel et al. (1965a))**

It is suggested that prism patterns vary between individuals and within one individual. One individual tooth may have all three patterns present and even some intermediate forms. It is important to note that the above-mentioned prism patterns are no more than diagrammatic concepts which help in seeing and describing the differences between these types of enamel and how they develop (Boyde, 1964).

In human enamel, the cross-sectional appearance of prismatic enamel mostly resembles a “keyhole pattern” (‘pattern 3’) with a head and a tail components, allowing for very close packing **(Figure 2.7c and Figure 2.8)** (Boyde, 1964, Meckel et al., 1965a). A number of authors refer to the head and tail regions of the “keyhole pattern” as prismatic and inter-prismatic enamel, respectively (Frank, 1979, Shellis, 1984, Palmer et al., 2008). Various studies argue against treating the inter-prismatic region as a distinct layer (Bernick et al., 1952, Watson and Avery, 1954, Quigley, 1959, Meckel et al., 1965a, Meckel et al., 1965b), claiming that this region is intra-prismatic and represent the tail of a prism.

It was previously thought that prismatic (“keyhole pattern” head) and inter-prismatic (“keyhole pattern” tail) enamel differ chemically, structurally and histogenetically (Chase, 1927). However, it has been established that they only differ in their levels of organic content (higher in prisms tails), crystallites lengths (shorter in prisms tails) and crystallites orientation since the forming enamel crystallites align at right angles to the secretory surfaces of the distal and proximal ends of Tomes’ process. In prisms heads the crystallites are orientated approximately parallel to the long axis of the prism toward the crown of the tooth, whereas, in prism tails the crystallites are orientated somewhat perpendicular to the prism long axis toward the root of the tooth (Boyde, 1964).

Moreover, it has been observed that the tail region or the so-called inter-prismatic substance is formed prior to the prism head or the so-called prismatic substance in order for the former to create the cavity in which the latter resides (Rönnholm, 1962a, Rönnholm, 1962b, Smith and Nanci, 1995, Goldberg et al., 1995, Simmer and Hu, 2001, Berkovitz et al., 2002, Nanci, 2012, Berkovitz et al., 2010, Stavrianos et al., 2010,

Habelitz, 2015), yet, the head region mineralises before the tail component (Watson and Avery, 1954, Quigley, 1959, Avery et al., 1961). It is also suggested that each prism is surrounded by an organic-rich layer termed the prism sheath (Scott et al., 1952), although a number of investigators such as Meckel et al. (1965a) seem to disagree with the existence of such layer, claiming that such structure is most likely artefactual (Boyde, 1990).

As the secretory stage progresses and the enamel approaches its full thickness, the Tomes' process membranes gradually become enriched with cholesterol and split up into small vesicles (Goldberg et al., 1995). The distal Tomes' process becomes thinner and squeezes out through cavities in prisms tails and disappears. This creates narrow discontinuities between the heads and tails of enamel prisms that later becomes filled with organic material most commonly and incorrectly called prism sheaths (Nanci, 2012), a term which according to Boyde (1964) correctly describes a structure which develops around the boundary in partially demineralised enamel (Boyde, 1964, Mishra et al., 2009).

During this stage, ameloblasts undergo changes in size and they will have similar appearance as when they were forming the initial enamel. Due to the absence of the distal Tomes' process, the outer 20-100μm portion of the enamel layer is prismless. Human enamel can therefore be organised into three layers, an initial aprismatic enamel layer near the EDJ, a prismatic enamel layer comprising the enamel bulk, and a thin layer of aprismatic enamel at the surface of the tooth (Smith and Nanci, 1995, Fincham et al., 1999, Nanci, 2012, Cao et al., 2015, Habelitz, 2015, Carneiro et al., 2016). It is speculated that the aprismatic regions of enamel serve as a toughening mechanism due

to their flexible nature (Palmer et al., 2008). At this stage, the enamel is considered immature and comprises of approximately 20-30% protein, 15-20% mineral and 50-60% water by volume (Fincham et al., 1995).

The paths of secretory ameloblasts from the EDJ peripherally determine the growth direction of enamel prisms. It has been suggested that the rate of ameloblasts movement equals the rate at which prisms increase in length maintaining a constant distance of approximately $100nm$ between the secretory surface and the lengthening prisms (Rönnholm, 1962a, Boyde, 1964, Osborn, 1970) and representing a time difference of about 15 minutes (Boyde, 1997). Skobe (2006) speculated that each "keyhole pattern" is the product of a single ameloblast. However, other workers suggested that more than one ameloblast contribute to the formation of each "keyhole pattern" (Rönnholm, 1962b, Boyde, 1964).

It is a widely held view that prisms run more or less perpendicular to the EDJ and the enamel surface. According to Boyde (1997), perpendicularity to enamel surface, allows for a more efficient packing of crystallites, maximises their strength and bendability and enhances their wear resistance capabilities. Each prism is believed to comprise of approximately one thousand (Uskoković, 2013) to several thousands (Simmer et al., 2012) c-HAp crystallites arranged in parallel arrays with their crystallographic c-axes co-aligned and, according to Glas (1962), Kerebel et al. (1979) and Elliott (1994), are predominantly oriented parallel to the long axis of the prism. A single prism measures at approximately 2-8 μm in diameter (Robinson et al., 1995a, Dorozhkin, 2007, Reyes-Gasga et al., 2013) and is on average longer than the enamel thickness measuring at approximately $2mm$ in length due to its wavy course towards the enamel surface. The c-

HAp crystallites of the “keyhole patterns” heads have a slightly different orientation to those in tails (Fincham et al., 1999, Cao et al., 2015, Habelitz, 2015, Carneiro et al., 2016).

2.2.1.3. *Transition Stage*

Prior to maturation, the same ameloblasts that were responsible for the formation and secretion of the enamel matrix undergo a transitional stage, during which matrix secretion comes to an end and some of the enamel matrix is degraded. During the transition stage the ameloblasts go through significant morphological changes such as height reduction, papillary layer formation, and formation of striated borders at their distal ends causing them to become ruffle-ended **(Figure 2.3 (5))** (Kallenbach, 1974, Nanci, 2012, Palmer et al., 2008, Berkovitz et al., 2010). Lacruz et al. (2017) perhaps incorrectly claimed that ameloblasts lose their Tomes’ process during the transition stage. However, it is a widely held view that the absence of Tomes’ process gives rise to aprismatic enamel, which is known to be defined at the end of the secretory stage resulting in the aprismatic outer layer of enamel (Smith and Nanci, 1995, Fincham et al., 1999, Nanci, 2012, Cao et al., 2015, Habelitz, 2015, Carneiro et al., 2016).

Various studies reported that during the transition stage the enamel matrix proteins’ coding genes are downregulated, whereas, the genes involved in ion transport, pH homeostasis and proteolysis are upregulated (Hu et al., 2002, Lacruz et al., 2012b, Wang et al., 2014, Yin et al., 2014). The total number of ameloblasts also reduces drastically by programmed cell death, a process termed apoptosis (Smith and Warshawsky, 1977), possibly due to calcium overload (Hubbard, 2000). Furthermore, organelles associated with matrix secretion within the remaining ameloblasts undergo a reduction in number. This stage is also characterised by a reduction in stellate reticulum,

causing blood vessels to be situated closer to the proximal ends of the ameloblasts. The mineral content is constant until the end of the transition stage, but then begins to rise (Nanci, 2012, Berkovitz et al., 2010).

2.2.1.4. *Maturation stage*

Immature enamel is porous, poor in mineral content and rich in organic content. Maturation proceeds from the dentine horn peripherally and cervically and begins when the maturation cellular phenotype develops. It is the maturation stage that is responsible for the decrease of the enamel organic content and the increase of the enamel inorganic phase (Angmar-Månsson, 1971, Fincham et al., 1989, Smith et al., 1989, Fincham et al., 1999, Cao et al., 2015, Habelitz, 2015, Carneiro et al., 2016).

Maturation stage ameloblasts have been reported to change morphology in a series of modulations between a ruffle-ended **(Figure 2.3 (5))** and a smooth-ended **(Figure 2.3 (6))** appearance. Modulation between ruffle- and smooth-ended phases were reported to alternate throughout maturation (Warshawsky and Smith, 1974, Josephsen and Fejerskov, 1977, Reith and Boyde, 1981) and may occur up to seven times during this stage (Goldberg et al., 1995). These shifts between ruffle and smooth phases introduce considerable vitiation to extracellular pH using various acid–base transport mechanisms, where higher and lower pH values were reported during the smooth- and ruffle-ended phases of ameloblast modulation, respectively (Sasaki et al., 1991, Lacruz et al., 2010). The modulation between smooth- and ruffle-ended phases have been suggested to play an important role in elevating the enamel mineral content and removing the majority of enamel matrix proteins (Smith, 1998, Nanci, 2012, Josephsen et al., 2010).

The pioneer works on developing pig enamel by Deakins (1942) and Weinmann et al. (1942) stated that, unlike odontogenesis and osteogenesis, during amelogenesis, organic matter and water are almost degraded or removed gradually shortly after reaching the full thickness of enamel. The process of organic reduction is maintained and controlled by ameloblasts, where water and enamel matrix degradation products pass through them away from the mineralising front (Avery and Chiego, 2006, Nanci, 2012, Berkovitz et al., 2010). This stage is possibly unique to dental enamel (Fincham et al., 1999). By the end of the biomineralisation process, the remaining proteins - with enamelins being the most abundant - accumulate at the crystallites surfaces. Although the effects of these remnant proteins on the mechanical properties of enamel remain unclear, it is suggested that they may play a role in moderating crack propagation and fracture in dental enamel (Fincham et al., 1999, Veis, 2003).

It has been suggested that as mineralisation proceeds, kallikrein4 (KLK-4) enzymes severely hydrolyse the matrix proteins. Subsequently, the resulting peptide debris is endocytosed almost completely by ameloblasts (Bartlett and Simmer, 1999, Fincham et al., 1999, Nanci, 2012, Lu et al., 2008, Lacruz et al., 2013b). By the end of the maturation stage the organic content reduces radically to 1-2 $wt.\%$ (LeFevre and Manly, 1938, Deakins and Volker, 1941, Robinson et al., 1971, Simmer and Fincham, 1995, Schmitz et al., 2014). Furthermore, the amelogenins and non-amelogenins ratio is inverted from approximately 1:10 respectively in the immature enamel to approximately 10:1 in the mature enamel (Aoba, 1996, Smith et al., 2005). It is important to note that ameloblasts do not secrete amelogenins and non-amelogenins in a constant, homogeneous 10:1 mix (Goldberg et al., 1995).

This loss of organic material is coupled with an increase in mineral ion uptake. Furthermore, ions of phosphate, calcium and bicarbonate, generated by enzymes such as alkaline phosphatase (ALP) and carbonic anhydrase II, pass through the ameloblasts and into the enamel matrix (Goldberg et al., 1995, Palmer et al., 2008). In addition to the formation of new c-HAp crystallites (Smith, 1998), existing crystallites expand progressively and rapidly in both thickness and width to fill the areas that were previously occupied by organic components (Crabb and Darling, 1960, Frazier, 1968, Daculsi et al., 1984, Boyde, 1997, Smith, 1998, Margolis et al., 2006), reaching the dimensions of mature crystallites with some extending throughout the entire thickness of enamel ($\leq 2\ mm$) (Avery and Chiego, 2006, Nanci, 2012, Berkovitz et al., 2010). Enamel lamellae and tufts may appear at the EDJ due to hypomineralisation and other faults (Avery and Chiego, 2006, Nanci, 2012, Berkovitz et al., 2010). Furthermore, it was speculated that when crystallites increase in size, they compress the organic matrix of the prism towards the EDJ forming organic crescents which are calcified later (Hirai, 1971). Furthermore, it has been proposed that some remaining enamel matrix proteins forms envelopes that surround individual crystallites (Mishra et al., 2009).

2.2.1.5. *Post-maturation stage*

Following maturation, ameloblasts undergo further morphological changes, where they flatten and become thinner **(Figure 2.3 (7))**. A primary enamel cuticle is formed, separating the ameloblasts from the enamel. The ameloblasts attach their distal ends to the cuticle and together with the remnants of the tooth organ form the reduced enamel epithelium. This epithelium protects the enamel against the formation of a cementum layer upon eruption and results in the formation of the Nasmyth's cuticle (remnant of the enamel organ). Upon tooth eruption, the enamel is believed to undergo further

mineralisation by the surrounding saliva, and the reduced enamel epithelium will become the junctional epithelium (Nanci, 2012, Berkovitz et al., 2010).

Unlike dentine and bone the growth of enamel crystallites proceeds gradually through all the developmental stages (Aoba, 1996). Enamel is considered to be fully mineralised when the tooth erupts into the oral cavity with concentrations of 96% mineral and 2-4% water and 1-2% organic matrix by weight (LeFevre and Manly, 1938, Deakins and Volker, 1941, Robinson et al., 1971, Simmer and Fincham, 1995, Schmitz et al., 2014) and approximately 86% mineral, 12% water and 2% organic material by volume (Crabb and Darling, 1960, Stack, 1967). It has been reported that during this stage the ameloblasts retract from the matrix and emerge as dormant, low columnar cells. When the tooth starts to erupt, these cells fuse with the oral epithelium, making mature enamel a non-living tissue (Palmer et al., 2008). Therefore, unlike other mineralised tissues such as dentine, cementum and bone, when enamel is fully mature it is no longer in contact with cellular elements and hence has no biological regenerative or self-repair capacity (Goldberg et al., 1995, Smith and Nanci, 1995, Fincham et al., 1999, Lacruz et al., 2012a, Cao et al., 2015, Habelitz, 2015, Carneiro et al., 2016). Various workers speculate that a final mineralisation stage takes place post eruption via mineral ions from the saliva, without cellular intervention (Robinson et al., 1997, Smith, 1998).

Therefore, it is crucial to understand the precise timing and spatial progression of biomineralisation in order to provide information for studies aiming to introduce new methods to regenerate enamel or synthesise smart materials similar to enamel. The biomineralisation process can be mapped by observing the route of c-HAp crystallites evolution and mineral density fluctuations. (Nanci, 2012, Berkovitz et al., 2010).

2.2.2. The enamel matrix

Mature dental enamel is believed to contain approximately 50-fold less proteins than dentine or bone, and are mostly found in the spaces between enamel prisms (Piez, 1963). Unlike other mammalian mineralised tissues, the dental enamel matrix contains no collagen and consists of several proteins, some of which are unique to enamel. New enamel matrix proteins are still being characterised and are divided into amelogenins with their processing products and non-amelogenins (Robinson et al., 1995a). The most abundant of the secreted enamel matrix proteins are amelogenin, ameloblastin, and enamelin (Hu et al., 1997). The heterogeneity of enamel proteins is thought to be related to variations in carbohydrate moieties (Akita et al., 1992).

2.2.2.1. *Amelogenins*

A complete amino acid sequence of a novel protein unrelated to any previously characterised protein was identified by Piez (1960) during his work with un-erupted human molars. It is now established that this unknown protein is called amelogenin and it is the main secretory product of ameloblasts. It corresponds to approximately 85-90% of the organic component secreted during amelogenesis and can be found in all stages of enamel development (Eastoe, 1963, Eastoe, 1965, Eastoe, 1979, Fincham et al., 1992, Aoba, 1996). Termine et al. (1980) employed dissociative extraction of developing bovine teeth and observed that amelogenins account for 70% of total matrix proteins during early foetal development at 2-4 months. This value increases to 85-90% at 5-6 months then drops to approximately 50% during enamel maturation, where the remaining percentages are made up for by non-amelogenins. Unpublished observations using dissociative extraction on developing bovine teeth by Fincham et al. (1999) suggested that these values may be greater than those presented by Termine et al. (1980).

Amelogenins are bipolar, lipid-like, mostly hydrophobic, glycosylated and phosphorylated proteins, insoluble in 0.5 M ethylenediaminetetraacetic acid (EDTA) (Veis, 2003). They appear as featureless globular particles with transmission electron microscopy (TEM) (Bai and Warshawsky, 1985) ranging in size from 5-27 kDa and have high concentrations of proline, glutamine, leucine, and histidine (Snead et al., 1985, Yamakoshi et al., 1994, Fincham et al., 1995, Aoba, 1996, Veis, 2003).

The human genome contains two amelogenin genes located on the X (AMELX) and Y (AMELY) chromosomes, however, AMELX is expressed at significantly higher levels and is linked to amelogenesis imperfecta (AI), an inherited condition leading to enamel defects (Salido et al., 1992, Goldberg et al., 1995, Fincham et al., 1999). Studies on rodents enamel established that *Amelx* mutant mice show abnormal enamel formation. (Fincham et al., 1999). Furthermore, it was reported that enamel from amelogenin-null animal models displayed a loss of prismatic architecture; however, there was no disturbance to the nucleation of c-HAp crystallites (Sigel et al., 2008).

Full-length amelogenins have between 173 and 210 amino acids, depending on the species (Veis, 2003). They comprise of three domains, an amino-terminal (N-terminal) domain commonly known as tyrosine-rich amelogenin peptide (TRAP), a hydrophobic central domain and a hydrophilic, highly charged carboxy-terminal (C-terminal) telopeptide domain (Aoba, 1996, Fincham et al., 1999, Palmer et al., 2008). It has been observed that amelogenins undergo extracellular proteolytic processing directly after secretion, and are gradually lost during the mineralisation process (Goldberg et al., 1995). It was reported that fluorosis and other tooth abnormalities may occur due to the

improper degradation of amelogenins (Aoba, 1996). The amelogenin gene produces more than 15 different alternatively spliced isoforms of amelogenin with varying proportions depending on the developmental stage of enamel (Goldberg et al., 1995). The most abundant amelogenin spliced isoform is known as M180 followed by the Leucine-rich amelogenin polypeptide (LRAP). LRAP is the smallest of the amelogenin splice products and contains only the N- and the C- terminals of the full amelogenin sequence (Gibson et al., 1991). The role of LRAP is not very well understood but it is suggested to be involved in ameloblast differentiation(Goldberg et al., 1995, Palmer et al., 2008, Stahl et al., 2013), crystallite growth (Goldberg et al., 1995, Ravindranath et al., 2007, Palmer et al., 2008) and regulation of mineralisation (Le Norcy et al., 2011, Stahl et al., 2013). Further, a recent study reported that LRAP plays a role in promoting the growth of mature enamel crystals and may be used to develop of an effective approach to regenerate enamel structure and properties (Kwak et al., 2017).

A number of structural roles of amelogenins were suggested by various studies including space-filling (Eastoe, 1963, Eastoe, 1979), inter-crystallite packing (Warshawsky et al., 1981), crystallite-crystallite bridging (Fincham et al., 1999), mineral nucleation (Moradian-Oldak et al., 2002, Tarasevich et al., 2007), crystallites organisation, inhibition of crystallite growth (Moreno and Aoba, 1987, Moradian-Oldak et al., 1998), prevention of crystallite fusion, facilitation of minerals diffusion to the calcifying sites on the growing crystallites (Warshawsky, 1985), regulation of precipitation kinetics and determination of crystallite orientation (Mura-Galelli et al., 1992). Furthermore, it has been reported in various studies that amelogenins could interact with members of the collagen family (Wang et al., 2005, Deshpande et al., 2010). It is speculated that the crystallite growth inhibition role of amelogenins help

control the number and orientation of crystallites in order to prevent random proliferation, fusion and overgrowth of crystallites (Aoba, 1996). Furthermore, the mineral nucleation ability was suggested to be due to the strong apatite binding affinity of amelogenins (Goldberg et al., 1995, Fincham et al., 1999). This binding affinity was reduced with the cleavage of the hydrophilic C-terminal of amelogenin (Aoba et al., 1987).

However, various workers refuted the idea of any direct involvement of amelogenins in the nucleation (Martinez-Avila et al., 2012, Smith et al., 2016, Lacruz et al., 2017), growth (Lacruz et al., 2017) and orientation (Smith et al., 2016) of enamel crystallites; instead, it was hypothesised that they support and separate enamel crystallites, expand the enamel matrix to allow for crystallite elongation and organisation (Smith et al., 2016) and act as a reservoir of mineralising ions (Martinez-Avila et al., 2012). Furthermore, Smith et al. (2016) proposed that amelogenins interact with c-HAp crystallites to control ACP transportation into c-HAp and prevent OCP formation.

2.2.2.1. *Non-amelogenins*

Non-amelogenins were previously referred to as enamelins but it was suggested that the term, enamelin is to be restricted to the protein and peptide components remaining in the enamel of mature teeth and the term non-amelogenin should be used as a general term for matrix components distinct from amelogenins which are found in developing and mature enamel (Goldberg et al., 1995). The non-amelogenin family include enamelins, ameloblastins (also called amelin or sheathlin), tuftelins, tuft proteins, sulphated glycoconjugates, amelotins, odontogenic ameloblast-associated proteins (ODAM, formerly designated APin), proteinases and serum proteins.

Table 2.1: List of non-amelogenins and their recognised or proposed functions.		
Protein		**Recognised or proposed function**
Enamelin		• Apatite nucleation (Hu et al., 2008). • Mineralisation and structural organisation of enamel. • Elongation of crystallites during the secretory stage of amelogenesis (Fincham et al., 1999, Veis, 2003).
Ameloblastin		• Maintenance and stabilisation of the ameloblast differentiation state. • Cell-matrix attachment (Fukumoto et al., 2004). • Regulation of crystallite growth (Yamakoshi et al., 2001).
Tuftelin		• Nucleation of enamel prisms crystallites. • Act as a calcium binding protein (Deutsch et al., 2002, Palmer et al., 2008).
Tuft protein		• Tooth protection under high functional forces (Myoung et al., 2009).
Sulphated glycoconjugates		• Amelogenin interaction (Fincham et al., 1999).
Amelotin		• Enzymatic cleavage (Iwasaki et al., 2005). • Cell adhesion. • Act as a molecule involved in transport (Somogyi-Ganss et al., 2012).
ODAM		• Amelotins and amelogenins interaction (Holcroft and Ganss, 2011). • Regulation of enamel maturation. • Adhesion of enamel organ to the enamel surface (Nanci, 2012). • Maintenance of the integrity of the dental junctional epithelium (JE) attachment (Nishio et al., 2013, Wazen et al., 2014).
Proteinases	MMP-20	• Processing and cleaving early-secreted matrix proteins (Caterina et al., 2002, Beniash et al., 2006, Palmer et al., 2008, Lu et al., 2008), with amelogenin being its major substrate (Llano et al., 1997, Ryu et al., 1999, Simmer and Hu, 2002). • Play a role in enamel formation and EDJ maintenance (Lacruz et al., 2017).
	KLK-4	• Degradation of enamel matrix proteins following the cessation of matrix formation (Simmer and Hu, 2001, Nanci, 2012, Lu et al., 2008, Palmer et al., 2008).
Serum albumin		• Inhibit crystal growth by binding to c-HAp (Garnett and Dieppe, 1990, Robinson et al., 1992)

Other matrix proteins, such as fetuin, γ-globulin, α-2 HS glycoprotein, proline-rich salivary protein (Strawich and Glimcher, 1990, Strawich et al., 1993) and biglycan

(Goldberg et al., 2005) were also identified in the enamel matrix.Furthermore, recent studies linked keratin 75 mutations with increased susceptibility to dental caries claiming that epithelial hair keratins are incorporated into mature enamel (Duverger et al., 2014, Duverger et al., 2016). Table 2.1 displays a list of the proposed and recognised functions of the main non-amelogenin proteins; a complete overview can be found elsewhere (Bartlett et al., 2006).

2.2.2.2. *Lipids*

Enamel lipids were reported to be extracellular (Goldberg and Septier, 2002). It has been suggested that lipids occupy approximately 0.2% by weight of developing enamel which may result from the lipid rich membrane of Tomes' process being trapped in the matrix (Fincham et al., 1999). A number of reports suggested that lipids may play a role in the enamel matrix (Shapiro et al., 1966, Prout et al., 1973). Fincham et al. (1999) stated that lipids induce structural alterations in the forming enamel impairing the initial mineralisation and may contribute to enamel formation.

2.2.3. Hydroxyapatite crystal structure

Calcium orthophosphates are abundant in both nature and living organisms, and consist of three major chemical elements: calcium, phosphorus and oxygen. HAp, $Ca_{10}(PO_4)_6(OH)_2$, is the least soluble and second most stable calcium orthophosphate after fluorapatite (FAp) (Kay et al., 1964). Precipitation of HAp occurs according to the following reaction (Lacruz et al., 2017):

$$10Ca^{2+} + 6HPO_4^{2-} + 2H_2O \rightarrow Ca_{10}(PO_4)_6(OH)_2 + 8H^+$$

Equation 2.1

It crystallises in the monoclinic system, and at temperatures above 250 °C, a phase transition to the hexagonal system occurs, with the latter being the more common form found in biological apatite (Dorozhkin, 2009). HAp forms the inorganic material of enamel, dentine, cementum, bone and various pathological calcifications. Any basic calcium phosphate with Ca/P ratio in the ranges of 1.5-1.67 decomposes into HAp and β-tricalcium phosphate upon heating at 1000°C. The HAp crystallite is insoluble in water and has a right rhombic prism unit cell of 18 ions (Kay et al., 1964, Elliott, 1964). Hexagonal HAp has the space group symmetry $P6_3/m$ with lattice parameters in the ranges of $a = b =$ 9.421-9432 Å and $c =$ 6.881-6.882 Å with $\gamma = 120°$ (Trautz, 1955, Carlstrom, 1955, Kay et al., 1964). Crystallite growth is preferentially in the c-axis direction. The structure of HAp can be described as being a collection of overlaid stacks of the above-mentioned ions. At the centre of the structure lies a hydroxyl column which extends through and parallel to the long axis (c-axis) of the crystallite. In the plane of the diagram, a triangle of calcium ions ($Ca\ II$) and a 60° out phase triangle of phosphate ions surrounds the hydroxyl column. The whole structure is enclosed by a hexagon of calcium ions ($Ca\ I$) **(Figure 2.9)** (Kay et al., 1964, Robinson et al., 1995b).

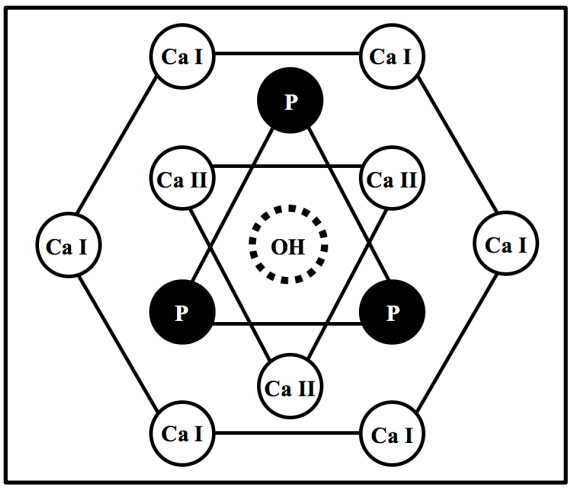

Figure 2.9: A schematic of hydroxyapatite viewed down the hydroxyl column **(Adapted from Robinson et al. (1995b))**.

According to Elliott (1964) the presence of HAp in dental enamel was corroborated in the early 1900s using X-ray diffraction. Stoichiometrically speaking, it is worthwhile to consider that the above-mentioned pure HAp composition is rarely found in human dental enamel. Instead, biological apatite, $Ca_{10-x}H_x(PO_4, CO_3)(OH)_{2-x}$, occurs mainly in the form of calcium-deficient, non-stoichiometric, carbonate (3.5-7.4 $wt.\%$), sodium (0.5-1 $wt.\%$), magnesium (0.4-1.2 $wt.\%$), potassium (0.02-0.08 $wt.\%$), chloride (0.01-0.3 $wt.\%$) and fluoride (0.01-0.06 $wt.\%$) containing HAp. These compositional values vary even between the core and periphery of a single prism (Daculsi et al., 1997, Finke et al., 2000).

It was reported that due to calcium deficiency, the phosphate groups are protonated in order to maintain electron polarity. The carbonate ions were suggested to incorporate into the crystalline lattice at two sites, resulting in two types of substitutions, type A and type B. In type A, carbonate replace the hydroxyl ion, and in type B it substitute for phosphate ions (Elliott, 1964, Elliott, 1965, Elliott et al., 1985, Aoba and Moreno, 1990, Penel et al., 1998, Veis, 2003). It was also suggested that the carbonate may be located on entrapped surfaces in the c-HAp lattice (Hendricks and Hill, 1950). Twelve H^+ protons are released for every unit cell of calcium deficient c-HAp crystallites, lowering the pH of the surrounding environment, according to the following equation (Lacruz et al., 2017):

$$18Ca^{2+} + 10HPO_4^{2-} + 2CO_3^{2-} + 4H_2O \rightarrow Ca_{18}(PO_4)_8(HPO_4)_2(CO_3)_2(OH)_4 + 12H^+$$

Equation 2.2

Furthermore, c-HAp crystallites may have substitutions of divalent and trivalent cations for calcium ions, and fluoride for hydroxide ions (Veis, 2003). Up to date there is no

evidence of biologically formed non-carbonated HAp (Elliott, 1964, Finke et al., 2000, Baeuerlein, 2004).

c-HAp is the most produced phosphate mineral, having smaller crystallites (Elliott, 1964), higher solubility, lower stability (Veis, 2003, Baeuerlein, 2004) and lower crystallinity (Dorozhkin, 2009) than pure apatite. Furthermore, synchrotron X-ray diffraction (S-XRD) studies on powdered human dental enamel found the lattice parameters to be different from that of pure HAp due to the impurities found in the former. Lattice parameters in the ranges of $a = b =$ 9.440-9450 Å and $c =$ 6.878-8.904 Å for dental enamel c-HAp have been reported in the literature (Trautz, 1955, Carlstrom, 1955, Glas, 1960, Glas, 1962, Young and Mackie, 1980, Wilson et al., 1999, Colaço et al., 2012). Chemically pure HAp on the other hand have been reported to have lattice parameters in the ranges of $a = b =$ 9.421-9.432 Å and $c =$ 6.881-6.882 Å (Carlstrom, 1955, Trautz, 1955, Kay et al., 1964) indicating a slight expansion of the a-axis in dental enamel (Elliott, 1964, LeGeros et al., 1969).

Biological apatite may vary widely between different hard tissues. For instance, dental enamel apatite has lower solubility, larger crystallites and lower concentrations of magnesium, fluoride and carbonate than bone or dentine (Brown and Constantz, 1994, Dorozhkin, 2007). Furthermore, it was found that the Ca/P mol. ratio of dental enamel was lower than pure HAp, whereas in bone and dentine the ratio was higher than pure HAp (Elliott, 1964).

In developing enamel, the first detectable crystallites have been reported to appear as long plates (Rönnholm, 1962a) or ribbons (Rönnholm, 1962a, Kerebel et al., 1979),

measuring approximately 1.5 nm in thickness (Rönnholm, 1962a, Kerebel et al., 1979, Beniash et al., 2009) and 15 nm in width (Kerebel et al., 1979). As enamel matures, the crystallites assume more irregular profiles, where the majority have a roughly flattened hexagonal cross-sections (Frazier, 1968, Jongebloed et al., 1975, Kerebel et al., 1979), measuring approximately 26.3 nm in thickness, 68.3 nm in width (Kerebel et al., 1979, Daculsi et al., 1984) and with lengths that, in some cases, span the entire thickness of enamel (Boyde, 1989, Shore et al., 1995b). In biological systems, the mechanisms that control the nucleation and growth of calcium phosphates are still largely unknown (Mura-Galelli et al., 1992). c-HAp is believed to be formed on an organic extracellular template by series of $[Ca^{+2}] \times [P_i]$ compounds that assemble to form c-HAp precursors. Suggested precursor pathways to c-HAp formation include dicalcium phosphate dihydrate (DCPD, $Ca(HPO_4).2H_2O$; the mineral brushite), OCP ($Ca_8H_2(PO_4)_6$) and ACP ($Ca_9(PO_4)_6(var.)$) (Elliott, 1994).

A number of workers suggested that OCP is the likely nucleating phase for c-HAp (Brown, 1966, Brown et al., 1987, Mura-Galelli et al., 1992, Dowker et al., 1999, Suvorova et al., 2001). OCP is less thermodynamically stable than apatite, possesses similar crystallographic features to that of HAp (Neuman, 1980), and can be prepared *in vitro* by the slow hydrolysis of DCPD (Elliott, 1994). It has been hypothesised that c-HAp and synthetically precipitated HAp contain a ‘‘central dark line’’ consisting of OCP, which further supports the belief that OCP is a possible HAp precursor (Dorozhkin, 2007). However, the conclusion that OCP is a precursor phase for biological apatite remains controversial due to lack of *in vivo* evidence (Aoba and Moreno, 1990, Grynpas and Omelon, 2007). Various workers argued that the thermodynamically unstable ACP is the likely initial c-HAp precursor which undergo

solid-state transition into poorly crystalline apatite (Betts et al., 1981, Lowenstam and Weiner, 1985, Beniash et al., 2009, Simmer et al., 2012). It was demonstrated that ACP is the precursor for apatite in the radular teeth of chitons (Lowenstam and Weiner, 1985), and more recently, ACP was detected around human amelogenin aggregates *in vitro* (Martinez-Avila et al., 2012).

2.2.4. Human enamel microstructure

2.2.4.1. *Cross striations*

The rate at which ameloblasts deposit enamel matrix varies in regular cycles giving rise to both circadian (daily) and circaseptan (approximately weekly) fluctuations. Many workers have held that the daily and weekly fluctuations in ameloblast activity can be seen in fully mineralised enamel as prism cross-striations and striae of Retzius, respectively **(See Section 2.2.4.2) (Figure 2.10)** (Boyde, 1964, Maas and Dumont, 1999).

With the light microscope, cross-striations appear as slight striations perpendicular to prisms long axes at regular intervals of approximately 4 μm (range 2–8 μm) (Boyde, 1964, Rozzi, 1998, Mishra et al., 2009) and as transverse lines across prisms under the polarised light **(Figure 2.10)** (Lacruz and Bromage, 2006). With the scanning electron microscope (SEM) cross striations appear as successive dark and light bands along prisms corresponding to prism varicosities and constrictions (Rozzi, 1998, Risnes, 1998). These varicosities and constrictions are believed to result from variations in the width of the ameloblastic pit in the surface of the developing enamel tissue (Boyde, 1964, Mishra et al., 2009).

Cross striations have been associated with daily changes in the rate of production of enamel matrix where varicosities and constrictions correspond to faster and slower phases of amelogenesis respectively. Nevertheless, of the association between the circadian clock and enamel development remains poorly understood (Boyde, 1964, Lacruz et al., 2012a). The existence of cross striations is incorrectly regarded by some to be artefacts produced by sectioning, or due to additive contrast effects as a result of the thickness of a ground section (Boyde, 1986).

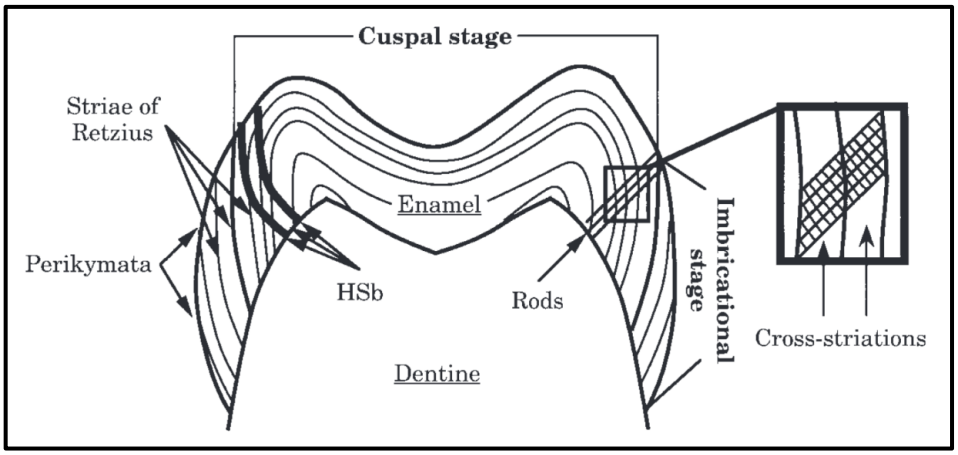

Figure 2.10: Incremental lines in enamel. HSb, Hunter-Schreger bands **(Reproduced with permission of the rights holder, Elsevier, from Rozzi (1998))**.

2.2.4.2. *Striae of Retzius, perikymata and the neonatal line*

Striae of Retzius are successive bend planes in dental enamel that reflect variation in structure and mineralisation (Boyde, 1964, Boyde and Jones, 1983, Mishra et al., 2009). Based on the striae, the tooth crown can be divided into two stages: the cuspal and the imbricational stages. The cuspal stage comprises of striae that does not reach the enamel surface. However, in the imbricational stage, the striae reach the surface to produce concentric grooves known as perikymata which is not necessarily present in all mammalian teeth. The first imbrication line reaching the enamel surface defines the limit between the cuspal and the imbricational stages (Beynon and Wood, 1987, Rozzi, 1998, Risnes, 1998). Each incremental line describes the plane of the developing

enamel surface at a given moment during enamel formation. The striae of Retzius are believed to act as barriers against carious lesions progression towards the enamel centre (Darling, 1958).

It is suggested that due to the abrupt metabolic changes that the infant undergoes at birth, a characteristic and prominent incremental line approximately parallel to the EDJ termed the neonatal line can be seen in slices of mature enamel (Schour, 1936, Avery and Chiego, 2006). The neonatal line separates pre- and post-natal enamel and is believed to act as a barrier against carious lesions progression (Schour, 1936, Mishra et al., 2009).

2.2.4.3. *Hunter-Schreger bands*

These bands extend up to two thirds of the thickness of enamel and are absent from the enamel near the tooth surface (**Figure 2.10**) (Avery and Chiego, 2006). It has been proposed that the outer enamel pattern of mammals consists of parallel prisms. However, towards inner enamel, prismatic bundles cross-over or decussate in a stepwise manner. When light is projected at the enamel surface, it is transmitted along the long axis of one prism group but not along the adjacent group giving rise to alternating light and dark bands of prism groups termed Hunter-Schreger bands (HSb) (**Figure 2.10**) (Hirota, 1982, Hirota, 1986, Macho et al., 2003, Lynch et al., 2010, Cox, 2013). This is suggested to be caused by secretory ameloblasts moving laterally, left or right parallel with neighbouring cells, where transverse rows of cells move in opposite directions (Boyde and Stewart, 1963, Hirota, 1982, Hirota, 1986, Hirota, 1989, Osborn, 1990, Boyde, 1997, Macho et al., 2003, Skobe, 2006, Avery and Chiego, 2006, Lynch et al., 2010, Cox, 2013).

Prisms within one HSb lie parallel to one another and at an angle to prisms in adjacent bands. HSb measure at approximately 50 μm in width in longitudinally sectioned human enamel, starting at the EDJ, curling and fading out towards the enamel surface (Osborn, 1990). It is believed that prism decussation gives rise to unequal wear rates (Boyde, 1997) and plays a role in preventing crack propagation while strengthening the enamel in respect to the horizontal tension forces (Koenigswald et al., 1987).

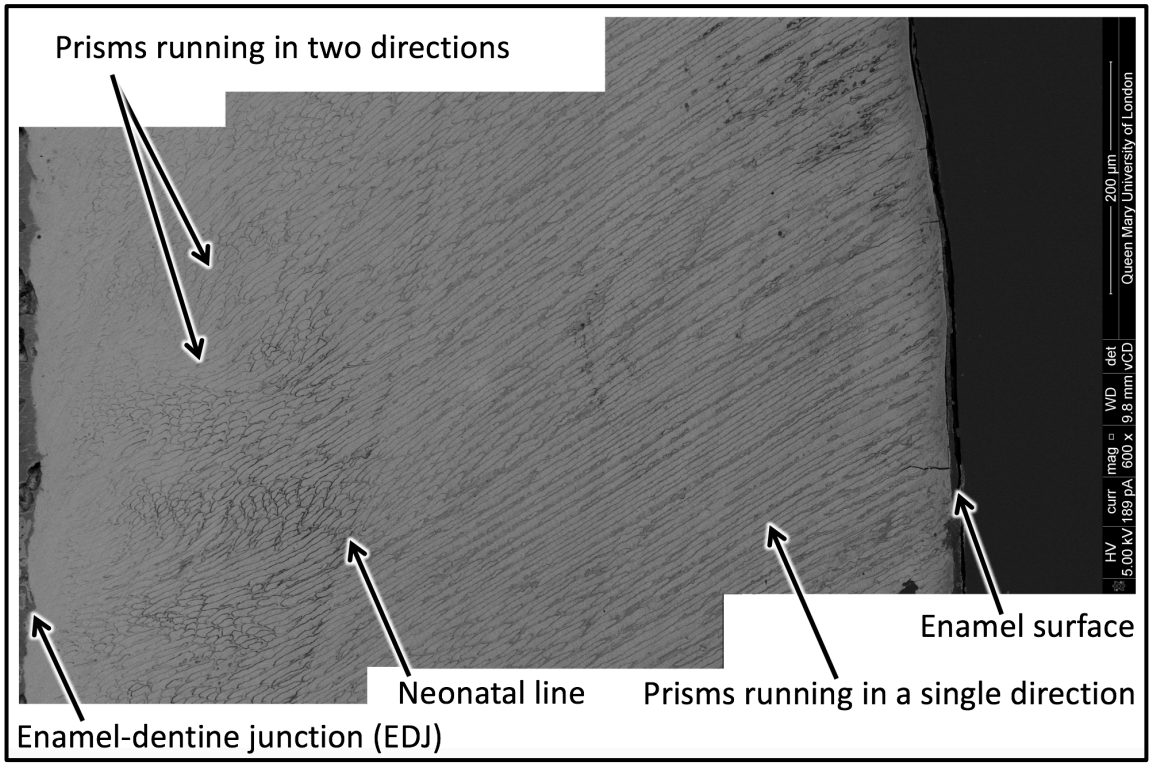

Figure 2.11: qBSE image of human incisal enamel displaying prisms directions from the EDJ towards the enamel surface. It can be seen that prisms run in a single direction and suddenly divide into two groups running at different orientations as they approach the EDJ

2.2.4.4. *Enamel lamellae and tufts*

Tufts and lamellae are organic-rich segments of enamel, believed to be regions of defective mineral content. Lamellae and tufts were reported to be absent in immature enamel and are thought to form either during enamel development or after eruption. Enamel lamellae are thin leaf-like hypo-mineralised spaces that extend from the enamel cuticle to the EDJ. Enamel tufts are several prisms wide and extend to up to one tenth towards the surface. They often arise from prisms close to the EDJ that remain

demineralised following full tooth development (Boyde, 1964). Furthermore, enamel tufts are believed to be crystallite growth initiators or nucleators (Fincham et al., 1999).

2.2.4.5. *Enamel spindles*

Enamel spindles are narrow, finger-like structures that are believed to be extensions of odontoblasts processes that extend from the EDJ and through the enamel layer. Since dentine forms before enamel, the odontoblastic process occasionally penetrates the junction, and enamel forms around this process, forming a tubule. These small tubules may contain a living process of the odontoblast, possibly contributing to the vitality of the EDJ. Tubules are found singularly or in groups and are shorter than tufts (Avery and Chiego, 2006, Berkovitz et al., 2010).

2.2.5. Variations in chemical composition, mechanical properties and texture magnitude in human dental enamel

‘‘Since the masticatory apparatus functions as an integrated unit, it follows that the structure of any of its parts can only be explained in terms of its function and that with reference to the mechanism of function of the system as a whole’’ (Hemae, 1967).

2.2.5.1. *Chemical composition*

An increase in calcium, phosphate and fluoride concentrations and a decrease in magnesium, carbonate and chloride concentrations from the EDJ peripherally were reported in human enamel (Brudevold et al., 1956, Little and Brudevold, 1958, Frank et al., 1966, Besic et al., 1970). The lower wt.% of calcium and phosphate in the enamel along the EDJ corresponds to a lower degree of mineralisation. This was hypothesised to be due to the presence of hypo-mineralised microstructural features such as enamel tufts, lamellae and spindles (Cuy et al., 2002). Furthermore, it was found that the ratio

of calcium and phosphorous was the lowest (Robinson et al., 1971) and the concentration of zinc, lead and tin was the highest (Brudevold and Steadman, 1956b, Brudevold and Steadman, 1956a, Suga, 1970) at the surface of human enamel.

Table 2.2: Chemical composition of human enamel, dentine and bone (Retief et al., 1971, Legeros, 1981).

Constituents	Enamel	Dentine	Bone
Calcium ($wt.\%$)	36.00	27.00	24.50
Phosphate ($wt.\%$)	17.70	13.00	10.50
Carbonate ($wt.\%$)	2.30	4.50	5.80
Sodium ($wt.\%$)	0.50	0.30	0.70
Magnesium ($wt.\%$)	0.40	1.10	0.60
Chloride ($wt.\%$)	0.30	0.01	0.10
Potassium ($wt.\%$)	0.08	0.05	0.03
Pyrophosphate ($wt.\%$)	0.02	0.08	0.05
Fluoride ($wt.\%$)	0.01	0.05	0.02
Zinc ($wt.\%$)	263 ppm	173 ppm	---
Barium ($wt.\%$)	125 ppm	129 ppm	---
Iron ($wt.\%$)	118 ppm	93 ppm	---
Strontium ($wt.\%$)	111 ppm	94 ppm	---
Aluminium ($wt.\%$)	86 ppm	69 ppm	---
Bromine ($wt.\%$)	34 ppm	114 ppm	---

Other workers reported the presence of molybdenum (Nixon et al., 1967), vanadium (Nixon et al., 1967, Brudevold and Soremark, 1967, Hardwick and Martin, 1967), selenium (Hadjimarkos and Bonhorst, 1959) and various other trace elements in human enamel (Weatherell et al., 1974). Moreover, a high content of carbonate was reported in developing enamel tissue compared to fully-developed enamel (Hiller et al., 1975). A comparison between the chemical compositions of human enamel, dentine and bone is given in Table 2.2.

2.2.5.2. *Mechanical properties*

It has been suggested that the Young's modulus and hardness of mature human enamel decrease from the cusp cervically (Craig and Peyton, 1958, Craig et al., 1961, Meredith

et al., 1996, Cuy et al., 2002). Furthermore, an increase in hardness (Willems et al., 1993, Cuy et al., 2002) and Young's modulus (Cuy et al., 2002) was reported when travelling from the EDJ peripherally **(Figure 2.12)**.

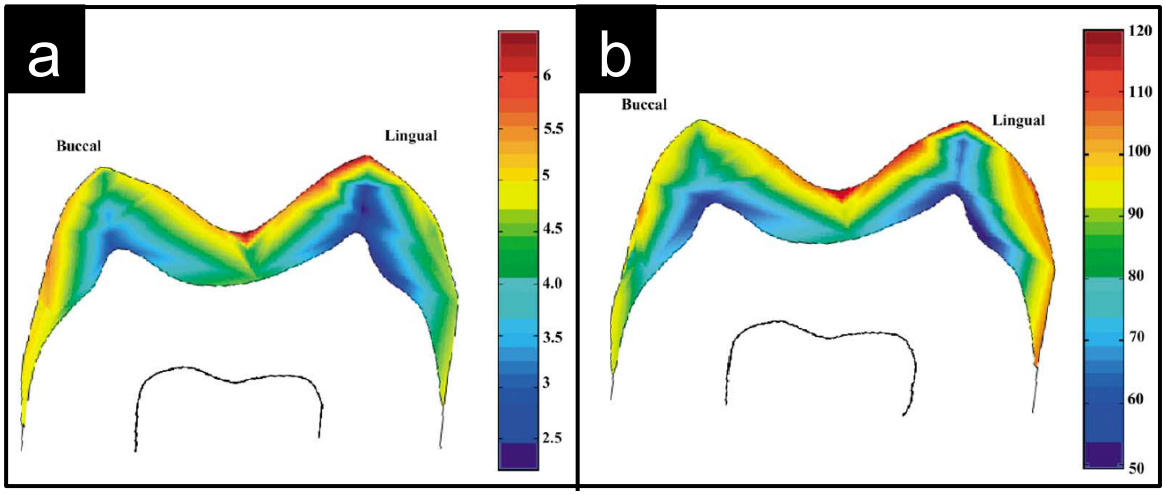

Figure 2.12: 2-D distribution maps for the **a)** hardness (GPa) and **b)** Young's modulus (GPa) maps of human molar enamel determined using nanoindentation **(Reproduced with permission of the rights holder, Elsevier, from Cuy et al. (2002))**.

Cuy et al. (2002) also reported that the hardness **(Figure 2.12a)** and Young's modulus **(Figure 2.12b)** were higher along the enamel surface in the lingual enamel compared to the buccal enamel, and higher along the EDJ in the buccal enamel compared to the lingual enamel. A number of studies suggested that the Young's modulus (Staines et al., 1981, Cuy et al., 2002) and hardness (Kodaka et al., 1992, Cuy et al., 2002) of human enamel correlate with its degree of mineralisation.

2.2.5.3. *Degree of texture*

Polycrystalline materials are composed of numerous small single crystallites (or grains) with different orientations joined at interfaces called grain boundaries. In materials science, the term texture implies preferred orientation and describes the distribution of crystallographic orientation directions of the grains of a polycrystalline material with respect to one another (Wenk and Van Houtte, 2004). Textured materials are anisotropic regarding their physical and mechanical properties with their grains aligning in a

preferred orientation, whereas un-textured materials have fully randomly orientated grains and are generally isotropic (Brokmeier and Yi, 2017). Textured materials have varying degree of texture (texture magnitude). In a textured material, the higher the alignment of grains with respect to one another, the higher texture magnitude of this material and vice versa.

Previous S-XRD studies on mature healthy human teeth have shown enamel to have the greatest degree of texture at the tooth surface, using permanent third molars (Low, 2004), permanent mandibular second premolars (Al-Jawad et al., 2007), permanent maxillary first premolars (Al-Jawad et al., 2008), deciduous maxillary incisors (20 μm beamspot) (Al-Jawad et al., 2012), permanent mandibular first molars (Simmons et al., 2013), a maxillary third molar (Egan et al., 2013) and permanent mandibular first molars (Siddiqui et al., 2014).

Furthermore, S-XRD studies on healthy fully-developed human teeth reported lower degree of texture in the enamel close to the cervical edge, showing that the areas of high crystallite alignment at the top of the crown match the expected biting surfaces (Al-Jawad et al., 2007, Al-Jawad et al., 2008, Simmons et al., 2013, Khan et al., 2016). Using S-XRD, Siddiqui and Al-Jawad (2016) compared healthy maxillary and mandibular deciduous incisors and reported that the enamel of the latter displayed lower degree of texture, emphasising the importance of choosing appropriate type-matched controls.

Simmons et al. (2011) analysed sequential mesio–distal slices of human permanent maxillary first premolar using S-XRD. They reported that enamel displayed lower

degree of texture in both the buccal and palatal slices than the central slice. The area near the marginal ridge in the most central slice was found to have lower degree of texture than the rest of the tooth slice. However, this was not the case in adjacent slices, where higher texture magnitude was reported near the marginal ridge. Furthermore, a decrease in the degree of enamel texture near the cusp in the most central slice was reported. This finding does not agree with most texture studies on dental enamel, where a higher degree of texture was reported near the cusp. However, since this was a slice from the centre of the tooth it is likely that this data is in fact from through the fissure and not the cusp.

Simmons et al. (2013) used S-XRD on permanent human lower first molars to study the evolution of texture magnitude as a function of maturation. It was shown that during the early stages of enamel development the degree of texture was more homogenous. Further, they demonstrated that in later stages of maturation the texture magnitude becomes more heterogeneous, increasing around the cusps and decreasing at the dentine horns and along the inner cervical sides.

Other S-XRD studies assessed variations in human dental enamel crystallite organisation in disease. For instance, it was reported that mucopolysaccharidosis (MPS) II and IVA affected deciduous incisors displayed constant texture magnitude throughout the thickness of labial enamel (Al-Jawad et al., 2012). Another study stated that MPS I affected deciduous incisors tend to have a consistent labial enamel texture magnitude, whereas lingual enamel displayed varying degree of texture with a higher texture magnitude near the cervical edge (Khan et al., 2016). Furthermore, using S-XRD on permanent mandibular first molars, Siddiqui et al. (2014) demonstrated that the

demineralisation in natural caries and artificially induced lesions was accompanied by a loss of crystallographic texture. The study also reported the recovery of texture magnitude during remineralisation. Further, a recent study on deciduous incisors showed that local hypoplastic AI affected enamel with known mutation in the enamelin gene resulted in disruption to the texture magnitude of crystallites located near the EDJ.

2.2.5.4. *Conclusion*

To conclude the outcome of the above mentioned studies, it is apparent that the majority of studies reported that the degree of texture in mature healthy human enamel increases from the EDJ peripherally (Low, 2004, Al-Jawad et al., 2007, Al-Jawad et al., 2008, Al-Jawad et al., 2012, Egan et al., 2013, Simmons et al., 2013, Siddiqui et al., 2014) and from the cervical edge towards the cusp (Al-Jawad et al., 2007, Al-Jawad et al., 2008, Simmons et al., 2013, Khan et al., 2016).

The above studies reported higher texture magnitude near the biting surfaces of the tooth, which according to finite element studies, need to withstand the high stresses induced by the process of mastication (Spears and Macho, 1998). The texture magnitude was also reported to increase from the EDJ toward the enamel surface. This follows the same trend found in studies assessing mineral density distribution in teeth. It is interesting to note that the enamel surface, the region where higher texture magnitude is reported, is in direct contact with the oral cavity and hence is expected to resist physical and chemical manipulations. Further, the higher degree of texture from the cusp cervically and from the EDJ peripherally correlates with the enamel degree of mineralisation, hardness and Young's modulus (Cuy et al., 2002). It is therefore likely that the degree of texture may relate to the mechanical properties of enamel. These studies therefore suggest a likely correlation between the degree of texture and the

functional demands, that is, the higher the texture magnitude in a region the higher the loading forces it is subjected to and vice versa.

This is further supported by Simmons et al. (2013) who reported a more homogenous texture magnitude during the early stages of enamel development, which may be explained in term of texture magnitude/functional demand relationship, since unerupted teeth are not yet subjected to loading forces. Furthermore, the texture magnitude distribution was reported to be more homogeneous in MPS I (Khan et al., 2016), II and IVA (Al-Jawad et al., 2012) affected enamel. MPS affected individuals experience various dental related abnormalities such as enamel thinning and enamel-dentine delamination at the EDJ (Hendriksz et al., 2013) which may be related to the inability of enamel to efficiently withstand the functional forces that result from mastication. Moreover, hypo-mineralised (natural or artificially induced) (Siddiqui et al., 2014) and AI affected (Siddiqui and Al-Jawad, 2016) enamel was found to have lower texture magnitude than healthy enamel. This means that a "material property can be designed by a proper control of the crystallographic texture" (Brokmeier and Yi, 2017).

In order to enhance the current understanding of the natural progression of dental enamel biomineralisation, this study will follow the footsteps of Simmons et al. (2013), who studied the mineral density and the texture magnitude and direction of dental enamel using three molars at various developmental stages. Higher temporal resolution regarding the progression of biomineralisation can be achieved by increasing the sample size in order to identify more subtle changes in biomineralisation as a function of maturation time. Furthermore, it would be beneficial to study different types of teeth

such as lateral and/or central incisors to assess and compare the differences in the biomineralisation progression in different dentitions.

2.2.6. Cross-species variations of enamel development

This section provides a basic overview of a limited selection of examples of cross-species variations in enamel development; for a more comprehensive overview, the reader is directed to Professor Alan Boyde's PhD thesis (Boyde, 1964).

There is significant evidence to suggest that the progression of enamel development varies across species (Smith, 2008). For instance, the development of rat enamel results in highly uniform, ordered and regular crystallites, unlike human enamel development where crystallites are subjected to less control, giving rise to irregular profiles. Moreover, initial crystallite sizes vary amongst species. In rat the dimensions were approximately 20-30 $nm \times 1\,nm$ compared to approximately 15 nm × 1.6 nm in humans. Furthermore, in rodents the crystallites at the final growth stage had a regular hexagonal shape with no evidence of crystallite fusion, unlike human enamel where crystallite fusion does occur giving rise to less regular crystallite shapes especially in the outer layers of enamel (Shore et al., 1995a).

Other workers reported large differences in the sizes, organisation (Veis, 2003) and patterns (Boyde, 1964) of the prisms in dental enamel across species. Further, differences in the lengths of Tomes' process have been reported across species, as well as the strength of enamel close to the ameloblasts, with elephant enamel being the strongest. Furthermore, various enamel microstructural features such as prism decussation and enamel tubules was shown to be present is some species and absent in others (Boyde, 1964). Moreover, the incisors of various animals such as rats exhibit

continuous eruption as opposed to limited eruption in human teeth **(Figure 2.7)** (Warshawsky et al., 1981). Therefore, despite the important role played by the use of animal models for understanding the process of enamel biomineralisation, it is still essential to use human samples due to the above-mentioned subtle differences identified across species.

2.3. Summary and rationale for the thesis

Unlike other mineralised tissues such as dentine, cementum and bone, when enamel is fully-developed, it is no longer in contact with cellular elements and hence has no biological regenerative or self-repair capacity (Fincham et al., 1999, Cao et al., 2015, Habelitz, 2015, Carneiro et al., 2016).

In restorative dentistry, traditional approaches tend to restore damaged enamel by filling enamel defects or capping tooth crowns using various dental restorative materials such as amalgam, ceramics and composite resin (Cao et al., 2015, Duverger et al., 2016). An ideal material would possess identical crystallite structure, physical and mechanical properties and chemical components to that of enamel, in order to withstand continuous stresses and to prevent abrasive damage to healthy enamel during the process of mastication. To date no such materials exist despite efforts to introduce novel enamel repair strategies focusing on biomimetic mineralisation of enamel (Palmer et al., 2008, Moradian-Oldak, 2012, Cao et al., 2015). It is therefore important to study the precise timing and spatial progression of dental enamel biomineralisation not only to obtain an insight on how the hierarchical structure found in enamel comes to existence but also to understand the pathway of its destruction. Furthermore, this information can be used to imitate the natural process of biomineralisation in order to optimise biomimetic

regenerative and reparative dentistry routes and to synthesise materials that are identical to dental enamel.

In order to gain a complete insight into the process of human dental enamel biomineralisation, enamel at different stages of development must be analysed. Central and lateral incisors were chosen in the current investigation due to the fact that single cusp dentitions have less complex enamel crystallite arrangement and therefore offer the simplest case. It has been reported that the enamel of permanent maxillary central incisors starts forming 3-4 months after birth and is fully formed by the age of 4-5 years, approximately 5 years prior to eruption. Furthermore, it was reported that in permanent maxillary lateral incisors, the apposition of enamel and dentine starts between the ages of 10-12 months after birth, the crown formation is completed at 4-5 years and the tooth erupts into the oral cavity between the ages of 10-11 years after birth (Schour and Massler, 1940b). Thus, to acquire developing enamel, un-erupted teeth must be extracted from children within the above-mentioned age range. However, such samples are not readily available for investigation due to the challenges associated with acquiring the necessary ethical approvals. Various studies overcame this issue by recovering developing human enamel samples belonging to diseased juveniles from archaeological sites (Peretz et al., 1997, Reid et al., 1998, Zeygerson et al., 2000, Antoine, 2000, Antoine et al., 2009, Mahoney, 2012, Simmons et al., 2013).

This investigation aims to understand the precise timing and spatial progression of the process of biomineralisation by studying the changes in human dental enamel c-HAp crystallites as a function of time. To do this, spatially resolved S-XRD, X-ray microtomography (XMT) and quantitative back-scattered electrons (qBSE) imaging

were used to acquire information regarding crystallography, relative mineral density and microstructure, respectively.

Chapter 3 - X-ray and scanning electron microscopy methods

3.1. X-ray methods

3.1.1. Introduction to X-rays

3.1.1.1. *X-rays and their interaction with matter*

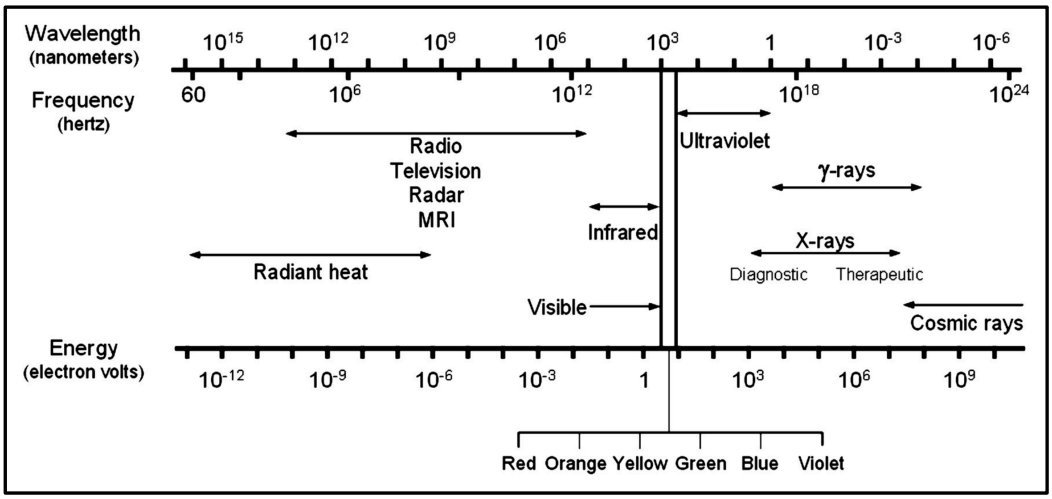

Figure 3.1: The electromagnetic spectrum **(Reproduced with permission of the rights holder, The Society of Nuclear Medicine and Molecular Imaging, from Seibert (2004)).**

X-rays are a form of electromagnetic radiation belonging to the high frequency end of the electromagnetic spectrum, with short wavelengths ranging from 0.01 to 100 Å and energies between 100 (soft X-rays) and 100,000 *eV* (hard X-rays). The electromagnetic spectrum provides a full range of wavelengths of electromagnetic radiation ranging from radio waves to gamma rays. X-rays occupy a small section of the electromagnetic spectrum overlapping with gamma-rays in the shorter wavelengths and with ultraviolet in the longer wavelengths **(Figure 3.1)**. Due to X-rays' high energies they have the ability to ionise most atoms and molecules and are therefore classified as ionising radiation (Seibert, 2004, Cierniak, 2011, He, 2009). X-rays consist of wave packets of energy called photons, where each photon is equivalent to one quantum of energy

(Whaites and Cawson, 2007). The energy (E) of X-rays is given by the following equation:

$$E = \frac{h\,c}{\lambda}$$

Equation 3.1

Where h is Planck's constant, c is the speed of light and λ is the wavelength.

Equation 3.1 shows that the higher the energy of an X-ray, the shorter the wavelength. Upon interaction with an atom, the X-ray photon can be absorbed, and/or it can be scattered. At the atomic level, the main interactions include coherent scattering (also known as Thomson, classical, unmodified or Rayleigh scattering and occurs in X-rays with low energies (10-30 KeV)), Compton effect (also known as Compton scatter, incoherent scatter or modified scattering and occurs in X-rays with energies greater than 30 KeV), photoelectric effect (X-ray energies between 10-150 KeV), pair production (X-rays with energies greater than 1.02 MeV) and photodisintegration (X-rays with energies greater than 10 MeV). X-ray attenuation is the term used to describe the reduction in intensity of the incident beam by both absorption and scattering (Whaites and Cawson, 2007).

Elastic and inelastic scattering are the two main forms of particle scattering in which the total momentum is conserved. In inelastic scattering, the kinetic energy of the colliding bodies is lost to other processes and hence is not conserved:

$$\Delta E \neq 0$$

Equation 3.2

Some of the kinetic energy may be lost to vibrations of the scattered bodies experienced as heat or sound. Other kinetic energy may go into the breakup of the chemical bonds holding the colliding particles together. The Compton effect is essentially an inelastic scattering process between the X-ray photons and electrons in the matter and may be used to collect information on the electronic structure of materials. Other examples of inelastic scattering include resonant inelastic X-ray scattering (RIXS) and X-ray Raman scattering (Grangeat, 2009, Als-Nielsen and McMorrow, 2011).

In elastic scattering, the kinetic energy of the colliding bodies is not lost to other process meaning that the total energy is conserved:

$$\Delta E = 0$$

Equation 3.3

Coherent scattering is an elastic scattering process in which, unlike inelastic scattering, the colliding particles remain intact. X-ray elastic scattering is the main process by which the atomic structures of materials are assessed and occurs when a particle is accelerated sinusoidally by an electromagnetic field radiating light at the same frequency; the process is therefore elastic. For X-rays, electrons are the principal scattering particle in a medium. Elastic scattering methods include wide-angle X-ray diffraction ($\theta > 5°$), small-angle X-ray diffraction ($\theta \approx 0°$), and X-ray reflectivity (films) (Grangeat, 2009).

3.1.2. Laboratory X-ray production

Research laboratories use X-ray tubes as source of X-ray radiation, consisting of a vacuum tube within which reside a negatively charged cathode emitter and a positively charged anode target. There are two X-ray producing interactions between the electrons

emitted and the atoms in the target. In the first, electrons are scattered by electrostatic interactions with the nuclei of the target material, resulting in the direct emission of X-rays from the electron as it loses energy **(Figure 3.2a)**. This process is termed "Bremsstrahlung" which is the German for "deceleration radiation". Bremsstrahlung radiation has a continuous spectrum corresponding to electrons losing different fractions of their initial kinetic energy. When an electron loses a small amount of energy, a longer wavelength of X-ray is produced. When it loses a larger amount of energy, a shorter wavelength X-rays is produced **(Figure 3.2b)**. The spectrum has a minimum wavelength below which X-rays are not produced; this corresponds to the highest energy X-rays which are produced when the electrons lose all their kinetic energy (Seibert, 2004, Cierniak, 2011).

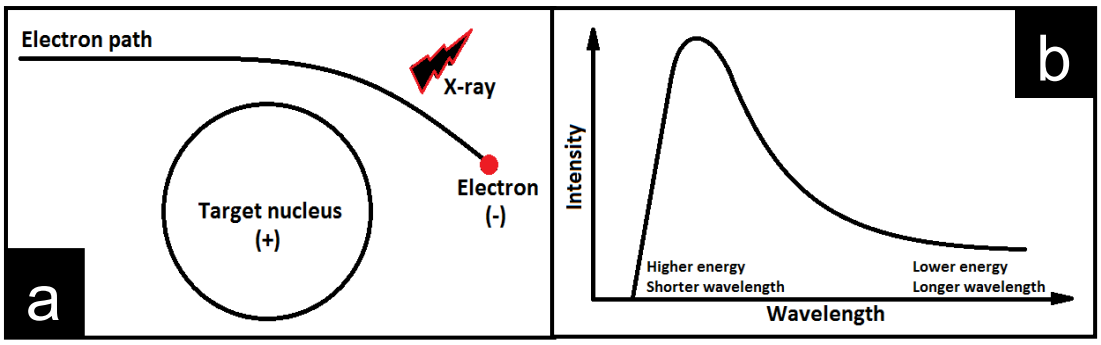

Figure 3.2: Diagrams of **a)** bremsstrahlung radiation, and **b)** bremsstrahlung spectrum.

The second interaction that can take place in the target is between the incoming electrons and the electrons of the target atoms. If the incident electron has certain characteristic energies it can eject electrons from the inner shells and ionise the target atoms. These are filled when the outer shell electrons make transitions by dropping down the quantum ladder to fill the vacant space **(Figure 3.3a)**. These transitions reduce the energy state of the atom by emitting X-rays with characteristic wavelengths. These characteristic spikes are superimposed on the continuous Bremsstrahlung spectrum **(Figure 3.3b)** (Seibert, 2004, Cierniak, 2011).

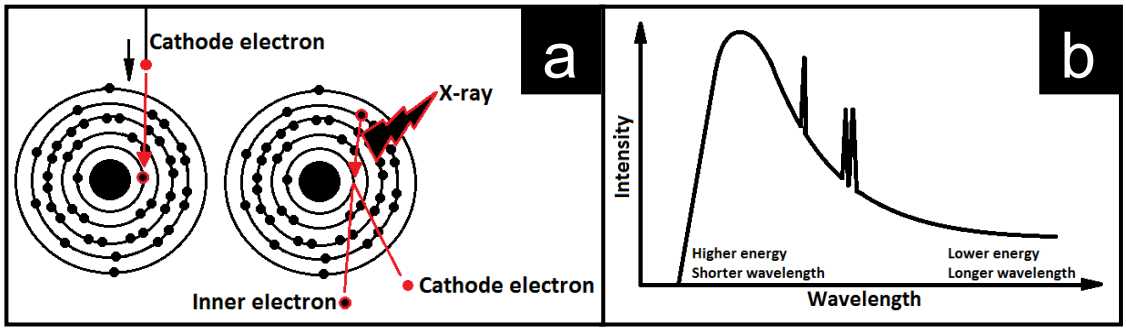

Figure 3.3: Diagrams of **a)** electrons interactions taking place in the target, and **b)** the resulting characteristic spikes superimposed on the bremsstrahlung spectrum.

3.1.3. Synchrotron X-ray production

3.1.3.1. *Introduction*

Synchrotron radiation (SR) was first observed by accident in 1947 using a small 70 MeV synchrotron at the research laboratory of General Electric (Schenectady, New York, USA) (Elder et al., 1947), and began to be used as a research tool in the mid-1960s. Currently, there are about 50 facilities around the world. Due to the continuous wavelength spectrum of SR from infra-red (IR) to X-rays, the photon energy can be tuned using appropriate monochromators to meet the demands of a variety of fields, ranging from physics and material sciences across biology, chemistry, crystallography and geology toward medical and industrial applications (Reimers et al., 2008).

Compared to a lab source, SR has a up to 1014 times higher flux (the number of photons for a given surface during a given time), which allows for higher spatial resolution, rapid scanning and the use of monochromators (Smith and Tafforeau, 2008, Asaizumi et al., 2014). Therefore, the X-rays are intense, tuneable, highly collimated, have a very small divergence and can be monochromatised (selection of a narrow part of the incoming polychromatic beam spectrum using a monochromator) using crystal monochromators (Reimers et al., 2008, Grangeat, 2009). A monochromator works by reflection of the wavelengths that obey Bragg's Law for the particular d-spacings of the

monochromator (Asaizumi et al., 2014). Furthermore, the SR source and the resulting beam diameter are typically few microns in size, which together with the high degree of collimation, allows the beam to be well suited for focusing onto small samples or for space resolved techniques using appropriate optics (Staron et al., 2017).

SR is electromagnetic radiation emitted by accelerating charged particles using magnetic fields. At SR facilities, electrons are generated in an electron gun by thermionic emission from a hot filament and are accelerated to approximately $100MeV$ using a linear accelerator (LINAC). The electrons are then injected into a booster ring where they are further accelerated to an energy up to that of the electrons in the main storage ring. Subsequently, the electrons are injected into and stored in bunches inside an ultra-high vacuum storage ring (providing clean, debris-free environment) where they are accelerated to a constant, relativistic velocities (99.99…% the speed of light) and deflected by a strong, uniform and static magnetic field which force them to travel in a loop along curved paths (Duke, 2000, Hofmann, 2004, Reimers et al., 2008, Als-Nielsen and McMorrow, 2011, Willmott, 2011).

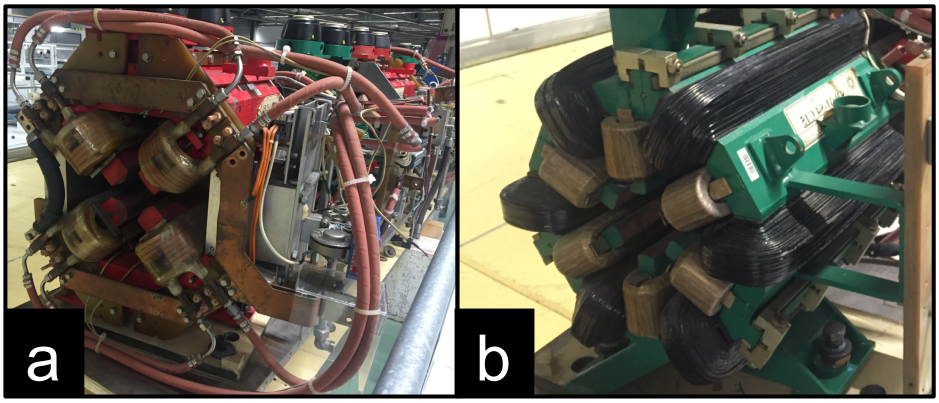

Figure 3.4: a) A Focusing quadrupole magnet and **b)** a correcting sextupole magnet.

Three types of magnets are commonly found in storage rings: dipole- or bending magnets that force electrons to execute a curved path **(Figure 3.5a)**, focusing

quadrupole magnets **(Figure 3.4a)** and chromatic aberrations correcting sextupole magnets **(Figure 3.4b).** Due to SR emission, the electrons of the storage ring lose energy and are reaccelerated every turn by radio frequency cavities to compensate for the lost energy (Willmott, 2011).

X-ray photons with a broad energy spectrum and very small divergence are emitted in a cone tangential to their orbital path either in arced sections of the storage ring containing bending magnets (BM) or straight sections used for magnetic insertion devices (ID) such as wigglers **(Figure 3.5b)** or undulators **(Figure 3.5c)** (Duke, 2000, Hofmann, 2004, Reimers et al., 2008, Als-Nielsen and McMorrow, 2011).

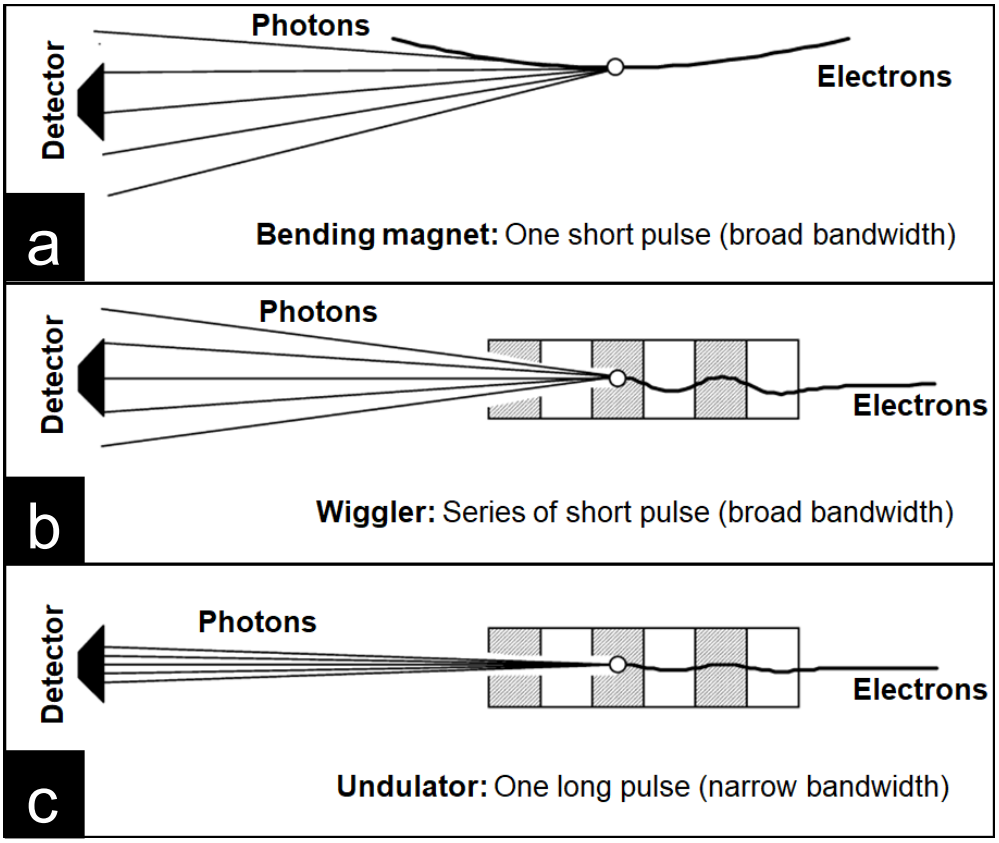

Figure 3.5: Types of SR sources: **a)** bending magnet; **b)** wiggler; and **c)** undulator **(Reproduced with permission of the rights holder, Elsevier, from Margaritondo (2001)**.

BMs are found in arced sections of the storage ring and produce SR that covers a wide and continuous spectrum but with reduced brilliance and focus compared to that from a

magnetic insertion device **(Figure 3.5a)**. BMs generate the curved trajectory of the electron and are arranged so that the magnetic field is pointing vertically so that the plane of the electron orbit lies horizontally (Duke, 2000).

IDs are few metres long straight structures of periodic magnetic multipole situated in the storage ring. They force the charged particles to travel in a sinusoidal trajectory in order to enhance the characteristics of the SR without causing a net deviation from the original beam direction. Wigglers **(Figure 3.5b)** and undulators **(Figure 3.5c)** are the two types of IDs (Duke, 2000, Staron et al., 2017).

Synchrotron beamlines run along BM and ID axes and are divided into three sections: the front end, the optic hutch and the experimental hutch (Willmott, 2011). Figure 3.6 displays a schematic of the main components found in a modern SR source.

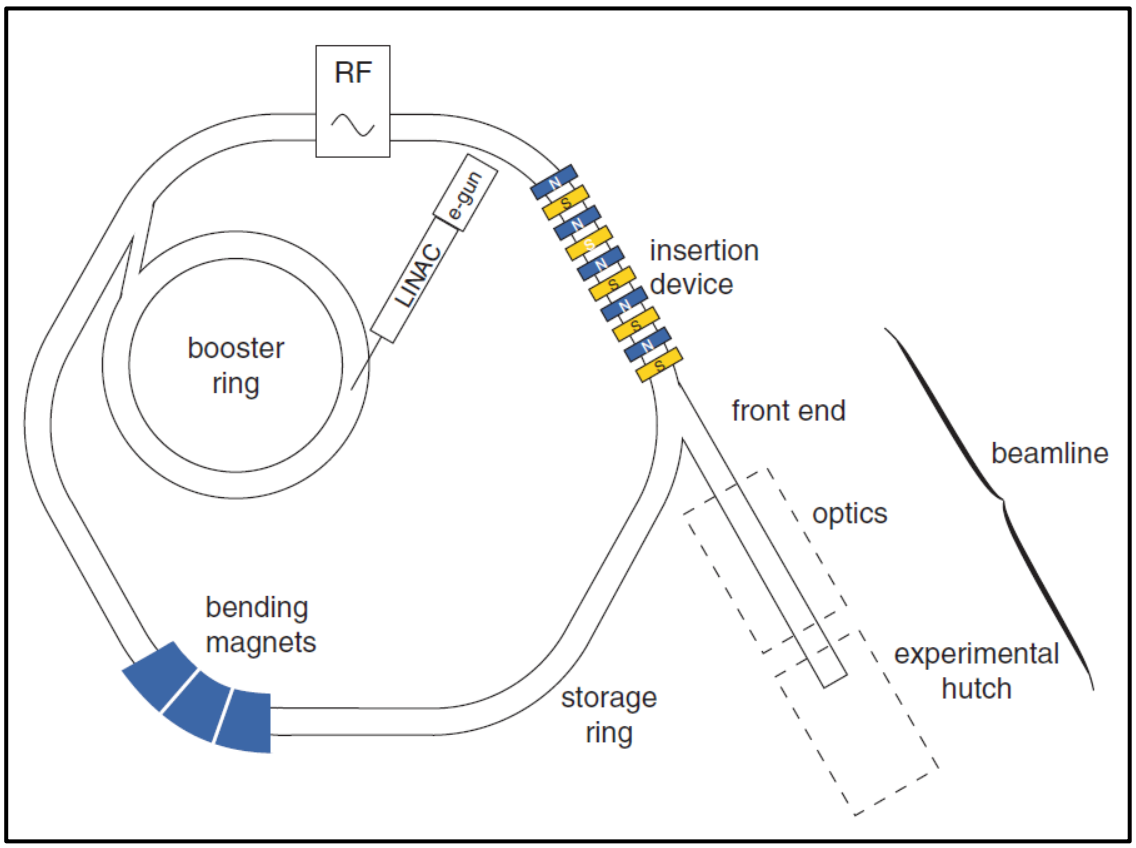

Figure 3.6: A schematic of the main components found in a modern SR facility. e-gun, electron gun. LINAC, linear accelerator. RF, radio frequency supply **(Reproduced with permission of the rights holder, John Wiley and Sons, from Willmott (2011)).**

3.1.3.2. *Synchrotron radiation facilities used in the current study*

To satisfy the objectives of this study, experiments were carried out using B16 and XMaS (BM28) beamlines at Diamond Light Source (DLS) and the European Synchrotron Radiation Facility (ESRF), respectively **(Table 3.1)**.

Table 3.1: A table of the SR sources used

SR facility	Location	Energy (GeV)	Emittance ($nm\,rad$)	Circumference (m)	Commissioned for SR studies
ESRF	Grenoble, France	6	4.0	844	1992
DLS	Oxfordshire, UK	3	6.5	561.6	2006

3.1.3.2.1 XMAS beamline at the European Synchrotron Radiation Facility

The XMaS (BM28) beamline is located on a bending magnet and covers a wide photon energy range from 2.5 to 15 keV. The first optical element on the beamline is the water-cooled Si(1 1 1) double crystal monochromator (DCM) which is located 24.5 m from the source point.

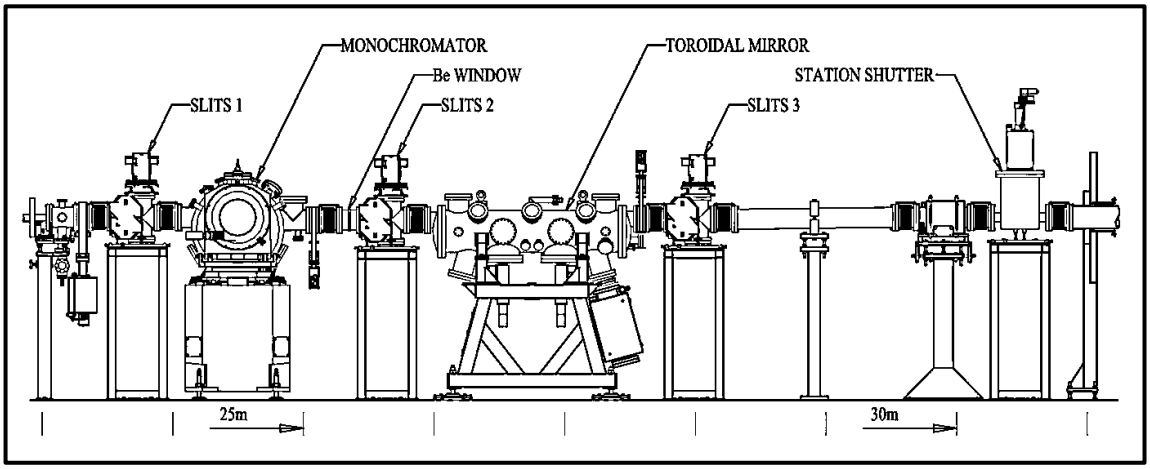

Figure 3.7: The optics of the XMAS (BM28) beamline. **(Reproduced with permission of the rights holder, International Union of Crystallography, from Brown et al. (2001)).**

The first crystal intercepts the full vertical fan of radiation, whereas the second crystal is mounted kinematically in a crystal cage and is positioned by three linear actuators. A cylindrical rhodium-coated Zeiss focusing mirror made from single crystal silicon is bent to a toroidal form and set at a grazing incidence angle of 4.5 $mrad$ providing 1:1

focusing at the sample position and an upper energy cut-off of approximately 15 keV (Brown et al., 2001). A schematic layout of the XMAS beamline is given in Figure 3.7.

In the experimental hutch **(Figure 3.8)**, the upper and lower beam pipes deliver focused and white or unfocused monochromatic beams, respectively. Two mirrors for harmonic rejection are located 49 m from the source and immediately before the modules. These modules are situated 50 m from the source and include attenuators, beam monitors and in-vacuum slits. The modules are followed by the phase plate assembly which is used to manipulate the incident polarisation upon the sample. The last component before the diffractometer is the telescopic vacuum flight path which is used to minimise the air path of the incident beam. The final microfocused beam size is defined by the in-vacuum tube slits which enables a wide range of beam-spot sizes with reduced background scatter (Brown et al., 2001).

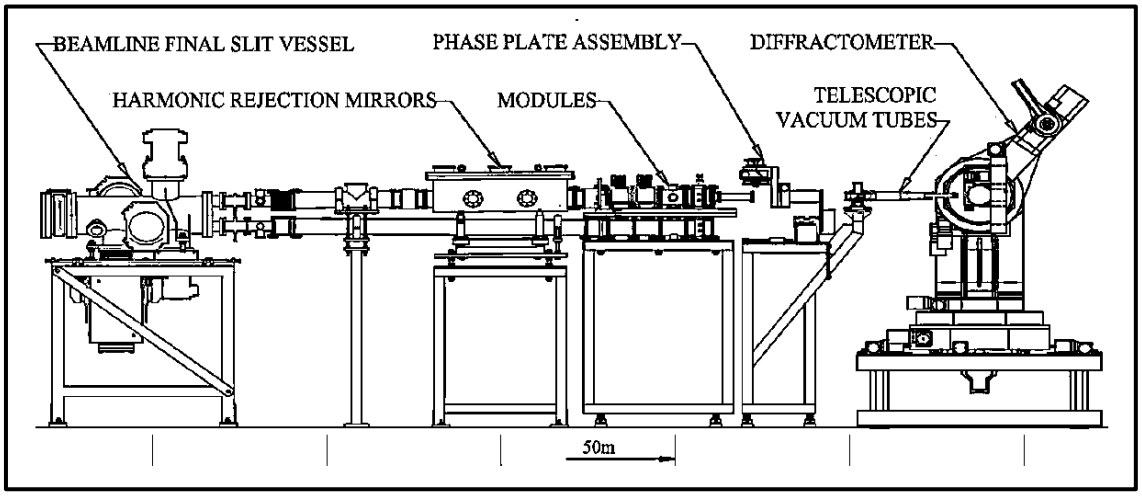

Figure 3.8: The experimental hutch at the XMAS (BM28) beamline. **(Reproduced with permission of the rights holder, International Union of Crystallography, from Brown et al. (2001)).**

3.1.3.2.2 The B16 Test beamline at the Diamond Light Source

The B16 Test beamline has been in user operation since 2008. It covers photon energies ranging from 2 to 25 KeV and, like the XMAS beamline, is located on a bending

magnet. The optics of the B16 beamline consist of a Si(111) DCM, a focusing toroidal mirror providing 1:1 focusing at the sample position and a double multilayer monochromator (DMM) **(Figure 3.9)**. When used in combination with DCM, the DMM provides a very high order harmonic suppression, and when used on its own, it provides a broader bandpass / magnified photon flux operational mode for the beamline. Alterations in the optics setup allows the beamline to operate in several operational modes that include focused and unfocused, white and pink beams (Sawhney et al., 2011).

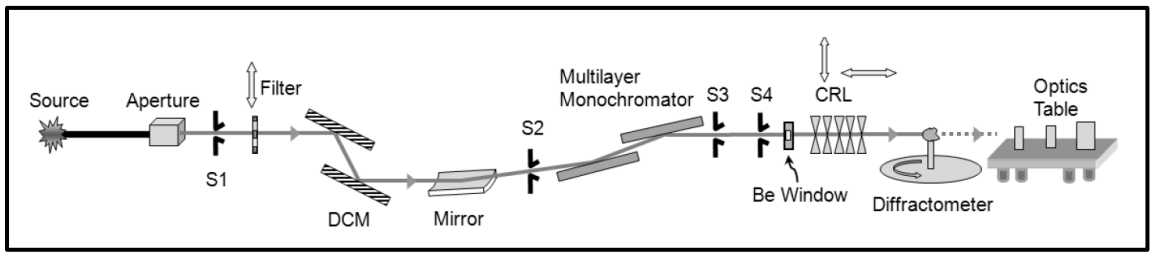

Figure 3.9: The optics of the B16 Test beamline. **(Figure courtesy: Kawal Sawhney, Diamond Light Source, UK. Reproduced with permission of the rights holder, The International Society for Optics and Photonics, from Sawhney et al. (2011))**

3.1.4. X-ray diffraction

X-ray diffraction is considered a subset of X-ray scattering, where scattering is elastic and the scattering object is crystalline **(See Section 3.1.1.1)**.

3.1.4.1. *Geometry of crystals*

Approximately 95% of all solids can be described as crystalline materials, although not all crystals are solid as in the case of liquid crystalline displays (LCD) polymers. A crystalline material comprises of a pattern, termed a motif, periodically repeated in all three dimensions by rotation, reflection and inversion. This motif can be a single atom, a group of atoms or other compounds (Razeghi, 2009). The unit cell is the basic repeating unit that defines the crystal structure and is characterized by a parallelepiped with cell edge lengths $a,\ b,\ c$ and inter axis angles α, β, γ. These unit cells belong to

one of the 14 Bravais lattices that in turn belong to one of the 7 crystal systems **(Figure 3.10)**.

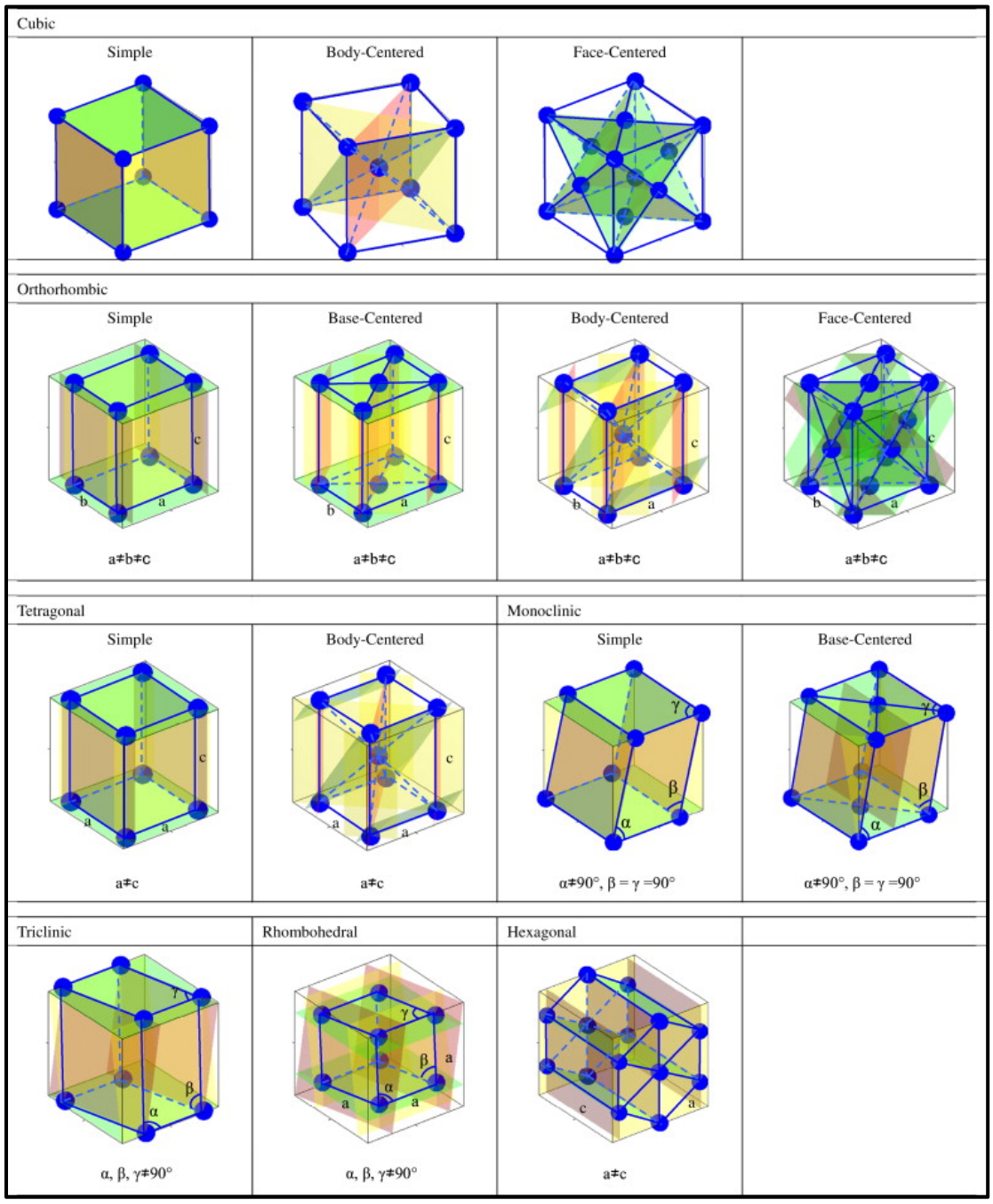

Figure 3.10: The 7 crystal systems and the 14 Bravais lattices. **(Reproduced with permission of the rights holder, Elsevier, from Qi and Wang (2009)).**

The crystal system and the lattice parameters describe the shape and the size of the unit cell respectively. The atomic arrangements within crystalline structures are defined by symmetry elements and it is these elements that are used to define the seven crystal

systems **(Figure 3.10)** (Kikuchi, 1990). The orientation and interplanar spacings of lattice planes are defined in terms of Miller indices $(h\ k\ l)$, a notation system introduced in 1839 by William Miller (Miller, 1839). The Miller indices define the reciprocal of the axial intercepts. d_{hkl} is the vector extending from the origin of the unit cell to intersect the plane $(h\ k\ l)$ at 90° angle. Therefore, d_{hkl} is the distance between parallel planes and is used in Bragg's law to determine where diffraction peaks will be observed.

3.1.4.2. *Bragg's law of diffraction*

The Bragg's law gives a simplistic model to understand what conditions are required for diffraction. X-rays wavelength ranges from 0.01 to 100 Å which is comparable to the range of the average distance between atoms in solids. When a collimated beam of X-rays strikes a pair of parallel lattice planes in a crystal, each atom (more correctly, the electrons about the atom) acts as a scattering centre and emits a secondary wave. Subsequently all of the secondary waves interfere with each other to produce the diffracted beam. For parallel planes of atoms, with an interplanar spacing d_{hkl}, constructive interference only occurs when the Bragg's law is satisfied.

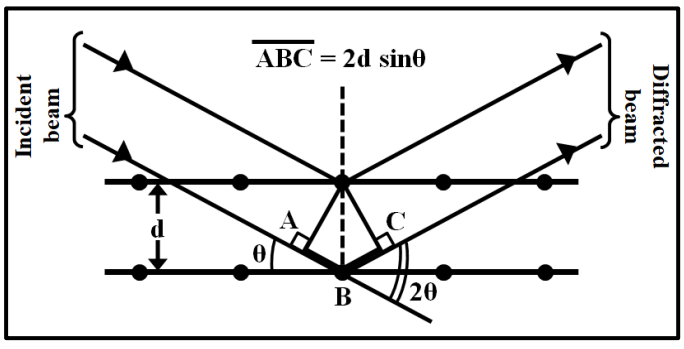

Figure 3.11: Simplified geometric construction to representing the conditions necessary for diffraction **(Adapted from He (2009)).**

These scattered X-rays are a function of the electron distribution within the sample. Therefore, the atomic arrangement within the sample determines the spatial distribution

and intensities of the scattering X-ray forming specific diffraction patterns (He, 2009). The Bragg's law is described by the equation:

$$n\lambda = 2d_{hkl}sin\theta$$

Equation 3.4

where n is an integer number, called the order of reflection, d is the distance between adjacent crystal planes (d-spacing), λ is the X-ray wavelength and θ is the Bragg angle at which one observes a diffraction peak. When $n = 1$, it is said to be a first order reflection and is from the fundamental energy. Higher order reflections are from harmonic energies n-fold the fundamental energy and can be considered as being from different lattice planes **(Figure 3.11) (He, 2009, Bragg and Bragg, 1913)**.

3.1.4.3. *Diffraction patterns*

In 1919, Hull gave a paper titled, "A New Method of Chemical Analysis", where he discovered that every crystalline substance gives a unique pattern. The apparatus comprised of a voltage source, a Coolidge X-ray tube, a metal filter that absorbs all but a single wave length, two slits to confine the beam, and a photographic film. His method involved reducing at least one cubic millimetre of crystalline material to powder and transferring it into a glass tube. A beam of monochromatic X-rays was then made to pass through the powder and the resulting diffraction patterns are photographed. It was concluded that X-ray diffraction patterns of crystalline materials is like a fingerprint of that material. A single crystal specimen produces one family of peaks in a diffraction pattern whereas in a polycrystalline sample all possible diffraction peaks can be observed. The powder diffraction method is thus ideally suited for characterisation and identification of different crystalline materials (Hull, 1919, He, 2009). Diffraction patterns from a single crystal appear in the form of isolated spots, while for a randomly

oriented polycrystalline material, the diffraction pattern contains concentric rings (Debye-Scherrer rings). In textured polycrystalline materials, the diffraction pattern consists of Debye-Scherrer rings, but the intensity distribution is non-uniform along the circumference of the these rings (Cullity, 1978).

3.1.4.4. *Texture analysis*

Polycrystalline materials are composed of a large number of small single crystallites (or grains) with different orientations joined at interfaces called grain boundaries. In this thesis, the term used to describe the arrangement of these grains within a polycrystalline material is texture (Raue et al., 2012). Being an intrinsic feature of many materials, texture is believed to influence the physical properties of these materials (particularly the anisotropy of these properties) and is thought to arise during growth or deformation and can be modified during recrystallisation or phase transformations (Wenk and Van Houtte, 2004).

The polycrystalline material is said to have no texture if the grains within it are arranged in a random manner i.e. has no crystallographic preferred orientation (isotropic material). Conversely, a textured polycrystalline material is one whose grains have a preferred orientation (anisotropic material). Such textured material has a texture magnitude, which is a measure of how aligned or diverged these orientated grains with respect to one another. The more diverge these orientated grains, the lower the texture of the material and vice versa (Raue et al., 2012).

Various techniques can be utilised to assess the orientation patterns and determine the orientation distribution of grains, most of them relying on diffraction, with X-ray diffraction being the routine method (Wenk and Van Houtte, 2004). When an X-ray

beam passes through a sample, it diffracts at the crystallite lattice if the diffraction condition is satisfied for the respective lattice plane $(h\ k\ l)$. Diffracted rings can be seen on a diffractogram imaged using an area detector. If the illuminated crystallites have a preferred orientation, maxima will appear on these rings **(Figure 4.8)** (Raue et al., 2012).

3.1.4.4.1 Current techniques for the measurement of texture

Texture is quantified by measuring the crystallographic orientation of a statistically representative set of crystallites (or grains) in the material. In the past, texture measurement was only possible using Laue X-ray diffractograms on single crystallites. Nowadays, various techniques can be used to determine preferred orientation in polycrystalline materials (Wenk and Van Houtte, 2004).

Orientation imaging microscopy (OIM) is readily available in SEM and has been widely applied for texture measurement studies. This electron backscatter diffraction (EBSD) technique produces a map of orientation measured on a grid of points. Here, the electron beam is fixed at a point within a single crystallite on the surface of the sample. The electrons diffract from the sample at particular angles to form a backscatter Kirkuchi pattern that can be displayed using a phosphor screen. The EBSD technique allows for determination of local orientation correlations, investigation of texture transition and characterisation of local texture and grain boundary. This technique can only be performed on finely polished surfaces and is not ideal for samples with many lattice defects. Another diffraction technique is electron diffraction using the transmission (TEM) or SEM. It is the most time consuming and is extremely expensive but permits

the correlation between microstructure and texture and is especially useful to interpret deformation processes (Wenk and Van Houtte, 2004).

Laboratory source XRD was used by Hirota (1982) to analyse the tilt of crystallites in the enamel of a human canine. However, due to the low brilliance of lab source X-rays and the resultant high data acquisition times, it was not possible to acquire data for the whole tooth, instead only 12 points within the tooth could be analysed. Two decades later, another study comparing the crystallography of healthy and carious deciduous molars using laboratory source XRD analysed six and two points for the healthy and carious tooth, respectively (Xue et al., 2008).

Neutron and synchrotron radiation have sufficient penetration power for non-destructive texture analysis of condensed matter. S-XRD is a powerful experimental technique that uses the diffraction of X-rays on crystalline samples for the structural characterisation of materials. It allows for rapid, non-destructive *in situ* analysis of multi-component mixtures without the need for extensive sample preparation. Neutron diffraction can be used in a similar way to S-XRD. Compared to S-XRD, neutron diffraction exhibits larger reduction in absorption but a much higher angular resolution. Neutron diffraction can be useful for the measurement of *in situ* texture changes due to environmental factors such as temperature and stress variations (Cullity, 1978).

S-XRD is capable of delivering structural information about structures ranging from a few to several hundreds of nanometres in size, a range well suited to studying c-HAp crystallites (Deyhle et al., 2014). Therefore, S-XRD can be used to obtain information

regarding c-HAp crystallite orientations, organisation and texture at different developmental stages for comparison.

3.1.4.4.2 Texture studies on dental enamel using synchrotron X-ray diffraction

One of the techniques used to satisfy the objectives of this study was S-XRD. Many studies assess the differences in the scattering properties of samples to reach valuable qualitative and quantitative results. This section provides an overview of the application of S-XRD in studies assessing human dental enamel.

A number of studies qualitatively estimated the degree of texture of human dental enamel by using the texture index (R) of a sample (Low, 2004, Seredin et al., 2013). Using grazing-incidence synchrotron X-ray diffraction (GIS-XRD), Low (2004) characterised the graded nature of molar human enamel in terms of crystallite disorder, texture, and microhardness. The preferred orientation was determined by the variation of intensity ratios of the three maximum reflections (2 1 1), (3 0 0) and (0 0 2). R is determined by the ratio of intensities of the strongest peaks, $I_{(2\,1\,1)}/I_{(3\,0\,0)}$ and $I_{(2\,1\,1)}/I_{(1\,1\,2)}$, which for the reference sample of powdered HAp equal to 1.63 and 1.94, respectively. The R values for (3 0 0) and (1 1 2) reflections can be calculated using the following equations:

$$R_{(3\,0\,0)} = \left(\frac{I_{(2\,1\,1)}}{I_{(3\,0\,0)}}\right)/1.63$$

Equation 3.5

$$R_{(1\,1\,2)} = \left(\frac{I_{(2\,1\,1)}}{I_{(1\,1\,2)}}\right)/1.94$$

Equation 3.6

If $R = 1$, then the c-HAp crystallites are said to be randomly distributed, however, an R value greater or less than 1 indicates the presence of texture. It was found that the degree of crystallite alignment increases from the EDJ peripherally. Moreover, it was shown that human enamel is a hierarchical graded biomaterial in term of crystallinity, texture, crystallite size, and hardness. However, this study only probed linear depth tracks from the EDJ peripherally. 9 years later, Seredin et al. (2013) used the texture index (R) to quantify the texture variation of fissure carries in human enamel and reported a decrease in the crystallinity and texture as well as a loss of the predominant orientation of c-HAp crystallites in the affected enamel. Again, only linear slices could be probed using this methodology.

Small angle X-ray scattering (SAXS) has become an established technique for studying the nanostructure of enamel. With SAXS, periodicity in samples is not a requirement and the signal is diffused. The particle size can be resolved between length scales from 1-100 nm which is equivalent to the smallest and the highest scattering angles, or q values (Hemonnot and Köster, 2017). A study examining a molar tooth using synchrotron XMT and SAXS confirmed the anisotropic morphologies of dentine and enamel on the micro- and nanometre scale (Deyhle et al., 2009). It was found that the crystallite orientation corresponds to the main direction of mechanical loading.

Subsequently, Deyhle et al. (2011) used synchrotron XMT and SAXS to asses 200-500 μm slices of five carious and three healthy teeth. The types of teeth used and their position in the mouth were not stated in the study. It was found that the nanostructures

of the mineral phases of the enamel are well oriented and aligned roughly perpendicular to the EDJ. Regarding dentine, it was found that the collagen network is conserved in both quantity and orientation during the initial stages of demineralisation and therefore may be suitable for remineralisation.

A further study conducted by the same workers, used the same methodology to analyse eight human teeth, six with and two without visible carious lesions. The study revealed strong anisotropy in enamel with inverse trends of scattering intensity for different q ranges (Gaiser et al., 2012). 2 years later, the same group assessed two carious third molars using the same techniques and found that the crystallite orientation was preserved throughout, even in carious lesions (Deyhle et al., 2014).

Sui et al. (2014a) measured the lattice strain variation related to the nanoscale crystallite distribution of human third molar enamel during *in situ* elastic compression using synchrotron wide-angle X-ray scattering (WAXS) and photo-elasticity techniques. They concluded that the mechanical behaviour shows strong dependence on the crystallite orientation distribution. In a subsequent study using synchrotron based SAXS/WAXS and nanoindentation mapping techniques, Sui et al. (2014b) were able to study the effects of heat treatment on human dental tissues. It was found that temperature has a significant effect on the texture magnitude and mean thickness of enamel crystallites. Furthermore, it was found that increasing the temperature decreased both the hardness and the modulus of enamel. The changes in the mechanical behaviour and the ultrastructure of enamel led the authors to confirm that the structure has a strong effect on the mechanical properties of enamel.

Egan et al. (2013) used S-XRD to quantify the texture magnitude and orientation of crystallites in the enamel of a human molar. The tilt and orientation angles where obtained using Equation 3.7 which was originally derived by Méheust et al. (2006).

$$I = I_0 + C\ exp(m[sin\theta\ sin\Theta\ + cos\,\theta\, cos\Theta\, cos(\varphi - \Phi)]^2)$$

Equation 3.7

Where I is the intensity, I_0 is the background, C and m are constants, θ is the diffraction angle, Θ is the tilt angle, φ is the azimuthal angle, and Φ is the in-plane orientation.

The texture magnitude was measured by comparing the relative peak heights of the (0 02) and (211) Bragg peaks from the complete radially integrated S-XRD patterns to those found in a pure powder sample. Relative peak height values (I_{002}/I_{211}) close to 1 indicate a powder distribution (non-textured). The crystallites were found to be orientated perpendicular to the enamel surface and the texture magnitude was found to be localised near the enamel surface.

Another method used for the measurement and representation of texture magnitude is the pole figures method. This method allows for the measurement of crystallite orientation with respect to external sample surface and is typically shown on special stereographic projection. However, the pole figures method does not give information regarding the orientation of crystallites with respect to one another. In order to gather more information, the crystal orientation distribution function (CODF) was introduced which combine data from several pole figures. This method was implemented in various studies measuring the texture magnitude of human dental enamel (Raue and Klein, 2010, Raue and Klein, 2011).

Raue and Klein (2010) used S-XRD to measure the texture distribution of upper central incisors. It was found that the tilt of the prisms and the one of the (0 0 1) normal is comparable, suggesting that c-HAp prisms are constructed by stacking and rotating of (0 0 1) planes along their long axis. The following year, the same workers implemented S-XRD to study the crystalline structure, the orientation and anisotropic properties of incisal dental enamel. It was found that human dental enamel possesses high texture magnitude with strong local change of orientation. Moreover, prisms were found to be orientated approximately perpendicular to the enamel surface with an inclining tilt towards the top of the tooth (Raue and Klein, 2011).

In a subsequent study by the same group, different locally measured points of 18 molars and incisors were examined by S-XRD via the pole figures method. In molar enamel, the texture was found to be higher near the cuspal region, compared to the fissure of the tooth, the cervical region and the inner cuspal region. In incisors, the upper region, the occlusal region and the bulk centre of the enamel were found to possess the highest texture magnitude. Furthermore, it was reported that the crystallites long axes were approximately perpendicular to the enamel surface. Moreover, the authors suggested that some schematic drawing of enamel prism orientation should be revised since it was found that prisms have a nearly vertical orientation and do not follow the morphology of the surface orthogonal (Raue et al., 2012). Few years later Raue et al. (2014) compared the anisotropic properties of dental enamel and dental materials using the same techniques. Unlike dental materials, dental enamel was found to have a strong direction dependence of its physical properties that varied as a function of position.

Other studies produced 2-D texture magnitude and direction maps for entire sections of teeth. The texture magnitude in these studies was refined by Rietveld refinement using the spherical harmonics function as per Von Dreele (1997) method. The texture

direction, however, was deduced using the intensity patterns around the Debye ring of the (0 0 2) reflection (Al-Jawad et al., 2007, Al-Jawad et al., 2008, Simmons et al., 2011, Simmons et al., 2013, Siddiqui and Al-Jawad, 2016).

In 2007, Al-Jawad et al. (2007) quantified the changes in texture and lattice parameters in dental enamel as a function of position within a 500 μm thick fully-developed molar tooth section using spatially resolved S-XRD at 150 μm spatial resolution. It was found that the cusps had the highest crystallite alignment. Furthermore, their results showed a large variation in lattice parameters from the enamel surface towards the EDJ. Their study also confirmed that the crystallites long axes run approximately perpendicular to the EDJ and to the enamel surface.

In the following year, the same group used S-XRD at 300 μm spatial resolution to study the texture orientation and magnitude of human maxillary first premolar. Here, the authors sectioned the teeth into six 500 μm sections and analysed these sections individually to provide a 3-D model of texture distribution within the whole crown. It was found that there is a 3-D curling of the crystallite orientation in both the mesio-distal and bucco-lingual directions. Furthermore, it was found that the long axes of the crystallites were perpendicular to the EDJ along the sides of the tooth in the central and proximal regions of the tooth crown, while on either side of the tooth cusps the crystallites' long axes were parallel to the EDJ (Al-Jawad et al., 2008).

A few years later, Simmons et al. (2011) used S-XRD to analyse the texture magnitude, orientation and tilt **(Equation 3.7)** of an entire maxillary first premolar tooth crown. They analysed eight 500 μm slices and found that both the magnitude and the direction of the crystallite orientation have a high spatial heterogeneity. Areas of high crystallite alignment were directed perpendicular to the biting surfaces, which is thought to meet

the functional requirements of mastication. Additionally, the tilt was found to be at its highest in the buccal and palatal sections, and in each case, is tilted away from the EDJ. It was also found that the degree of anisotropy is not restricted to the crystallite orientation but also to the magnitude of crystallite alignment.

Subsequently, Simmons et al. (2013) used S-XRD together with XMT to analyse the texture distribution and the mineral density of the enamel of human molars at various developmental stages, respectively. It was found that as enamel matures the mineral content increases and the mineral density distribution becomes more homogeneous. Moreover, enamel crystallites become more oriented and larger; and the crystallite organisation becomes spatially more complex and heterogeneous. They concluded that in human dental enamel, the rate of mineral formation and mineral organisation are not identical.

In a recent study, Siddiqui and Al-Jawad (2016) used the same method to compare healthy maxillary and mandibular deciduous incisors. A lower degree of texture was reported in mandibular enamel compared to maxillary enamel, emphasising the importance of choosing appropriate type-matched controls. The above studies measured the texture magnitude using Rietveld refinement. The shortcoming of using such method is its inability to measure the texture magnitude of multiple populations.

Various studies also provided 2-D texture magnitude and direction maps of tooth sections without using Rietveld refinement; instead, these studies measured both the texture magnitude and direction using profile fitting of the azimuthal intensity around the (0 0 2) reflection (Al-Jawad et al., 2012, Siddiqui et al., 2014, Khan et al., 2016).
This method was used for the comparison of the texture distribution in enamel from healthy and MPS affected individuals (Al-Jawad et al., 2012). Significant differences

were observed in the texture distribution of the MPS affected enamel as compared to healthy tissue, characterised by less gradation of enamel crystallite orientation in MPS-affected enamel compared to healthy tissue.

A subsequent study by the same group found that MPS I and MPS IVA affected deciduous enamel have lower enamel texture magnitude compared to healthy deciduous enamel indicating that the GAGs play an important role in causing loss of enamel texture, leading to defects in the enamel texture (Khan et al., 2016).

In a recent study, the mineral density, the microstructure and the crystallographic preferred orientation of human mandibular first molar enamel were assessed after demineralisation and remineralisation using S-XRD, SEM and XMT respectively (Siddiqui et al., 2014). It was confirmed that calcium and phosphate integrate into the apatite crystallite structure giving it a preferred orientation and do not simply precipitate on the surface. Furthermore, a reduction of crystallographic texture as a function of demineralisation was observed. This loss of texture was reversed as a result of remineralisation. The authors concluded that enamel which has lost mineral density and crystallographic texture via apatite dissolution can be restored to its original healthy state by a careful remineralisation regime.

Another study that utilised S-XRD to assess human dental enamel was conducted by Li et al. (2015). In this study, the outermost enamel of a human premolar and the rostrum of the whale *Mesoplodon densirostris* were compared. Compared to the whale rostrum, the outer tooth enamel was found to be more homogeneous, have greater mechanical strength, lower incorporation of non-apatitic ions, and higher degree of crystallite preferred orientation.

The above studies did not rely on Rietveld refinement for texture magnitude measurement; instead they used profile fitting (to measure the FWHM) of the azimuthal intensity around the (0 0 2) reflection. The advantage of using such method is its ability to detect and measure the texture magnitude of multiple populations. This approach can be useful in detecting multiple crystallite orientation populations and hence makes it possible to analyse the texture magnitude and direction for each orientation population individually. However, these studies plotted the texture direction manually on each diffraction pattern in the composite map of the tooth. A faster and a more accurate approach would be to use an automated software that extracts the peak positions of the azimuthally integrated (0 0 2) reflection and plotting the direction into 2-D maps.

3.1.4.4.3 Other applications of synchrotron X-ray diffraction in dental enamel research

S-XRD studies on powdered human dental enamel confirmed the impure nature of HAp in enamel, where it was found that c-HAp had different lattice parameters than that of pure HAp (Wilson et al., 1999, Colaço et al., 2012). Reyes-Gasga et al. (2012) S-XRD study on powdered human dental enamel rejected the suggestion of former studies (Elliott et al., 1973, Ma and Liu, 2009) that the HAp phase found in enamel was monoclinic and confirmed that the unit cell is hexagonal.

Almeida et al. (2009) attempted to characterise the differences between healthy and fluorotic 100 μm thick slices of third molar human enamel using S-XRD. No significant differences were observed between the two samples. The authors concluded that the observed similarity is due to the fact that both HAp and fluorapatite (FAp) are usually described in space group $P6_3/m$, having lattice parameters very close and due to low levels of fluoride present in fluorotic enamel samples.

3.1.5. X-ray microtomography

3.1.5.1. *Tomography*

The term tomography refers to the reconstruction of objects from their projections, and the word is derived from the Greek tomos (slice) and graphein (to write). It was introduced to overcome the limitations associated with projection imaging such as structure foreshortening and superposition. It started in 1917 when the Czech mathematician Johann Radon conceived the mathematical solution to the problem. Since then tomography attracted many scholars into the field leading to the production of the first tomograms in the 1950s using Radon (and inverse-Radon) transform (Grangeat, 2009). In the 1960s, the South African physicist Allan Cormack developed the initial algorithms (Cormack, 1963, Cormack, 1964).

3.1.5.2. *Computed tomography*

Developed in the 1960s, computed tomography (CT) uses X-rays to view and analyse the internal structures of samples in high detail. It is a non-destructive, non-invasive technique, so an advantage to image the internal organs of the body to confirm or rule out a suspected diagnosis without the need for surgically invasive procedures (Stock, 1999). The major development was made by the English engineer Godfrey Hounsfield. Hounsfield tested whether a 3-D representation of the contents of a box can be reconstructed from a set of readings taken at randomly selected directions. Hounsfield imagined the scanned subject as being divided into axial slices, where he used an algebraic type of reconstruction algorithm based in part on mathematical methods developed by Allan Cormack (Cormack, 1963, Cormack, 1964) to reconstruct these slices (Videla et al., 2007). In 1968, Hounsfield started his project proposal with the aim to "investigate the employment of a computer to make better use of the information obtained when an object is examined by gamma rays or X-rays" where he compared the

conventional X-ray system with the one he proposed (Beckmann, 2006, Goldman, 2007).

In his proposal, he introduced the lathe bed model which relies on gamma reconstruction of slices through an object, which was later replaced with an X-ray source that reduced the scanning duration. The X-ray in this model was collimated into a thin beam, 3 mm in size within the slice plane and 13 mm in width perpendicular to the slice, where the later determined the thickness of the slice to be imaged. The X-ray tube was linked to a detector located on the other side of the subject, and together scanned across the subject, passing the beam through the slice. During a translation which is the linear transverse scanning motion across the subject, measurements of X-ray transmission at many locations through the subject were collected by the detector. Hounsfield's scanner measured the transmission of 160 rays (X-ray beam across the subject for each measurement) per view (set of measurements made during a translation). The tube-detector assembly was then rotated around the subject by 1° following the initial translation to collect the next view. The early scanner repeated this process in 1° increments to collect 180 views over 180° (Goldman, 2007).

In 1969, James Ambrose from Atkinson Morley's Hospital in South London heard about the new approach and wanted to assess its ability to produce clinically relevant images and, consequently, a bottled specimen of a brain was tested using Hounsfield's system. Subsequently, the first X-ray CT scanner prototype for medical diagnosis was constructed by Hounsfield and his team, and was used to successfully scan the first patient in 1971 (Beckmann, 2006, Goldman, 2007). The CT scanner was first presented in 1973 by Hounsfield and Ambrose at the Congress of the British Institute of Radiology, where they showed the first clinical images (Ambrose, 1973, Hounsfield,

1973). Shortly afterward, Hounsfield's system was installed in a number of hospitals around the UK and the USA. Various companies built their own CT scanners, each adding their own touches of improvements to the apparatus (Beckmann, 2006).

CT is now a recognised method used to produce cross-sectional and 3-D images of the internal structures of specimens providing the ability to obtain information regarding the nature of a material occupying an exact position in the specimen. These scanners produce a map called a sinogram of the variations in X-ray attenuation within a specimen. From this sinogram, a 2-D image of the X-ray attenuation coefficient distribution in the cross section is produced. The subsequent reconstruction of the parallel cross sections followed by further computer processing leads to the precise 3-D shape of the specimen. Modern CT scanners can measure more than 750 rays per view and collect more than 1000 views over 360° (Goldman, 2007).

Like all imaging techniques, CT scanners come with a number of limitations. CT scanners are expensive systems, the reason why they are not widely available in developing countries. Moreover, due to involuntary movement made by patients during scans, data acquisition must be quick and should not take more than few seconds in order to avoid blurring. Furthermore, to avoid dangerous X-ray radiation exposure, the X-ray dose is always kept to minimum. Short duration scanning, and low X-ray dose decrease the signal to noise ratio (SNR) and result in noisy tomographic images. Having said that, in non-biological studies like damage propagation assessment and structural analysis of materials, CT images with much higher SNR can be achieved due to the longer scan duration and the higher X-ray doses applied (Stock, 2008, Stock, 1999).

3.1.5.3. *X-ray microtomography*

XMT (or micro-CT) is a microscopic, miniaturised version of CT, similar in principle to third generation medical CT scanners. These systems produce detailed, 3-D, and X-ray attenuation images of the inner structures of specimens at high spatial resolution. The simplest XMT scanner was invented by Elliott and Dover (1982) using a pinhole collimator and a single detector (Davis and Wong, 1996, Lo et al., 2010). Elliott and Dover (1982) used their new system to produce a cross sectional image of a tropical fresh-water snail, *Biomphalaria glabrata*, about 400 μm across at a resolution of approximately 15 μm. Compared to CT systems, XMT scanners can produce images of smaller specimens of sizes in the millimetre range with a higher resolution at a scale between 1 to 100 μm (Stock, 1999, Davis et al., 2013). Compared to medical CT images, whose voxel size (the size of each elemental component of the 3-D volume) is typically 1 mm^3, XMT scanners can produce images with voxels approximately 1 million times smaller in volume (Swain and Xue, 2009).

A typical XMT system uses a single laboratory source to project an X-ray cone through a sample and onto a detector array with an integrated scintillator that converts the attenuated X-rays into visible light. The optimal X-ray energy is influenced by the object thickness and the attenuation of the material. In XMT systems, the source and the detector are normally fixed while the sample is rotated to obtain 2-D radiographic projections at different angles (Davis and Elliott, 1997). These 2-D images contain information regarding X-ray attenuation variations and can be mathematically reconstructed into a 3-D volume (tomogram) **(see Section 4.2.3)** where each voxel represents the X-ray attenuation for each point (Landis and Keane, 2010).

Early XMT scanners were uncommon and custom built (Swain and Xue, 2009). First generation or pencil beam XMT scanners use a point like source, a pinhole collimator, a scatter shield and a single detector. While the X-ray source, collimator, scatter shield and detector are stationary, the sample moves linearly to scans multiple points along the length of the sample. Subsequent views are acquired by rotating the sample and repeating the process. Although advantageous in terms of simplicity, flexibility and scatter resistance, this system requires several hours to obtain data for a single slice. It should be noted that this used a photon counting system that recorded the energy of the detected photons. This allowed the use of quasi-monochromatic radiation, yielding good quantitative accuracy that is not matched by modern energy integrating detector arrays (Stock, 1999).

This limitation (long scanning time) was minimised by the introduction of fan beam systems, where the single detector was replaced by a one-dimensional (1-D) linear detector consisting of an array of discrete elements, able to acquire a whole projection at a time. Here, at each sequential rotation, a flat fan of X-ray beams covering the whole slice passes through the sample and a scatter shield into the detector. In a fan beam XMT scanner, the X-ray source, collimator, scatter shield and detector stay stationary while the sample rotates, and each complete rotation produces a data necessary to reconstruct a single slice. Although this improvement reduced the collection time by several orders of magnitudes, the image produced suffered greatly from beam-hardening artefacts due to the use of polychromatic radiations. Moreover, ring artefacts due to variations in the responses of detector elements can also affect the image (Stock, 1999).

Parallel beam scanners comprise of an X-ray source (usually a synchrotron source) that produces parallel X-ray beams and a high performance 2-D area detector. These scanners have the ability to acquire multiple slices at the end of each complete sample rotation. Due to the parallel nature of the X-ray beams of these systems, the projection of each slice is independent of the other (Stock, 1999). Compared to conventional sources, the use of synchrotron source XMT systems produce brighter X-rays increasing the signal to noise ratio (SNR), reduce scanning times and simplify the tomographic reconstruction (Landis and Keane, 2010).

Cone beam scanners use a 2-D detector array, and instead of the 2-D beam used in the fan beam system, the X-rays of these systems form a volumetric cone to produce the projections. These systems have the shortest collection time compared to other laboratory X-ray source scanners (Park et al., 2011). Unlike the previous systems, here, the beam reconstruction algorithm is an approximation and not absolute, giving rise to increased probability of blurring, except where helical scanning is used (Stock, 1999).

Modern XMT systems can be divided into two main types, namely synchrotron based systems producing parallel monochromatic X-rays and commercial and in-house micro/nano focus X-ray tube systems producing cone-beam polychromatic X-rays (Huang et al., 2007). XMT is presently widely used in academic and research laboratories to assess mineralised tissues such as teeth and bones in addition to various materials like ceramics, polymers and biomaterial scaffolds (Swain and Xue, 2009). Nowadays, helical and multiple XMT scanners, with new X-ray detectors that have improved speed, efficiency and spatial resolution can give "exact" reconstructions (Stock, 1999, Stock, 2008).

3.1.5.4. *Current techniques for obtaining mineral density information*

One way to evaluate the success of any technique is to compare it with existing measurement methods. qBSE imaging is a widely used method to quantify mineral density in bony tissues. Although back-scattered electrons (BSE) can provide nanometre resolution, it can only be used to analyse 2-D surface slices without tissue depth information. Moreover, BSE requires careful sample preparation procedures and sufficient tissue volume to backscatter the electrons (Boyes, 2000, Willmott et al., 2007).

Microradiography is another widely accepted 2-D technique to determine mineral densities at the microscopic level *in vitro* (Engfeldt and Hammarlund-Essler, 1956, Crabb and Darling, 1960, Avery et al., 1961, Avery, 1962, Angmar et al., 1963, Angmar-Månsson, 1971, Elliott et al., 1994). This method is almost completely independent of the mineral physical state, crystallite orientation, and the presence or absence of air, water, and other components. Microradiography was first introduced to dental research by Thewlis (1940). This technique is specific for the determination of calcium content, making it a useful technique in enamel studies, since calcium contribute to approximately 75% of the total X-ray attenuation in healthy enamel (Angmar et al., 1963). However, microradiography is expensive, time-consuming and involves teeth embedding, drying and precise cutting into thin slices before examination under X-rays. Another disadvantage is the loss of specimen detail in the direction of the beam due to superimposition (Gao et al., 1993, Damen et al., 1997, Hamba et al., 2012). Other disadvantages associated with the microradiographic technique include secondary radiation from the sample, stray light in the microdensitometry and inhomogeneities in the X-ray field (Angmar-Månsson, 1971).

A less expensive technique widely used for the determination of mineral density is polarised light microscopy (PLM). PLM is quick and requires little preparation time. However, PLM is more of a qualitative method, requiring a high degree of sophistication and can only analyse small volumes of samples. Unlike microradiography, PLM results can be affected by the mineral physical state, crystallite orientation, and the presence or absence of air, water, and other components (Angmar et al., 1963). It is a widely accepted view that developing and mature dental enamel comprise of small amounts of water which is generally replaced by air particles upon drying (Angmar et al., 1963, Elliott, 1994). Water and air can introduce some form of birefringence that may influence the polarised light picture of enamel and hence prevent accurate determination of mineral density. Furthermore, PLM is nonspecific and is sensitive to alterations in the mineral quantity, composition and structural organisation (Angmar et al., 1963).

Further, various workers reported the use of confocal microscopy (Willmott et al., 2007) and chemical methods (Angmar-Månsson, 1971) to acquire mineral density information. The above techniques are all destructive and involve the physical cutting of the samples which is difficult for materials that are brittle or those containing hard and soft regions. Cutting the samples physically results in irregularities and loss of information between sections, in addition to the possibility of losing delicate tooth fragments during the course of the study.

Methods used for the assessment of mineral density that do not require cutting the sample include ultrasonic techniques, optical coherence tomography (OCT) and XMT

(Nazari et al., 2013). Furthermore, fibre-optic coupled polarised Raman spectroscopy was used to detect the loss of enamel mineral content during carious attacks in vivo, non-destructively and site-specifically (Ko et al., 2008).

With the assumption that enamel is a homogenous mixture of apatite and protein, Ng et al. (1988) reported that variations in the degree of mineralisation could be related to variations in the ultrasonic velocity. They found that the gradient of amplitude ratio curve is proportional to the degree of demineralisation and concluded that ultrasonic waves may be used to differentiate between healthy and demineralised enamel. Although this technique can provide valuable information regarding the degree of mineralisation/demineralisation non-destructively, it does not give absolute quantitative values for mineral density.

OCT is similar to ultrasound imaging, except that it uses light instead of sound. It uses infra-red laser to produce cross-sectional tomographic images of internal structures by measuring the back-scattered light and therefore poses no radiation danger (Fujimoto et al., 2000). OCT can image structures up to a depth of 2-3 *mm* (depending on composition) with a resolution of 5-10 μm. OCT cannot provide accurate quantitative mineral density measurements since the grey level drops when travelling deeper into the sample (Northrop, 2001).

The XMT technique's main advantage is being non-invasive and non-destructive while producing high resolution 3-D analytical information of internal features, though this comes at the expense of increased complexity and observation time (Gao et al., 1993, Willmott et al., 2007). The non-destructivity feature of XMT allows the sample to be

examined repeatedly for further research using other techniques and to be assessed following biologically and mechanically induced changes. Furthermore, XMT has put an end to the controversy associated with sectioning endangered or rare fossil samples (Swain and Xue, 2009). XMT's main disadvantage is its poor sensitivity at high resolutions, as the signal collected is inherently weak, even when using high-intensity and monochromatic X-ray sources such as synchrotron facilities (Boyes, 2000).

With XMT, there is no compression of 3-D data into 2-D images as with conventional radiographic imaging, since a true 3-D attenuation map of the sample is produced free from superimposition. Therefore, the reconstructed 3-D model can be sliced virtually along any axis without being affected by overlapping attenuations. Furthermore, the thickness of the virtual slices produced by XMT is constant and depends on the beam size, giving rise to slices much thinner than those sliced using a cutting machine. The ability of XMT to accurately detect changes in the mineral content is attributable to the good radiopacity correspondence to mineral density in teeth making it well-suited to longitudinal studies (Huang et al., 2007).

3.1.5.5. *Application in dentistry*

XMT is a non-destructive technique used to image the interior structures of materials in 3-D. It is widely accepted that there is a linear correlation between grey scale values and the mineral density of mineralised tissues (Schwass et al., 2009, Neves et al., 2010). Such information is determined from variations in X-ray attenuations that depends on the atomic structure, density (Deyhle, 2014) and composition (Swain and Xue, 2009). By comparing the mineral density of enamel from the least developed toward the fully-developed tooth, it is possible to construct a map revealing the progression of biomineralisation during enamel formation (Simmons et al., 2013).

3.1.5.5.1 Human dental enamel mineral density determination

XMT has emerged as one of the non-destructive 3-D analytical techniques in the field of mineral density of dental mineralised tissues and has been used in a wide range of studies (Elliott et al., 1998, Swain and Xue, 2009). The first study that made an effective and practical use of XMT in the field of mineral density of calcified tissues was done by Elliott et al. (1989) determining the linear attenuation coefficients of dentine and enamel of human premolars. Further, Fearne et al. (1994) assessed the enamel of deciduous incisors from low birth weight children and found that the enamel of low birth weight children had reduced mineral density (2.3-2.5 $g\ cm^{-3}$) when compared to a control (2.65-2.78 $g\ cm^{-3}$) .

2 years later, Anderson et al. (1996) used the XMT technique with a 40 *kV* X-ray energy and 2 *mA* current to compare and asses the mineral contents of enamel and dentine of premolars and enamel pearls. They established that the process of mineralisation is different in pearl dentine compared to permanent coronal dentine. Another study investigated the mineral density of healthy and idiopathic enamel, where they observed a 20% reduction in mineral density in effected enamel (Fearne et al., 2004). Unlike the study by Anderson et al. (1996), the authors here failed to document important aspects in their publication such as the voltage, current, sample to detector distance, detector resolution and beam resolution used.

The technique has also been used to determine the mineral density distribution in the enamel of 11 deciduous caries-free molars using 15 μm × 15 μm X-ray beam size (Wong et al., 2004). Although no intra-tooth variations in enamel mineral density was found, an 8% variation was observed between different teeth. The authors also reported

an increase in mineral density from the EDJ toward the enamel surface. In the same year, Dowker et al. (2004) investigated the mineral densities of sound and carious enamel using synchrotron XMT (at 20.5 *KeV* X-ray energy and 1.9 μm voxel resolution) yielding results consistent with previous measurements from microradiographic projections. The authors concluded that unlike mineral densities, variations in pore fraction volume within carious lesions cannot be determined by attenuation measurements alone.

Additionally, two studies utilised XMT at 25 μm voxel resolution to examine the effect of bleaching with carbamide peroxide on the demineralisation of enamel and dentine (Efeoglu et al., 2005, Efeoglu et al., 2007). In the first study, it was concluded that the application of 10% carbamide peroxide demineralised enamel to a depth of 50 μm from the surface using six sound upper 2nd molar teeth sectioned into 12 slices. In the second study, the authors investigated the effect of 35% carbamide peroxide on enamel surface layers, subsurface layers and the EDJ in 11 tooth prisms sections. It was found that demineralisation extended to a depth of 250 μm from enamel surface, whereas no significant difference in dentine mineral density was found. A more comprehensive study would examine more samples in order to reliably reflect the population mean.

Other studies used the XMT technique to determine the mineral density of dentine (Wong et al., 2006, Willmott et al., 2007). At 15 μm voxel resolution, Wong et al. (2006) showed using 10 carious primary molars that carious lesions have a bowl-shaped morphology when rendered in 3-D and not conical as previously believed. Willmott et al. (2007) assessed 10 carious deciduous molars and came to the conclusion that using a bur to remove carious lesions is not selective in removing carious dentine only.

Moreover, XMT made it possible for researchers to measure and visualise longitudinal changes in mineral density resulting from hyper- and hypo-mineralisation (Nakata et al., 2012), and it has been used for the characterisation of enamel lesions (Gao et al., 1993, Dowker et al., 2003, Huang et al., 2007). Furthermore, XMT (at 90 *kV* X-ray energy, 256 μA current and 29.55 μm voxel resolution) was used to study the loss of mineral in compacted carbonate apatite powders (Elliott et al., 2005). Simmons et al. (2013) used the MuCat2 scanner (at 60 and 90 *kV* X-ray energy, 0.27 and 0.18 *mA* current and 15 and 18 μm voxel resolution, respectively) built at Queen Mary, University of London (QMUL) to investigate the mineral density of molar enamel at different developmental stages. By comparing the mineral density of enamel from the least developed toward the fully-developed tooth, it was possible to construct a map revealing the progression of biomineralisation during enamel formation.

A recent study conducted by Shahmoradi and Swain (2016) used the Skyscan 1172 XMT system (at 100 *KeV* energy, 100 μA current and 8.82 μm voxel resolution) along with de-noising and colourisation methods to acquire mineral density information of fissural enamel lesions in human molar and premolar teeth. It was found that the lesion was extended in two directions towards the pulp horns, which may explain the early inflammation of the pulp in fissural lesions even when the lesion base appears to be far from the pulp roof in normal radiographs.

One study optimised XMT (at 120 *kV* X-ray energy and 147 μA current) to compare the mineral density of hypo-mineralised and sound enamel using 8 human permanent first molars. Using a voxel size of 7 μm, a significant reduction in mineral density of 19%

was shown in hypomineralised enamel compared to healthy enamel. Since these authors did not use any reference system, they were not able to determine quantitatively the variations in mineralisation. Instead, the authors obtained grey values and presented changes in mineral density as percentage change of these values (Garot et al., 2016).

3.1.5.5.2 Other applications in dentistry

XMT has been used for tooth measurements to quantify the thickness of dental mineralised tissues (Olejniczak and Grine, 2006, Kim et al., 2007). Both studies assessed the accuracy of XMT for the determination of enamel thickness. The authors measured the thickness of dental mineralised tissues from physical sections and compared them to measurements from virtual XMT slices. Other studies utilised the technique in experimental endodontology, and it was shown to be accurate for the assessment of root canal systems (Dowker et al., 1997, Rhodes et al., 1999). Moreover, XMT has been applied to implantology (Schicho et al., 2007, Freilich et al., 2009), dental biomechanics (Verdonschot et al., 2001, Magne, 2007) and tissue engineering (Cartmell et al., 2004, Hollister et al., 2005) in relation to dentistry.

3.1.5.6. *Limitations*

3.1.5.6.1 Monochromatic and polychromatic X-ray beams

If a source of radiation produces X-rays with the same wavelength, it is said to be a monochromatic source; alternatively, a source producing a wide range of wavelengths is called a polychromatic source. Unlike the monochromatised beam produced in synchrotron facilities using monochromators of high harmonic rejection, the polychromatic beam produced by conventional impact X-ray sources has many disadvantages such as beam hardening and low SNR (Johnson et al., 1986, Davis and Elliott, 2003). With a monochromatic beam, if the sample is homogenous, different

regions will yield the same linear attenuation coefficient (LAC) values yielding accurately representative results. With a polychromatic beam, even if the sample is homogenous, different regions will have different LAC values resulting in biased results.

3.1.5.6.2 Living subjects

The high-resolution images provided by XMT systems come with various artefacts some of which can only be minimised by increasing the X-ray dose. Due to the extremely high X-ray dosage and the long scans durations required by XMT, it has not been possible to scan living tissues of live small organisms (Paulus et al., 2000). This is considered as a limitation since it limits our ability to study the microstructure of living organisms non-destructively.

3.1.5.6.3 Signal to noise ratio

The conventional microfocus X-ray sources used in XMT scanners produce X-rays with lower flux (the number of photons for a given surface during a given time) compared to medical CT scanners. This reduction in flux lowers the X-ray exposure which in turn causes the contrast and the SNR to decline. To stabilise the SNR when increasing the pixel count of detectors and hence the resolution, the exposure time must be increased. Doubling the resolution requires an exposure time increase of two to the power of four to maintain the same SNR. Increasing the exposure does elevate the SNR but there is a limit at which other systematic errors such as ring artefacts become dominant (Davis et al., 2013).

3.1.5.6.4 Ring artefacts

Ring artefacts can be observed as full or partial circles in the 3-D volume around the centre of the rotational axis caused by non-linearity of adjacent detector elements in the charge-coupled devices (CCD) detector (Stock, 1999, Davis et al., 2013). These artefacts may be caused by damaged or miscalibrated detector elements, a defect in the scintillator, and/or by impurities on the scintillator screen or the detector such as dust, scratch or dirt. It can be also the result of the object attenuating X-rays differently in different projection direction (Stauber and Müller, 2008, Anas et al., 2011, Rashid et al., 2012). Hardware modifications can also reduce the intensity of ring artefacts. This can be achieved by replacing the entire CCD array, re-calibrating and reducing the non-linearity of CCD elements, replacing scratched or damaged scintillator crystals, cleaning scintillator screens and/or moving the sample or the detector slightly between projections (Anas et al., 2011).

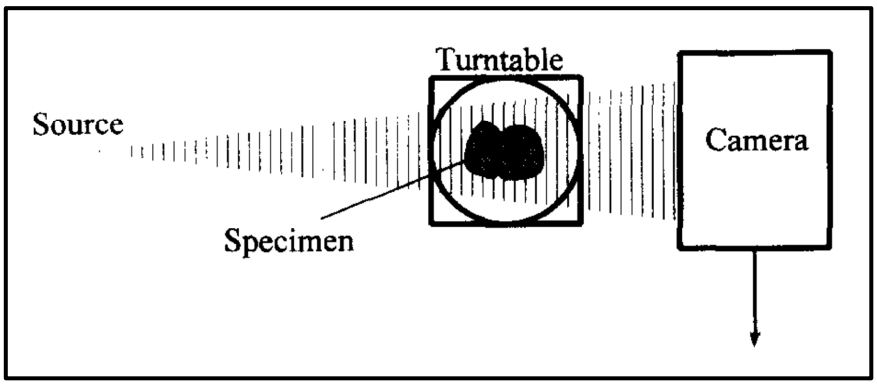

Figure 3.12: A schematic of the time delay integration (TDI) method used to eliminate ring artefact. At each projection, the sample remains stationary while the CCD is moved
(Reproduced with permission of the rights holder, Elsevier, from Davis and Elliott (1997))

A method that proved to eliminate all ring artefacts involves moving the CCD detector in the axis perpendicular to that of the beam during readout then averaging all the detector elements characteristics in each row of the projection was introduced to XMT by Davis and Elliott (1997) **(Figure 3.12)**. This technique, namely time delay

integration (TDI) was originally used to increase exposure time when acquiring linearly moving images (Zhu et al., 2013).

3.1.5.6.5 Beam hardening effects

The beam hardening effect results in dishing or cupping artefacts to appear in the reconstructed image and depends on the incident beam energy spectrum and the size, composition and shape of the sample. XMT systems using laboratory X-ray sources produce polychromatic X-rays with multiple photon energies that have varying absorption rates along the beam. Due to the photoelectric effect, low energy X-rays are attenuated and absorbed more readily by the sample compared to high energy X-rays leading to artefacts following reconstruction, such as brightening of the sample borders and false bridging of dense structures (Johnson et al., 1986).

The simplest way to alleviate this artefact is to use higher energy; however, this reduces the contrast. Another possible method is narrowing the X-ray spectrum through filtering the beam with a thin metal plate such as copper or aluminium before reaching the sample (Grangeat, 2009, Zou et al., 2011). Furthermore, synchrotron X-ray sources XMT systems produce monochromatic X-rays using crystal monochromators eliminating the likelihood of the beam hardening effect (Stenström, 2001). Another effective method is to use a reference material with similar attenuation to that of the sample. A recent study deployed a multi-element calibration carousel with attenuation plates made of titanium, aluminium and copper to increase the range of attenuations available in order to produce a correction polynomial. It minimises the beam hardening affect and provides a good approximation of equivalent monochromatic X-ray attenuation for the samples (Davis et al., 2013).

3.1.5.6.6 Partial volume effects

With insufficient spatial resolution, some voxels contain partial volumes in which a single voxel may have multiple phases that are averaged into a single intensity value resulting in blurred interfaces in the XMT image. Depending on the nature of the study it is possible to completely ignore these voxels during data analysis. It is important to minimise this effect when performing quantitative studies. Software such as Drishti (Australia National University, Canberra, Australia), has the feature of using gradient information to identify partial volume effects. Moreover, increasing the resolution allows for smaller features to be distinguished and hence can decrease the partial volume effect (Johnson et al., 1986, Davis and Wong, 1996, Stenström, 2001).

3.1.5.6.7 Resolution

Resolution describes the ability of an imaging system to distinguish between two objects within a sample. The size and number of the detector elements, the X-ray spot size, the source to sample distance, the sample to detector distance (Li, 2018) and the X-ray exposure time (Davis et al., 2013) influence the XMT resolution. Furthermore, in order to achieve higher resolution in XMT systems, the sample must be small in size (Ahmed, 2011).

3.1.5.6.8 Mechanical and technical instabilities

Artefacts in the reconstructed image may occur when the number of projections is insufficient or if the projection data are under sampled and can be minimised by elevating projections quantity or by decreasing the intervals within each projection. Additionally, improper calibration and set up of the equipment can result in miss-alignment of the centre of rotation (Olander, 1994). Moreover, XMT suffers greatly from the lack of reproducibility which is due to system imperfections and environmental

variations such as temperature changes, accelerating potential changes, beam current changes, and movement of the electron beam position on the target (Stenström, 2001).

3.2. Scanning electron microscopy

3.2.1. Introduction

SEM is an analytical technique, capable of providing high magnification visualisation of structures without altering the specimen using an electron beam (Krinsley et al., 2005). A typical SEM consists of an electronics console and an electron column where electrical and magnetic fields are used to control the electron beam. An electron gun is located at the top of the column and provides a source of electrons, where a beam of electrons is emitted under vacuum conditions from a thermionic or a field-emission cathode to be accelerated by an anode to a voltage in the range of 1-50 kV. A cylinder, called the Wehnelt cylinder controls the number of electrons leaving the gun. The beam is then demagnified to a small spot size with the aid of two- or three-stage electron lens system (Lyman et al., 1990, Saghiri et al., 2012). The closest lens to the electron gun is termed the condenser lens, while the lens closest to the sample is called the final or objective lens. To reduce lens aberration effects and increase the image depth of field, a platinum disk with a small hole termed the objective aperture is usually located inside the objective lens (Lyman et al., 1990). Deflection coils scan the sample surface in a raster pattern and the signal is detected using an appropriate detector (Lyman et al., 1990, Saghiri et al., 2012).

The narrower the diameter of this electron beam the higher the spatial resolution of the image and the larger the depth of field. The change in contrast across particles gives

different shades in the micrograph depending on the operation mode of the SEM and the working distance (Saghiri et al., 2012). This determines the type and quality of information that can be gathered from the sample (Boyde and Jones, 1983).

The initial primary electrons (PE) interaction with matter involves elastic and inelastic scattering processes (Potts, 2012). A multitude of signals are emitted from different depths of the bombarded surface that contain information regarding the sample properties, surface topography and composition. The produced signals include secondary electrons (SE), back-scattered electrons (BSE), Auger electrons, light (cathodoluminescence), specimen current, transmitted electrons, electron beam induced current (EBIC), characteristic X-rays and continuum X-rays. **(Figure 3.13)** (Krinsley et al., 2005, Potts, 2012). This work will concentrate on the BSEs and SEs signals.

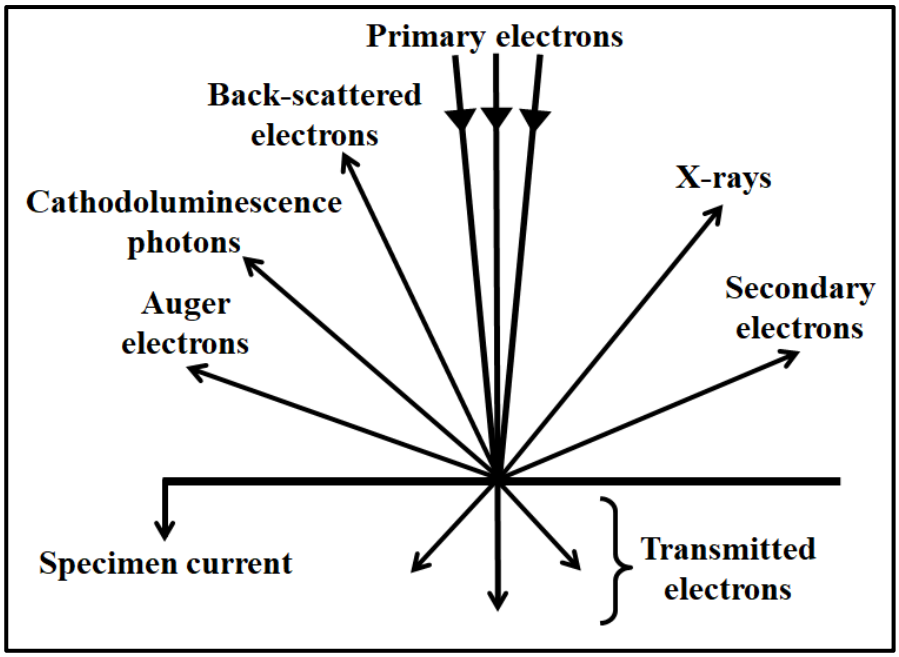

Figure 3.13: Signals resulting from the interaction between the primary electrons beam and the sample **(Adapted from Krinsley et al. (2005))**.

3.2.2. Secondary electrons modality

SEs are electrons that originally reside in the specimen. When a specimen is impacted by an electron beam, the PEs transfer some of their energy to the specimen electrons,

ionising them in the process. As a result, some of the specimen electrons are detached from the specimen atoms as SEs. These dislodged SEs have a very low kinetic energy, the average being only few electron volts, and are readily captured by nearby ionised atoms. The SEs closer to the specimen surface can be emitted into the vacuum; however, due to their very low energy, SEs cannot escape from depths greater than approximately 50Å within the specimen. SEs are thus produced from atoms within a very thin surface layer and from a small localised region around the impact point of the PEs beam. Therefore, the SEs signal is generated from a smaller sample volume than BSEs, making it ideal for high resolution surface imaging (Watt, 1997, Krinsley et al., 2005, Saghiri et al., 2012, Potts, 2012). An artifact termed "edge effect" may occur in which sharp edges of a sample appear abnormally brighter than the rest of the sample. Furthermore, due to SEs very low energy, a buildup of charges in the order of few electron volts on a conductive surface is enough to result in charging artifacts (Krinsley et al., 2005).

3.2.3. Back-scattered electrons modality

BSEs are PEs that decelerate upon collision with the sample atoms and scatter back out of the sample surface. Therefore, BSEs have a broad energy spectrum from zero up to the PE beam energy, and are emitted from the top third of the excited volume (Potts, 2012). The intensity of the BSEs signal in SEM strongly depends on the mean atomic number of the elements making up the sample and can thus be used to assess, for example, the chemical phases present in the specimen and the variations in mineral density within the sample (Lloyd, 1987, Wang and Weiner, 1997).

BSEs are emitted from greater sample depths and at a more significant distance from the incident beam than do SEs, limiting the resolution of this imaging mode (Cole et al.,

2000, Krinsley et al., 2005). Due to their higher energy, they can be distinguished from SE. PEs are scattered more effectively by atoms with high atomic weight, allowing BSEs images to contain subsurface compositional detail that yield information regarding, for example, variations in mineral density (Pearce and Nelson, 1989). The use of BSE has the advantage that the BSEs have an average energy of 50-90% of the PEs, therefore, a very high charge build up is required before charging effect appear; thus the 'charging' problems of SE imaging can be simply overcome. Furthermore, it is possible to generate BSE images from uncoated specimens, unlike SEs mode where the sample has to be coated with carbon or gold before being scanned (Boyde and Jones, 1983, Krinsley et al., 2005).

3.2.4. Quantitative back-scattered electrons microscopy to investigate human enamel

Scanning electron microscopy is used routinely to study the microstructure of dental hard tissues; however, there are a few studies that have had a particularly important contribution to our understanding of the microstructure of enamel and these are described here.

Pearce and Nelson (1989) used BSE to produce mineral density maps of carious human enamel. It was found that on a surface prepared parallel to the natural surface, mineral was lost from prism core and the so-called inter-prismatic region. However, in a surface prepared perpendicular to the natural surface, the lesion body displayed higher mineral content at the prism periphery. Furthermore, widening of the prism junction at the advancing fronts of the lesions was reported.

Bell et al. (1991) studied the diagenetic alterations to archeological human teeth using BSE and concluded that human enamel was unaffected by diagenesis. Arima and

Matsumoto (1993) demonstrated using BSE as a complementary technique that human enamel can be cut by ArF:excimer laser without inducing thermal injury. Fearne et al. (1994) studied hypo-mineralised and hypoplastic primary teeth from children born with very low birth weights using BSE and demonstrated a reduction in mineral content of almost 10% in hypo-mineralised teeth.

Wang and Weiner (1997) used BSE to study the level of mineralisation of human enamel and dentine. Boyde (1998) confirmed the existence of cross striations using BSE. Mahoney et al. (2004) used BSE to compare the mineral density between sound and hypo-mineralised human enamel. A reduction in mineral density by approximately 5% in comparison to sound enamel was reported.

Shellis et al. (2005) used BSE imaging for studying unerupted human enamel and found that the rate of erosion of enamel surfaces exposed to erosive solution depends on liquid velocity, exposure time and total volume of solution. Götz et al. (2007) studied the ultrastructure effect of hydrogen peroxide bleaching on human enamel using BSE. It was found that hydrogen peroxide had no significant effects on enamel surface or subsurface. Xue et al. (2009) compared the demineralisation of human enamel natural and abraded surfaces using BSE. It was concluded that natural enamel surface protects deep enamel from acid dissolution.

Chapter 4 - Materials and methods

4.1. Sample selection

Maxillary permanent central and lateral incisors were chosen in the current investigation due to the fact that single cusp dentitions are less complex regarding enamel crystal arrangement and therefore offer the simplest case. It was reported that permanent central incisal enamel starts forming approximately 4-5 months after birth and erupts into the oral cavity between the ages of 9-10 years after birth. Furthermore, the formation of permanent maxillary lateral incisal enamel was reported to begin at approximately 10-12 months after birth and tooth eruption takes place approximately between the ages of 10-11 years after birth (Schour and Massler, 1940b).

Therefore, in order to gain a complete insight on how mineralisation is progressing, permanent central and lateral incisors at various stages of development before they erupt into the mouth are required. However, such samples are not readily available for investigation due to the challenges associated with acquiring the necessary ethical approvals. Various studies overcame this issue by recovering developing human enamel samples belonging to deceased juveniles from archaeological sites (Peretz et al., 1997, Reid et al., 1998, Zeygerson et al., 2000, Antoine, 2000, Antoine et al., 2009, Mahoney, 2012, Simmons et al., 2013) as has been done successfully with this current work through collaboration with archaeologists. Through such collaboration it was possible to obtain various developing human teeth for comparison.

The stage of development was determined according to Alqahtani et al. (2010). Teeth were considered to be in early development if the crown was less than three quarters (Cr ¾) completed; in mid development if the root length was less than the crown length

(R ½); and in full development if three quarters (R ¾) or more of the root length was developed **(Figure 4.1)**.

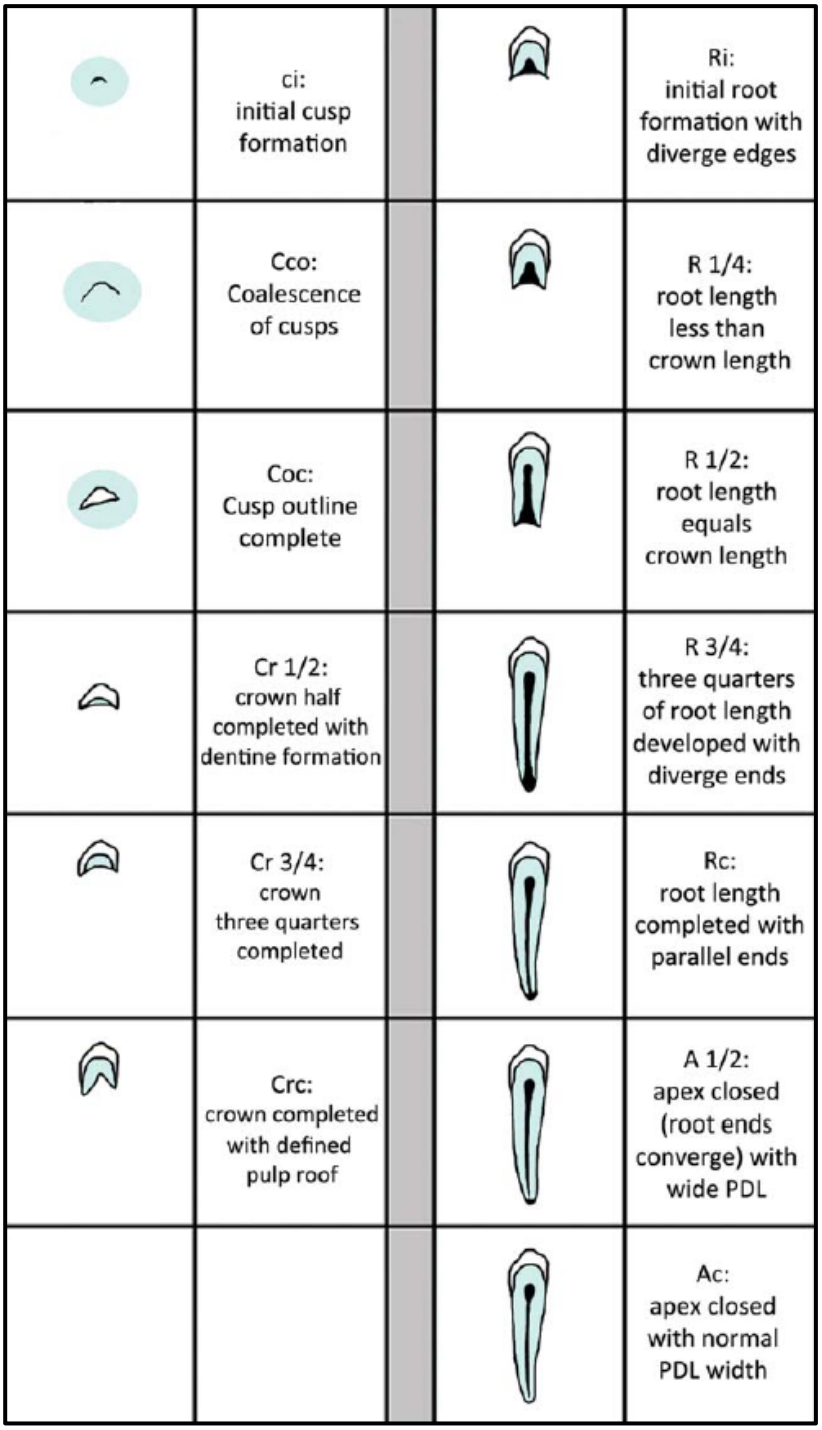

Figure 4.1: Description of tooth developmental stages of single rooted dentitions **(Reproduced with permission of the rights holder, John Wiley and Sons, from Alqahtani et al. (2010))**.

One maxillary lateral incisor at mid-development (sample L1) and four maxillary central incisors at early (samples C1 and C2) and mid-development (samples C3 and

C4) were obtained from the skeletal assemblage excavated from the 12th-16th century AD mediaeval cemetery of Blackfriars (Gloucester, UK) curated by the Biological Anthropology Research Centre, University of Bradford (Bradford, UK) **(Figure 4.2)**. Type-matched mature contemporary teeth (samples C5 and L2) collected with informed consent from patients treated at Barts and the London Dental Hospital (London, UK) paediatric clinics were used for comparison.

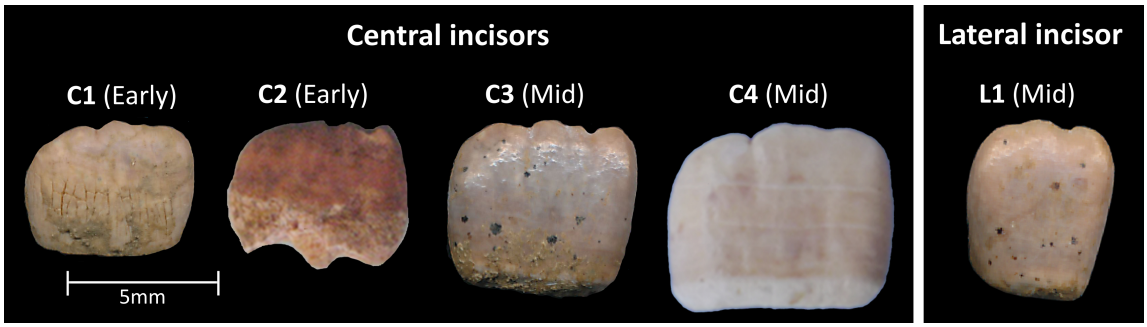

Figure 4.2: Photographs of the five developing human permanent maxillary incisors obtained from the

4.2. X-ray microtomography

4.2.1. Sample preparation

Whole teeth were analysed using XMT to quantify and compare relative mineral density variations. Due to the dry nature of archaeological teeth (samples C1, C2, C3, C4 and L2), no further sample preparation took place. Contemporary mature teeth (samples C5 and L2) were stored in 100% ethanol solution prior to scanning.

4.2.2. Experimental setup

XMT experiments were performed using a fourth generation in-house XMT scanner (MuCAT2) developed at Queen Mary, University of London (QMUL) (Davis et al., 2013). The scanner consists of a microfocus X-ray source (X-Tek Systems Ltd., Herts, UK) with 225 kV microfocus X-ray generator and 5 μm focal spot size, a tungsten target, a kinematic sample stage and an area detector (Spectral Instruments, Tucson,

Arizona, USA). The detection system comprises of a cooled 4000 × 4000 CCD detector coupled via a parallel fibre-optic faceplate to a columnar caesium iodide (CsI) scintillator (Applied Scintillation Technologies, Essex, UK) (Davis et al., 2013).

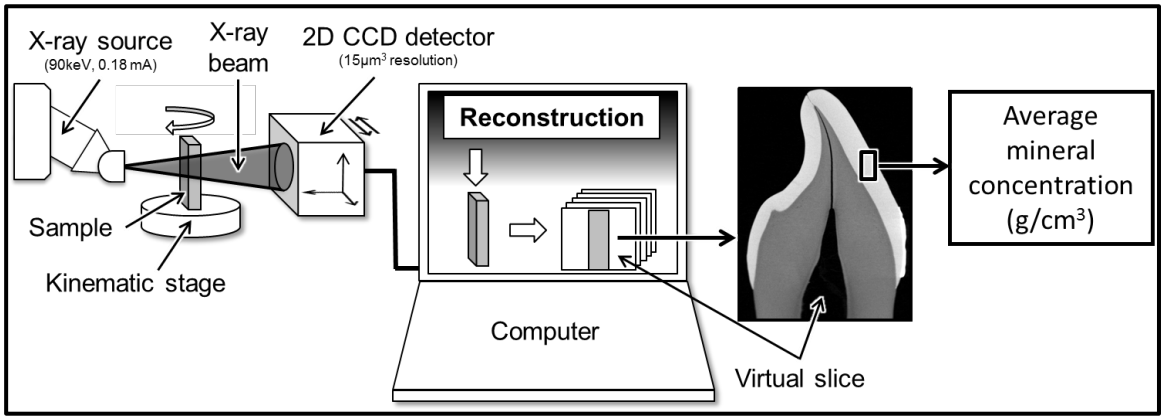

Figure 4.3: A schematic diagram of the XMT experimental setup using the MuCAT 2 scanner (QMUL).

The CCD and the specimen were mounted on mechanical stages (Physique Instrumente, Palmbach, Karlsruhe, Germany). The X-ray source could be demounted allowing the target and emitter to be easily changed if higher power is required. Time-delay integration **(See Section 3.1.5.6.4)** CCD readout was employed to eliminate ring artefacts (Davis and Elliott, 1997). The spectral spread was minimised using 1.2 mm aluminium and 0.05 mm copper X-ray filter (Davis et al., 2013). In order to correct for beam hardening **(See Section 3.1.5.6.5)**, each scan was calibrated for 40 keV equivalent monochromatic energy using a multi-element calibration carousel with 9 attenuation plates (1 copper, 3 titanium and 5 aluminium plates) (Evershed et al., 2012). The samples were scanned with a beam voltage of 90 kV and a beam current of 0.18 mA**.** The XMT temperature was maintained at 26 $°C \pm 0.1\ °C$ to maintain dimensional stability. Cubic voxel resolutions of 13, 15 and 18 μm were set depending on time restrictions **(Table 4.1)**. A schematic of the experimental setup is shown in Figure 4.3.

Table 4.1: The voxel sizes set for the various samples

Sample	C1	C2	C3	C4	C5	L1	L2
Voxel size (μm)	15	18	15	13	15	15	15

4.2.3. Data analysis

The 2-D projections were mathematically reconstructed into stacked 2-D images as a 3-D volume via filtered Feldkamp back-projection algorithm (Feldkamp et al., 1989) using an in-house cone beam reconstruction program (ConeRec). When the X-ray cone beam scan the object, a projection is produced. In order to view the internal features of the object, a series of projections at various angles around an axis perpendicular to the object are collected. For each projection, Fourier transform is performed, and a frequency weighted filter is applied in order to magnify the low frequency proportion before carrying inverse Fourier transform. Each filtered projection is then smeared across the image plane (back-projected) at an angle parallel to the X-ray beam using inverse Radon Transform. The filtered back-projected projections are added together (back-projection summation), producing a reconstructed image of the internal structure of the scanned object.

LAC describes the fraction of a beam of X-rays that is absorbed or scattered per unit thickness of the material. In the present study, the LACs of the specimens were calibrated for a 40 keV equivalent monochromatic energy. When a monochromatic X-ray beam passes through a homogenous absorbing material the relation between incident intensity (I_0), and attenuated intensity (I) is given by Beer's Law (Stock, 1999):

$$I = I_0 \exp(-\mu_{LAC} t)$$

Equation 4.1

Where μ_{LAC} is the LAC and t is the thickness of the object material. The minimum number of projections (P) required for specimen reconstruction is given by:

$$P = \frac{\mu_{LAC}}{2} w$$

Equation 4.2

Where w is the width of the specimen and μ_{LAC} is the LAC.

From the calibrated 2-D projections, 3-D image reconstruction was performed with a modified Feldkamp cone-beam back projection algorithm (Feldkamp et al., 1984) using software developed at QMUL. The final output file was a data set of LACs that were scaled to 256 grey levels.

Assuming that the component absorbing the X-rays was pure HAp, LACs were then used to calculate the enamel relative mineral density values (x) expressed in g/cm^3:

$$x = \frac{\mu_{LACm}}{\mu_{MAC}}$$

Equation 4.3

Where μ_{LACm} is the LAC, and μ_{MAC} is the mass attenuation coefficient (MAC).

The value of the MAC depends on the absorption and scattering of the incident beam. It is defined as μ_{MAC} which describes the attenuation per unit mass of material traversed. MAC is typically expressed in units of $cm^2\ g^{-1}$ and is obtained by:

$$\mu_{MAC} = \frac{\mu_{LACp}}{\rho}$$

Equation 4.4

Where μ_{LACp} is the LAC of the pure sample of the mineral, and ρ is the sample density.

Combining Equation 4.3 and Equation 4.4 yields the following equation:

$$x = \frac{\mu_{LACm}}{\mu_{LACp}}\rho$$

Equation 4.5

Where x is the relative mineral density, μ_{LACm} is the measured sample LAC, μ_{LACp} is the LAC of the pure sample of the mineral (LAC of pure HAp mineral at 90 kV is 3.12 cm^{-1} (Davis et al., 2013)), and ρ is the sample density (XMT ρ is equal to 3.16 $g\ cm^{-3}$ (Davis et al., 2013)).

Two software packages were used to analyse the reconstructed data, namely ImageJ (Open source, Rashband, 2006) and Tomview (Prof. Graham Davis, QMUL, London, UK). ImageJ is an image processing program that was used to calculate morphometric parameters from reconstructed data and set colour scales to mineral density values. Tomview, an in-house analysis tool developed by Prof. Graham Davis (QMUL, London, UK), was used to read .tom files, present the tomographic dataset in the three Cartesian planes, apply mineral density colour scales and collect values of LAC expressed in units of cm^{-1}.

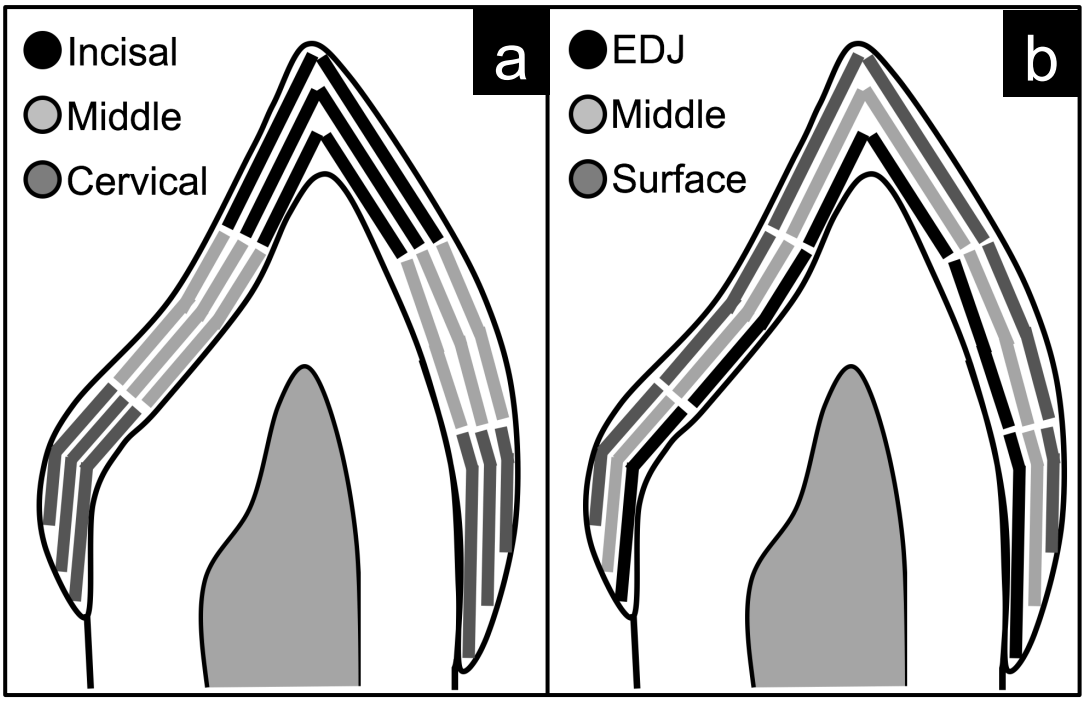

Figure 4.4: A schematic diagram representing a typical XMT slice showing the 18 regions, and how they are divided for **a)** vertical and **b)** horizontal analysis. For each tooth section, labial is on the right-hand side.

A total of 18 regions (9 palatal and 9 labial) were selected for each tooth. 200 points were selected from each region and the LAC values were averaged. The average mineral density for each region was calculated using Equation 4.5. Figure 4.4 shows the method used to divide the labial and palatal sides into 18 regions. This method allows for analysing vertical **(Figure 4.4a)** and horizontal **(Figure 4.4b)** mineral density.

4.3. 2-D synchrotron X-ray diffraction

4.3.1. Sample preparation

The specimens were embedded in fast curing acrylic cold mounting resin (ClaroCit Kit, Steuers, Ballerup, Denmark). This involved placing each tooth in a cylindrical mould. Subsequently, the ClaroCit powder and liquid were mixed as per manufacturer's instruction, poured into the mould and left to cure for 20 minutes at room temperature **(Table 4.2).**

Table 4.2: Acrylic resin preparation	
Mounting material	Steuers ClaroCit
Recommended mixing ratio weight	Liquid: 6 parts Powder: 10 parts
Mixing time	1.5 minutes
Curing time	20 minutes

Each of the embedded teeth was cut through the mid-point perpendicular to the bucco-lingual surface using a Struers Accutom-5 diamond saw (Struers, Willich, Germany**)** to produce 0.3 mm thick mid slice for each tooth **(Figure 4.5 and Figure 4.6)**. Samples C1, C3 and C5 were each further sectioned into three additional, 0.3 mm thick longitudinal sections for full crown analysis. Table 4.3 displays the parameters used for cutting.

Table 4.3: Diamond cutter parameters	
Feed speed	0.2 mm/s
Wheel speed	3000 RPM
Force	Low
Blade thickness	150 μm

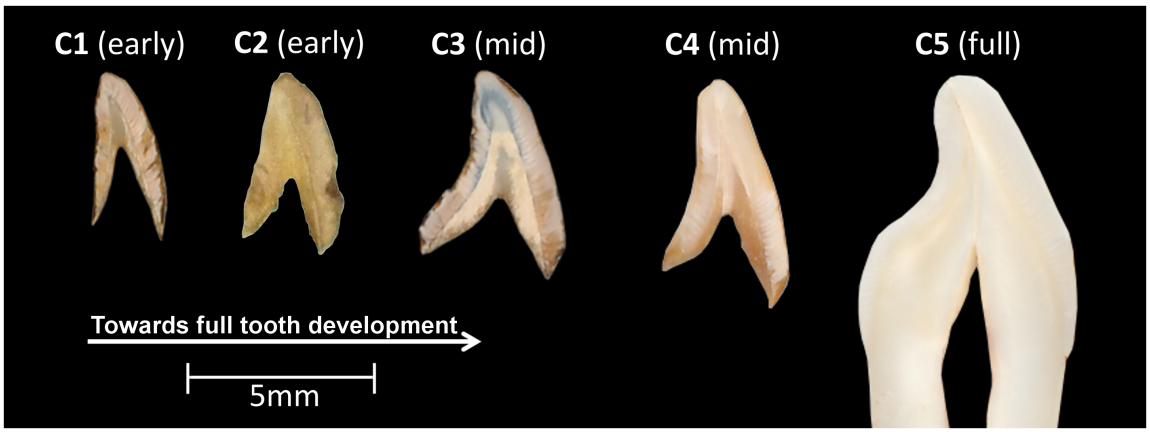

Figure 4.5: 0.3 *mm* thick slices of permanent maxillary central incisors at various developmental stages. For each tooth section labial is on the right-hand side.

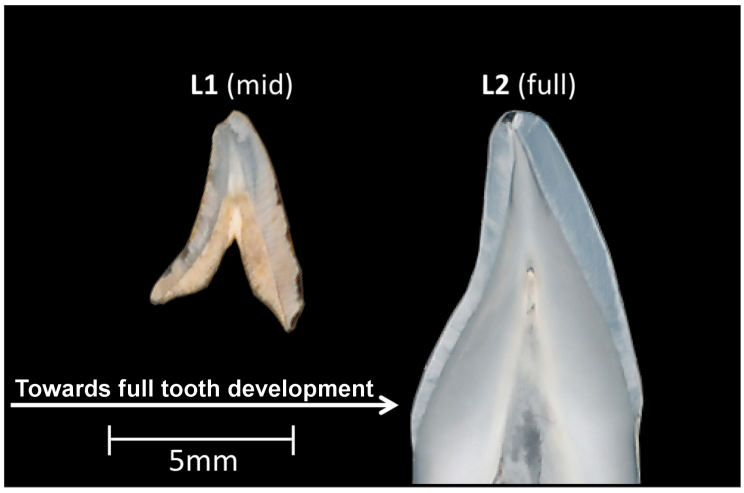

Figure 4.6: 0.3 *mm* thick slices of permanent maxillary lateral incisors at various developmental stages. For each tooth section labial is on the right-hand side.

4.3.2. Experimental setup

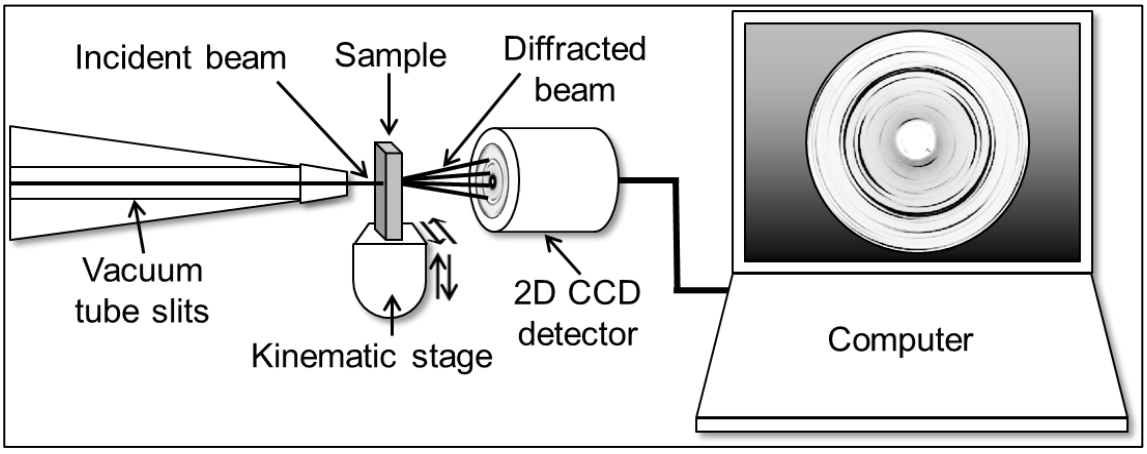

Figure 4.7: S-XRD experimental setup at XMaS and B16 beamlines at the ESRF and DLS respectively.

S-XRD on XMaS (BM28) beamline at the ESRF and B16 beamline at the DLS were used to map the crystallographic structural parameters of the specimens. Both of the above-mentioned beamlines were suitable for the measurements required for the current study. A schematic of the experimental setup is shown in Figure 4.7. The experimental parameters used, and a list of the samples analysed at the two synchrotron beamlines are given in Table 4.4. The X-ray energies at the two beamlines were selected in order to achieve a similar X-ray flux value. In order to fully assess the similarity of data collected from the BM28 and B16 beamlines, we performed a back-to-back comparison test using a region of sample C3 assessed at both beamlines. The data collected at the two beamlines were similar confirming that the data were independent of the beamline used.

Table 4.4: Experimental parameters used at XMaS and B16 beamlines at the ESRF and DLS respectively.

	Synchrotron facility beamline	
	XMaS (BM28)	**B16**
X-ray energy (*KeV*)	15	18
Beam size (μm^2)	50	43
Beam wavelength (Å)	0.82	0.69
CCD detector model	MarCCD165 (Rayonix, L.L.C., IL, USA)	ImageStar9000 (Photonic Science Ltd., East Sussex, UK)
CCD detector resolution (pixels)	2048 × 2048	3056 × 3056
CCD detector pixel size (μm^2)	80	30
Kinematic stage	Huber (Rimsting, Germany)	Newport (California, USA)
Analysed samples	C1 (palatal) C1-S1 (labial + palatal) C1-S2 (labial + palatal) C1-S3 (labial + palatal) C2 (labial + palatal) C3 (palatal) C3-S1 (labial + palatal) C3-S2 (labial + palatal) C3-S3 (labial + palatal) C4 (labial + palatal) C5 (labial + palatal) C5-S1 (labial + palatal) C5-S2 (labial + palatal) C5-S3 (labial + palatal) L1 (labial + palatal) L2 (labial + palatal)	C1 (labial) C3 (labial)

Samples were mounted on a custom-built sample holder that was fastened to the beamline kinematic sample stage. The kinematic stages at the two synchrotron facilities allowed samples to be scanned at two orthogonal axes perpendicular to the X-ray beam. The 2-D CCD detectors were mounted behind the samples and perpendicular to the incident beam. The dental enamel of each specimen was selected and scanned according to our established methods to produce XRD diffraction images (Al-Jawad et al., 2007).

Table 4.5: Data acquisition parameters

Sample	Tooth side	Beam Size (μm^2)	S-D distance (mm)	Horizontal step size (μm)	Vertical step size (μm)	Number of patterns	Exposure time (s)
C1	Labial	43	145	100	100	625	120
	Palatal	50	105	50	50	3900	5
C1-S1	Labial	50	190	50	100	1140	10
	Palatal	50	190	50	100	800	5
C1-S2	Labial	50	175	50	50	2860	2
	Palatal	50	190	50	100	940	5
C1-S3	Labial	50	190	50	100	1248	10
	Palatal	50	190	50	100	900	5
C2	Labial	50	190	50	100	864	10
	Palatal	50	190	50	100	1102	10
C3	Labial	43	145	100	100	906	120
	Palatal	50	105	50	50	1564	5
C3-S1	Labial	50	190	50	100	1795	10
	Palatal	50	190	100	100	882	5
C3-S2	Labial	50	175	50	100	1898	2
	Palatal	50	190	100	100	900	5
C3-S3	Labial	50	190	50	100	1808	10
	Palatal	50	190	100	100	840	5
C4	Labial	50	145	50	50	4396	5
	Palatal	50	190	50	100	1612	10
C5	Labial	50	175	50	100	2100	3
	Palatal	50	175	50	100	1861	3
C5-S1	Labial / Palatal	300	170	300	300	504	5
C5-S2	Labial / Palatal	300	170	300	300	440	5
C5-S3	Labial / Palatal	300	170	300	300	600	5
L1	Labial	50	175	50	50	2860	2
	Palatal	50	190	50	50	3668	10
L2	Labial	50	175	50	100	3264	5
	Palatal 1	50	175	50	100	1410	3
	Palatal 2	50	190	50	50	1932	10

The sample to detector (S-D) distance was set so that a 2θ range of approximately 5-25° could be explored. A total of 49,619 diffraction patterns were collected at $\omega = 0°$, i.e. the incident beam is perpendicular to the sample surface. The instrument parameters such as the X-ray wavelength, the sample to detector (S-D) distance, and the peak-shape profile were determined using a lanthanum hexaboride (LaB_6) standard sample via the ESRF software package Fit2D (Hammersley, 1997). Data for samples C5-S1, C5-S2 and C5-S3 were collected by Dr Maisoon Al-Jawad before the start of the thesis. Variations in instrument parameters depended on the operating mode of the synchrotron facilities at the times of the experiments (five synchrotron visits in total) and are summarised in Table 4.5.

4.3.3. Data analysis

Figure 4.8 shows a typical diffraction image from human dental enamel where the Debye rings can be seen; the Bragg angle 2θ is marked. The high maxima seen on the rings are the result of the preferred orientation of the dental enamel crystallites. The positions of these maxima contain the information of the spatial orientation of the corresponding lattice plane $(h\ k\ l)$ (Al-Jawad et al., 2007).

Fit2D (Hammersley, 1997) was used to generate composite maps of the 2-D diffraction patterns for entire tooth sections. It is established that the (0 0 2) lattice plane reflection ($2\theta = 13.71°$, highlighted in Figure 4.8) does not overlap with other major reflections and has the greatest variation in intensity with maxima since it is the plane normal to the c-axes of the crystallites (Simmons et al., 2013, Sui et al., 2014a).

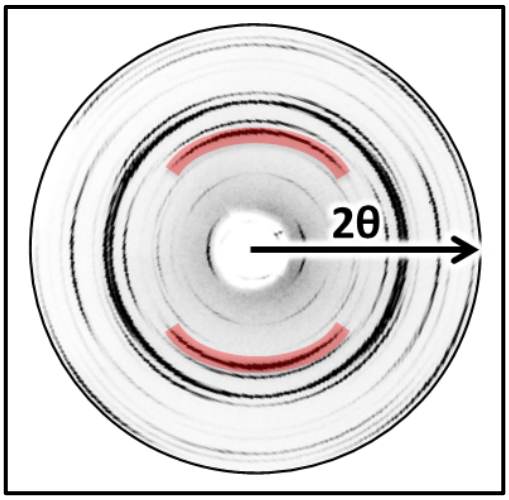

Figure 4.8: A typical diffraction pattern of human enamel at ω = 0° showing Debye–Scherrer rings with distinct maxima, resulting from the preferred orientation. The (0 0 2) reflection maxima are highlighted and the Bragg angle 2θ is marked.

Therefore, it is possible to obtain an overview of the directions of preferred orientations for the entire tooth slice by plotting a fibre axis that passes through the centres of the opposing (0 0 2) reflection maxima on each diffraction pattern **(Figure 4.9e)** in the composite map (Trautz et al., 1953, Glas, 1962, Simmons et al., 2013, Sui et al., 2014a).

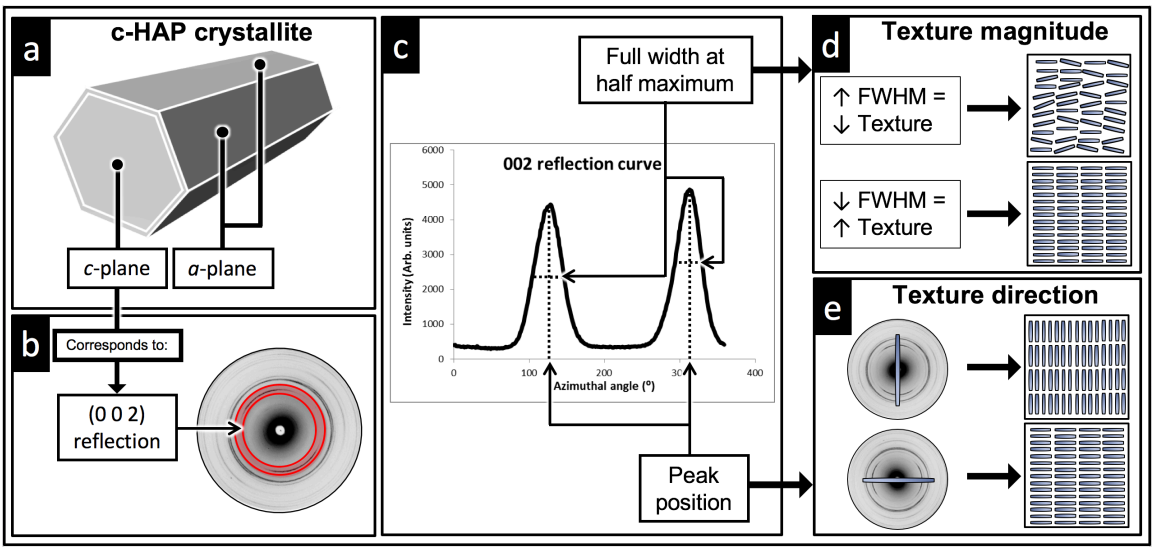

Figure 4.9: A diagram showing the relation between **a)** the *c*-axis of a c-HAp crystallite and **b)** the (0 0 2) reflection in a typical diffraction pattern. **c)** The azimuthal 1-D profile of the (0 0 2) reflection obtained from the deconvolution of the 2-D diffraction patterns can be used to determine crystalline texture **d)** magnitude and **e)** direction.

The azimuthal 1-D profiles of the (0 0 2) reflections were obtained from the deconvolution of the 2-D diffraction patterns using Fit2D. The radial integration width

was selected to be close to the width of the (0 0 2) reflection **(Figure 4.9b)**. The azimuthal profiles were integrated intensity as a function of all azimuthal angles over a narrow band covering the (0 0 2) reflection **(Figure 4.9c)**. The graph in Figure 4.9c displays a typical (0 0 2) reflection curve from a sample containing a single preferred orientation. The two pronounced peaks seen in Figure 4.9c represent the opposing (0 0 2) reflection maxima and are separated by approximately 180°.

However, the (0 0 2) reflection curves obtained during this investigation did not show the expected two pronounced peaks seen in Figure 4.9c. Instead, they had either four pronounced peaks or two pronounced peaks each with a shoulder. Spatial analysis of developing and fully-developed enamel showed a similar trend regarding the occurrence of these peaks **(Figure 4.10)**.

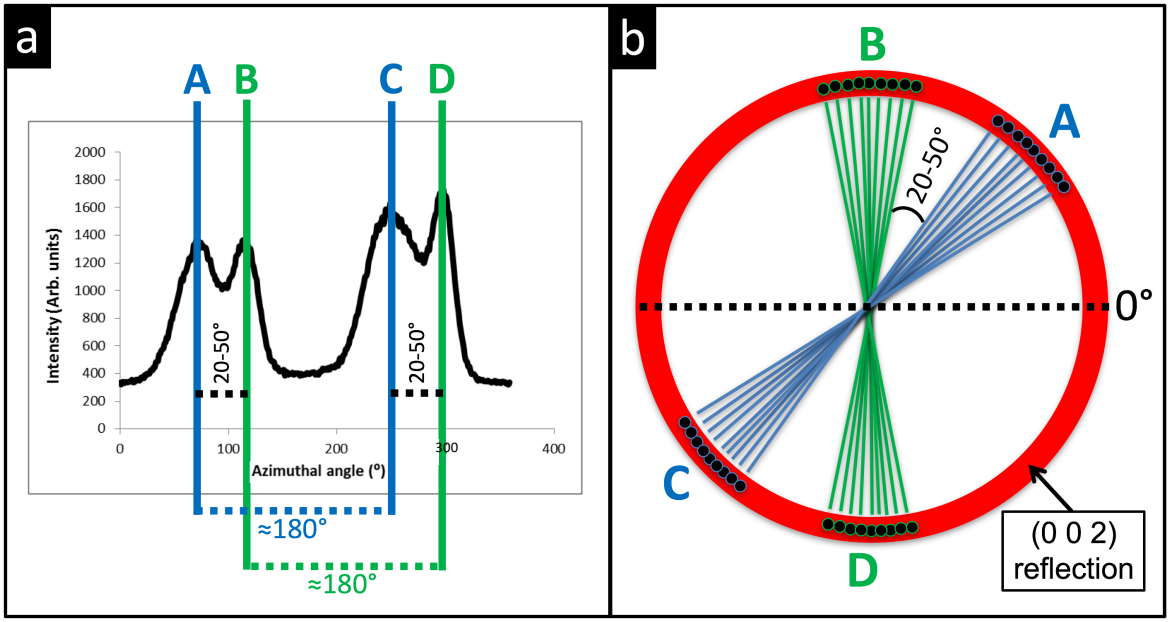

Figure 4.10: a) A typical (0 0 2) reflection curve displaying the variations in intensity around the (0 0 2) reflection. Peaks *A* and *C* are separated by approximately 180°, as with peaks *B* and *D*. Peaks *A* and *B*, and peaks *C* and *D* are separated by 20-50°. **b)** A schematic showing the two orientation populations of crystallites, where peaks that *A* and *C* represent the first population and peaks *B* and *D* represent the second population with an angular separation of 20-50° between them.

The two additional peaks indicate the presence of two populations of crystallites with distinct preferred orientations. The four peaks were named $A, B, C,$ and D. Peaks A and

C are separated by approximately 180°, as with peaks B and D. Peaks A and B, and peaks C and D are separated by 20°-50° **(Figure 4.10a)**. Therefore, we suggest that A and C represent the first population and peaks B and D represent the second population with an angular separation of 20-50° between them **(Figure 4.10b)** – this parameter is explored quantitatively during the data analysis.

The author's own automated batching procedure (MoFit) built with MatLab R2017a (MathWorks, Natick, Massachusetts, USA) was used to fit the (0 0 2) peaks to a Gaussian peak shape using Equation 4.6:

$$y = \sum_{i=1}^{n} a_i e^{-\left[\left(\frac{x-b_i}{2c_i}\right)^2\right]}$$

Equation 4.6

Where a is the peak intensity, b is the azimuthal angle (peak position), c is the root mean squared width (RMSW), and n is the number of peaks to fit (four in this case).

4.3.3.1. *Texture magnitude*

The term texture or preferred orientation is used to describe the organisation of crystallites within a polycrystalline material (Al-Jawad et al., 2007, Al-Jawad et al., 2008, Simmons et al., 2011, Simmons et al., 2013). The parameter c **(Equation 4.6)** is related to the FWHM of the peak according to:

$$FWHM = 2\sqrt{2ln2}\, c$$

Equation 4.7

FWHM values of peaks A ($FWHM_A$) and C ($FWHM_C$) and those of peaks B ($FWHM_B$) and D ($FWHM_D$) were averaged to provide an average FWHM values for the first ($FWHM_{pop1}$) and second ($FWHM_{pop2}$) populations respectively:

$$FWHM_{pop1} = \frac{FWHM_A + FWHM_C}{2}$$

Equation 4.8

$$FWHM_{pop2} = \frac{FWHM_B + FWHM_D}{2}$$

Equation 4.9

$FWHM_{pop1}$ and $FWHM_{pop2}$ values were used to create texture magnitude contour maps for the first and second orientation population respectively using SigmaPlot 10 (Systat Software Inc., San Jose, California, USA). A lower FWHM value correlates with a higher degree of texture and vice versa **(Figure 4.9d)** (Trautz et al., 1953, Glas, 1962, Gwinnett, 1966).

4.3.3.2. *Texture direction*

The texture direction was determined using the intensity pattern around the Debye ring of the (0 0 2) reflection **(Figure 4.9e)**. For consistency and clarity, a constant 100 μm × 100 μm spatial resolution was used for each 2-D crystallite direction map with the aid of Kutools for Microsoft® Excel® v 7.50 (Detong Technology Ltd. Hainan, China). Parameter b from Equation 4.6 represents the azimuthal angle and was used to determine the crystallite direction using an automated in-house software built with MatLab R2017a (MathWorks, Natick, Massachusetts, USA).

A table of X (columns), Y (rows), and Z (azimuthal angles) values was created for each specimen. Subsequently, a 2-D mesh plot was created were the azimuthal angle value

(Z) was assigned to each column (X) and row (Z) point in the mesh, in the required order. For example, the X, Y, and Z values in Table 4.6 yields the 4 × 3 mesh in Figure 4.11a.

Table 4.6: An example XYZ mesh format

X data (Columns)	Y data (Rows)	Z data (Angle (°))
1	1	0
2	1	0
3	1	0
1	1	0
2	2	0
3	2	0
1	2	90
2	2	90
3	3	90
1	3	90
2	3	90
3	3	90

A 51 × 51 pixels base circular image with a strip in the middle was defined. The base circular image was set to rotate by the value of each cell in the mesh. A loop was then employed to stack all of the rotated images in a grid that resembles the azimuthal angles seen in the rotation values matrix. A final output image which has as many images as there are cells in the mesh can then be generated **(Figure 4.11b)**.

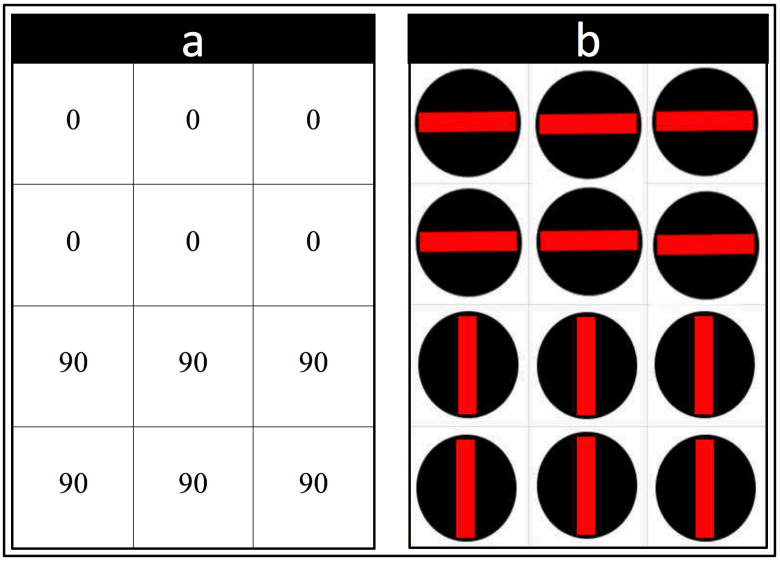

Figure 4.11: a) The resultant 3 × 4 mesh from Table 4.6 and **b)** the corresponding texture direction map.

4.3.3.3. *Angle between populations*

Parameter b from Equation 4.6 represents the azimuthal angle and was used to calculate the angular separation (Δ_b) between the two orientation populations. Δ_b was quantified by subtracting the azimuthal angle of peak B (b_B) from that of peak A (b_A), and the azimuthal angle of peak D (b_D) from that of peak C (b_C) and averaging the two subtracted values

$$\Delta_b = \frac{(b_B - b_A) + (b_D - b_c)}{2}$$

Equation 4.10

Δ_b was calculated for each diffraction pattern and used to construct contour maps using SigmaPlot 10 (Systat Software Inc., San Jose, California, USA).

4.3.3.4. *Populations percentage*

Parameter a from Equation 4.6 represents the peak intensity and was used to calculate the percentage of the first orientation population ($\%_{pop1}$). Peaks intensities of the (0 0 2) reflection curve correlate with the quantity of crystallites c-planes satisfying the Bragg law. This allows for predicting the relative quantity of each population in every probed region. The intensity of the first orientation population (a_{pop1}) was calculated by averaging the intensities of peaks A (a_A) and C (a_C) according to the following equation:

$$a_{pop1} = \frac{a_A + a_c}{2}$$

Equation 4.11

Similarly, the intensity of the second orientation population (a_{pop2}) was calculated by averaging the intensities of peaks B (a_B) and D (a_D) according to the following equation:

$$a_{pop2} = \frac{a_B + a_D}{2}$$

Equation 4.12

The values from Equation 4.11 and Equation 4.12 was used to calculate the percentage of the first orientation population ($\%_{pop1}$):

$$\%_{pop1} = \frac{a_{pop1}}{a_{pop1} + a_{pop2}} \times 100$$

Equation 4.13

The $\%_{pop1}$ values were used to create contour maps using SigmaPlot 10 (Systat Software Inc., San Jose, California, USA).

4.4. Quantitative back-scattered electrons imaging

4.4.1. Sample preparation

The samples were sectioned as per the method discussed previously in Section 4.3.1. The mid slices of specimens C1, C3, C5, L1 and L2 were assessed using qBSE imaging. The slices were wet-ground with 100-, 220-, 320-, 400- and 600-grit silicon carbide abrasive papers (Buehler, Illinois, USA) on an automatic lapping and polishing unit (Kent 4, Kemet International Ltd., Maidstone, UK). Using successively finer grades of abrasive paper removed damage produced by the earlier grit.

The samples were then polished using a sequence of successively finer particle size diamond polishing pastes ranging from 6 to 0.25 μm (MetPrep, Coventry, UK) to

remove the damage imparted by the sawing and grinding operations. Samples were placed in distilled water with 1 g of multi-purpose detergent (Teepol, Kent, UK) and ultrasonically cleaned for five minutes using an ultrasonic bath (Kerry PUL-125, Guyson International Ltd., North Yorkshire, UK) between the successive grades of abrasive papers and polishing pastes. The samples were then washed with distilled water and mounted on an aluminium stub. As enamel is electrically non-conductive, a surface conductive coating of evaporated carbon was applied (Fearne et al., 1994).

4.4.2. Experimental setup and data analysis

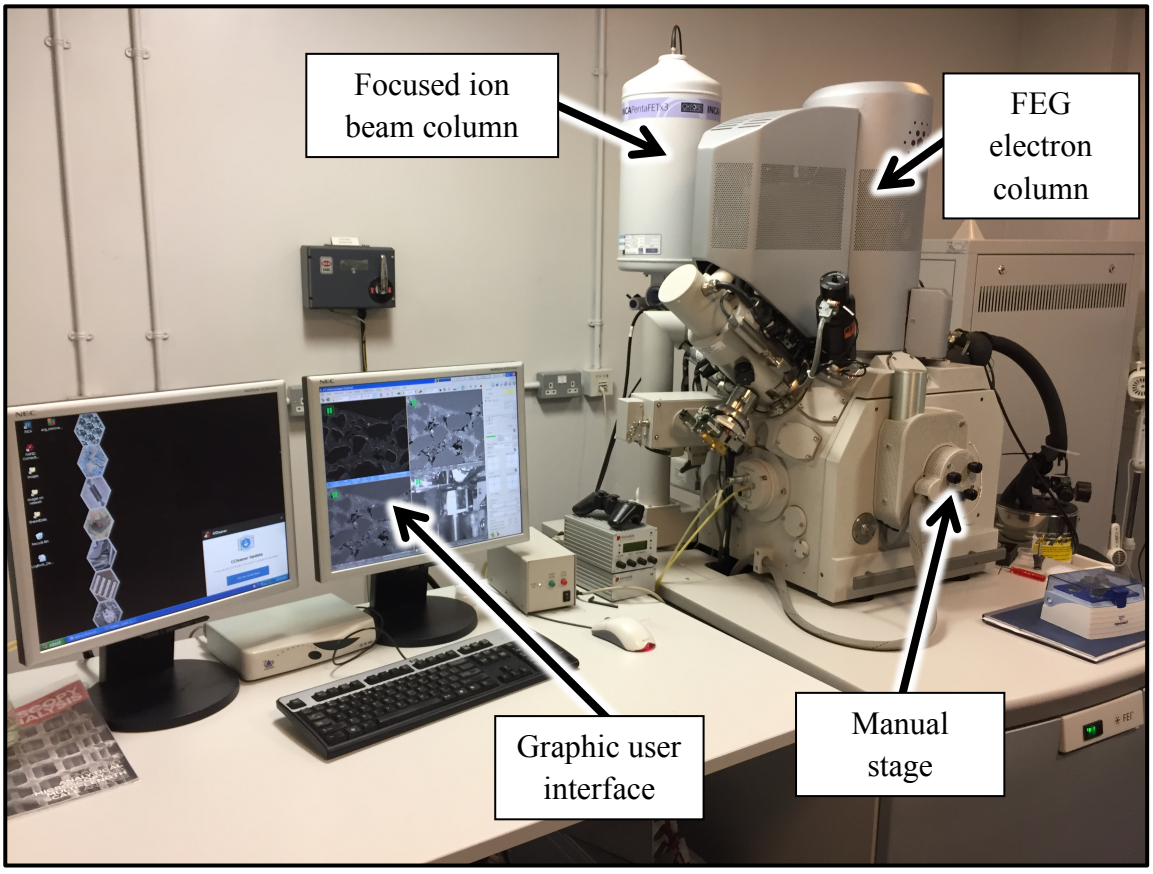

Figure 4.12: A photograph of the Quanta 3-D FEG dual beam SEM at QMUL

Microstructural images were collected using Quanta 3-D field emission gun (FEG) dual beam SEM (FEI, Eindhoven, The Netherlands) equipped with a solid-state BSE detector **(Figure 4.12)**. The SEM was operated at 5 kV with ≈10 mm working distance. These

parameters were kept constant during the taking of BSE micrographs. 9 images at 2400× magnification were obtained from each of samples C3, C5, L1 and L2, and 7 images at the same magnification were obtained from sample C1.

Chapter 5 - Investigating developing human enamel using permanent central and lateral incisors

5.1. Intoduction

In this chapter, a study focusing on assessing the natural biomineralisation process of human dental enamel is presented. S-XRD and XMT, together with qBSE imaging, have been utilised to correlate the crystallography, microstructure and relative mineral density in developing and mature human dental enamel. Five developing maxillary permanent central and lateral incisors (samples C1, C2, C3, C4 and L1) were collected from an archaeological source. Two fully mature type matched teeth (samples C5 and L2) were used for comparison.

5.2. Results

5.2.1. X-ray microtomography

Figure 5.1 and Figure 5.2 display relative mineral density contour maps of enamel at various developmental stages. The relative mineral density was calculated using Equation 4.5. It was found that specimens at early stages of maturation (samples C1 and C2) possessed high level of cracks **(arrows in Figure 5.1)** which may be related to their lower mineral content since they are more prone to shrinkage cracking with drying. From samples C1 to C5 **(Figure 5.1)** and from samples L1 to L2 **(Figure 5.2)**, a general trend of increasing relative mineral density and increasing spatial uniformity of relative mineral density as a function of maturation was observed. Comparing samples C1 to C4 **(Figure 5.1)** it can be seen that there is a bi-directional mineral density "front" that starts at the cusp tip and at the EDJ and travels towards the cervical end and the enamel surface until the relative mineral density is uniform in the fully mature tooth **(Figure 5.1 C5)**.

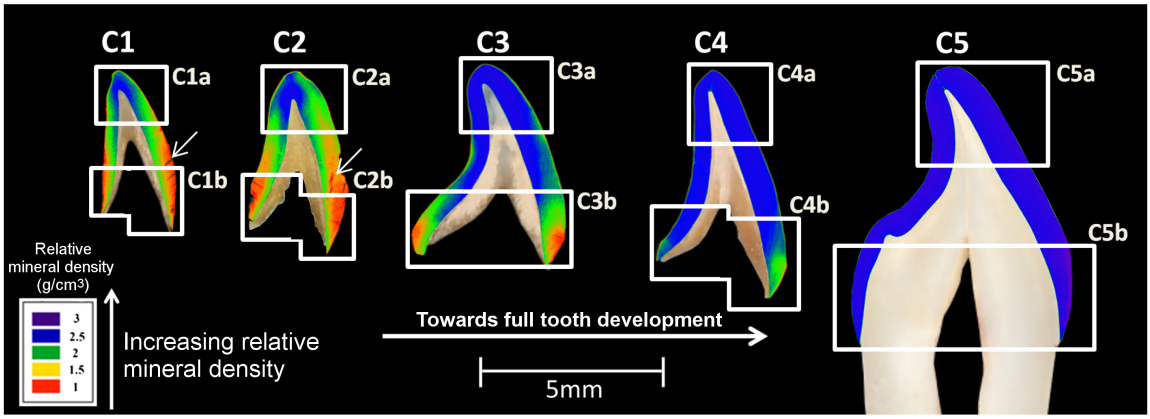

Figure 5.1: Relative mineral density distribution maps of central incisal enamel at various developmental stages. For each tooth section, labial is on the right-hand side.

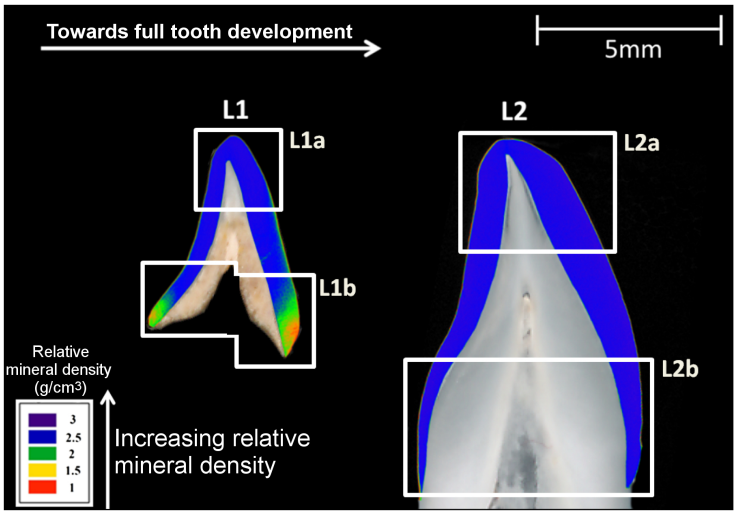

Figure 5.2: Relative mineral density distribution maps of developing (sample L1) and mature (sample L2) lateral incisal enamel. For each tooth section, labial is on the right-hand side.

Table 5.1: Vertical distribution of relative mineral density of central and lateral incisal enamel at various developmental stages. Positions are highlighted in Figure 5.1 and Figure 5.2.

Sample	Position	Relative mineral density (g/cm^3)
C1	C1a (incisal)	2.35 ± 0.01
	C1b (cervical)	1.59 ± 0.01
C2	C2a (incisal)	2.42 ± 0.01
	C2b (cervical)	1.61 ± 0.01
C3	C3a (incisal)	2.73 ± 0.01
	C3b (cervical)	1.94 ± 0.02
C4	C4a (incisal)	2.74 ± 0.01
	C4b (cervical)	2.40 ± 0.01
C5	C5a (incisal)	2.76 ± 0.01
	C5b (cervical)	2.74 ± 0.01
L1	L1a (incisal)	2.78 ± 0.01
	L1b (cervical)	2.16 ± 0.01
L2	L2a (incisal)	2.84 ± 0.01
	L2b (cervical)	2.85 ± 0.01

Table 5.2: Horizontal distribution of relative mineral density of central and lateral incisal enamel at various developmental stages.

Sample	Relative mineral density (g/cm^3)	
	EDJ	Enamel Surface
C1	2.12 ± 0.02	1.74 ± 0.02
C2	2.20 ± 0.01	1.84 ± 0.02
C3	2.53 ± 0.02	2.26 ± 0.02
C4	2.63 ± 0.01	2.57 ± 0.01
C5	2.69 ± 0.01	2.81 ± 0.01
L1	2.59 ± 0.01	2.44 ± 0.01
L2	2.79 ± 0.01	2.91 ± 0.01

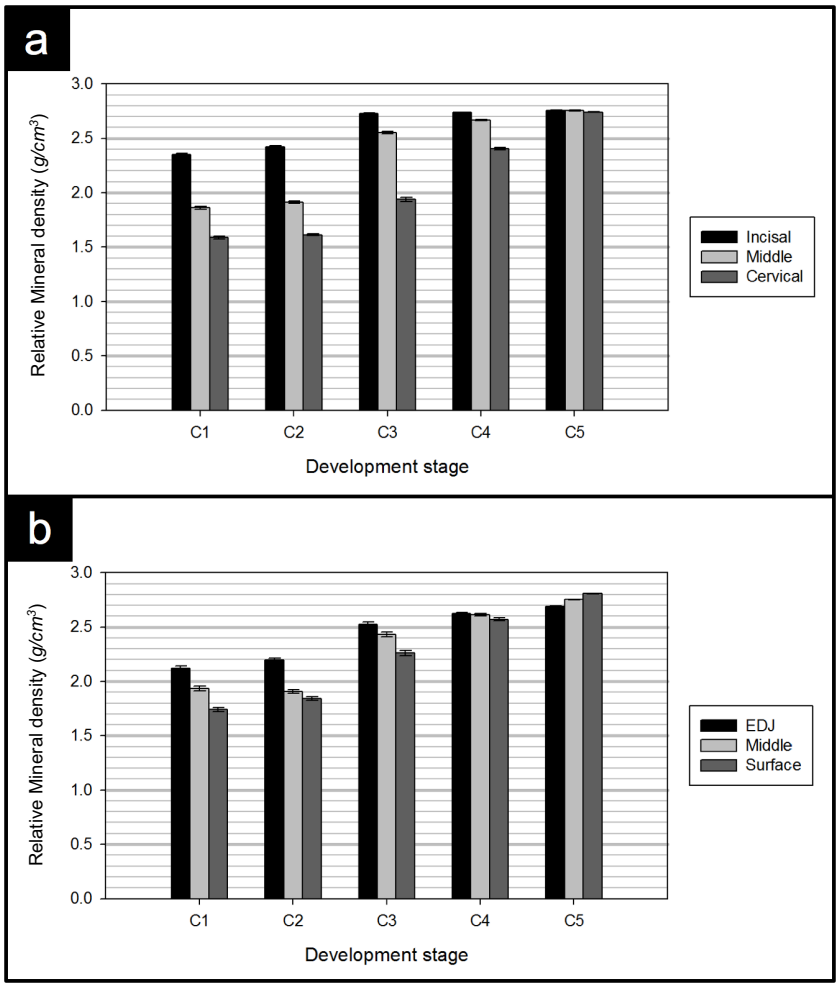

Figure 5.3: a) Vertical and **b)** horizontal distribution of relative mineral density of central incisal enamel at various developmental stages.

Quantitatively assessing the variation in relative mineral density vertically, i.e. from the cusp toward the cervical end, developing enamel in specimens C1, C2, C3, C4 and L1 had substantially higher average relative mineral density near the incisal edge compared

to the cervix of the tooth. In contrast, fully-developed enamel in samples C5 and L2 displayed a more uniform relative mineral density when comparing the incisal and cervical ends **(Figure 5.1, Figure 5.2 and Table 5.1)**. For comparison, Figure 5.3a and Figure 5.4a show the vertical variations in relative mineral density for the 18 regions displayed in Figure 4.4.

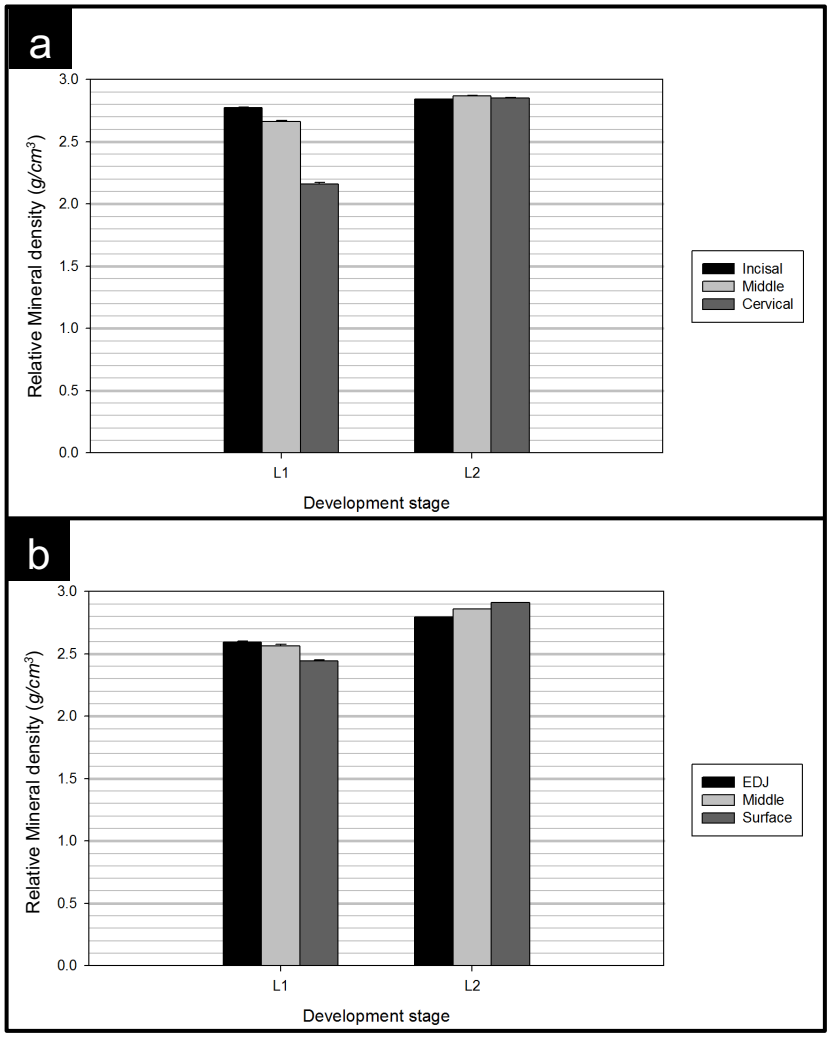

Figure 5.4: a) Vertical and **b)** horizontal distribution of relative mineral density of developing (sample L1) and fully-developed (sample L2) lateral incisal enamel.

Further analysis showed that in developing enamel the relative mineral density was higher near the EDJ compared to the enamel surface. Conversely, in the fully-developed enamel (samples C5 and L2), it was found that the highest relative mineral density was near the surface and the lowest was near the EDJ **(Figure 5.3b, Figure 5.4b and Table**

5.2). The standard error of the mean values of the above-mentioned relative mineral density measurements were found to be less than 0.02 g/cm^3.

5.2.2. 2-D synchrotron X-ray diffraction

5.2.2.1. *Texture direction*

S-XRD revealed that within one probed region, two populations of crystallite orientations coexist simultaneously with an angular separation of 20-50°.

Figure 5.5 and Figure 5.6 display the texture direction maps of the first population of c-HAp crystallites of enamel at various developmental stages. These values represent the peak positions extracted from the Gaussian model fitted to the (0 0 2) reflection curve **(Equation 4.6)** using the author's own automated software (MoFit) built with MatLab R2017a (MathWorks, Natick, Massachusetts, USA). For clarity, three regions were selected and magnified **(inserts in Figure 5.5 and Figure 5.6)** to show the texture directions of both populations in samples C2, C3 and L1.

It can be seen from Figure 5.5 and Figure 5.6, that the long axes of c-HAp crystallites were approximately perpendicular to both the enamel surface and the EDJ. Moreover, the crystallites of the most developed of the developing central incisors (sample C4), the fully-developed central incisor (sample C5) and the fully-developed lateral incisor (sample L2) were directed more gingivally near the cervical parts of the crowns. This phenomenon was not present in the developing lateral incisor (sample L1) and the three least developed central incisors (samples C1, C2 and C3), where the directions of crystallites were approximately horizontal cervically.

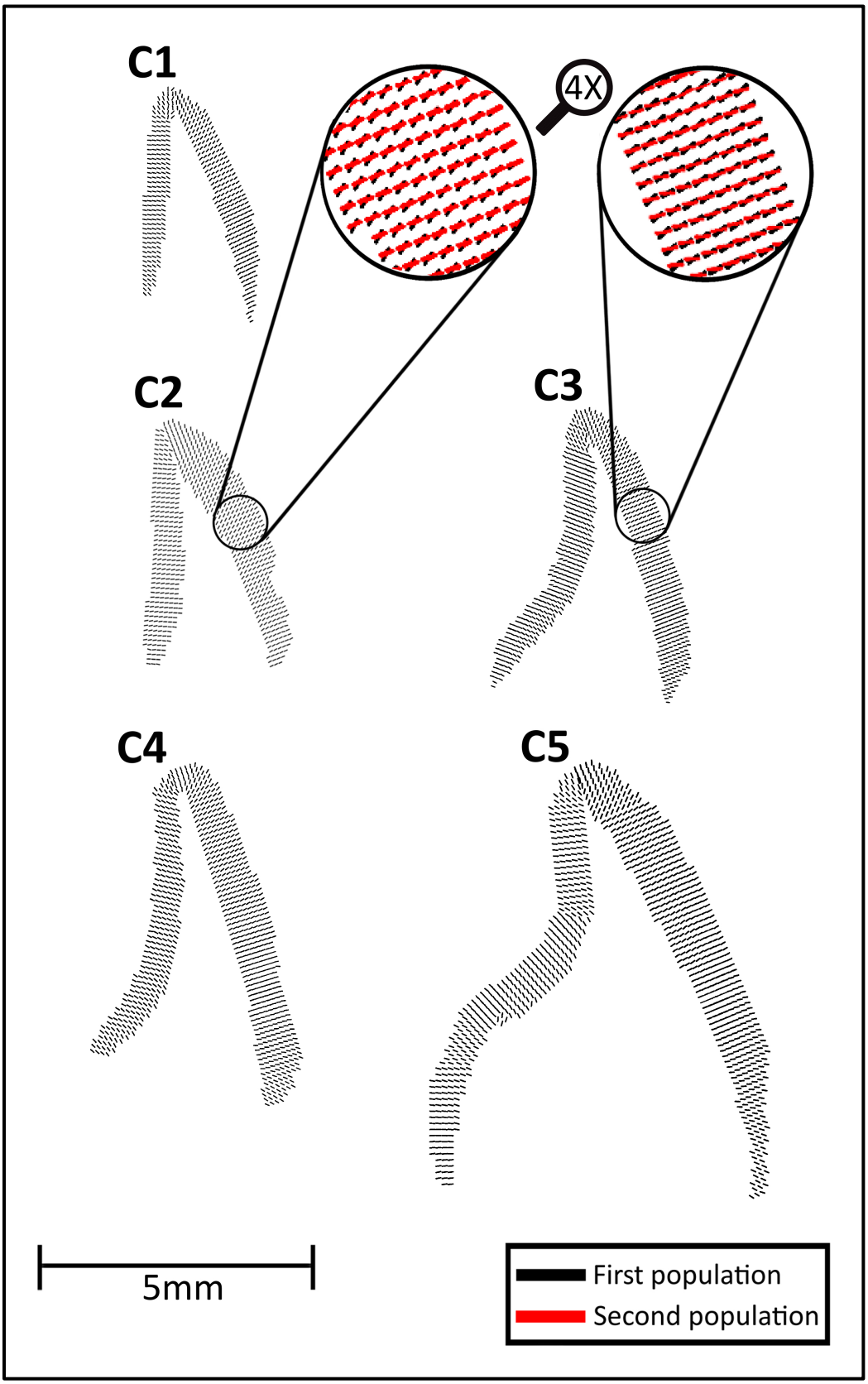

Figure 5.5: Texture direction maps of crystallites from the first orientation population in enamel at various developmental stages. Two regions were selected and magnified to show the texture directions of crystallites from both orientation populations. For each tooth section, labial is on the right-hand side.

In the central part crystallites were found to be somewhat horizontal in all developmental stages. Near the incisal edge, the directions of crystallites in all developmental stages were found to change gradually to an increasingly oblique direction until they were almost vertical.

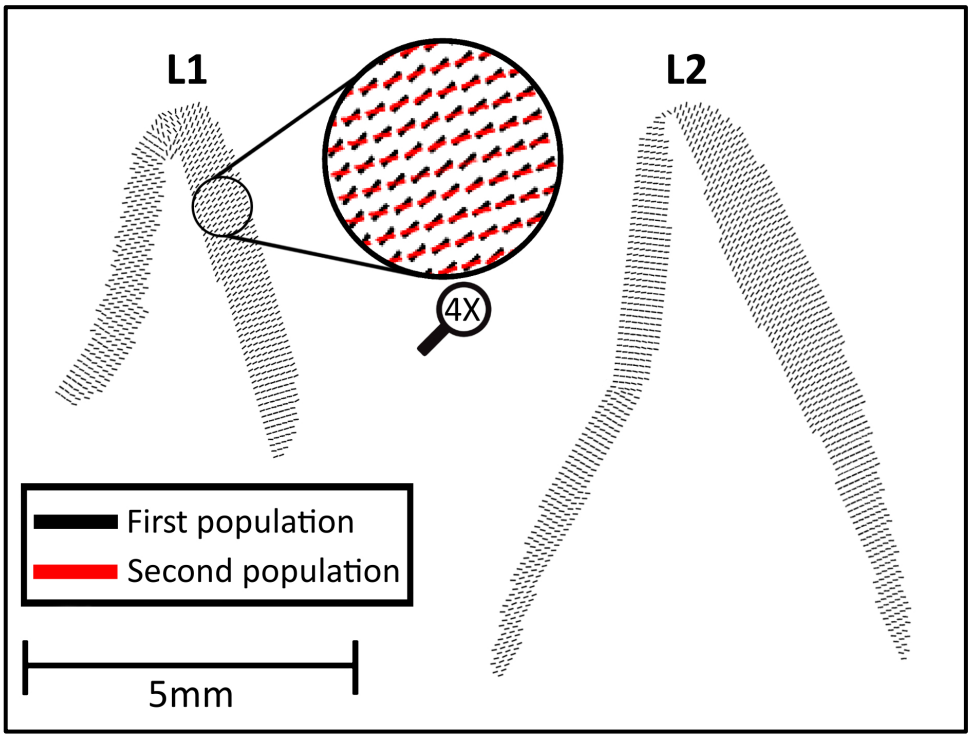

Figure 5.6: Texture directions maps of crystallites from the first orientation populations in developing (sample L1) and mature (sample L2) lateral incisal enamel. A region was selected and magnified to show the texture directions of crystallites from both orientation populations. For each tooth section, labial is on the right-hand side.

5.2.2.2. *Population percentage*

Peaks intensities from the azimuth of the (0 0 2) reflection correlate with the quantity of *c*-planes in the c-HAp crystallites satisfying the Bragg law **(Equation 3.4)**. This allows for predicting the relative percentage of the two orientation populations in each diffraction pattern as per the method described in Section 4.3.3.4.

It can be seen from Figure 5.7 and Figure 5.8 that the first orientation population was the dominant population in all samples **(Table 5.3)**. Furthermore, the number of crystallites belonging to the first orientation population was lower along the EDJ in all

developmental stages of lateral and central incisors. In labial enamel, less crystallites belonging to the first orientation population could be seen along the enamel surface in all stages of development. Moreover, the number of crystallites belonging to the first orientation was found to decrease from the incisal tip cervically in the fully-developed enamel (samples C5 and L2). Detailed descriptions of the observed variations in the percentage of the first orientation population for each sample are provided below.

Table 5.3: Average percentage of crystallites belonging to the first orientation population in enamel at various developmental stages

Sample	C1	C2	C3	C4	C5	L1	L2
Percentage (%)	73.9 ±16.0	64.3 ±15.9	69.9 ±14.8	70.2 ±11.4	73.4 ±10.7	70.4 ±16.0	71.0 ±15.3

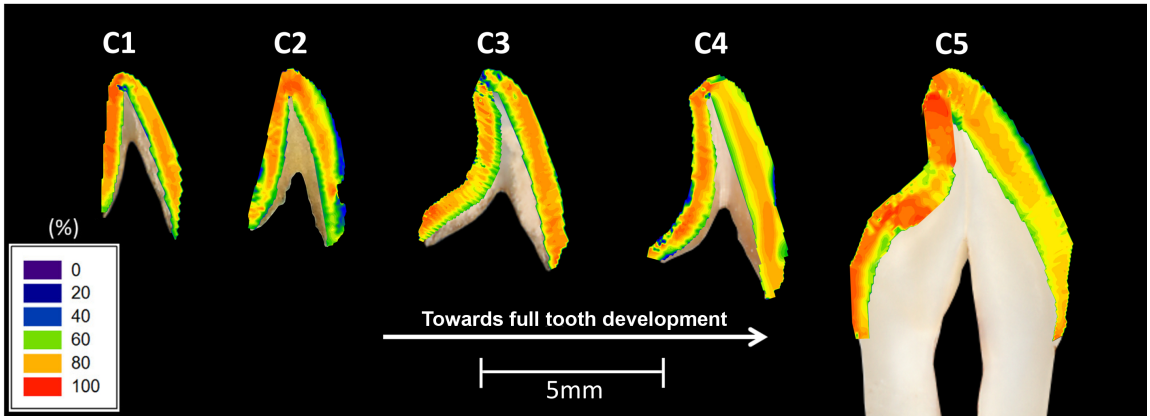

Figure 5.7: The percentage of crystallites belonging to the first orientation population in central incisal enamel at various development stages. For each tooth section, labial is on the right-hand side

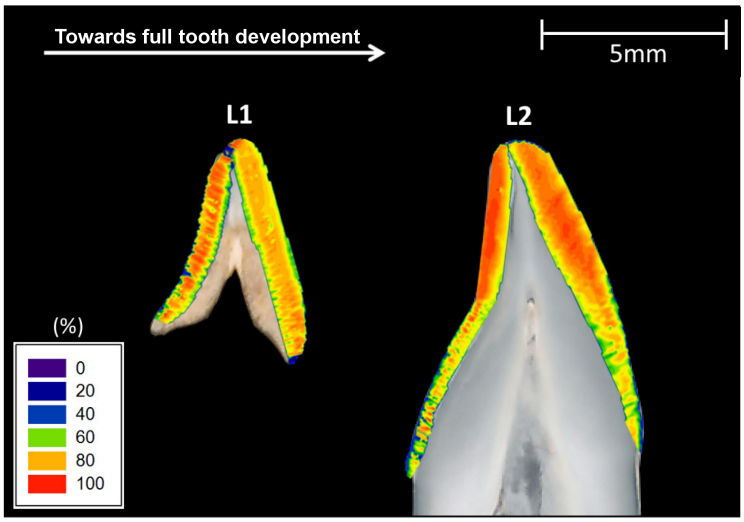

Figure 5.8: The percentage of crystallites belonging to the first orientation population in developing (sample L1) and mature (sample L2) lateral incisal enamel. For each tooth section, labial is on the right-hand side.

5.2.2.2.1 Sample C1

In the least developed central incisor, the percentage of crystallites from the first orientation population was 6.7% higher in palatal enamel compared to labial enamel. In labial enamel, higher percentage of crystallites from the first orientation population was found in the cervical part compared to the incisal part of the tooth. However, in palatal enamel, the percentage of crystallites from the first orientation population was found to be higher at the incisal part compared to the cervical part of the tooth. Furthermore, lower amounts of crystallites belonging to the first orientation population could be observed over a thin area along the EDJ **(Figure 5.7 C1)**.

5.2.2.2.2 Sample C2

The percentage of crystallites from the first orientation population was 3.2% higher in palatal enamel compared to labial enamel. Moreover, both palatal and labial enamel had higher percentage of crystallites (11.8% higher) in the incisal part compared to the cervical part of the tooth. Further, lower amounts of crystallites belonging to the first orientation population could be observed over a thin band along the entire length of the contour of the EDJ in both sides of the tooth and along the surface of the cervical half of the labial side of the tooth **(Figure 5.7 C2)**.

5.2.2.2.3 Sample C3

The percentage of crystallites belonging to the first orientation population was found to decrease (7.2% decrease) from the cervical part of the tooth toward the incisal tip. Moreover, the percentage of crystallites from the first orientation population in the palatal side was found to be 2% lower than that in the labial side of the tooth. Palatal enamel was found to display higher spatial variations in the percentage of crystallites belonging to the first orientation population than labial enamel. Furthermore, lower

amounts of crystallites belonging to the first orientation population can be observed over a thin band along the contour of the EDJ **(Figure 5.7 C3)**.

5.2.2.2.4 Sample C4

Labial enamel displayed lower percentage of crystallites belonging to the first orientation population (1.5% lower) than palatal enamel. In labial enamel, the percentage of crystallites from the first population was higher in the enamel bulk compared to the EDJ and the enamel surface, and lower at the incisal part compared to the cervical part of the tooth. In palatal enamel, lower percentage of crystallites from the first orientation was observed near the cervical end compared to the incisal regions. Furthermore, lower amounts of crystallites belonging to the first orientation population can be observed over a thin area along the EDJ **(Figure 5.7 C4)**.

5.2.2.2.5 Sample C5

The percentage of crystallites belonging to the first population in the mature sample was found to be 12.1% lower in labial enamel compared to palatal enamel. In labial enamel, the percentage of crystallites belonging to the first population was found to decrease from the incisal tip towards the cervical part of the tooth. Moreover, higher spatial variations in the percentage of first population orientation crystallites was found in palatal enamel compared to that in labial enamel. Lower amounts of crystallites belonging to the first orientation population can be observed over a thin band along the contour of the EDJ and along the surface in the incisal half of the labial side of the tooth **(Figure 5.7 C5)**.

5.2.2.2.6 Sample L1

In the developing lateral incisor (sample L1), the percentage of crystallites belonging to the first orientation population in palatal enamel was higher than that in labial enamel. Furthermore, there were higher spatial variations in the percentage of first population orientation crystallites in palatal enamel compared to labial enamel. Labial enamel possessed lower percentage of crystallites from the first population at the incisal part compared to the cervical part of the tooth. However, in palatal enamel, the percentage of crystallites belonging to the first population was found to increase from the cervical part towards the incisal tip of the crown. Moreover, lower amounts of crystallites belonging to the first orientation population could be observed over a thin area along the EDJ **(Figure 5.8 L1)**.

5.2.2.2.7 Sample L2

The percentage of crystallites belonging to the first orientation population in the mature sample was 10.1% higher in labial enamel compared to palatal enamel. Furthermore, the percentage of crystallites belonging to the first population was found to increase (21% increase) from the cervical part towards the incisal tip of the tooth. Lower amounts of crystallites belonging to the first orientation population can be observed along the contour of the EDJ and along the surface in the incisal half of the labial side of the tooth (**Figure 5.8 L2)**.

5.2.2.3. *Angle between the two orientation populations*

Figure 5.9 and Figure 5.10 display the spatial distribution of angular separation for the seven samples as per the method described in Section 4.3.3.3. It was found that the angular difference between the two orientation populations of the samples at the various developmental stages increased from the enamel surface towards the EDJ. Further, the

angular separation was found to decrease from the incisal tip cervically in samples C4, C5, L1 and L2. Furthermore, the angular separation was found to be lower in palatal enamel in all developmental stages. Moreover, a relatively small region above the dentine horn with low angular separation was found in samples C1, C3, C4, C5 and L1. Detailed descriptions of the observed variations in the angular separation between the two populations for each sample are provided below.

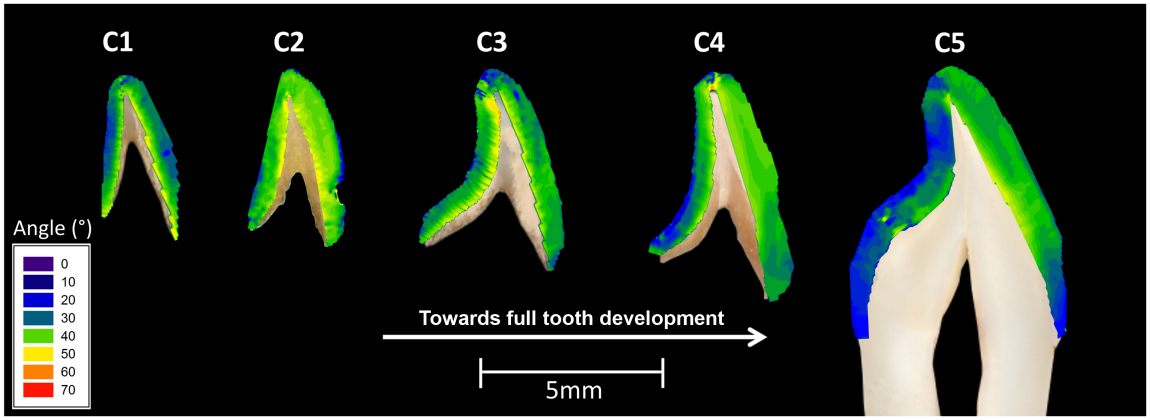

Figure 5.9: The average angle between the crystallites from the first and second orientation populations in central incisal enamel at various developmental stages. For each tooth section, labial is on the right-hand side.

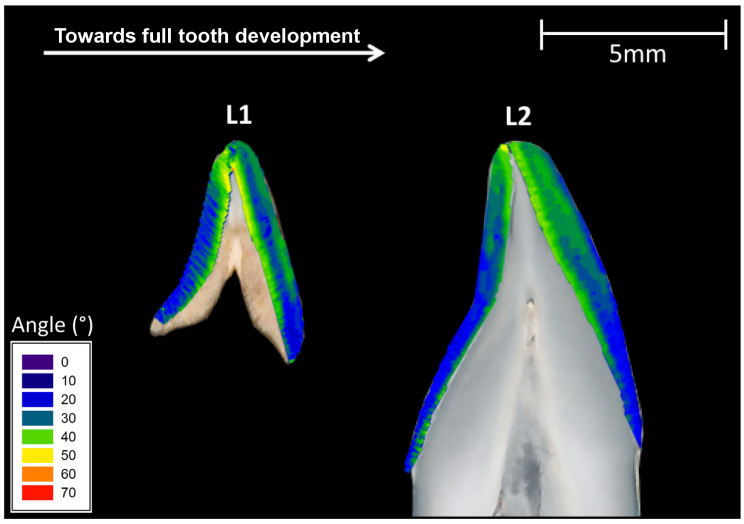

Figure 5.10: The average angle between the crystallites from the first and second orientation populations in developing (sample L1) and mature (sample L2) lateral incisal enamel. For each tooth section, labial is on the right-hand side.

5.2.2.3.1 Samples C1

In the least developed central incisor, the angular separation between orientation populations was found to decrease from the cervical part towards the incisal tip of the

tooth. Furthermore, palatal enamel was found to have lower angular separation between the two populations of crystallites than labial enamel. The lowest angular separation values were observed along the enamel surface and the enamel bulk at the central part of the tooth **(Figure 5.9 C1)**.

5.2.2.3.2 Sample C2

The angle between orientation populations was found to increase from the cervical part towards the incisal tip of the crown. Furthermore, palatal enamel was found to have lower angular separation between the two populations of crystallites than labial enamel. The lowest angular separation values were observed along the enamel surface near the cervical part of the tooth **(Figure 5.9 C2)**.

5.2.2.3.3 Sample C3

Palatal enamel was found to have higher angular separation between the two orientation populations of crystallites than labial enamel. In palatal enamel, the angular separation between the two populations was found to increase from cervical part towards the incisal tip of the tooth. However, in labial enamel, the angular separation between the two populations was found to increase from the incisal tip towards the cervical part of the crown. Furthermore, a region of considerably low angular separation was observed between the dentine horn and the incisal tip **(Figure 5.9 C3)**.

5.2.2.3.4 Sample C4

The angle between orientation populations was found to decrease from incisal tip towards the cervical part of the tooth. Moreover, palatal enamel was found to have lower angular separation between the two populations than labial enamel. Furthermore, there were higher spatial variations in the angular separation between orientation

populations in palatal enamel compared to that in labial enamel. Further, a relatively small region above the dentine horn with small angular separation between the two populations was observed **(Figure 5.9 C4)**.

5.2.2.3.5 Sample C5

The angle between the two orientation populations of crystallites was found to decrease from the incisal tip towards the cervical part of the mature central incisor. Moreover, palatal enamel was found to have considerably lower angular separation between the two populations than labial enamel. Furthermore, there were higher spatial variations in the angular separation between orientation populations in palatal enamel compared to that in labial enamel **(Figure 5.9 C5)**.

5.2.2.3.6 Samples L1 and L2

Both developing (sample L1) and mature (sample L2) lateral incisors had on lower angle between orientation populations near the cervical ends compared to those near the incisal tips. Further, both mature and developing lateral incisors had on lower angle between orientation populations in the palatal side compared to the labial side. Moreover, in developing labial enamel, the enamel bulk (the region between the enamel surface and the EDJ) displayed small angle between the two orientation populations **(Figure 5.10)**.

5.2.2.4. *Texture magnitude*

The FWHM values of peaks A, B, C and D **(Figure 4.10)** were obtained from each diffraction pattern as per the method described in Section 4.3.3.1. The average FWHM of the peaks corresponding to the first orientation population (Peaks A and C) was

calculated for each diffraction pattern **(Figure 5.11 and Figure 5.12)**. Similarly, the average FWHM of peaks *B* and *D* was calculated for the second orientation population **(Figure 5.13 and Figure 5.14)**.

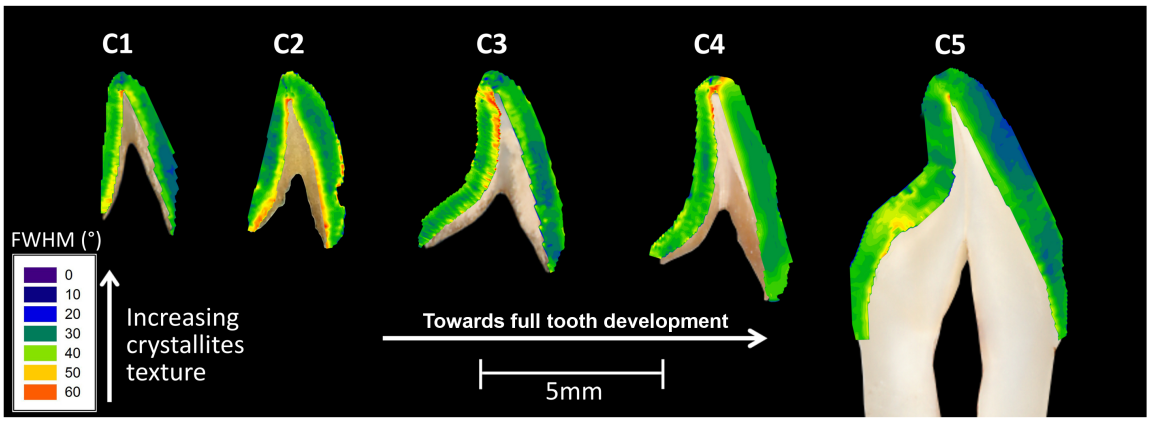

Figure 5.11: Texture magnitude distribution of crystallites from the first orientation population in central incisal enamel at various developmental stages. For each tooth section, labial is on the right-hand side.

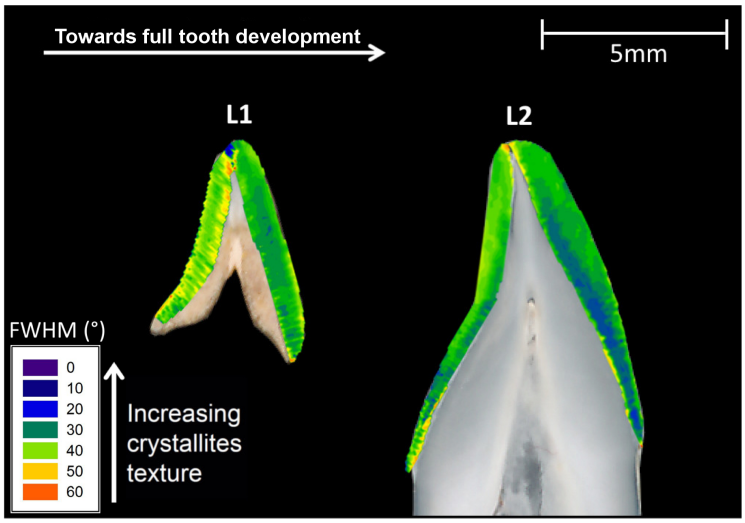

Figure 5.12: Texture magnitude distribution of crystallites from the first orientation population in developing (sample L1) and mature (sample L2) lateral incisal enamel. For each tooth section, labial is on the right-hand side.

In central incisors, the degree of orientation of crystallites from the first population in palatal enamel in sample C2 was on average higher than that in sample C1, decreasing slightly in sample C3, increasing again in sample C4 and finally increasing further in the fully-developed sample (sample C5). The texture magnitude of crystallites from the first population in labial enamel was high in the least developed enamel (sample C1),

decreasing in sample C2, increasing again in sample C3, then reducing in sample C4 and increasing considerably in the fully-developing sample (sample C5) **(Figure 5.11)**. Furthermore, the degree of texture of crystallites from the second population in palatal enamel of central incisors was found to be high in sample C1, reducing in sample C2, increasing in sample C3, decreasing again in sample C4 and finally increasing further in

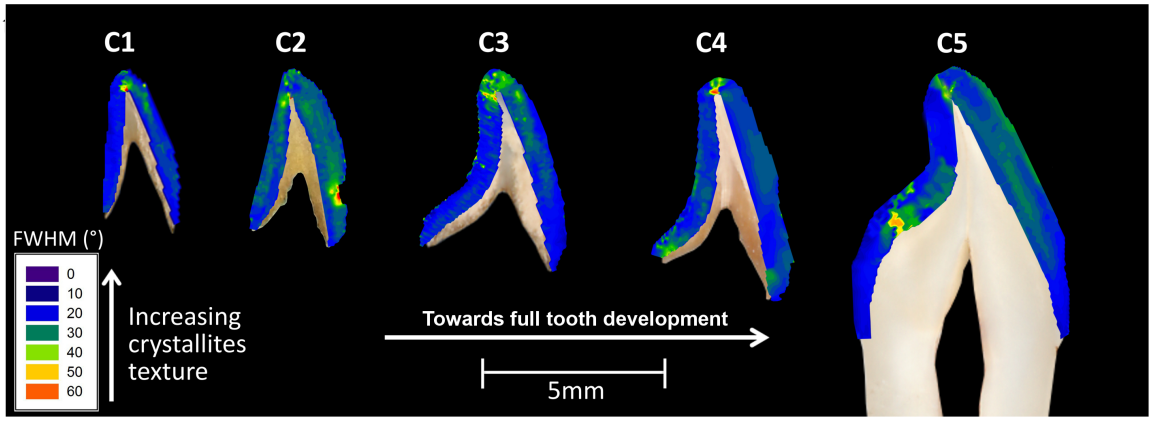

Figure 5.13: Texture magnitude distribution of crystallites from the second orientation population in central incisal enamel at various developmental stages. For each tooth section, labial is on the right-hand side.

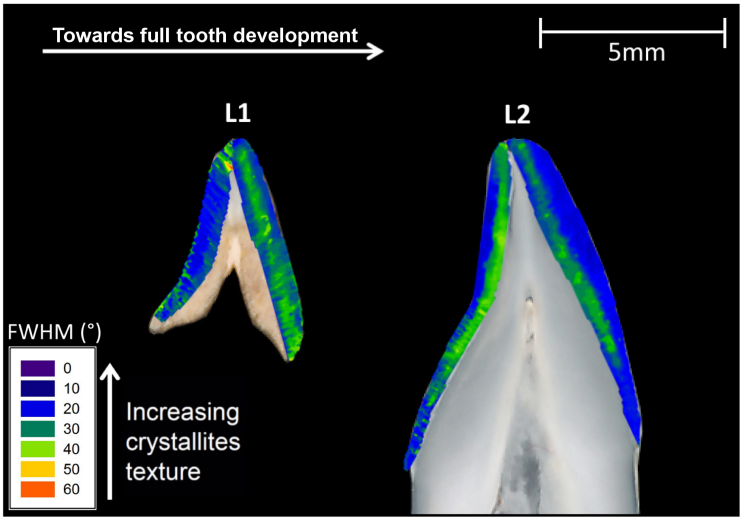

Figure 5.14: Texture magnitude distribution of crystallites from the second orientation population in developing (sample L1) and mature (sample L2) lateral incisal enamel. For each tooth section, labial is on the right-hand side.

On average, the texture magnitude of crystallites from the second population in labial enamel was found to be high in the least developed enamel (sample C1), decreasing in sample C2, increasing in sample C3, then decreasing in sample C4 and reducing further

in the fully-developing sample (sample C5) **(Figure 5.13)**. In addition to the considerable local variations in crystallite texture magnitude, it was observed that in all assessed samples, the first orientation population of crystallites **(Figure 5.11 and Figure 5.12)** had lower texture magnitude than the second population **(Figure 5.13 and Figure 5.14)**. Detailed descriptions of the observed variations in the texture magnitude of both the first and second orientation populations for each sample are provided below.

5.2.2.4.1 Sample C1

The crystallites from the first population possessed lower texture magnitude along the EDJ in both palatal and labial enamel. Overall, the texture magnitude of crystallites in labial enamel was found to increase from the incisal tip towards the cervical part of the tooth. Conversely, in palatal enamel, the texture magnitude of crystallites was found to decrease from the incisal tip towards the cervical part of the tooth. Moreover, the crystallites in palatal enamel were found to have lower texture magnitude than those in labial enamel **(Figure 5.11 C1)**.

The crystallites from the second orientation population displayed low degree of texture at a region near the incisal tip, extending up to one third through the bulk (the area sandwiched between the enamel surface and the EDJ) of labial enamel. Furthermore, the texture magnitude was found to decrease from the cervical part towards the incisal tip of labial enamel. In palatal enamel, the crystallites displayed more homogeneous texture magnitude than those found in labial enamel. Further, the crystallites in palatal enamel had higher texture magnitude than those in labial enamel **(Figure 5.13 C1)**.

5.2.2.4.2 Sample C2

Similar to sample C1, the crystallites from the first orientation population had lower texture magnitude along the contour of the EDJ in both palatal and labial enamel. In labial enamel, the crystallites degree of texture was found to increase from cervical part towards the incisal tip of the tooth. Moreover, it was revealed that the highest texture magnitude was in the bulk of the tooth (the area between the EDJ and the enamel surface). In palatal enamel, the central region was found to contain crystallites with higher texture magnitude than those in the incisal and cervical parts of the tooth. On average, the crystallites from the first orientation population were found to have lower texture magnitude in labial enamel than those in palatal enamel **(Figure 5.11 C2)**.

On the other hand, the crystallites of the second orientation population were found to have lower texture magnitude than those of the least developed sample (sample C1). The texture magnitude was found to increase from the incisal tip towards the cervical part of the tooth. Additionally, an area with crystallites having considerably low texture magnitude was observed around a chipped section of the tooth in labial enamel. Further, the crystallites in palatal enamel had higher texture magnitude than those in labial enamel **(Figure 5.13 C2)**.

5.2.2.4.3 Sample C3

The texture magnitude of crystallites from the first orientation population in both palatal and labial enamel was found to increase from incisal tip towards the cervical part of the tooth. In labial enamel, the crystallites in the incisal half of the tooth had lower texture magnitude along the EDJ compared to those along the enamel surface. However, the crystallites in the cervical half of the tooth displayed higher texture magnitude along the EDJ compared to those along the enamel surface. In palatal enamel, it was observed that

the crystallites along the EDJ in the incisal half of the tooth had considerably lower degree of texture than those along the enamel surface. However, the crystallites along the EDJ and the enamel surface in the cervical half of the tooth displayed similar degree of texture, with crystallites having higher texture magnitude in the enamel bulk. Further, crystallites in palatal enamel were found to display on average lower texture magnitude than those in labial enamel **(Figure 5.11 C3)**.

The crystallites from the second orientation population displayed low texture magnitude in a region near the incisal tip. In labial enamel, the texture magnitude of crystallites was found to decrease from cervical part towards the incisal tip of the tooth. However, in palatal enamel, the texture magnitude of crystallites was found to be more homogeneous throughout, and on average higher than that of labial enamel **(Figure 5.13 C3)**.

5.2.2.4.4 Sample C4

In the most developed of the developing samples, the crystallites of the first orientation population near the dentine horn was found to display low texture magnitude. Furthermore, it was observed that crystallites in the bulk of palatal and labial enamel displayed the highest texture magnitude, whereas the areas near the EDJ and enamel surface contained less textured crystallites. Additionally, the results showed a region of relatively lower degree of texture near the cervical ends of both palatal and labial enamel **(Figure 5.11 C4)**.

Crystallites from the second orientation population were found to possess low degree of texture in a small area extending from the dentine horn towards the tip of the tooth. Moreover, areas consisting of crystallites with low texture magnitude could be seen near the cervical ends of palatal and labial enamel. Further, crystallites along the EDJ of

labial enamel had higher degree of texture than those along the enamel surface **(Figure 5.13 C4)**.

5.2.2.4.5 Sample C5

The texture magnitude of crystallites belonging to the first orientation population was found to increase from the cervical part towards the incisal tip of the tooth in both labial and palatal enamel. In labial enamel, it was observed that crystallites along the EDJ displayed lower texture magnitude than those along the enamel surface. In palatal enamel, crystallites along the EDJ and the enamel surface in the incisal half of the tooth were found to have similar degree of texture. However, crystallites along the EDJ in the cervical half of palatal enamel displayed lower texture magnitude than those along the enamel surface. Overall, crystallites in labial enamel were observed to have considerably higher degree of texture than those in palatal enamel **(Figure 5.11 C5)**.

Crystallites from the second orientation population in labial and palatal enamel were found to have higher degree of texture near both the incisal and cervical ends than those in the central part of the tooth. In labial enamel, crystallites along the enamel surface in the incisal half of the tooth had considerably lower texture magnitude than those along the EDJ. However, the crystallites along the EDJ and the enamel surface in the cervical half of labial enamel were found to display similar degree of texture **(Figure 5.13 C5)**.

5.2.2.4.6 Sample L1

In the labial and palatal sides of the developing lateral incisor, the texture magnitude of crystallites belonging to the first orientation population was found to decrease from the cervical part towards the incisal tip of the tooth. Moreover, the incisal three quarters of palatal enamel displayed lower texture magnitude of crystallites belonging to the first

population along the contours of the EDJ than that those along the enamel surface. This was not the case in the cervical quarter of palatal enamel, where crystallites belonging to the first orientation population had higher texture magnitude along the enamel surface. Alternating lines of high and low values of texture magnitude spanning the enamel thickness were seen in the palatal side of the tooth. Moreover, it was found that on average the crystallites in palatal enamel displayed lower texture magnitude than those in labial enamel **(Figure 5.12 L1)**.

The crystallites from the second orientation population in labial enamel were found to display high texture magnitude along both the EDJ and enamel surface. Further, the crystallites near the incisal tip of labial enamel had higher texture magnitude than those found in cervical enamel. Although, the crystallites in palatal enamel did not display clear variations in texture magnitude from the EDJ peripherally, they were found to have lower texture magnitude near the incisal tip and near the cervix of the tooth. Further, the crystallites in palatal enamel were found to have on average higher texture magnitude than those found in labial enamel **(Figure 5.14 L1)**.

5.2.2.4.7 Sample L2

The texture magnitude of crystallites from the first orientation population was found to decrease from the cervical part towards the incisal tip of the tooth. In palatal enamel the most cervical region had somewhat lower texture magnitude values than the rest of the tooth. On average it was found that the crystallites in palatal enamel displayed lower texture magnitude than those in labial enamel. Furthermore, higher texture magnitude of crystallites was observed along the EDJ than that along the enamel surface **(Figure 5.12 L2)**.

The spatial variations in texture magnitude of the crystallites from the second orientation population were found to follow a similar trend in both palatal and labial enamel. It can be seen that a region of crystallites with very low texture magnitude exist along the EDJ at the incisal three quarters of the tooth. Further, the crystallites in palatal enamel were found to have on average lower texture magnitude than those in labial enamel **(Figure 5.14 L2)**.

5.2.3. Quantitative back-scattered electron imaging

Developing enamel was found to have lighter shades of grey near the EDJ and the incisal regions than the enamel surface and cervical regions. However, the greyscale spatial variations in mature dental enamel was found to be more homogenous. The enamel prism boundaries near the less mineralised regions could not be identified, becoming more prominent towards the more mineralised regions. Moreover, the least mineralised regions of enamel displayed dark areas between the crystallites within the prisms.

Furthermore, near the EDJ, two groups of prisms with two distinct morphologies were observed. The prisms within one group were circular in shape and those in the adjacent group were longitudinal in shape, with their long axes approximately perpendicular to the EDJ. However, the prisms near the enamel surface displayed a single morphology and were mostly longitudinal in shape (and some with distorted keyhole shape) with their long axes approximately perpendicular to the enamel surface. Detailed descriptions of the qBSE observations for each sample are provided below.

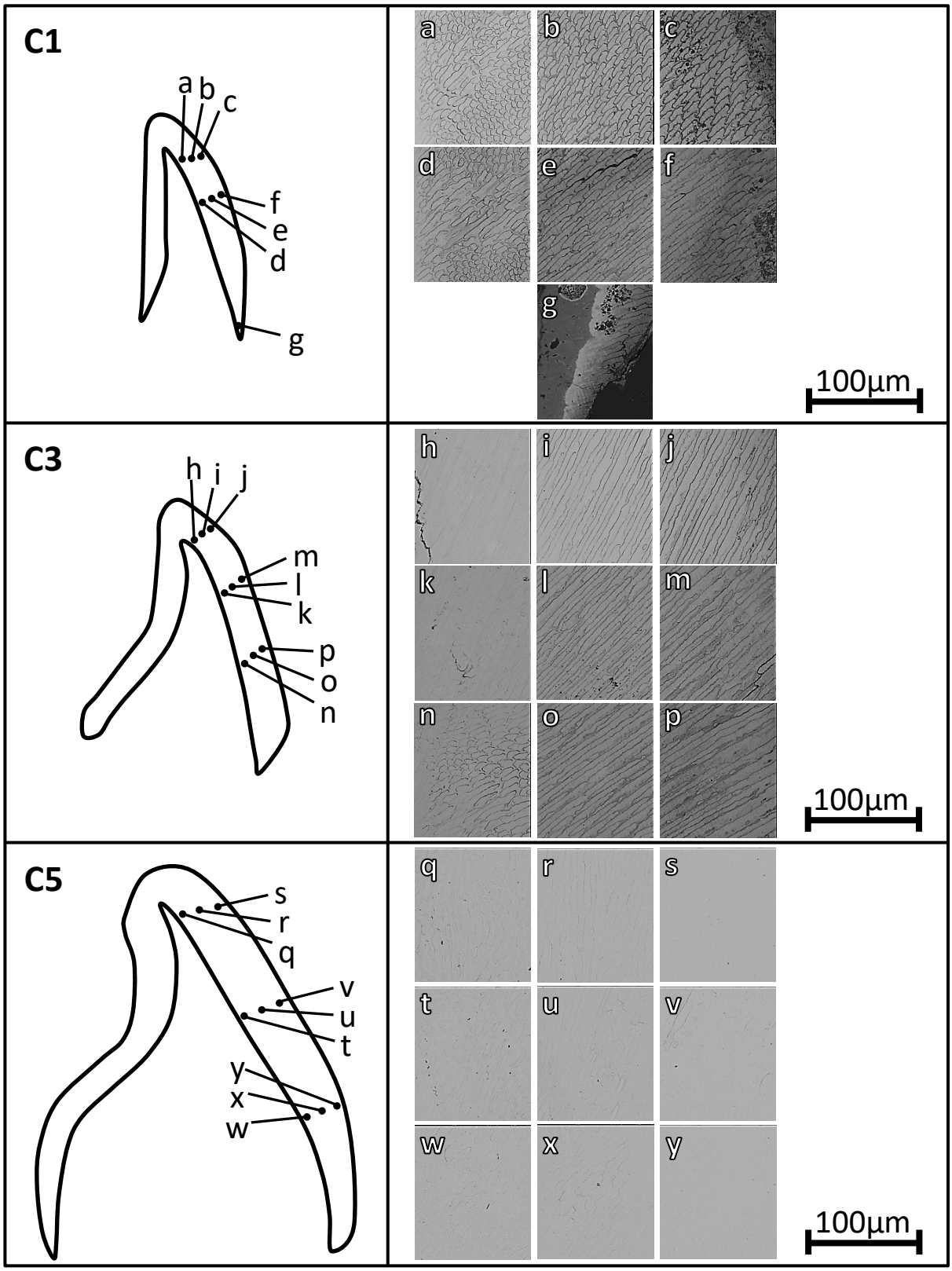

Figure 5.15: qBSE images at various locations of central incisors at **(a-g)** early- (sample C1), **(h-p)** mid- (sample C3) and **(q-y)** full- (sample C5) development. For each labial section, the enamel surface is on the right-hand side.

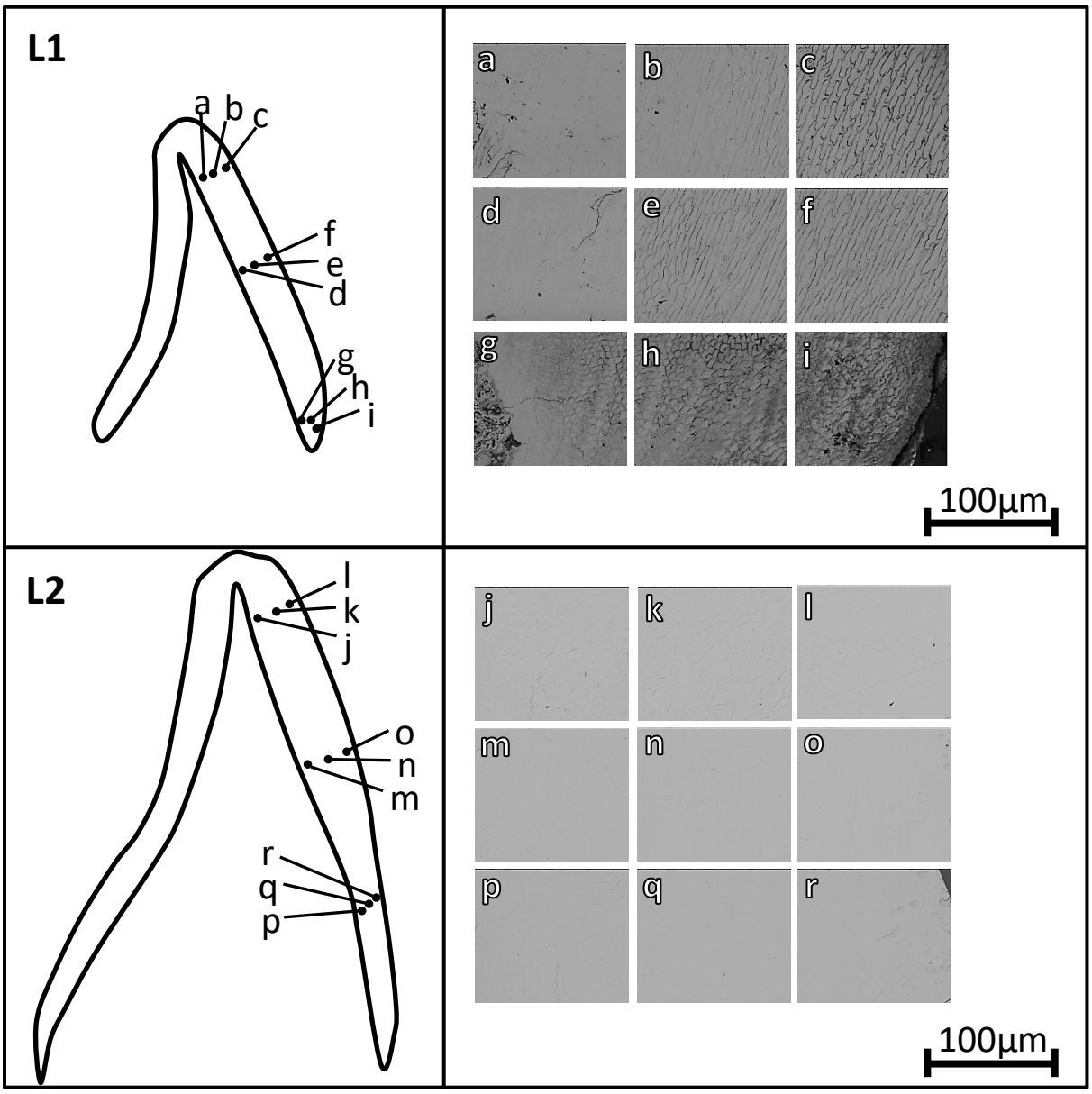

Figure 5.16: qBSE images of **(a-i)** developing (sample L1) and **(j-r)** mature (sample L2) lateral incisal enamel. For each labial section, the enamel surface is on the right-hand side.

5.2.3.1. *Sample C1*

The enamel prism boundaries were found to be prominent throughout the thickness of the crown **(Figure 5.15)**. Furthermore, near the EDJ, the incisal **(Figure 5.15a)** and central **(Figure 5.15d)** parts of the crown, two groups of prisms with two distinct morphologies were observed. In one group, the prisms were longitudinal in shape (with their long axes approximately perpendicular to the EDJ), whereas the other group, consisted of prisms with circular morphologies. This phenomenon continued through

the bulk of enamel in the central part of the tooth **(Figure 5.15e)**. However, the enamel prisms in the cervical part of the tooth **(Figure 5.15g)** did not display major variations in morphology, with most prisms being somewhat longitudinal in shape. Moreover, the enamel near the surface in the central **(Figure 5.15f)** and cervical **(Figure 5.15g)** part of the tooth displayed dark areas between the crystallites within the prisms.

In the incisal part of the crown, the prisms in the enamel bulk **(Figure 5.15b)** and near the surface **(Figure 5.15c)** had similar morphologies with distorted keyhole shape and were shorter than those in the central part of the tooth **(Figure 5.15e and f)**. Furthermore, groups of prisms in the enamel bulk **(Figure 5.15e)** and near the enamel surface **(Figure 5.15f)** in the central parts of the tooth displayed slight difference in direction.

5.2.3.2. *Sample C3*

The enamel prism boundaries near the EDJ in the incisal part of the crown **(Figure 5.15h)** could not be identified, becoming more prominent towards the enamel bulk **(Figure 5.15I and L)** and near the enamel surface **(Figure 5.15j and m)**. However, in the cervical part of the tooth, the prism boundaries were prominent throughout the thickness of the enamel **(Figure 5.15n, o and p)**. Moreover, the enamel near the surface in the cervical part of the tooth **(Figure 5.15p)** displayed dark areas between the crystallites within the prisms.

Furthermore, near the EDJ, the central **(Figure 5.15k)** and cervical **(Figure 5.15n)** parts of the crown displayed two groups of prisms with two distinct morphologies. Prisms in one group were longitudinal in shape (with the long axes approximately perpendicular to the EDJ), whereas the prisms of the adjacent group were somewhat circular. Prisms

in the enamel bulk **(Figure 5.15i, l and o)** and near the enamel surface **(Figure 5.15j, m and p)** were found to be somewhat longitudinal in shape.

5.2.3.3. *Sample C5*

The prism boundaries in the fully-developed enamel were more difficult to distinguish compared to those in developing enamel. In the enamel near the EDJ in the incisal **(Figure 5.15q)** and central **(Figure 5.15t)** parts of the tooth, two groups of prisms were identified, one with longitudinal appearance (with the long axes approximately perpendicular to the EDJ) and the other with a somewhat circular morphology. This phenomenon was found to continue through to the bulk of enamel in the central **(Figure 5.15u)** and cervical **(Figure 5.15x)** parts of the tooth. However, the prisms in the enamel bulk at the incisal part of the crown **(Figure 5.15r)** were longitudinal in shape with their long axes approximately perpendicular to the enamel surface. The prism boundaries could not be identified in the enamel near the surface **(Figure 5.15s, v and y)**.

5.2.3.4. *Sample L1*

The enamel prism boundaries at the incisal and central parts of the developing lateral incisor (sample L1) could not be easily distinguished near the EDJ **(Figure 5.16a and d)**, becoming more prominent near the enamel surface **(Figure 5.16c and f)**. However, in the cervical part of the tooth, the prism boundaries were prominent throughout the thickness of enamel **(Figure 5.16g, h and i)**.

Furthermore, near the EDJ, the incisal **(Figure 5.16a)** and central **(Figure 5.16d)** parts of the crown displayed two groups of prism with two distinct morphologies. One group of prisms was longitudinal in shape (with the long axes approximately perpendicular to the EDJ), whereas the other group was somewhat circular. This phenomenon continued

through the bulk of enamel at the incisal **(Figure 5.16b)** and central **(Figure 5.16e)** parts of the tooth. However, the enamel prisms at the enamel bulk **(Figure 5.16h)** and near the EDJ **(Figure 5.16g)** at the cervical part of the tooth did not display major variations in morphology, with most prisms being somewhat circular in shape.

Prisms near the enamel surface were found to have similar morphologies **(Figure 5.16c, f and i)**. At the incisal part of the tooth, the prisms near the surface **(Figure 5.16c)** were somewhat longitudinal, had distorted keyhole shape and were shorter than those at the central part of the tooth **(Figure 5.16f)**. Furthermore, the prisms near the surface at the incisal and central parts of the tooth were slightly longer closer to the surface **(Figure 5.16c and f)** suggesting a slight difference in direction between adjacent groups of prisms. However, the enamel prisms near the surface at the cervical part of the tooth were not longitudinal but rather circular in shape **(Figure 5.16i)**.

5.2.3.5. *Sample L2*

The prism boundaries in the fully-developed lateral incisor (sample L2) were more difficult to distinguish compared to those in developing enamel (sample L1). The enamel near the EDJ and the enamel bulk close to the incisal edge of the tooth displayed two groups of prisms, one with longitudinal appearance (with the long axes approximately perpendicular to the EDJ) and the other with a somewhat circular morphology **(Figure 5.16j and k)**. However, the enamel near the surface displayed a single orientation of prisms with a mostly longitudinal morphology with the long axes approximately perpendicular to the enamel surface **(Figure 5.16l, o and r)**.

5.3. Discussion

The XMT results, as shown in Figure 5.1 and Figure 5.2, indicated that there was a progressive increase in the amount of mineral in human enamel as a function of

maturation, agreeing with studies using FTIR on pig enamel (Rey et al., 1991) and polarised light analysis (Allan, 1959) and XMT (Simmons et al., 2013) on human enamel. It is also believed that as enamel matures, the Ca/P molar ratio and the OH^- content increases, and the acid phosphate and carbonate contents decrease (Elliott, 1994).

Upon closer examination, the results showed that on average the relative mineral density was highest at the cusp in developing enamel decreasing from the incisal tip cervically. This suggests that biomineralisation proceeds cervically from the tip of the tooth, agreeing with previous studies assessing developing human enamel using chemical analysis (Deutsch and Gedalia, 1980), hardness analysis (Avery et al., 1961), polarised light analysis (Allan, 1959) and microradiographic analysis (Avery et al., 1961, Suga, 1989, Beynon et al., 1998). Furthermore, the fully-developed teeth (samples C5 and L2) were found to have much more uniform relative mineral density compared to developing enamel **(Figure 5.1 and Figure 5.2)**, agreeing with Avery et al. (1961) microradiographic and microhardness assessments and Simmons et al. (2013) XMT analysis.

Further analysis of the fully-developed enamel (samples C5 and L2) showed that the enamel near the incisal part of the tooth had very similar relative mineral density (C5 = 2.76 g/cm^3 and L2 = 2.84 g/cm^3) to cervical enamel (C5 = 2.74 g/cm^3 and L2 = 2.85 g/cm^3) **(Figure 5.3a)** which agrees with the trend seen in previous studies on mature enamel using density gradient measurements (Weidmann et al., 1967), microradiography (Wilson and Beynon, 1989) and XMT (Simmons et al., 2013).

It was also observed that mature enamel exhibited a continuous decrease in mineral content from the surface towards the EDJ **(Figure 5.3b)**. The higher relative mineral density at the surface compared to the EDJ in mature human enamel agrees with earlier studies using polarised light (Hals, 1953, Allan, 1959), hardness analysis (Avery et al., 1961), physical density analysis (Weatherell et al., 1967), density gradient measurements (Weidmann et al., 1967, Weatherell et al., 1967), chemical analysis (Robinson et al., 1983), microradiographic analysis (Angmar et al., 1963, Bergman and Lind, 1966, Hirota, 1989, Suga, 1989, Wilson and Beynon, 1989, Beynon et al., 1998) and XMT (Anderson et al., 1996, Wong et al., 2004, Fearne et al., 2004, Simmons et al., 2013). The increase in relative mineral density of mature enamel from the EDJ towards the tooth surface is correlated with a decrease in organic material, fluid and porosity from the EDJ peripherally (Robinson et al., 1995b, Robinson et al., 2000). Fearne et al. (2004) speculated that the higher mineral density near the surface may be due to post-eruptive mineralisation.

Moreover, Figure 5.3b and Figure 5.4b show that, unlike mature enamel (samples C5 and L2), developing enamel (samples C1, C2, C3, C4 and L1) possess higher relative mineral density near the EDJ than the tooth surface. This phenomenon was reported in various studies assessing developing human enamel, using soft X-ray analysis (Applebaum, 1943) polarised light microscopy (Allan, 1959), fluorescence microscopy (Hals, 1953) microradiography (Engfeldt and Hammarlund-Essler, 1956, Crabb and Darling, 1960, Avery et al., 1961, Angmar-Månsson, 1971, Suga, 1989) and XMT (Simmons et al., 2013).

Furthermore, previous work on developing bovine enamel revealed that the highest mineral density was near the EDJ until maturation begins (Shore et al., 1995a). However, it was reported that the crystallites of developing human enamel are thinner at the EDJ than the crystallites close to the enamel surface (Rönnholm, 1962a, Simmons et al., 2013). It is also believed that the mineral near the enamel surface is the most soluble and the solubility decreases as the tooth develops (Elliott, 1994). Furthermore, it is suggested that the carbonate (Robinson et al., 1995a) and magnesium (Robinson et al., 1995b) contents of mature enamel decrease from the EDJ towards the enamel surface.

It was also observed that there is a decrease in the number of crystallites in mature enamel from the enamel surface towards the EDJ which suggests that crystallites near the EDJ may undergo fusion (Kerebel et al., 1979). It is also believed that prism diameter increases from the EDJ towards the enamel surface in order to accommodate the larger outer radius (Skobe and Stern, 1980, Macho et al., 2003). The findings of this study together with the above-mentioned supporting literature, suggest that enamel biomineralisation progresses from the EDJ towards the surface. The reason why crystallites grow from inside to outside following the sequence of protein removal is, most probably, to prevent sealing the surface as ions enter from the ameloblast layer (Robinson, 2014)

It is a widely held view that dental enamel is the hardest mammalian tissue and, as such, is the most resistant to changes both in the biological and diagenetic environments, and may be perfectly preserved even in fossils (Boyde, 1986, Carter, 1990). Moreover, various researchers confirmed that the crystallites in dental enamel are highly resistant to changes due to diagenetic alterations following death and burial of the animal (Hoppe

et al., 2003, Simmons et al., 2013). In further evidence, as part of a pilot study, Raman spectroscopy of the partially mineralised archaeological teeth revealed that calcium phosphate was the only measurable mineral compound present in both fully and partially mineralised areas. There was no evidence of calcium carbonate, which would be the expected result of diagenesis, in the less mineralised areas. Furthermore, electron microprobe analysis and laser-ablation inductively coupled mass spectroscopy (LA-ICPMS) scans of sections through a developing archaeological tooth showed no evidence for exogenous elements which are not present in *in vivo* enamel (Beaumont, 2007). Therefore, teeth belonging to deceased children who lived in medieval times can be used with the assumption that the temporal changes in the dental enamel crystallography and mineralisation are due solely to enamel natural formation and not to diagenetic alterations.

These results serve as a confirmation that the mineral content in the archaeological samples follow the expected route of mineralisation, where the highly mineralised region continue to advance toward the enamel surface and the tooth cervix as a function of maturation. Therefore, the results obtained from such samples indicate that burial for extended periods has had little effect on the mineral content of enamel and gives further validity to the S-XRD results.

It has been established previously that the long axes of c-HAp crystallites in dental enamel are approximately perpendicular to the EDJ and to the enamel surface (Low, 2004, Al-Jawad et al., 2007, Deyhle et al., 2009, Raue and Klein, 2011, Raue et al., 2012, Simmons et al., 2013, Egan et al., 2013). Boyde and Fortelius (1986) suggested that prisms with their long axes perpendicular to the enamel surface offer the greatest

resistance to abrasion during function. The results in Figure 5.5 and Figure 5.6 showed that this feature was persistent in the two populations of crystallites regardless of the developmental stage, which is in agreement with a previous study on developing molars (Simmons et al., 2013), indicating that initial preferred growth directions of apatite crystallites persist from early through to full maturation **(Figure 5.5 and Figure 5.6)**. This gives direct evidence to previous assumptions that crystallite orientations are defined early in development (Robinson et al., 1998, Beniash et al., 2009). This also supports the early assumption by Boyde (1964) that crystallites, once formed, tend to continue growing in the same (c-axis) direction.

A number of S-XRD studies reported that although crystallites were approximately perpendicular to the EDJ in the cervical and central parts of the tooth, the texture direction on either side of the tooth cusps was parallel to the EDJ (Al-Jawad et al., 2008, Simmons et al., 2011). This phenomenon was not seen in the current investigation, in which the texture direction was almost always approximately perpendicular to the EDJ and enamel surface. The disagreement between the results presented in the current study and those from premolars suggests that there are considerable variations in the 3-D arrangement of crystallites between dental dentitions. Therefore, subsequent studies should concentrate on analysing the 3-D orientation of crystallites in all tooth dentitions, in order to manufacture more specific dental materials targeting each tooth type to improve the clinical performance of utilised dental restorations.

Using 2-D S-XRD has allowed us to understand that within one probed region, crystallites group along two main directions with respect to their c-axes with an angular separation between the two main directions varying spatially across the enamel crown in

a range of 20-50° **(Figure 5.9 and Figure 5.10)**. Although the two orientation populations have been reported in other studies on dental enamel using S-XRD (Yagi et al., 2009, Yagi et al., 2010) and lab source XRD (Thewlis, 1936, Thewlis, 1940, Trautz et al., 1953, Glas, 1962, Poole and Brooks, 1961, Gwinnett, 1966, Gwinnett, 1967, Hirota, 1982, Jodaikin et al., 1984, Hirota, 1986)**,** here we have been able to quantify and spatially map the direction and magnitude of organisation of crystallites within each population. This spatial quantification allows deeper understanding of the potential origins and functional significance of these two populations.

A single 2-D diffraction pattern, contains information averaged over several hundred prisms (average prism diameter is approximately 5 μm), therefore, the two orientations observed could be the result of orientation variation between the "heads" and "tails" of the prismatic keyhole pattern, or due to prism decussation occurring throughout the probed thickness of the sample.

It has been reported using SEM on human enamel that not all crystallites within a single prism run parallel to the prism long axis. Some crystallites have their long axes orientated toward the keyhole tail fanning out in a range of 0-70° in relation to the prism long axis (Lyon and Darling, 1957, Meckel et al., 1965a). Thewlis (1940) suggested that the two crystallite orientation populations observed using lab source XRD represent differences in orientation between crystallites in the head and tail of the 'keyhole pattern'. In contrast, we observe two populations with discrete orientations **(Figure 4.10)**, and not a gradual "fanning" of crystallites. In addition, Glas (1962) observed the two orientation populations while assessing a 10μm thick slice, therefore, it is unlikely

that the two populations arise as a result of overlapping prisms through the sample volume.

A study on bovine enamel speculated that the two orientation populations do not exist within a single prism, but are the result of probing two groups of prisms, or prisms from different regions of the enamel (Glimcher et al., 1965). Therefore, the two orientation populations observed could be the result of probing two zones of HSb simultaneously (Hirota, 1986). It was previously shown that there are little crossing of prisms in the outer quarter of human enamel where prisms run approximately parallel to one another, then suddenly twist as they approach middle and inner enamel and divide into two groups deviating in opposite orientations corresponding to the two zones of the HSb (Osborn, 1968b, Osborn, 1968a, Hirota, 1982, Hirota, 1986). These are the features that can be observed in detail in Figure 5.9 and Figure 5.10, where the angular difference between the two orientation populations decreases from the EDJ peripherally.

Furthermore, the fully-developed central **(Figure 5.9 C5)** and lateral **(Figure 5.10 L2**) incisors displayed lower angular difference between the two orientation populations near the cervical regions, which according to Lynch et al. (2010), have little or no prism decussation, most likely due to the fact that enamel in these regions is not subjected to high loading forces. Moreover, Figure 5.9 and Figure 5.10 show that samples in all developmental stages - with the exception of samples C2 and L2 - possessed a small region with low angular difference near the incisal tip, a region that is believed to contain no HSb (Lynch et al., 2010). Lynch et al. (2010) suggested that the absence of prism decussation at the incisal tip allows for rapid abrasion of this region to expose the HSb-rich region underneath in order for the enamel edges to be kept sharp leading to

enhanced mastication. In further support of this evidence-based hypothesis, Macho et al. (2003) developed a 3-D model based on processes governing enamel formation in humans and dogs where it can be seen that the prism decussations increase from the EDJ towards the enamel surface.

The observations presented in the current study agree with Hirota (1986) speculation that the two orientation populations observed are most likely caused by the reflections from the two zones of the HSb being recorded simultaneously. However, Hirota (1989) later observed that the ratios and the degrees of preferred orientation in the two zones of the bands showed almost the same value, which is not the case with the results presented in this study, where it was found that, in all assessed samples, the first orientation population of crystallites **(Figure 5.11 and Figure 5.12)** had considerably lower degree of texture than the second orientation population **(Figure 5.13 and Figure 5.14)**.

It has been previously reported that mature enamel possess higher texture magnitude near the cusps of premolars (Al-Jawad et al., 2007, Al-Jawad et al., 2008), molars (Raue et al., 2012, Simmons et al., 2013) and incisors (Raue et al., 2012). Furthermore, it was found that the Young's modulus and hardness of mature human enamel decrease from the cusp cervically **(Figure 2.12)**. This suggests that the degree of texture is somewhat linked to hardness and Young's modulus which are in turn related to wear resistance (Craig and Peyton, 1958, Craig et al., 1961, Meredith et al., 1996, Cuy et al., 2002). Furthermore, it was suggested that the crystallites at the cusp have high orientation due to the mechanical needs the teeth have to fulfil. Due to the high expected load forces at

the cusps, the highest degree of orientation is present in order to absorb these forces (Deyhle et al., 2009, Raue and Klein, 2011, Raue et al., 2012).

Moreover, it was observed in a study assessing 160 human incisors, canines, premolars and molars, that the most axial surface possesses the highest mean HSb packing densities compared to other regions of the tooth (Lynch et al., 2010). Our results from the mature central incisor (sample C5) showed that the first population of crystallites at the incisal half of the tooth displayed higher texture magnitude than the cervical half, agreeing with the above-mentioned studies **(Figure 5.12 C5)**. However, the second population of crystallites at the incisal and cervical parts of the mature central incisor displayed similar texture magnitude values, which were higher than those at the central part of the tooth **(Figure 5.14 C5)**.

In the labial side of the mature lateral incisor (sample L2), the crystallites from the first orientation population near the incisal tip displayed lower texture magnitude than those at the central and cervical parts of the tooth. However, in the palatal side of mature enamel, the crystallites of the first population had the lowest texture near the cervical end **(Figure 5.12 L2)**. Further, the texture magnitude of the crystallites from the second orientation population near the incisal tip of palatal and labial enamel was similar to that at the central part of the tooth and was lower than that at the cervical part of the tooth **(Figure 5.14 L2)**. These observations do not agree with recent studies on mature human enamel as it has been previously reported that mature enamel possess higher texture magnitude near the cusp (Al-Jawad et al., 2007, Al-Jawad et al., 2008, Simmons et al., 2013).

Further, Lyon and Darling (1957) and Glas (1962) who assessed mature enamel using PLM and XRD respectively, suggested that the crystallites near the EDJ had the poorest texture magnitude. Moreover, using S-XRD to assess human mature premolars (Al-Jawad et al., 2007, Al-Jawad et al., 2008, Simmons et al., 2011) and molars (Simmons et al., 2013, Egan et al., 2013), it was reported that crystallites near the EDJ displayed the lowest degree of orientation, which is the site where the first enamel crystallite are believed to form (Shore et al., 1995a). Although this was the case in our assessment of the labial side of the mature central incisor regarding the first orientation population of crystallites **(Figure 5.11 C5)**, the second population of crystallites along the EDJ had higher degree of texture than those along the enamel surface **(Figure 5.13 C5)**. This was also the case in the results obtained from the developing central incisors (samples C1, C2, C3 and C4), where the crystallites of the first orientation population were found to display lower degree of texture along the contour of the EDJ **(Figure 5.11).**

Furthermore, the second population of crystallites in both palatal and labial sides of the mature lateral incisor was found to possess a low degree of texture along a narrow band near the incisal three quarters of the contour of the EDJ **(Figure 5.14 L2)**, agreeing with the above-mentioned studies. However, the opposite was observed in the crystallites from the first orientation population. Here, crystallites were found to possess higher texture magnitude along the EDJ than the enamel surface **(Figure 5.12 L2)**. This indicates that the above-mentioned studies analysed one of the populations observed in our investigation.

Simmons et al. (2013) also reported that the sample in earliest development displayed a relatively homogenous texture distribution. Our results from the least developed central

incisor (sample C1) showed that the texture magnitude of the crystallites from the second population was more homogeneous than the other specimens **(Figure 5.13 C1)** agreeing with Simmons et al. (2013) findings. However, the first population of crystallites displayed similar local variations in texture magnitude in all analysed teeth **(Figure 5.11 and Figure 5.12)**. Moreover, Simmons et al. (2013) reported that, overall, the texture magnitude reduces with development. However, the results from both the first **(Figure 5.11 and Figure 5.12)** and second **(Figure 5.13 and Figure 5.14)** orientation populations showed that the texture magnitude of the crystallites does not follow a clear trend as a function of maturation.

Various studies observed that in cuspal enamel, the prisms are arranged in a tight spiral around a central axis and appeared to cross in a more random and irregular manner compared to those found in enamel at the sides of teeth (Osborn, 1968a, Osborn, 1968b, Skobe and Stern, 1980). This may explain - with the exception of the first population of crystallites of samples C2 and C3 **(Figure 5.11 C2 and C3)** - the high degree of texture near the dentine horn observed in both crystallite populations in developing (samples C1, C4 and L1) and mature enamel (samples C5 and L2) **(Figure 5.11, Figure 5.12, Figure 5.13 and Figure 5.14)**.

Lower texture magnitude was observed in crystallites belonging to the first orientation population near the EDJ of the labial and palatal sides of samples C1, C2, C3, C4 and C5, and the palatal side of sample L1. Moreover, lower texture magnitude of crystallites belonging to the second population was found near the EDJ of the labial and palatal sides of samples C3 and L2 and the palatal sides of samples C1, C5 and L1. These results are in agreement with previous studies on dental enamel reporting a reduced

texture near the EDJ (Lyon and Darling, 1957, Glas, 1962, Carlström, 1964, Al-Jawad et al., 2007, Al-Jawad et al., 2008, Simmons et al., 2011, Simmons et al., 2013).

Crystallites belonging to the first orientation population were found to have a higher texture magnitude at the incisal part of the labial and palatal sides of samples C2, C4, C5 and L1 and the palatal side of sample C1. Further, a higher degree of texture was found in crystallites belonging to the second orientation population at the incisal part of the labial and palatal side of sample C4. These results agree with previous studies reporting a higher degree of texture at the incisal part of human dental enamel (Al-Jawad et al., 2007, Al-Jawad et al., 2008, Simmons et al., 2011, Raue et al., 2012, Simmons et al., 2013) .

We observed differences the organization of crystallites when comparing the labial and palatal side of the crown. The first population of crystallites in the labial sides of developing (samples C1, C2, C3, C4 and L1) and mature (samples C5 and L2) enamel possessed higher degree of texture than those in the palatal sides. Conversely, the second population of crystallites in the labial sides of the majority of samples (samples C1, C2, C3, C5 and L1) possessed lower texture magnitude than those in palatal enamel.

In samples C2, C4 and C5, the texture magnitude of one population was inversely related to the other. That is, generally speaking, when the texture magnitude of one population was higher in a region; the texture magnitude of the other population was lower at that same region and vice versa.

According to Hirota (1986), the two populations are the result of two zones of overlapping groups of decussating prisms being recorded simultaneously. If this explanation is taken into account, it means, according to our results, that one group of decussating prisms tends to have a higher degree of orientation (texture magnitude) than the other. This phenomenon was persistent from early (sample C1) through to full maturation (sample C5).

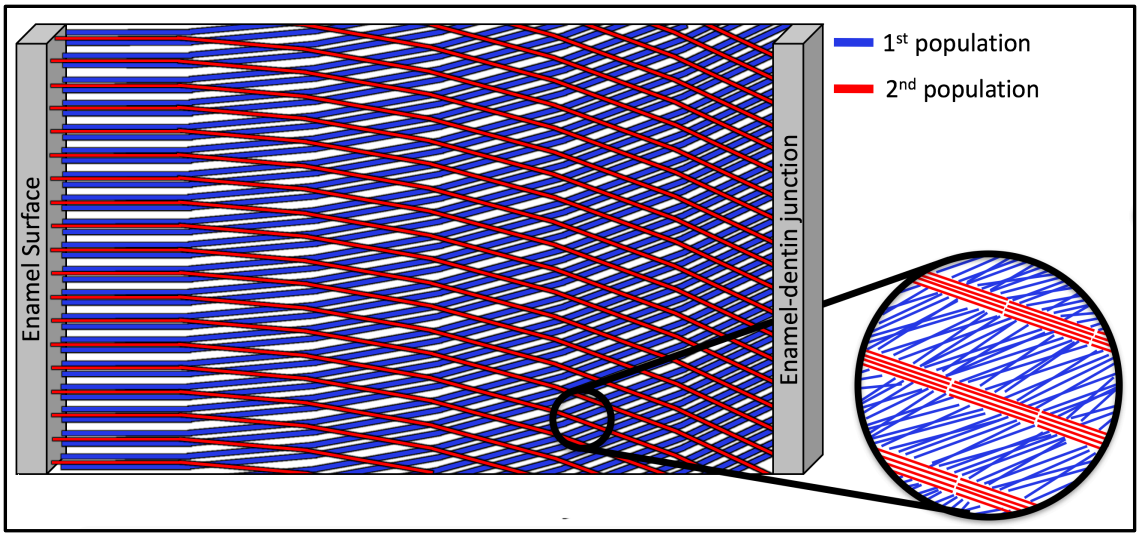

Figure 5.17: A proposed model representing the texture magnitude and direction of the two orientation populations as they span the enamel thickness. The thicker the lines, the lower the texture magnitude and the higher the number of lines, the higher the population percentage.

According to Simmer et al. (2012), in inner enamel, one row of ameloblasts move in the same direction, while those of adjacent rows move in the opposite direction, resulting in prism decussation **(Figure 5.15 and Figure 5.16)**. As can be seen in the proposed model **(Figure 5.17)**, the ameloblast movement direction determines the degree of crystallite orientation. Rows of ameloblasts moving in one direction result in the growth of highly ordered crystallites (second population of crystallite orientation) according to Figure 5.13 and Figure 5.14. However, rows of ameloblast moving in the opposite direction, give rise to crystallites with a lower degree of texture (first population of crystallites) according to Figure 5.11 and Figure 5.12. Furthermore, the results from the

current study **(Figure 5.7 and Figure 5.8)** showed that one row of ameloblasts resulted in higher percentage of crystallites than adjacent rows.

It is evident from our results that there are complex processes occurring during apatite formation between the different developmental stages which strongly affect the degree of texture magnitude **(Figure 5.11 and Figure 5.13)** and the amount of mineral present whilst the direction of texture orientation is not, if at all, greatly variable **(Figure 5.5)**. This indicates that the directions of the crystallite orientations are determined early in the development and are retained until full development. Our results fit well with current understanding that prism directions are determined by the ameloblasts prior to crystallisation, defining the texture direction at an early stage (Boyde, 1964, Robinson et al., 1998, Beniash et al., 2009).

It has been reported previously that in developing enamel, the mineral density near the EDJ is higher than that near the enamel surface (Applebaum, 1943, Hals, 1953, Engfeldt and Hammarlund-Essler, 1956, Allan, 1959, Crabb and Darling, 1960, Avery et al., 1961, Angmar-Månsson, 1971, Suga, 1989, Simmons et al., 2013), suggesting that mineralisation starts from the EDJ peripherally. qBSE images showed that the least mineralised regions of the developing teeth **(Figure 5.15f, g, m, o and p and Figure 5.16g, h and i)** had dark prism boundaries and displayed dark areas between the crystallites within the prism cores. The more mineralised regions of developing teeth **(Figure 5.15a, b, i and j and Figure 5.16b and e)** also had dark prism boundaries, however, there were no dark regions within the prism cores. This suggests that the enamel matrix comprising the prisms heads mineralises first followed by that

comprising the prism tails, agreeing with previous studies (Avery et al., 1961, Avery, 1962).

Prism boundaries are believed to be organic-rich discontinuities in the overall structure between different orientations of crystallites. According to Boyde (1997), the organic material is not concentrated in those locations at the initiation of enamel formation but is concentrated there during the re-mobilisation of the matrix during the maturation of enamel. The prism boundaries near the EDJ at the incisal part of the mid-developed central incisor (sample C3) **(Figure 5.15h**) and the incisal **(Figure 5.16a)** and middle **(Figure 5.16d)** parts of the developing lateral incisor (sample L1) could not be easily distinguished, becoming more prominent when moving peripherally and cervically across the crown. The results presented here therefore suggest that prism cores were mineralised prior to prism boundaries. This further supports the theory that the prisms calcify from the centre peripherally (Avery et al., 1961). The reason behind this could be that during enamel development, the prism tails become the route taken by the mineralising ions to reach the prism centres to calcify them. Once the prism centres calcify, those boundaries are then sealed by mineralising later (Avery et al., 1961).

Further, near the central **(Figure 5.15k-m)** and cervical **(Figure 5.15n-p)** parts of the mid-developed central incisor (sample C3), as well as the cervical part (**Figure 5.16g-i**) of the developing lateral incisor (sample L2), the prism boundaries were prominent throughout the thickness of enamel. It was reported previously, that the cervical parts of developing teeth displayed lower mineral density and hence are less developed than the coronal regions of the crown (Allan, 1959, Avery et al., 1961, Deutsch and Gedalia, 1980, Suga, 1989, Beynon et al., 1998), confirming that mineralisation progresses from

the incisal region of the crown cervically. This explains the prominence of prism boundaries at this region, and confirms the hypothesis stating that prism cores mineralise prior to prism boundaries.

Furthermore, various qBSE images displayed two groups of prisms with two distinct morphologies. One group of prisms was found to be longitudinal in shape, whereas the other group was somewhat circular. The two groups of prisms were visible near the EDJ at the incisal **(Figure 5.15a)** and central **(Figure 5.15d**) parts of the least developed central incisor (sample C1) as well as the central **(Figure 5.15k)** and cervical **(Figure 5.15n)** parts of the mid-developed central incisor (sample C3). Moreover, in the developing lateral incisor (sample L1) the two groups of prisms were visible near the EDJ at the incisal **(Figure 5.16a)** and central **(Figure 5.16d**) parts of the tooth and at the enamel bulk at the incisal **(Figure 5.16b)** and central **(Figure 5.16e)** parts of the tooth. The two groups of prisms could also be seen near the EDJ at the incisal **(Figure 5.15q)** and central parts **(Figure 5.15t)** of the mature central incisor (sample C5), as well as the incisal part **(Figure 5.16j and k)** of the mature lateral incisor (sample L2). This phenomenon was found to continue through to the bulk of the mature central incisor (sample C5) at the central **(Figure 5.15u)** and cervical **(Figure 5.15x)** parts of the tooth. The prism boundaries could not be identified in the enamel near the surface of the mature central incisor **(Figure 5.15s, v and y)** and near the EDJ and the enamel bulk at the central **(Figure 5.16m and n)** and cervical **(Figure 5.16p and q)** parts of the mature lateral incisor (sample L2) and therefore could not be analysed.

It has been suggested in a number of studies that towards inner enamel, prismatic bundles cross-over or decussate in a stepwise manner, giving rise to HSb (**Figure 2.10**).

This is suggested to be caused by secretory ameloblasts moving laterally, left or right, parallel with neighbouring cells, where transverse rows of cells move in opposite directions (Boyde and Stewart, 1963, Hirota, 1982, Hirota, 1986, Hirota, 1989, Osborn, 1990, Boyde, 1997, Macho et al., 2003, Skobe, 2006, Avery and Chiego, 2006, Lynch et al., 2010, Cox, 2013). It was hypothesised that prism decussation gives rise to unequal wear rates (Boyde, 1997) and prevents crack propagation while strengthening the enamel in respect to the horizontal tension forces (Koenigswald et al., 1987).

The prisms at the enamel bulk **(Figure 5.15b)** and the surface **(Figure 5.15c)** at the incisal part of the least developed central incisor (sample C1), and those at the surface (**Figure 5.16c**) at the incisal part of the developing lateral incisor (sample L1), had similar morphologies with distorted keyhole shape. This morphology was observed in a model constructed by Meckel et al. (1965a), who reported it to appear when the plane of the model surface deviates by 5° from the surface **(Figure 2.8)**. The prisms of the mid-developed central incisor (sample C3), at the bulk of enamel **(Figure 5.15i, l and o)** and near the enamel surface **(Figure 5.15j, m and p)** and those near the surface at the central part **(Figure 5.16f)** of the developing lateral incisor (sample L1) were somewhat longitudinal in shape. Furthermore, the prisms of the fully-developed central incisor (sample C5) the prisms at the enamel bulk at the incisal part of the crown **(Figure 5.15r)**, as well as those near the surface **(Figure 5.16r)** of the mature lateral incisor (sample L2) were longitudinal in shape. However, the enamel prisms near the surface at the lowest part of the developing lateral incisor (sample L1) were not longitudinal but rather circular in shape **(Figure 5.16i)** representing cross-sections of prisms, suggesting that the prismatic long axes were approximately parallel to the enamel surface. This may be due to the enamel not reaching its full thickness at this stage of development.

The similarity in prism morphologies near the surface reported in the current study agrees with the accepted understanding that the outer enamel pattern of mammals consists of groups of prisms running in similar directions that suddenly divide into two groups running in two different directions as they approach the EDJ (Hirota, 1982, Hirota, 1986, Macho et al., 2003, Lynch et al., 2010, Cox, 2013).

5.4. Conclusions

The results from XMT measurements reveal where around the tooth the apatite mineral has been deposited. Whereas, interpreting the texture distribution maps from S-XRD measurements gives insight as to where on or within the forming crystallites the new apatite mineral is deposited during maturation. When comparing texture magnitude contour maps from S-XRD **(Figure 5.11 to Figure 5.14)** with the relative mineral density maps from XMT **(Figure 5.1 and Figure 5.2)**, it is evident that there is no correlation between the amount of apatite mineral present and the texture orientation or magnitude.

XMT data reveal that the mineral density increases and becomes more uniform as a function of maturation. Also, with the aid of XMT, this study confirms the current understanding regarding the direction of mineral progression, starting from the cusp and moving cervically as a function of time. The XMT relative mineral density results validate the feasibility of using the selected archaeological samples to study their biomineralisation progression, since they agree with the current accepted model of enamel biomineralisation (Shore et al., 1995a).

From S-XRD data it was possible to investigate both texture magnitude and direction of the c-HAp crystallites in detail within all examined teeth. It was revealed that crystallites were found to group into two main directions with respect to their long axes. The texture magnitude was found to vary considerably as a function of time in both orientation populations, unlike texture direction where no variations were observed regardless of the developmental stage. The c-HAp crystallites were found to be approximately perpendicular to both the EDJ and the enamel surface **(Figure 5.5 and Figure 5.6)** allowing for a more efficient packing of crystallites, maximising their strength and flexibility and enhancing their wear resistance capabilities (Boyde, 1997).

S-XRD revealed that crystallites tended to group into two main directions with respect to their long axes. The angular separation between the two populations was found to be higher near the EDJ compared to the enamel surface **(Figure 5.9 and Figure 5.10)**. qBSE images revealed that prisms near the enamel were approximately parallel to one another, then divide into two groups running at two different directions as they approach the EDJ **(Figure 5.15 and Figure 5.16)**. This is suggested to be caused by the lateral movement of secretory ameloblasts, left or right, where transverse rows of cells move in opposite directions (Simmer et al., 2012). Therefore, we propose that the two orientations observed correspond to the two groups of the decussating prisms.

Figure 5.17 displays a proposed model based on the gathered data, displaying the two crystallite orientation populations as prisms decussate from the enamel surface towards the EDJ. As can be seen in the proposed model **(Figure 5.17)**, the ameloblast movement direction determines the crystallite degree of orientation. Rows of ameloblasts moving in one direction result in the growth of highly ordered crystallites (second orientation

population). However, rows of ameloblast moving in the opposite direction, give rise to crystallites with lower degree of orientation (first population of crystallites). Furthermore, the first orientation population was observed to comprise of a larger number of crystallites than the second orientation population **(Figure 5.7 and Figure 5.8)** suggesting that one group of prisms have higher percentage of crystallites compared to neighbouring groups of prisms.

By assessing the relative mineral density, crystallography and microstructure of central and lateral incisors we reveal deeper insights into the precise timing and spatial progression of human enamel biomineralisation. These results provide new insights into the fundamental understanding of the natural growth and formation of human incisal enamel and would facilitate the development of successful reparative or regenerative biomimetic medical and dental strategies.

Chapter 6 - Using Synchrotron X-ray diffraction to investigate the distribution of enamel crystallite texture through entire permanent central incisal crowns at various developmental stages

6.1. Introduction

In this chapter, we present a study focusing on assessing the natural biomineralisation process of human dental enamel across entire crowns of central incisors each serially sectioned into four mesio-distal slices. Synchrotron X-ray diffraction (S-XRD) was used to assess the texture magnitude and orientation of c-HAp crystallites in developing and mature human dental enamel. Two developing central incisors (samples C1 and C3) were collected from an archaeological source and compared to a fully-mature type-matched tooth (sample C5).

6.2. Results

6.2.1. Texture direction

Figure 6.1, Figure 6.2 and Figure 6.3 display the texture direction maps of crystallites from the first orientation population of enamel at various developmental stages from the first, second and third slice, respectively.

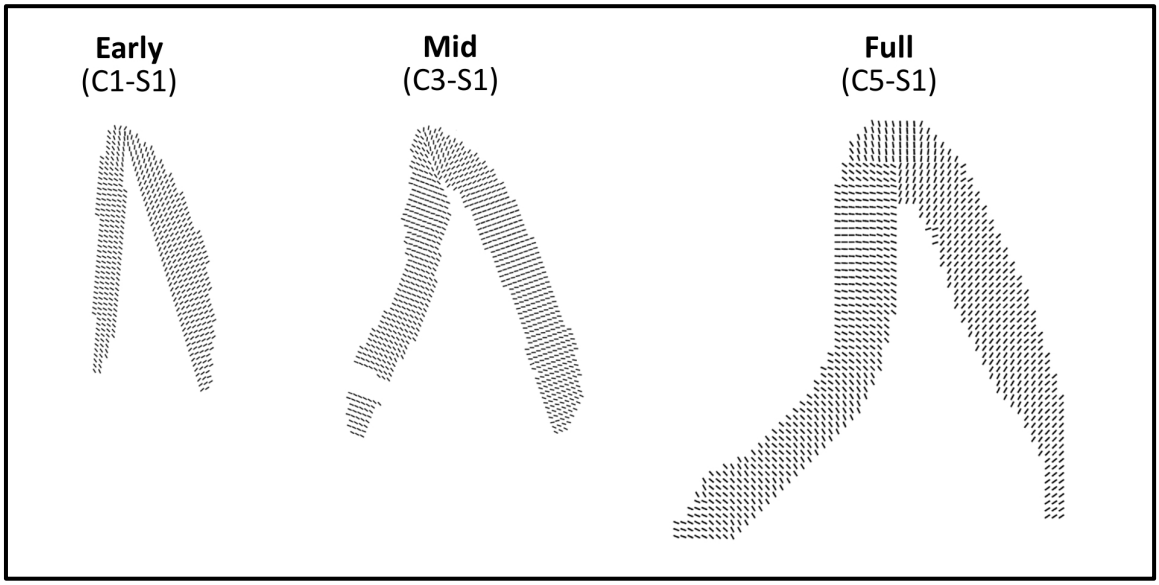

Figure 6.1: Texture direction maps of crystallites belonging to the first orientation population from the first slice of central incisal enamel in early- (C1-S1), mid- (C3-S1) and full- (C5-S1) development. For each tooth section, labial is on the right-hand side.

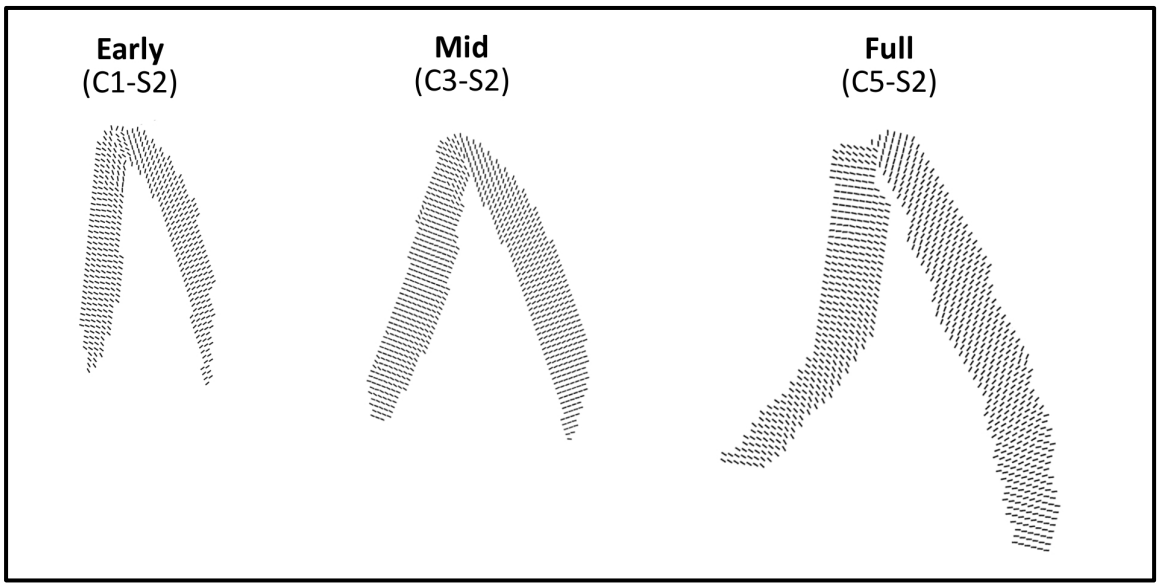

Figure 6.2: Texture direction maps of crystallites belonging to the first orientation population from the second slice of central incisal enamel in early- (C1-S2), mid- (C3-S2) and full- (C5-S2) development. For each tooth section, labial is on the right-hand side.

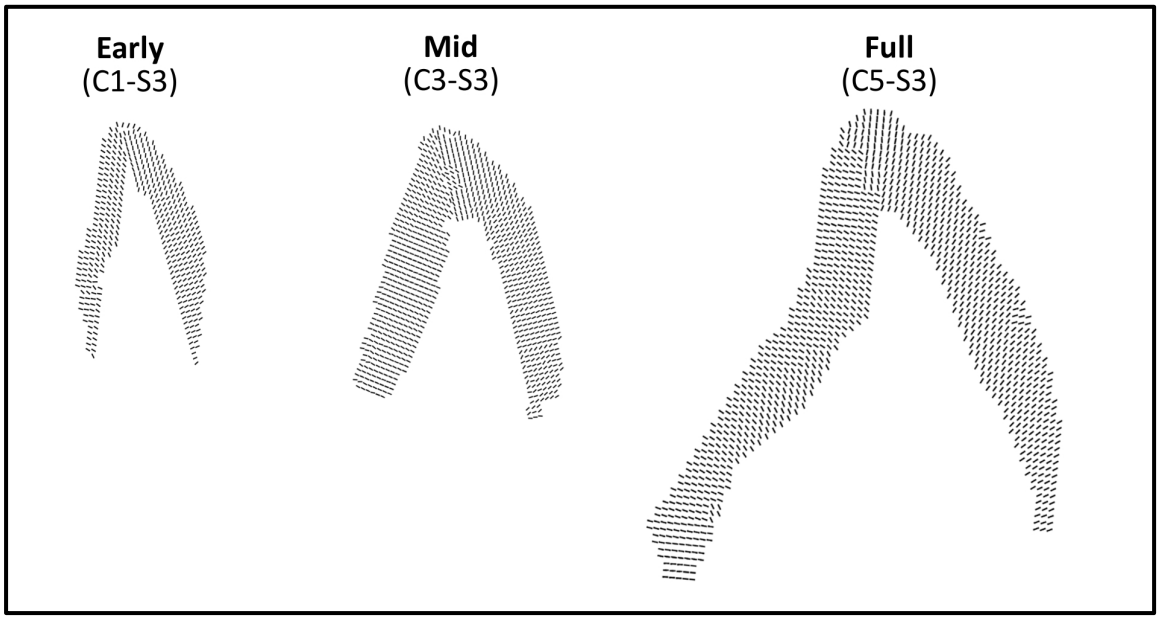

Figure 6.3: Texture directions maps of crystallites belonging to the first orientation population from the third slice of central incisal enamel in early- (C1-S3), mid- (C3-S3) and full- (C5-S3) development. For each tooth section, labial is on the right-hand side.

These values represent the peak positions extracted from the Gaussian model fitted to the (0 0 2) reflection curve **(Equation 4.7)** using the author's own automated in-house software (MoFit) built with MatLab R2017a (MathWorks, Natick, Massachusetts, USA) as per the method described in Section 4.3.3.2. It can be seen that the long axes of c-HAp crystallites were approximately perpendicular to both the enamel surface and the

EDJ. Furthermore, the directions of crystallites near the incisal edge in all developmental stages were found to change gradually to an increasingly oblique direction until they were almost vertical.

6.2.2. Population percentage

The peak intensities of the azimuthally integrated (0 0 2) reflection curve relate to the quantity of *c*-planes of the crystallites that satisfy the Bragg law (Equation 3.4). This allows for predicting the percentage of the two orientation populations in each diffraction pattern as per the method described in Section 4.3.3.4.

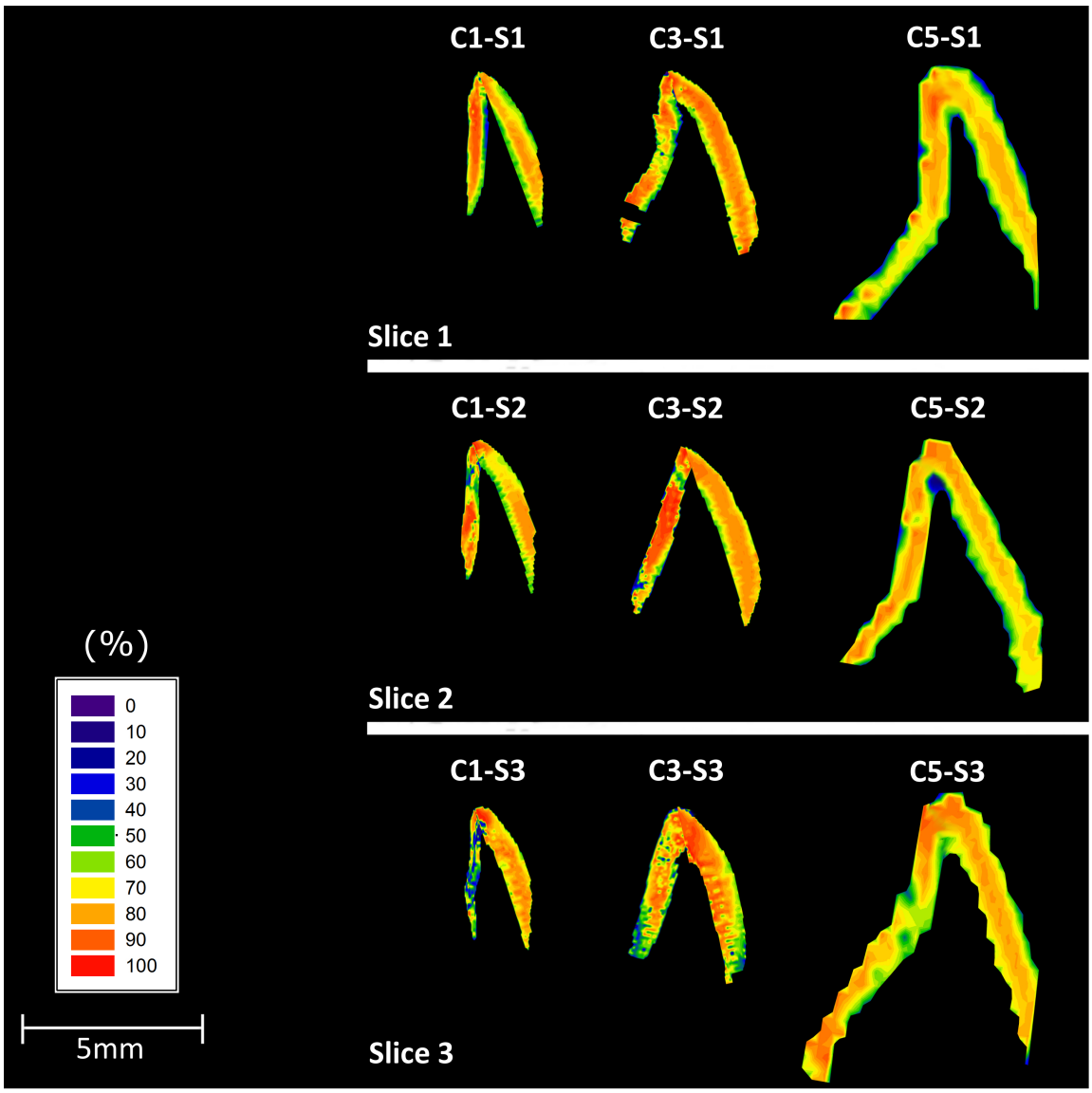

Figure 6.4: The percentage of crystallites belonging to the first orientation population in sequential slices of central incisal enamel at early- (sample C1), mid- (sample C3) and full- (sample C5) development. For each tooth section, labial is on the right-hand side.

The results from Figure 6.4 revealed that the first orientation population was the dominant population in all of the measured slices **(Table 6.1)**. Furthermore, it was found that all slices, with the exception of slice C3-S3, had lower percentage of crystallites belonging to the first orientation population along the contour of the EDJ than the enamel bulk (the region between the EDJ and the enamel surface). Moreover, the slices furthest away from the mid-slice of the tooth (samples C1-S3, C3-S3 and C5-S3) were found to have higher spatial variation in the percentage of crystallites belonging to the first orientation population. The results from the mid-slices (samples C1, C3 and C5) were discussed previously in Section 5.2.2.2. Detailed descriptions of the observed variations in the percentage of the first orientation population for each sample are provided below.

Table 6.1: Average percentage of crystallites belonging to the first orientation population in sequential slices of central incisal enamel at various developmental stages

Sample	Early-development			Mid-development			Full-development		
	C1-S1	C1-S2	C1-S3	C3-S1	C3-S2	C3-S3	C5-S1	C5-S2	C5-S3
Percentage (%)	68.8 ±14.8	69.3 ±16.5	67.6 ±18.3	74.3 ±13.9	77.2 ±13.2	70.6 ±19.2	70.4 ±14.1	69.5 ±11.7	68.4 ±13.2

6.2.2.1. *Early-development*

In slice 1 (sample C1-S1), a lower percentage of crystallites belonging to the first orientation population was observed along the contour of the EDJ in both palatal and labial enamel. In labial enamel, a lower percentage of crystallites from the first orientation population was found along the incisal two thirds of the enamel surface. Furthermore, palatal enamel was found to have a higher percentage of crystallites belonging to the first orientation population than labial enamel **(Figure 6.4 C1-S1**).

In slice 2 (sample C1-S2), a lower percentage of crystallites from the first orientation population was observed along a thin band near the EDJ in both palatal and labial enamel. In labial enamel, a lower percentage of crystallites from the first orientation

population was found along the incisal third of the enamel surface. Furthermore, a considerably higher percentage of crystallites belonging to the first population was observed near the incisal tip and near the cervical part of palatal enamel **(Figure 6.4 C1-S2**).

In slice 3 (sample C1-S3), palatal enamel was found to have considerably lower percentage of crystallites belonging to the first orientation population than labial enamel. Moreover, substantially higher percentage of crystallites belonging to the first population was observed near the incisal tip. A thin band containing lower percentage of crystallites belonging to the first orientation population was found along the EDJ and at the incisal half of the enamel surface **(Figure 6.4 C1-S2**).

6.2.2.2. *Mid-development*

In slice 1 (sample C3-S1), a lower percentage of crystallites from the first orientation population was observed along the contour of the EDJ in both palatal and labial enamel. In labial enamel, lower percentage of crystallites from the first orientation population was found along the cervical third of the enamel surface. Furthermore, higher percentage of crystallites belonging to the first orientation population was observed near the incisal tip **(Figure 6.4 C3-S1**).

In slice 2 (sample C3-S2), the central part of palatal enamel displayed lower percentage of crystallites belonging to the first orientation population along both the EDJ and the enamel surface. Furthermore, the central part of labial enamel displayed higher percentage of crystallites belonging to the first population compared to the incisal and cervical parts of the tooth **(Figure 6.4 C3-S2**).

In slice 3 (sample C3-S3), labial enamel was found to have higher percentage of crystallites belonging to the first orientation population compared to palatal enamel. In

labial enamel, the percentage of crystallites belonging to the first orientation population was found to increase from the cervical part towards the incisal tip of the tooth. However, in palatal enamel the central part of the tooth displayed a higher percentage of crystallites belonging to the first orientation population compared to the incisal and cervical parts of the tooth. Furthermore, a higher percentage of crystallites belonging to the first orientation population was found along the EDJ compared to the enamel surface **(Figure 6.4 C3-S3**).

6.2.2.3. *Full-development*

In slice 1 (sample C5-S1), labial enamel was found to have a lower percentage of crystallites belonging to the first orientation population than palatal enamel. In labial enamel, a lower percentage of crystallites belonging to the first orientation could be seen along the enamel surface and the EDJ. Moreover, the percentage of crystallites belonging to the first orientation population was found to be consistent throughout labial enamel. However, in palatal enamel, the percentage of first orientation crystallites was found to increase from the cervical part towards the incisal tip of the tooth **(Figure 6.4 C5-S1)**.

In slice 2 (sample C5-S2), labial enamel was found to have a lower percentage of crystallites belonging to the first orientation population than palatal enamel. A lower percentage of crystallites belonging to the first orientation could be seen along the enamel surface and the EDJ. In labial enamel, the percentage of first orientation crystallites was found to increase from the cervical part towards the incisal tip of the tooth. This was not the case with palatal enamel, where the percentage of crystallites belonging to the first orientation population was found to decrease from the cervical part towards the incisal tip of the tooth **(Figure 6.4 C5-S2)**.

In slice 3 (sample C5-S3), the percentage of crystallites belonging to the first orientation population was found to increase from the cervical part towards the incisal tip of the tooth. Furthermore, in labial enamel, a lower percentage of crystallites belonging to the first orientation population could be seen along the enamel surface compared to the EDJ. In palatal enamel, the central part of the tooth had a lower percentage of crystallites belonging to the first orientation population than the incisal and cervical parts of the tooth. Moreover, in palatal enamel, a low percentage of crystallites from the first orientation population were found along the EDJ compared to the enamel surface **(Figure 6.4 C5-S3)**.

6.2.3. Angle between populations

Figure 6.5 displays the spatial distribution of angular separation for all the measured slices as per the method described in Section 4.3.3.3. It was found that on average the angular difference between the two orientation populations of the samples at the various developmental stages, with the exception of the labial enamel in sample C3-S3, increases when traveling from the enamel surface towards the EDJ. The least developed enamel (slices C1-S1, C1-S2 and C1-S3), the angular separation was found to increase from incisal tip towards the cervical part of the tooth. However, in the mid- (slices C3-S1, C3-S2 and C3-S3) and fully-developed (C5-S1, C5-S2 and C5-S3) enamel, with the exception of the palatal side of slice C3-S3, the angle between the two population was found to decrease from the incisal tip cervically. Further, all the slices had lower angular separation between the two population in palatal enamel than labial enamel. The results from the mid slices (samples C1, C3 and C5) were discussed previously in Section 5.2.2.3. Detailed descriptions of the observed variations in the angular separation between the two orientation populations for each sample are provided below.

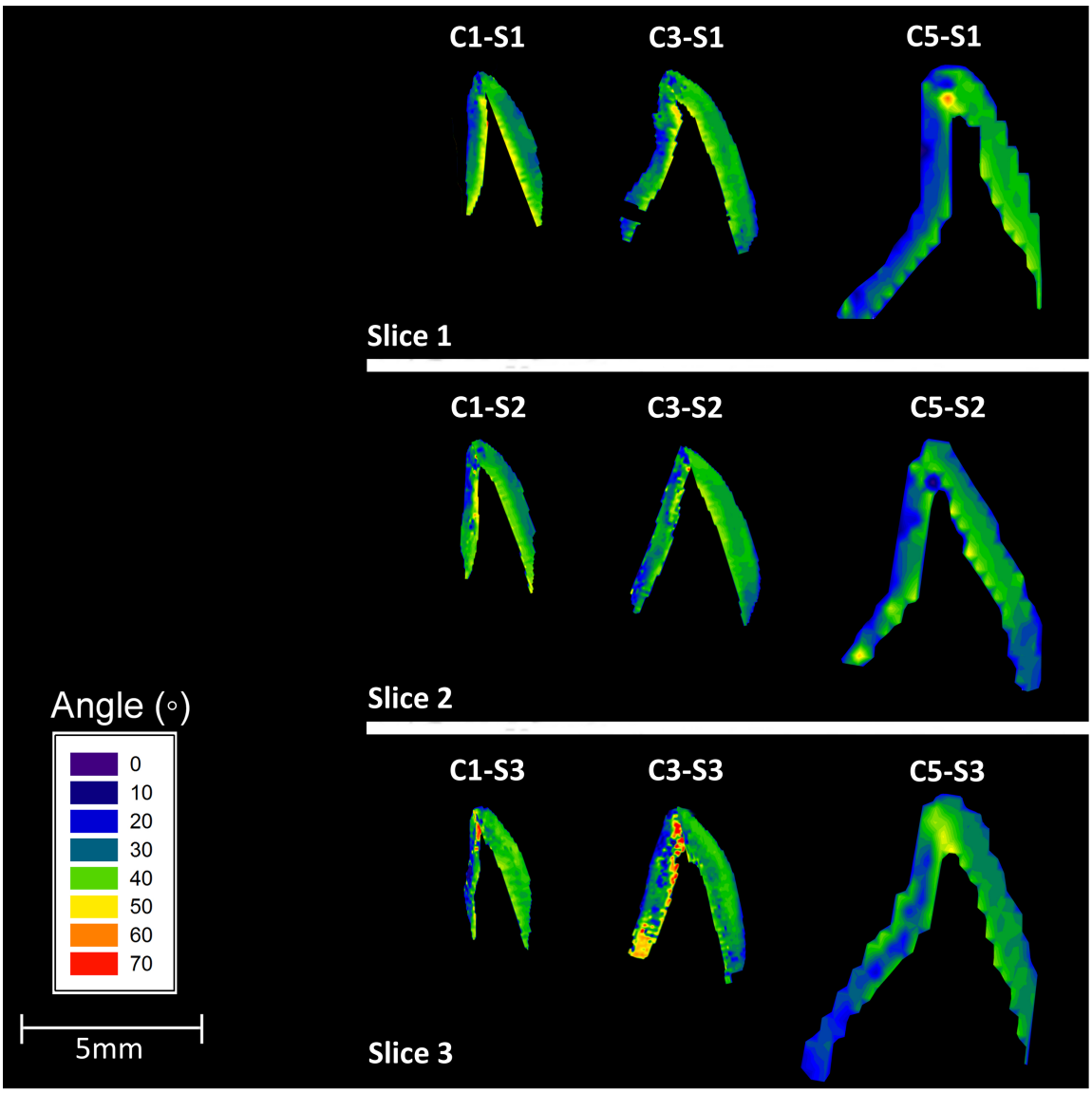

Figure 6.5: The average angle between the crystallites of the first and second orientation populations in sequential slices of central incisal enamel at early- (sample C1), mid- (sample C3) and full- (sample C5) development. For each tooth section, labial is on the right-hand side.

6.2.3.1. *Early-development*

The average angular separation between the first and second orientation populations in slices 1 (sample C1-S1) and 2 (sample C1-S2) was found to decrease from the cervical part towards the incisal tip of the tooth. However, the angular separation between the two orientation populations in the palatal enamel of slice 3 (sample C1-S3) was found to increase from the cervical part towards the incisal tip of the tooth.

Moreover, the average angular separation between the two orientation populations values in slices 1 (sample C1-S1), 2 (sample C1-S2) and 3 (sample C1-S3) were higher in labial enamel compared to palatal enamel, with the latter having higher spatial variations of angular separation **(Figure 6.5 C1-S1, C1-S2 and C1-S3)**.

6.2.3.2. *Mid-development*

The average angular separation between the two orientation populations values in slices 1 (sample C3-S1) and 2 (sample C3-S2) were found to increase from the cervical part towards the incisal tip of the tooth. In slice 3 (sample C3-S3), the angular separation between the two population in palatal enamel was found to decrease from the cervical part towards the incisal tip of the tooth. However, in the labial side of slice 3, the angular separation between the two populations was found to increase from the cervical part towards the incisal tip of the tooth.

Moreover, the average angular separation between the two orientation populations values in slices 1 (sample C3-S1) and 2 (sample C3-S2) were higher in labial enamel compared to palatal enamel. However, in slice 3 (sample C3-S3), the angular separation between the two orientation populations was found to be lower in labial enamel compared to palatal enamel, with the latter displaying considerably higher spatial variations of angular separation **(Figure 6.5 C3-S1, C3-S2 and C3-S3)**.

6.2.3.3. *Full-development*

The average angular separation between the first and second orientation populations in slice 1 (sample C5-S1) was found to increase from the incisal tip towards the cervical part of the tooth. However, in slices 2 (sample C5-S2) and 3 (sample C5-S3), the average angular separation between the first and second orientation populations were found to decrease from the incisal tip towards the cervical end of the tooth. Moreover,

the average angular separation between the two orientation populations values in slices 1 (sample C5-S1), 2 (sample C5-S2) and 3 (sample C5-S3) were higher in labial enamel compared to palatal enamel **(Figure 6.5 C5-S1, C5-S2 and C5-S3)**.

6.2.4. Texture magnitude

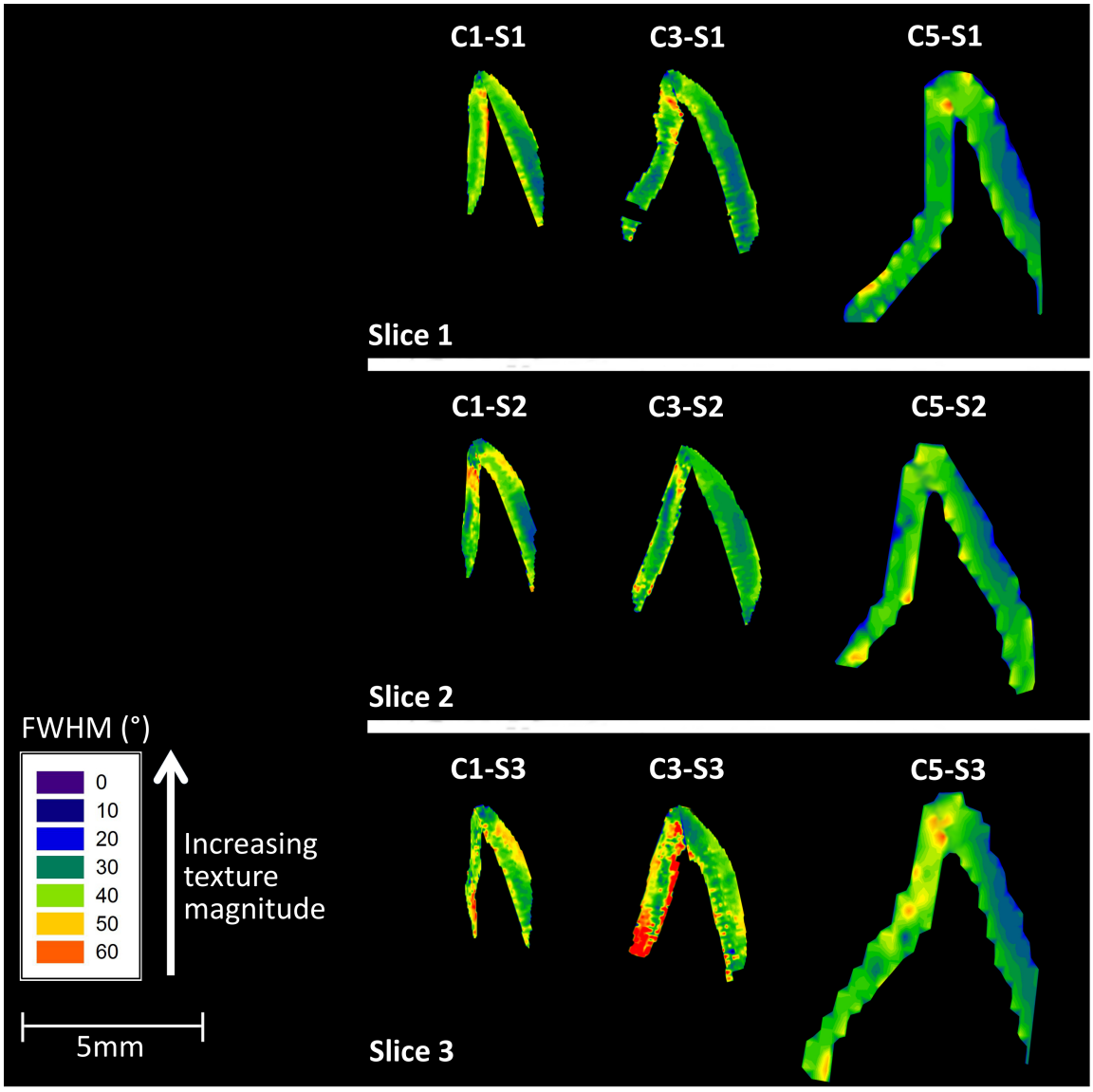

Figure 6.6: Texture magnitude distribution of crystallites from the first orientation population in sequential slices of central incisal enamel at early- (sample C1), mid- (sample C3) and full- (sample C5) development. For each tooth section, labial is on the right-hand side.

The FWHM values **(Equation 4.7)** of peaks A, B, C and D **(Figure 4.10)** were obtained from each diffraction pattern as per the method described in Section 4.3.3.1. The average FWHM of the peaks corresponding to the first orientation population (peaks A and C) was calculated **(Equation 4.8)** for each diffraction pattern **(Figure 6.6)**.

Similarly, the average FWHM of peaks *B* and *D* was calculated **(Equation 4.9)** for the second population **(Figure 6.7)**.

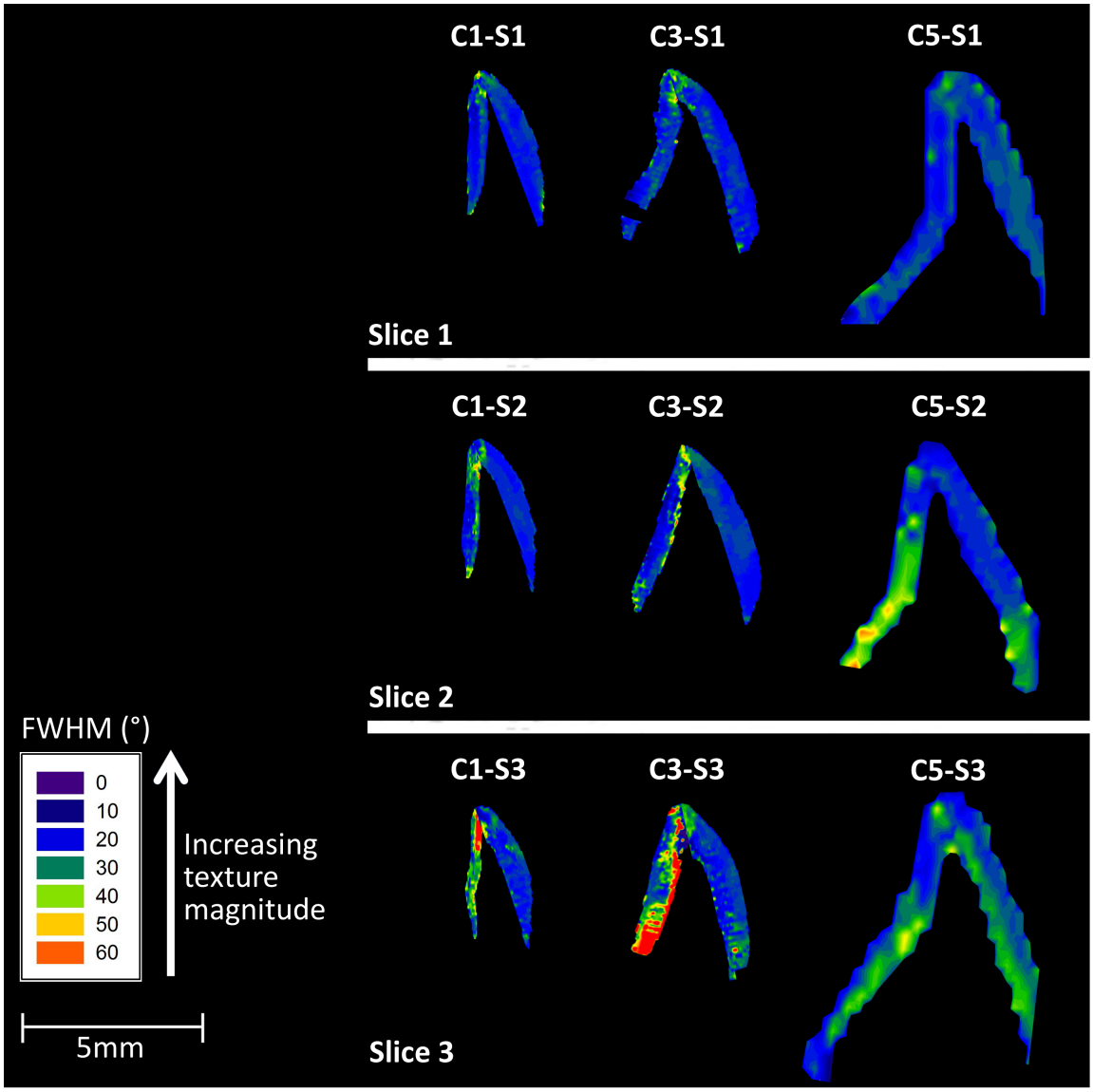

Figure 6.7: Texture magnitude distribution of crystallites from the second orientation population in sequential slices of central incisal enamel at early- (sample C1), mid- (sample C3) and full- (sample C5) development. For each tooth section, labial is on the right-hand side.

In all slices, the crystallites from the first orientation population were found to have higher texture magnitude in labial enamel compared to palatal enamel. This was also the case with the crystallites from the second orientation population with the exception of slices C5-S1 and C5-S3. Further, crystallites of both populations were found to have on average lower texture magnitude in the slices furthest away from the mid-slice. In

addition to the considerable local variations in crystallite texture magnitude, it was observed that in all assessed samples, with the exception of palatal enamel of samples C1-S3 and C3-S3, the crystallites from the first orientation population **(Figure 6.6)** had lower texture magnitude than those from the second population **(Figure 6.7)**. The results from the mid-slices (samples C1, C3 and C5) **(Figure 5.11 and Figure 5.13)** were discussed previously in Section 5.2.2.4. Detailed descriptions of the observed variations in the texture magnitude of both orientation populations for each sample are provided below.

6.2.4.1. *Early-development*

6.2.4.1.1 First orientation population

In slice 1 (sample C1-S1), it was found that on average, palatal enamel comprised of crystallites with lower texture magnitude than those in labial enamel. Crystallites with low texture magnitude were found to be present along the entire contour of the EDJ in palatal enamel. At the incisal quarter of labial enamel, crystallites along the EDJ were found to have higher texture magnitude than those along the enamel surface. However, the crystallites at the cervical three quarters of labial enamel had lower texture magnitude along the EDJ compared to the enamel surface. Furthermore, the texture magnitude of crystallites in both palatal and labial enamel was found to decrease from the cervical part towards the incisal tip of the tooth **(Figure 6.6 C1-S1)**.

In slice 2 (sample C1-S2), the crystallites in palatal enamel were found to have lower texture magnitude than those in labial enamel. Crystallites of both sides of enamel displayed lower texture magnitude at the incisal and cervical parts of the enamel and higher texture magnitude at the central part of the tooth. The crystallites along the EDJ at the cervical two thirds of palatal enamel displayed lower texture magnitude than

those along the enamel surface. Furthermore, the crystallites along the EDJ at the cervical two thirds of labial enamel displayed lower texture magnitude than those along the enamel surface. However, the crystallites along the EDJ at the incisal third of labial enamel displayed higher texture magnitude than those along the enamel surface **(Figure 6.6 C1-S2)**.

In slice 3 (sample C1-S3), the crystallites along the EDJ at the incisal half of labial and palatal enamel displayed higher texture magnitude than those along the enamel surface. However, the crystallites along the EDJ at the cervical half of the labial and palatal enamel displayed lower texture magnitude than those along the enamel surface. In labial enamel, the texture magnitude was found to increase from the incisal tip towards the cervical end of the tooth. However, in palatal enamel the texture magnitude was found to decrease from the incisal tip towards the cervical part of the tooth **(Figure 6.6 C1-S3)**.

6.2.4.1.2 Second orientation population

In slice 1 (sample C1-S1), crystallites with low texture magnitude can be seen near the incisal tip. In palatal enamel, a thin band of low textured crystallites running along the EDJ was observed. Furthermore, in palatal enamel, crystallites with low texture magnitude were observed in a small area near the cervical end of the tooth. Further, in labial enamel, a band of crystallites with low texture magnitude can be seen along the enamel surface. Moreover, the crystallites in palatal enamel were found to have lower texture magnitude than those in labial enamel **(Figure 6.7 C1-S1)**.

In slice 2 (sample C1-S2), the crystallites in labial enamel displayed a higher and a more homogenous texture magnitude than those in palatal enamel. Palatal enamel comprised

of crystallites with low texture magnitude along the EDJ, near the incisal quarter and at the most cervical part of the tooth **(Figure 6.7 C1-S2)**.

In slice 3 (sample C1-S3), crystallites in palatal enamel had considerably lower texture magnitude than those in labial enamel. The crystallites in labial enamel displayed lower texture magnitude along the EDJ and the enamel surface than the rest of the tooth. Furthermore, in palatal enamel, crystallites were found to have the highest texture magnitude near the most cervical region of the tooth. Moreover, crystallites with low texture magnitude were found along the EDJ with the lowest texture magnitude near the incisal quarter of the EDJ **(Figure 6.7 C1-S3)**.

6.2.4.2. *Mid-development*

6.2.4.2.1 First orientation population

In all measured slices, crystallites with higher texture magnitude can be found in a small region near the incisal tip. In slice 1 (sample C3-S1), the crystallites along the EDJ displayed lower texture magnitude than those along the enamel surface. An area comprising of crystallites with high degree of texture can be seen at the bulk (the region between the EDJ and the enamel surface) along the entire length of the crown. Furthermore, the texture magnitude of crystallites was found to decrease from the cervical part towards the incisal tip of the tooth **(Figure 6.6 C3-S1)**.

In slice 2 (sample C3-S2), an area comprising of crystallites with high degree of texture can be seen in the enamel bulk (the region between the EDJ and the enamel surface) along the entire length of palatal enamel. The crystallites at the incisal and cervical regions of palatal enamel displayed low texture magnitude than the central region of the tooth. The crystallites along the EDJ at the incisal two thirds of labial enamel displayed lower degree of texture than those along the enamel surface. Furthermore, the

crystallites along the EDJ at the cervical third of labial enamel displayed higher degree of texture than those along the enamel surface **(Figure 6.6 C3-S2)**.

In slice 3 (sample C3-S3), it was found that on average, palatal enamel comprised of crystallites with lower texture magnitude than labial enamel. The crystallites along the incisal three quarters of the EDJ in palatal enamel had lower texture magnitude than the crystallites along the enamel surface. Furthermore, an area comprising of crystallites with high degree of texture was observed in the enamel bulk (the region between the EDJ and the enamel surface) along the incisal three quarter of palatal enamel. Moreover, the crystallites at the cervical quarter of palatal enamel displayed low texture magnitude along the entire thickness of enamel. Crystallites along the EDJ in labial enamel displayed higher texture magnitude than the crystallites along the enamel surface **(Figure 6.6 C3-S3)**.

6.2.4.2.2 Second orientation population

In all measured slices, crystallites with lower texture magnitude can be found near the incisal tip. Furthermore, it was found that on average, palatal enamel comprised of crystallites with lower texture magnitude than labial enamel. In Slice 1 (sample C3-S1), the crystallites in both palatal and labial sides displayed lower texture magnitude near the EDJ compared to the enamel surface. Moreover, the texture magnitude of crystallites was found to decrease from the cervical end towards the incisal tip of the tooth. **(Figure 6.7 C3-S1)**.

In Slice 2 (sample C3-S2), a band of crystallites with low texture magnitude can be seen along the EDJ of palatal enamel. Moreover, the crystallites displayed lower degree of texture near the incisal and most cervical regions of palatal enamel. Furthermore, in labial enamel, crystallites with low texture magnitude were observed near the EDJ at the

incisal half of the crown. Further, the texture magnitude of crystallites was found to decrease from the cervical end towards the incisal tip of the tooth **(Figure 6.7 C3-S2)**.

In Slice 3 (sample C3-S3), a band of crystallites with low degree of texture can be seen along the EDJ of palatal enamel. Moreover, the crystallites near the most cervical regions of both labial and palatal enamel displayed low degree of texture. Further, the crystallites in palatal enamel were found to have considerably lower degree of texture than those in labial enamel. Furthermore, the texture magnitude was found to decrease from the incisal tip towards the cervical part of the tooth **(Figure 6.7 C3-S3)**.

6.2.4.3. *Full-development*

6.2.4.3.1 First orientation population

In all measured slices (samples C5-S1, C5-S2 and C5-S3), crystallites in palatal enamel displayed lower texture magnitude than the crystallites in labial enamel. In slice 1 (sample C5-S1), the crystallites in labial enamel displayed higher texture magnitude along the enamel surface compared to the crystallites along the EDJ. Furthermore, crystallites at the incisal and cervical parts of labial enamel had lower texture magnitude than the central part of the tooth. An area comprising of crystallites with high degree of texture can be seen at the enamel bulk (the region between the EDJ and the enamel surface) along the entire length of palatal enamel. Moreover, a small area near the most cervical part of the tooth was found to comprise of crystallites with high texture magnitude **(Figure 6.6 C5-S1)**.

In slice 2 (sample C5-S2), the crystallites at the incisal two thirds of labial enamel displayed higher texture magnitude along the enamel surface compared to the crystallites along the EDJ. Further, crystallites at the incisal and cervical parts of labial enamel had lower texture magnitude than the central region of the tooth. The crystallites

in palatal enamel displayed higher texture magnitude along the enamel surface compared to the crystallites along the EDJ **(Figure 6.6 C5-S2)**.

In slice 3 (sample C5-S3), the crystallites of labial enamel displayed lower degree of texture along the EDJ than those along the enamel surface. Furthermore, crystallites at the incisal and cervical parts of labial enamel had lower texture magnitude than the central part. Further, the texture magnitude was found to increase from the incisal tip towards the cervical end of the tooth. However, a small area near the most cervical part of the tooth was found to comprise of crystallites with low texture magnitude **(Figure 6.6 C5-S3)**.

6.2.4.3.2 Second orientation population

In slice 1 (sample C5-S1), crystallites with low texture magnitude were observed near the incisal tip of the tooth. Furthermore, crystallites in palatal enamel had on average higher texture magnitude than those in labial enamel. Moreover, crystallites had lower texture magnitude along the incisal three quarters of EDJ in palatal enamel. Additionally, the cervical quarter had crystallites with higher texture magnitude near the EDJ compared to those along the enamel surface. Further, the texture magnitude of crystallites was found to decrease from the incisal tip towards the cervical end of the tooth. Crystallites with lower degree of texture can be seen along the incisal half of the surface of labial enamel **(Figure 6.7 C5-S1)**.

In slice 2 (sample C5-S2), crystallites in labial enamel had on average higher texture magnitude than those in palatal enamel. Furthermore, the incisal third of palatal enamel contained crystallites with higher texture magnitude. Moreover, the enamel surface at the cervical third of the tooth displayed crystallites with high texture magnitude. However, the cervical third of labial enamel was found to be occupied by crystallites

with lower texture magnitude. Further, the texture magnitude was found to decrease from the incisal tip towards the cervical end of the tooth **(Figure 6.7 C5-S2)**.

In slice 3 (sample C5-S3), the texture magnitude values of crystallites in labial enamel were found to increase from the EDJ peripherally. Further, crystallites with higher texture magnitude values were observed at the incisal and cervical regions of palatal enamel. Moreover, the crystallites at the central region of palatal enamel displayed low texture magnitude along the EDJ. Furthermore, crystallites of labial enamel had on average higher texture magnitude near the incisal half compared to the cervical half of the tooth. Additionally, the texture magnitude was found to decrease from the incisal tip towards the cervical end of the tooth **(Figure 6.7 C5-S3)**.

6.3. Discussion

The texture direction maps of the enamel in the fully-developed central incisor slices revealed that the long axes of the c-HAp crystallites in the mid-slice **(Figure 5.5 C5)**, slice 1 **(Figure 6.1 C5-S1)**, slice 2 **(Figure 6.2 C5-S2)** and slice 3 **(Figure 6.3 C5-S3)** were approximately perpendicular to the EDJ and to the enamel surface, as was the case with the mid-slice of the fully-developed lateral incisor **(Figure 5.6 L2)**. This phenomenon was previously reported in a number of studies on mature human enamel (Low, 2004, Al-Jawad et al., 2007, Deyhle et al., 2009, Raue and Klein, 2011, Raue et al., 2012, Simmons et al., 2013, Egan et al., 2013). This arrangement was suggested to provide resistance to abrasion during the process of mastication (Boyde and Fortelius, 1986).

Furthermore, the results presented here, agree with other S-XRD studies analysing sequential slices of a mature human premolars which reported similar crystallite

directions in all analysed slices. However, these studies reported that although crystallites were approximately perpendicular to the EDJ in the cervical and central parts of the tooth, the texture direction on either side of the tooth cusps was parallel to the EDJ (Al-Jawad et al., 2008, Simmons et al., 2011). This phenomenon was not seen in the current investigation, in which the texture direction was almost always approximately perpendicular to the EDJ and enamel surface. This disagreement, suggests that there are considerable variations in the 3-D arrangement of crystallites between dental dentitions. Therefore, future studies should analyse the 3-D orientation of crystallites in all tooth dentitions, in order to synthesis more specific dental materials targeting specific tooth types to improve the clinical performance of utilised dental restorations.

The long axes of crystallites in all slices of early- (samples C1-S1, C1-S2 and C1-S3) and mid-developed (samples C3-S1, C3-S2 and C3-S3) enamel, were also found to be approximately perpendicular to the EDJ and the enamel surface **(Figures 6.1, 6.2 and 6.3)**. These results were similar to those seen in the mid-slices of developing central **(Figure 5.5 C1, C2, C3 and C4)** and lateral **(Figure 5.6 L1)** incisors, suggesting that the initial preferred growth directions of apatite crystallites persist from early through to full maturation. This is in agreement with previous assumptions made by a number of workers (Boyde, 1964, Robinson et al., 1998, Beniash et al., 2009, Simmons et al., 2013).

Furthermore, similar to the results from the mid-slices of central **(Figure 5.9)** and lateral **(Figure 5.10)** incisors, the results from the sequential slices revealed that within one probed region the c-HAp crystallites tend to group along two main directions with

respect to their long axes with a spatially varying angular separation in the range of 20-50° **(Figure 6.5)**. This phenomenon had been reported in other studies on dental enamel using S-XRD (Yagi et al., 2009, Yagi et al., 2010) and lab source XRD (Thewlis, 1936, Thewlis, 1940, Trautz et al., 1953, Glas, 1962, Poole and Brooks, 1961, Gwinnett, 1966, Gwinnett, 1967, Hirota, 1982, Jodaikin et al., 1984, Hirota, 1986). Moreover, it was revealed that considerably more crystallites belonged to one orientation population (first population) compared to the other (second population) in all analysed slices **(Figure 6.4)**. This phenomenon was also present in the mid-slices of central **(Figure 5.7)** and lateral **(Figure 5.8)** incisors.

As mentioned in the previous chapter, the two orientation populations observed are more likely due to probing two groups of prisms, or prisms from different regions of the enamel (Poole and Brooks, 1961, Glimcher et al., 1965), suggesting that the two orientation populations arise by probing two zones of HSb simultaneously (Hirota, 1986).

Figure 6.5 revealed that, in all measured slices, with the exception of labial enamel of sample C3-S3, the angular separation between the first and second orientation populations values decrease from the EDJ peripherally. This agrees with the current understanding; that prisms run approximately parallel near the enamel surface then divide as they approach inner enamel into two groups deviating in opposite directions corresponding to the two zones of the HSb (Hirota, 1982). Moreover, Macho et al. (2003) developed a 3-D model where it was shown that prism decussations increase from the EDJ towards the enamel surface. Furthermore, Cox (2013) found that a transition exists from a region marked by prism decussation to a region where prisms lie

parallel with respect to one another. Therefore, the observations presented in the current study agree with Hirota (1986) hypothesis that the two orientation populations observed arise from the two zones of the HSb being recorded simultaneously.

It is suggested that the texture magnitude of dental enamel crystallites relates to the mechanical needs that the teeth are required to fulfil. The regions of the tooth that exhibit high loading forces are expected to display a high degree of texture. Similarly, regions with lower crystallite texture magnitude represent a lower demand of strength in that position (Deyhle et al., 2009, Raue and Klein, 2011, Raue et al., 2012).

In the current investigation, two orientation populations of crystallites were found to exist simultaneously within one probed region. The texture variations of the two populations of crystallite orientations have not been reported previously. It is also worth mentioning as can be seen in Figure 6.4 that the first orientation population of crystallites is the dominant population in all of the analysed enamel slices and is most likely the population analysed in previous texture studies. The existence of the two orientation populations were reported in a number of studies (Thewlis, 1936, Thewlis, 1940, Trautz et al., 1953, Glas, 1962, Poole and Brooks, 1961, Gwinnett, 1966, Gwinnett, 1967, Hirota, 1982, Jodaikin et al., 1984, Hirota, 1986, Yagi et al., 2009, Yagi et al., 2010). However, no attempts were made to this date to measure the texture magnitude of the two orientation populations individually.

Hirota (1986) suggested that the two populations are the result of two zones of overlapping groups of decussating prisms being recorded simultaneously. It was found that, in all measured slices, the first orientation population of crystallites **(Figure 6.6)**

displayed a lower degree of preferred orientation than the second population **(Figure 6.7)**. If Hirota (1989) explanation is taken into account, it means that according to our results, one group of decussating prisms had higher texture magnitude than the other. However, these observations do not agree with the findings of Hirota (1989) who reported similar degrees of texture in the two zones of the HSb. According to Simmer et al. (2012), in inner enamel, one row of ameloblasts move in one direction while those in adjacent rows move in the opposite direction, resulting in prism decussation. Therefore, we propose that the movement direction of ameloblasts determines the crystallites' degree of orientation, i.e. rows of ameloblasts moving in one direction results in the growth of crystallites with low degree of texture **(Figure 6.6)**, whereas, adjacent rows of ameloblasts moving in opposite directions give rise to highly ordered crystallites **(Figure 6.7)**. Furthermore, from the results seen in Figure 6.4, the current study suggests that one row of ameloblasts produce higher number of crystallites than adjacent rows.

In all slices of mature enamel, the crystallites of the first orientation population near the incisal tip displayed similar texture magnitude values to those found at the cervical end in both tooth sides and lower values than those at the central region of labial enamel **(Figure 5.11 C5 and Figure 6.6 C5-S1, C5-S2 and C5-S3)**. However, the texture magnitude values of the crystallites from the second orientation population near the incisal tip were different in different slices. In the mid-slice **(Figure 5.13 C5)** and slice 1 **(Figure 6.7 C5-S1)**, these values were similar to those near the cervical ends. However, in slices 2 **(Figure 6.7 C5-S2)** and 3 **(Figure 6.7 C5-S3)** the second population crystallites at the incisal tip were found to have a higher texture magnitude compared to the cervical tooth regions. The observations from the crystallites belonging

to the first orientation population **(Figure 5.11 C5 and Figure 6.6 C5-S1, C5-S2 and C5-S3)** do not agree with recent studies which reported an increase in texture magnitude (Al-Jawad et al., 2007, Al-Jawad et al., 2008, Raue et al., 2012, Simmons et al., 2013) and HSb packing densities (Lynch et al., 2010) near the cusps of mature human enamel. However, the above-mentioned studies agree with the results obtained from the second orientation population crystallites in slices 2 **(Figure 6.7 C5-S2)** and 3 **(Figure 6.7 C5-S3)**.

Furthermore, the first population of crystallites in all slices of mature labial enamel was found to have higher texture magnitude values along the EDJ than those along the enamel surface **(Figure 5.11 C5 and Figure 6.6 C5-S1, C5-S2 and C5-S3)**. This was also the case with crystallites belonging to the second population in palatal enamel in the mid-slice **(Figure 5.13 C5)**, and slice 2 **(Figure 6.7 C5-S2)**. However, slice 3 **(Figure 6.7 C5-S3)** was the only slice with crystallites from the second orientation displaying higher texture magnitude along the enamel surface than along the EDJ**.**

Lyon and Darling (1957) and Glas (1962) who assessed mature enamel using PLM and XRD respectively, suggested that the poorest crystallite texture was found near the EDJ. Moreover, using S-XRD to assess human mature premolars (Al-Jawad et al., 2007, Al-Jawad et al., 2008, Simmons et al., 2011) and developing (Simmons et al., 2013) and mature molars (Simmons et al., 2013, Egan et al., 2013), it was reported that crystallites near the EDJ displayed the lowest degree of orientation; the site believed to accommodate the first formed enamel crystallites (Shore et al., 1995a). Although these observations agree with the majority of the results from the first orientation population **(Figure 5.11 C5 and Figure 6.6 C5-S1, C5-S2 and C5-S3)**, they are not in agreement

with the results (with exception of sample C5-S3) regarding the second orientation population **(Figure 5.13 C5 and Figure 6.7 C5-S1 and C5-S2)**. This indicates that the above-mentioned studies most likely analysed one of the populations observed in the current investigation.

In all measured slices, the crystallites from the first orientation population in early- **(Figure 5.11 C1 and Figure 6.6 C1-S1, C1-S2 and C1-S3)** and mid-developed **(Figure 5.11 C3 and Figure 6.6 C3-S1, C3-S2 and C3-S3)** enamel displayed high texture magnitude at the incisal tip. However, crystallites belonging to the second orientation population in all slices of the early- **(Figure 5.13 C1 and Figure 6.7 C1-S1, C1-S2 and C1-S3)** and mid-developed **(Figure 5.13 C3 and Figure 6.7 C3-S1, C3-S2 and C3-S3)** enamel had high texture magnitude at the incisal tip.

Differences in the organisation of crystallites were observed when comparing the labial and palatal side of the crown. Simmons et al. (2013) reported that when compared to buccal enamel, the crystallites in palatal enamel displayed higher texture magnitude in the developing molar. This is in agreement with the results obtained from the crystallites belonging to the second orientation population in the mid-slices of enamel at early- (sample C1) and mid- (sample C3) development, which displayed higher degree of texture in palatal enamel compared to those in labial enamel. However, this was not the case in the sequential slices of the enamel at early- (samples C1-S1, C1-S2 and C1-S3) and mid- (samples C3-S1, C3-S2 and C3-S3) development, where crystallites from the second orientation population displayed higher degree of texture in labial enamel compared to those in palatal enamel. Furthermore, crystallites from the first orientation

population in all slices of enamel at early- and mid-development also displayed higher degree of texture in labial enamel compared to those in palatal enamel.

Simmons et al. (2013) S-XRD study on developing human molars reported that the crystallites along the contours of the EDJ displayed the lowest texture magnitude. This phenomenon was seen in crystallites of both orientation populations in some slices of the early- and mid-developed enamel. Crystallites from the first orientation population had lower texture magnitude near the EDJ of both sides of early- and mid- developed enamel of the mid-slice **(Figure 5.11 C1 and C3)** and slice 1 **(Figure 6.6 C1-S1 and C3-S1)** and the palatal mid-developed enamel of slice 3 **(Figure 6.6 C3-S3)**. Furthermore, crystallites from the second orientation population had lower texture magnitude near the EDJ in palatal early-developed enamel of slice 1 **(Figure 6.7 C1-S1)**, labial mid-developed enamel of slice 1 **(Figure 6.7 C3-S1)**, palatal early- and mid-developed enamel of slice 2 **(Figure 6.7 C1-S2 and C3-S2)** and palatal early- and mid-developed enamel of slice 3 **(Figure 6.7 C1-S3 and C3-S3)**.

Simmons et al. (2013) reported that, overall, the texture magnitude reduces with development and the sample in earliest development displayed a relatively homogenous texture distribution. A similar trend could be seen in the crystallites belonging to the second orientation population in all slices of labial enamel **(Figure 5.13 C1 and Figure 6.7 C1-S1, C1-S2 and C1-S3)**. However, this phenomenon was not present in crystallites belonging to the first orientation population **(Figure 5.11 C1 and Figure 6.6 C1-S1, C1-S2 and C1-S3)**.

6.4. Conclusions

Sequential slices of upper central incisors at various developmental stages were examined using S-XRD. In all analysed slices, the enamel crystallites were found to group into two main populations with their long axes having an angular separation between 20-50°. In the majority of the analysed slices, the angular separation between the two populations was found to decrease from the EDJ peripherally. Exceptions include the palatal fully-developed enamel of slice 3 (sample C5-S3) and the labial mid-developed enamel of slice 3 (sample C3-S3). In the former (sample C5-S3), the angular separation values decrease from the EDJ peripherally and then increase again at the enamel surface. In sample C3-S3, the angular separation was found to increase from the EDJ peripherally.

The percentage of the first orientation populations was considerably larger than the second orientation population. This was also seen in mid-slices of upper lateral incisors. The texture direction of crystallites in both orientation populations was found to be approximately perpendicular to the EDJ and the enamel surface in all developmental stages confirming that crystallite directions are defined early in maturation. Furthermore, the texture direction was persistent in all sequential slices. The crystallites from the first orientation population displayed substantially lower degree of texture than the crystallites from the second orientation population. Unlike the texture direction, the texture magnitude of enamel crystallites was found to vary considerably as a function of maturation and position. The crystallites from the first orientation population were found to display a more spatially heterogeneous distribution of texture magnitude than those from the second orientation population.

Due to the higher angular separation near the EDJ, the current study proposes that the two populations represent two groups of decussating prisms. Accordingly, this current study suggest that one group of prisms consists of crystallites with a higher degree of preferred orientation than neighbouring groups of prisms. Furthermore, this study revealed that one group of prisms has higher percentages of crystallites compared to neighbouring groups of prisms. It is widely accepted that prism directions are dictated by ameloblast movement direction away from the EDJ. Simmer et al. (2012) suggested that prism decussation comes into existence as one row of ameloblasts move in one direction while those in adjacent rows move in the opposite direction. Therefore, the current study proposes that the movement direction of ameloblasts determines the degree of crystallite orientation, i.e. rows of ameloblasts moving in the one direction give rise to highly ordered crystallites, whereas adjacent rows of ameloblasts moving in the opposite direction results in the growth of higher number of crystallites with low degree of texture. The presence of this phenomenon in early-developed enamel suggests that the texture magnitude as well as the texture direction is defined during the secretory stage of amelogenesis.

Chapter 7 - Combined discussion, conclusions and future work

7.1. Discussion

The main aim of this present work was to analyse and understand the progression of dental enamel biomineralisation in human incisors using X-ray techniques and scanning electron microscopy. The goals of this study were to characterise the crystallographic texture, microstructure and relative mineral density in the human enamel of the single cusp dentition at different developmental stages using archaeological sources of immature enamel. Ultimately, this work aims to produce the data and understanding needed to contribute towards a 4-D spatio-temporal model of human enamel biomineralisation in order to inform emerging regenerative dentistry technologies.

In Chapter 5, the crystallographic texture, microstructure and mineral density of the enamel from permanent upper central and lateral incisors at various developmental stages were characterised. The enamel relative mineral density was found to progress from the EDJ peripherally and from incisal tip cervically. Two crystallite orientation populations were characterised in all stages of development, with considerably more c-HAp crystallites belonging to the first orientation population. The angular separation between the two orientation populations was found to increase from the enamel surface towards the EDJ. The texture directions of c-HAp crystallites from both populations were found to be persistent throughout enamel development suggesting the crystallite orientation persist from early through to full maturation. Crystallites from both orientation populations were somewhat perpendicular to the enamel surface in all measured samples. However, the texture magnitude was found to vary considerably as a function of maturation. The texture magnitude of the first population was found to be

much higher than that of the second population with no obvious identifiable trend as a function of maturation.

In Chapter 6, sequential slices of upper central incisors at various developmental stages were examined using S-XRD. In all analysed slices, the enamel crystallites were found to group into two main populations, with their long axes having an angular separation between 20-50°. In the majority of the analysed slices, the angular separation between the two populations was found to decrease from the EDJ peripherally. The percentage of the first orientation population was considerably larger than the second orientation population. This was also seen in mid-slices of upper lateral incisors. The texture direction of crystallites in both orientation populations was found to be approximately perpendicular to the EDJ and the enamel surface in all developmental stages confirming that crystallites directions are defined early in maturation. Furthermore, the texture direction was persistent in all sequential slices. The crystallites from the first orientation population displayed substantially lower degree of texture than the crystallites from the second orientation population. Unlike the texture direction, the texture magnitude of enamel crystallites was found to vary considerably as a function of maturation and position. The crystallites from the first orientation population were found to display a more spatially heterogeneous distribution of texture magnitude than those from the second orientation population.

The small sample size used in this study was a constraint, due to the scarcity of developing human enamel available for investigation. The other limitation of this study was beamtime allocation; even if a large sample set was to be acquired it is not guaranteed that sufficient beamtime would be awarded, due to the competitive nature of

the selection process. Furthermore, due to time restrictions, there were some variations in beamspot size, spatial resolution and counting time leading to small differences between experimental set ups. Moreover, the beam setup was not constant in all experiments, due to a number of factors such as variations in filling mode, optics set-up, slits and compound refractive lenses (CRLs). Furthermore, the X-ray beam spot size used for this investigation was much greater (50-300 μm) **(Table 4.5)** than the diameter of a single prism (≈ 2-8 μm) (Robinson et al., 1995a, Dorozhkin, 2007, Reyes-Gasga et al., 2013) and hence several prisms were averaged in a single diffraction pattern. In future studies it would be insightful to use an X-ray beam with a diameter smaller than a single enamel prism in order to provide more accurate intra-prism data.

7.2. Conclusions

There are several implications of the findings presented in this study. Firstly, two crystallite orientation populations were identified in central and lateral incisors using S-XRD. One population (first orientation population) comprised of higher numbers of crystallites than the other (second orientation population). The angular separation between the two populations was found to increase from the enamel surface towards the EDJ. This increase in angular separation was found to correlate with the pattern of prism decussation identified using qBSE imaging. Therefore, this study proposes that the two identified populations represent the two groups of decussating prisms

Secondly, enamel crystallite directions from the two populations were found to be approximately perpendicular to the enamel surface with an angular separation of 20-50° between the two orientation populations. This phenomenon was found to persist from early through to full maturation in central and lateral incisors.

Thirdly, the texture magnitude values of the two crystallite populations were found to vary considerably with no apparent trend as a function of time. The texture magnitude of crystallites belonging to the first orientation population was considerably lower than that of the second orientation population. This arrangement was found to persist throughout the crown from early through to full maturation, suggesting that the texture magnitude is defined during the early stages of enamel biomineralisation.

Finally, XMT revealed that like texture magnitude, relative mineral density varies as a function of time. Accordingly, it was found that enamel biomineralisation progresses from the EDJ peripherally and from the incisal tip cervically as a function of maturation.

7.3. Recommended future work

7.3.1. Further crystallographic analysis of the S-XRD data:

Full Rietveld refinement should be performed using diffraction data from all teeth in order to quantify and describe the crystallite structure parameters spatially, such as crystallite size, lattice spacing, atomic position, site occupancies, particle sizes.

7.3.2. 2D lattice strain analysis

In order to improve our understanding of the two identified populations, further studies are required to investigate the 2-D variations in crystallographic strain (a dimensionless number related to the crystallite d-spacings) in both orientation populations. A pilot analysis was performed in the current work where GSAS-II (Toby and Von Dreele, 2013) was implemented to analyse the d-spacing variations azimuthally via a method devised by He and Smith (1997).

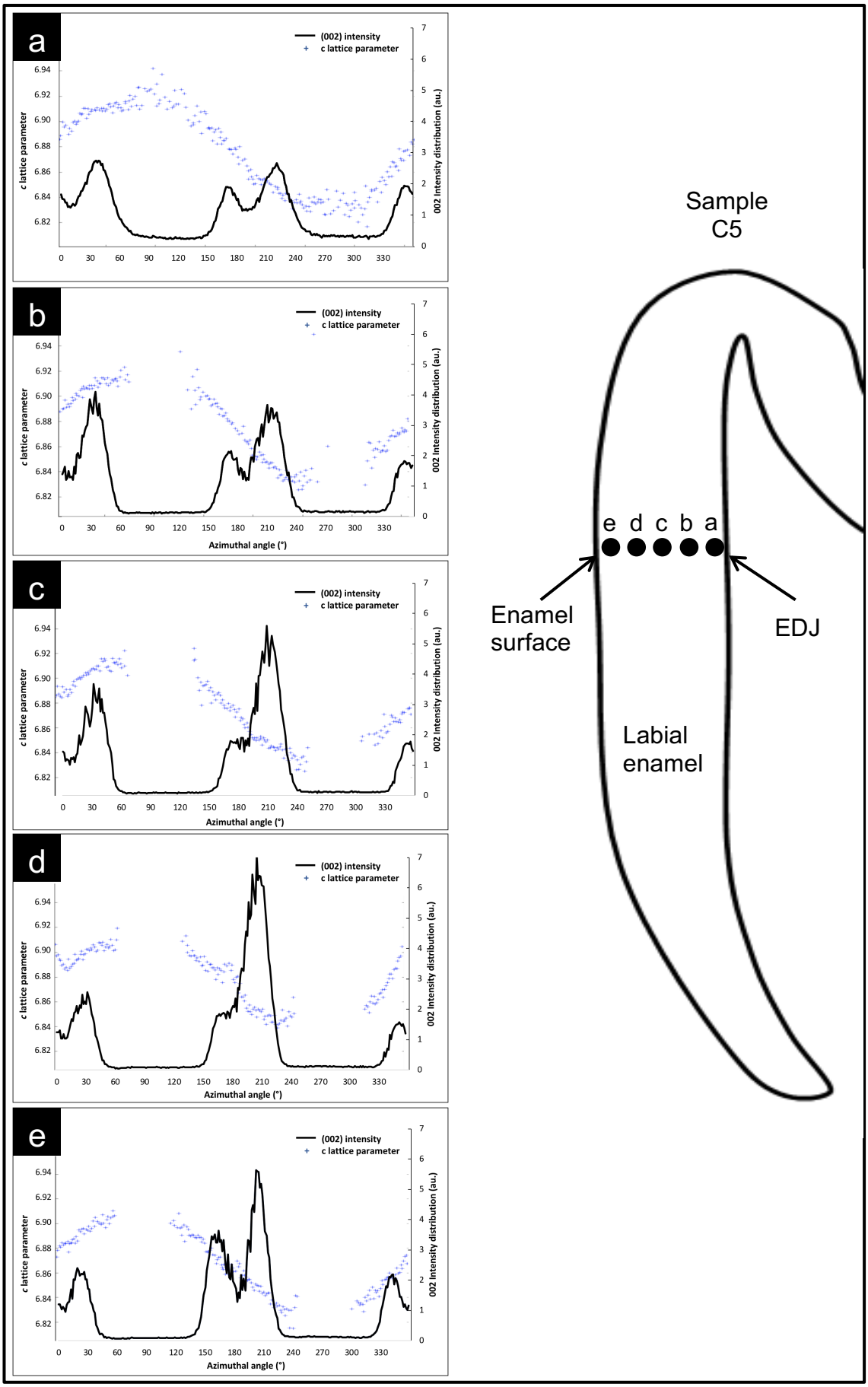

Figure 7.1: Azimuthal (0 0 2) reflection intensities and the corresponding variations in c-lattice parameters.

This particular method uses the diffraction images directly without the need for Rietveld refinements. The (*0 0 2*) plane is the normal to the *c*-axis of HAp and was therefore used to measure relative changes in the *c*-lattice parameters. The relationship between the d-spacing and Miller indices for a given Bragg peak in a hexagonal unit cell is given by:

$$\frac{1}{d^2} = \frac{4}{3}\left(\frac{h^2 + hk + k^2}{a^2}\right) + \frac{l^2}{c^2}$$

Equation 7.1

Where a is a-lattice parameter, c is the c-lattice parameters and h, k, l are the Miller indices. Substituting the (0 0 2) indices into Equation 7.1 gives the following relation:

$$c = 2d$$

Preliminary results from sample C5 using five points from the EDJ peripherally are presented in Figure 7.1 and indicate variations in c-lattice parameter between the two orientation populations. To build on the results obtained from this study, it is necessary to analyse the crystallographic strain variations spatially as a function of enamel maturation time.

7.3.3. Characterising tooth morphologies

Analysing different tooth types will equip us with a more in-depth understanding of the process of biomineralisation. More tooth morphologies at various developmental stages should be acquired through collaboration with archaeologists and compared to our upper lateral and central incisors data. Moreover, sequential slices of different tooth morphologies should be assessed to provide a 3-D representation of the biomineralisation process.

7.3.4. Complementary X-ray chemical analyses

Energy dispersive X-ray spectroscopy and X-ray florescence spectroscopy can be utilised to assess and compare the atomic composition of the mineral phase in enamel at different developmental stages. This will help identify any intermediate mineral phase that could not be identified using X-ray diffraction alone.

7.3.5. Verification studies for XMT

Verification studies for XMT are being carried by others in the group as part of a wider continual improvement and optimisation of accuracy of values of relative mineral density measured with XMT.

References

AHMED, F. 2011. *Multiscale quantitative imaging of human femoral heads using x-ray microtomography.*

AKITA, H., FUKAE, M., SHIMODA, S. & AOBA, T. 1992. Localization of glycosylated matrix proteins in secretory porcine enamel and their possible functional roles in enamel mineralization. *Archives of oral biology,* 37**,** 953-962.

AL-JAWAD, M., ADDISON, O., KHAN, M. A., JAMES, A. & HENDRIKSZ, C. J. 2012. Disruption of enamel crystal formation quantified by synchrotron microdiffraction. *Journal of Dentistry,* 40**,** 1074-1080.

AL-JAWAD, M., SIMMONS, L. M., STEUWER, A., KILCOYNE, S. H., SHORE, R. C., CYWINSKI, R. & WOOD, D. J. 2008. Three dimensional mapping of texture in dental enamel. *Key engineering materials,* 361-363**,** 877-880.

AL-JAWAD, M., STEUWER, A., KILCOYNE, S. H., SHORE, R. C., CYWINSKI, R. & WOOD, D. J. 2007. 2D mapping of texture and lattice parameters of dental enamel. *Biomaterials,* 28**,** 2908-2914.

ALLAN, J. 1959. Investigations into the mineralization pattern of human dental enamel. *Journal of dental research,* 38**,** 1096-1107.

ALMEIDA, A. P., BRAZ, D., COLAÇO, M. V., BARROSO, R. C., PORTO, I. M., GERLACH, R. F. & DROPPA JUNIOR, R. 2009. Analysis of synchrotron X-ray diffraction patterns from fluorotic enamel samples. *Proceedings of the 20 RAU: Annual meeting of the LNLS users abstracts of scientific papers,* 41**,** 273.

ALQAHTANI, S. J., HECTOR, M. & LIVERSIDGE, H. 2010. Brief communication: the London atlas of human tooth development and eruption. *American Journal of Physical Anthropology,* 142**,** 481-490.

ALS-NIELSEN, J. & MCMORROW, D. 2011. *Elements of modern X-ray physics*, John Wiley & Sons, West Sussex, UK.

AMBROSE, J. 1973. Computerized transverse axial scanning (tomography). Part 2. Clinical application. *British Journal of Radiology,* 46**,** 1023-47.

ANAS, E. M. A., KIM, J. G., LEE, S. Y. & HASAN, M. K. 2011. Comparison of ring artifact removal methods using flat panel detector based CT images. *Biomedical engineering online,* 10**,** 72.

ANDERSON, P., ELLIOTT, J., BOSE, U. & JONES, S. 1996. A comparison of the mineral content of enamel and dentine in human premolars and enamel pearls measured by X-ray microtomography. *Archives of oral biology,* 41**,** 281-290.

ANGMAR-MÅNSSON, B. 1971. A quantitative microradiographic study on the organic matrix of developing human enamel in relation to the mineral content. *Archives of oral biology,* 16**,** 135-145.

ANGMAR, B., CARLSTRÖM, D. & GLAS, J.-E. 1963. Studies on the ultrastructure of dental enamel-IV: The mineralization of normal human enamel. *Journal of ultrastructure research,* 8**,** 12-23.

ANTOINE, D. 2000. *Evaluating the periodicity of incremental structures in dental enamel as a means of studying growth in children from past human populations.* PhD Thesis, University College London, London, UK.

ANTOINE, D., HILLSON, S. & DEAN, M. C. 2009. The developmental clock of dental enamel: a test for the periodicity of prism cross-striations in modern humans and an evaluation of the most likely sources of error in histological studies of this kind. *Journal of anatomy,* 214**,** 45-55.

AOBA, T. 1996. Recent observations on enamel crystal formation during mammalian amelogenesis. *Anatomical Record,* 245**,** 208-218.

AOBA, T., FUKAE, M., TANABE, T., SHIMIZU, M. & MORENO, E. 1987. Selective adsorption of porcine-amelogenins onto hydroxyapatite and their inhibitory activity on hydroxyapatite growth in supersaturated solutions. *Calcified tissue international,* 41**,** 281-289.

AOBA, T. & MORENO, E. 1990. Changes in the nature and composition of enamel mineral during procine amelogenesis. *Calcified tissue international,* 47**,** 356-364.

APPLEBAUM, E. 1943. Grenz ray studies of enamel matrix formation and calcification. *Journal of dental research,* 22**,** 7-11.

ARIMA, M. & MATSUMOTO, K. 1993. Effects of ArF: Excimer laser irradiation on human enamel and dentin. *Lasers in surgery and medicine,* 13**,** 97-105.

ASAIZUMI, M., UESUGI, K., HOSHINO, M., KATO, T., MACKEY, A. C. & KARLINSEY, R. L. 2014. In vitro assessments of white-spot lesions treated with NaF plus tricalcium phosphate (TCP) toothpastes using synchrotron radiation micro computed tomography (SR micro-CT). *Journal of Dentistry and Oral Hygiene,* 6**,** 10-21.

AVERY, J. K. 1962. Microradiographic and microhardness studies of developing enamel. *Archives of Oral Biology,* 7, Supplement**,** 245-256.

AVERY, J. K. & CHIEGO, D. J. 2006. *Essentials of oral histology and embryology: a clinical approach*, Mosby Elsevier, St. Louis, Missouri, USA.

AVERY, J. K., VISSER, R. L. & KNAPP, D. E. 1961. The pattern of the mineralization of enamel. *Journal of dental research,* 40**,** 1004-1019.

BAEUERLEIN, E. 2004. *Biomineralization: Progress in Biology, Molecular Biology and Application*, Wiley-VCH, Weinheim, Germany.

BAI, P. & WARSHAWSKY, H. 1985. Morphological studies on the distribution of enamel matrix proteins using routine electron microscopy and freeze-fracture replicas in the rat incisor. *The Anatomical Record,* 212**,** 1-16.

BARTLETT, J. D., GANSS, B., GOLDBERG, M., MORADIAN-OLDAK, J., PAINE, M. L., SNEAD, M. L., WEN, X., WHITE, S. N. & ZHOU, Y. L. 2006. Protein–protein interactions of the developing enamel matrix. *Current topics in developmental biology,* 74**,** 57-115.

BARTLETT, J. D. & SIMMER, J. P. 1999. Proteinases in developing dental enamel. *Critical Reviews in Oral Biology & Medicine,* 10**,** 425-441.

BEAUMONT, J. 2007. *Timelines in teeth: an evaluation of scientific methods used to assess the pattern of human enamel mineralization.* PhD Thesis, University of Bradford, Bradford, UK.

BECKMANN, E. C. 2006. CT scanning the early days. *British Journal of Radiology,* 79**,** 5-8.

BELL, L., BOYDE, A. & JONES, S. 1991. Diagenetic alteration to teeth in situ illustrated by backscattered electron imaging. *Scanning,* 13**,** 173-183.

BENIASH, E., METZLER, R. A., LAM, R. S. & GILBERT, P. 2009. Transient amorphous calcium phosphate in forming enamel. *Journal of structural biology,* 166**,** 133-143.

BENIASH, E., SKOBE, Z. & BARTLETT, J. D. 2006. Formation of the dentino–enamel interface in enamelysin (MMP-20)-deficient mouse incisors. *European journal of oral sciences,* 114**,** 24-29.

BERGMAN, G. & LIND, P. O. 1966. A quantitative microradiographic study of incipient enamel caries. *Journal of dental research,* 45**,** 1477-1484.

BERKOVITZ, B. K., HOLLAND, G. R. & MOXHAM, B. 2002. *Oral anatomy, embryology and histology*, Mosby, Edinburgh, UK.

BERKOVITZ, B. K., MOXHAM, B. J., LINDEN, R. W. & SLOAN, A. J. 2010. *Master Dentistry: Oral Biology*, Churchill Livingstone, Elsevier, London, UK.

BERNICK, S., BAKER, R., RUTHERFORD, R. & WARREN, O. 1952. Electron microscopy of enamel and dentin. *The Journal of the American Dental Association,* 45**,** 689-696.
BESIC, F., KNOWLES, C., KELLER, O. & WIEMANN JR, M. 1970. Detailed electron probe microanalysis of three teeth sections with early enamel caries. *Journal of dental research,* 49**,** 111-118.
BETTS, F., BLUMENTHAL, N. C. & POSNER, A. S. 1981. Bone mineralization. *Journal of crystal growth,* 53**,** 63-73.
BEYNON, A. & WOOD, B. 1987. Patterns and rates of enamel growth in the molar teeth of early hominids. *Nature,* 326**,** 493-496.
BEYNON, A. D., CLAYTON, C. B., ROZZI, F. V. R. & REID, D. J. 1998. Radiographic and histological methodologies in estimating the chronology of crown development in modern humans and great apes: a review, with some applications for studies on juvenile hominids. *Journal of Human Evolution,* 35**,** 351-370.
BOSKEY, A. L. 1998. Biomineralization: conflicts, challenges, and opportunities. *Journal of cellular biochemistry,* 72**,** 83-91.
BOYDE, A. 1964. *The structure and development of mammalian enamel.* PhD Thesis, University of London, London, UK.
BOYDE, A. 1986. Applications of Tandem Scanning Reflected Light Microscopy and Three-Dimensional Imaginga. *Annals of the New York Academy of Sciences,* 483**,** 428-439.
BOYDE, A. 1987. A 3-D model of enamel development at the scale of one inch to the micron. *Advances in dental research,* 1**,** 135-140.
BOYDE, A. 1989. Enamel. *Teeth. Handbook of Microscopic Anatomy (Continuation of Handbuch der mikroskopischen Anatomie des Menschen).* Springer, Berlin, Germany.
BOYDE, A. 1990. Physical effects of clinical procedures on the hard dental tissues. *The Dentition and Dental Care,(Edited by Elderton R.J.)* Butterworth-Heinemann,Oxford, UK.
BOYDE, A. 1997. Microstructure of enamel. *Dental enamel (Ciba Foundation Symposium).* John Wiley & Sons, West Sussex, UK.
BOYDE, A. 1998. Cross-Striations Revisited: Backscattered Electron Imaging of Human and Equine Enamel Mineralisation. *Connective Tissue Research,* 38**,** 43-43.
BOYDE, A. & FORTELIUS, M. 1986. Development, structure and function of rhinoceros enamel. *Zoological Journal of the Linnean Society,* 87**,** 181-214.
BOYDE, A. & JONES, S. J. 1983. Backscattered electron imaging of dental tissues. *Anatomy and embryology,* 168**,** 211-226.
BOYDE, A. & STEWART, A. 1963. Scanning electron microscopy of the surface of developing mammalian dental enamel. *Nature,* 198**,** 1102-1103.
BOYES, E. 2000. On low voltage scanning electron microscopy and chemical microanalysis. *Microscopy and Microanalysis,* 6**,** 307-316.
BRAGG, W. & BRAGG, W. 1913. The reflection of X-rays by crystals. *Proceedings of the Royal Society of London. Series A,* 88**,** 428-438.
BROKMEIER, H. G. & YI, S. 2017. Textures in Engineering Materials. *Neutrons and Synchrotron Radiation in Engineering Materials Science: From Fundamentals to Applications (Edited by Staron P.,Chreyer, A., Clemens H. and Mayer, S.).* Wiley-VCH, Weinheim, Germany.
BROWN, P. W. & CONSTANTZ, B. 1994. *Hydroxyapatite and related materials*, CRC press, Florida, USA.
BROWN, S., BOUCHENOIRE, L., BOWYER, D., KERVIN, J., LAUNDY, D., LONGFIELD, M., MANNIX, D., PAUL, D., STUNAULT, A. & THOMPSON, P.

2001. The XMaS beamline at ESRF: instrumental developments and high-resolution diffraction studies. *Journal of synchrotron radiation,* 8**,** 1172-1181.
BROWN, W., EIDELMAN, N. & TOMAZIC, B. 1987. Octacalcium phosphate as a precursor in biomineral formation. *Advances in dental research,* 1**,** 306-313.
BROWN, W. E. 1966. Crystal growth of bone mineral. *Clinical orthopaedics and related research,* 44**,** 205-220.
BRUDEVOLD, F., GARDNER, D. E. & SMITH, F. A. 1956. The distribution of fluoride in human enamel. *Journal of Dental Research,* 35**,** 420-429.
BRUDEVOLD, F. & SOREMARK, R. 1967. Chemistry of the mineral phase of enamel. *Structural and chemical organization of teeth (Edited by Mills, A.).* Academic Press, Elsevier, Massachusetts, USA.
BRUDEVOLD, F. & STEADMAN, L. T. 1956a. The distribution of lead in human enamel. *Journal of dental research,* 35**,** 430-437.
BRUDEVOLD, F. & STEADMAN, L. T. 1956b. A study of tin in enamel. *Journal of dental research,* 35**,** 749-752.
CAO, C. Y., MEI, M. L., LI, Q.-L., LO, E. C. M. & CHU, C. H. 2015. Methods for Biomimetic Mineralisation of Human Enamel: A Systematic Review. *Materials,* 8**,** 2873-2886.
CARLSTROM, D. 1955. X-ray crystallographic studies on apatites and calcified structures. *Acta radiologica. Supplementum,* 121**,** 1.
CARLSTRÖM, D. 1964. Polarization microscopy of dental enamel with reference to incipient carious lesions. *Advances in oral biology,* 1**,** 255.
CARNEIRO, K. M., ZHAI, H., ZHU, L., HORST, J. A., SITLIN, M., NGUYEN, M., WAGNER, M., SIMPLICIANO, C., MILDER, M. & CHEN, C.-L. 2016. Amyloid-like ribbons of amelogenins in enamel mineralization. *Scientific reports,* 6**,** 23105.
CARTER, J. G. 1990. *Skeletal biomineralization: patterns, processes and evolutionary trends*, Wiley Online Library.
CARTMELL, S., HUYNH, K., LIN, A., NAGARAJA, S. & GULDBERG, R. 2004. Quantitative microcomputed tomography analysis of mineralization within three-dimensional scaffolds in vitro. *Journal of Biomedical Materials Research Part A,* 69**,** 97-104.
CATERINA, J. J., SKOBE, Z., SHI, J., DING, Y., SIMMER, J. P., BIRKEDAL-HANSEN, H. & BARTLETT, J. D. 2002. Enamelysin (matrix metalloproteinase 20)-deficient mice display an amelogenesis imperfecta phenotype. *Journal of Biological Chemistry,* 277**,** 49598-49604.
CHASE, S. W. 1927. The enamel prisms and the interprismatic substance. *The Anatomical Record,* 36**,** 239-258.
CIERNIAK, R. 2011. *X-Ray computed tomography in biomedical engineering*, Springer-Verlag London Ltd., London, UK.
COLAÇO, M., BARROSO, R., PORTO, I., GERLACH, R., COSTA, F., BRAZ, D., DROPPA, R. & DE SOUSA, F. 2012. Synchrotron X-ray diffraction characterization of healthy and fluorotic human dental enamel. *Radiation Physics and Chemistry,* 81**,** 1578-1585.
COLE, D., SHALLENBERGER, J., NOVAK, S., MOORE, R., EDGELL, M., SMITH, S., HITZMAN, C., KIRCHHOFF, J., PRINCIPE, E. & NIEVEEN, W. 2000. SiO2 thickness determination by x-ray photoelectron spectroscopy, Auger electron spectroscopy, secondary ion mass spectrometry, Rutherford backscattering, transmission electron microscopy, and ellipsometry. *Journal of Vacuum Science & Technology B: Microelectronics and Nanometer Structures Processing, Measurement, and Phenomena,* 18**,** 440-444.

CORMACK, A. M. 1963. Representation of a function by its line integrals, with some radiological applications. *Journal of applied physics,* 34**,** 2722-2727.
CORMACK, A. M. 1964. Representation of a function by its line integrals, with some radiological applications. II. *Journal of Applied Physics,* 35**,** 2908-2913.
COX, B. N. 2013. How the tooth got its stripes: patterning via strain-cued motility. *Journal of The Royal Society Interface,* 10**,** 20130266.
CRABB, H. & DARLING, A. 1960. The gradient of mineralization in developing enamel. *Archives of oral biology,* 2**,** 308-318.
CRAIG, R. & PEYTON, F. 1958. The microhardness of enamel and dentin. *Journal of Dental Research,* 37**,** 661-668.
CRAIG, R. G., PEYTON, F. A. & JOHNSON, D. W. 1961. Compressive Properties of Enamel, Dental Cements, and Gold. *Journal of Dental Research,* 40**,** 936-945.
CULLITY, B. 1978. *Elements of X-ray Diffraction*, Addison-Wesley.
CUY, J. L., MANN, A. B., LIVI, K. J., TEAFORD, M. F. & WEIHS, T. P. 2002. Nanoindentation mapping of the mechanical properties of human molar tooth enamel. *Archives of Oral Biology,* 47**,** 281-291.
DACULSI, G., BOULER, J.-M. & LEGEROS, R. 1997. Adaptive crystal formation in normal and pathological calcifications in synthetic calcium phosphate and related biomaterials. *International review of cytology,* 172**,** 129-191.
DACULSI, G., MENANTEAU, J., KEREBEL, L. & MITRE, D. 1984. Length and shape of enamel crystals. *Calcified tissue international,* 36**,** 550-555.
DAMEN, J., EXTERKATE, R. & TEN CATE, J. 1997. Reproducibility of TMR for the determination of longitudinal mineral changes in dental hard tissues. *Advances in dental research,* 11**,** 415-419.
DARLING, A., I, 1958. Studies of the early lesion of enamel caries. Its nature, mode of spread, and points of entry. *British Dental Journal,* 105**,** 119-135.
DAVIS, G. & ELLIOTT, J. 2003. High definition X-ray microtomography using a conventional impact X-ray source. *Journal de Physique IV,* 104**,** 131-134.
DAVIS, G. R. & ELLIOTT, J. C. 1997. X-ray microtomography scanner using time-delay integration for elimination of ring artefacts in the reconstructed image. *Nuclear Instruments and Methods in Physics Research Section A,* 394**,** 157-162.
DAVIS, G. R., EVERSHED, A. N. Z. & MILLS, D. 2013. Quantitative high contrast X-ray microtomography for dental research. *Journal of Dentistry,* 41**,** 475-482.
DAVIS, G. R. & WONG, F. S. 1996. X-ray microtomography of bones and teeth. *Physiological measurement,* 17**,** 121.
DEAKINS, M. 1942. Changes in the ash, water, and organic content of pig enamel during calcification. *Journal of Dental Research,* 21**,** 429-435.
DEAKINS, M. & VOLKER, J. 1941. Amount of organic matter in enamel from several types of human teeth. *Journal of Dental Research,* 20**,** 117-121.
DESHPANDE, A. S., FANG, P.-A., SIMMER, J. P., MARGOLIS, H. C. & BENIASH, E. 2010. Amelogenin-collagen interactions regulate calcium phosphate mineralization in vitro. *Journal of Biological Chemistry,* 285**,** 19277-19287.
DEUTSCH, D. & GEDALIA, I. 1980. Chemically distinct stages in developing human fetal enamel. *Archives of oral biology,* 25**,** 635-639.
DEUTSCH, D., LEISER, Y., SHAY, B., FERMON, E., TAYLOR, A., ROSENFELD, E., DAFNI, L., CHARUVI, K., COHEN, Y. & HAZE, A. 2002. The human tuftelin gene and the expression of tuftelin in mineralizing and nonmineralizing tissues. *Connective tissue research,* 43**,** 425-434.
DEYHLE, H. 2014. *Micro-and Nanostructure of Human Teeth: A Synchrotron Radiation-based X-ray Study.* PhD Thesis, University of Basel, Basel, Switzerland.

DEYHLE, H., BUNK, O., BUSER, S., KRASTL, G., ZITZMANN, N. U., ILGENSTEIN, B., BECKMANN, F., PFEIFFER, F., WEIGER, R. & MÜLLER, B. Bio-inspired dental fillings. Society of Photo-Optical Instrumentation Engineers (SPIE) NanoScience+ Engineering, San Diego, California, USA, 2009. 74010E1-74010E11.
DEYHLE, H., BUNK, O. & MULLER, B. 2011. Nanostructure of healthy and caries-affected human teeth. *Nanomedicine,* 7**,** 694-701.
DEYHLE, H., WHITE, S. N., BUNK, O., BECKMANN, F. & MÜLLER, B. 2014. Nanostructure of carious tooth enamel lesion. *Acta Biomaterialia,* 10**,** 355-364.
DIAMOND, M. & WEINMANN, J. P. 1940. The enamel of human teeth. *Columbia Dent. Rev.,* 11**,** 918-921.
DIEKWISCH, T. G., BERMAN, B. J., GENTNER, S. & SLAVKIN, H. C. 1995. Initial enamel crystals are not spatially associated with mineralized dentine. *Cell and tissue research,* 279**,** 149-167.
DOROZHKIN, S. V. 2007. Calcium orthophosphates. *Journal of materials science,* 42**,** 1061-1095.
DOROZHKIN, S. V. 2009. Calcium orthophosphates in nature, biology and medicine. *Materials,* 2**,** 399-498.
DOWKER, S., ANDERSON, P., ELLIOTT, J. & GAO, X. 1999. Crystal chemistry and dissolution of calcium phosphate in dental enamel. *Mineralogical Magazine,* 63**,** 791-791.
DOWKER, S., ELLIOTT, J., DAVIS, G. & WASSIF, H. 2003. Longitudinal study of the three-dimensional development of subsurface enamel lesions during *in vitro* demineralisation. *Caries research,* 37**,** 237-245.
DOWKER, S., ELLIOTT, J., DAVIS, G., WILSON, R. & CLOETENS, P. 2004. Synchrotron x-ray microtomographic investigation of mineral concentrations at micrometre scale in sound and carious enamel. *Caries research,* 38**,** 514-522.
DOWKER, S. E., DAVIS, G. R., ELLIOTT, J. C. & WONG, F. S. 1997. X-ray microtomography: 3-dimensional imaging of teeth for computer-assisted learning. *European Journal of Dental Education,* 1**,** 61-65.
DU, C., FALINI, G., FERMANI, S., ABBOTT, C. & MORADIAN-OLDAK, J. 2005. Supramolecular assembly of amelogenin nanospheres into birefringent microribbons. *Science,* 307**,** 1450-1454.
DUKE, P. J. 2000. *Synchrotron Radiation: Production and Properties*, Oxford University Press Inc., New York, USA.
DUMONT, E. R. 1995. Mammalian enamel prism patterns and enamel deposition rates. *Scanning Microscopy,* 9**,** 429-442.
DUVERGER, O., BENIASH, E. & MORASSO, M. I. 2016. Keratins as components of the enamel organic matrix. *Matrix Biology,* 52**,** 260-265.
DUVERGER, O., OHARA, T., SHAFFER, J. R., DONAHUE, D., ZERFAS, P., DULLNIG, A., CRECELIUS, C., BENIASH, E., MARAZITA, M. L. & MORASSO, M. I. 2014. Hair keratin mutations in tooth enamel increase dental decay risk. *The Journal of clinical investigation,* 124**,** 5219-5224.
EASTOE, J. 1963. The amino acid composition of proteins from the oral tissues—II: The matrix proteins in dentine and enamel from developing human deciduous teeth. *Archives of Oral Biology,* 8**,** 633-652.
EASTOE, J. 1965. The chemical composition of bone and tooth. *Advances in Fluorine Research and Dental Caries Prevention,* 21**,** 5.
EASTOE, J. 1979. Enamel protein chemistry - past, present and future. *Journal of Dental Research,* 58**,** 753-764.

EFEOGLU, N., WOOD, D. & EFEOGLU, C. 2005. Microcomputerised tomography evaluation of 10% carbamide peroxide applied to enamel. *Journal of dentistry,* 33**,** 561-567.
EFEOGLU, N., WOOD, D. J. & EFEOGLU, C. 2007. Thirty-five percent carbamide peroxide application causes *in vitro* demineralization of enamel. *Dental Materials,* 23**,** 900-904.
EGAN, C. K., JACQUES, S. D., DI MICHIEL, M., CAI, B., ZANDBERGEN, M. W., LEE, P. D., BEALE, A. M. & CERNIK, R. J. 2013. Non-invasive imaging of the crystalline structure within a human tooth. *Acta biomaterialia,* 9**,** 8337-8345.
ELDER, F., GUREWITSCH, A., LANGMUIR, R. & POLLOCK, H. 1947. Radiation from electrons in a synchrotron. *Physical Review,* 71**,** 829.
ELLIOTT, J. 1965. The interpretation of the infrared absorption spectra of some carbonate-containing apatites. *Tooth enamel: Its composition, properties, and fundamental structure (Edited by Stack M.V. and Fearnhead R.W.).* John Wright, Bristol, UK.
ELLIOTT, J., ANDERSON, P., BOAKES, R. & DOVER, S. 1989. Scanning X-ray microradiography and microtomography of calcified tissues. *Calcified Tissues***,** 41-63.
ELLIOTT, J., ANDERSON, P., GAO, X., WONG, F., DAVIS, G. & DOWKER, S. 1994. Application of scanning microradiography and X-ray microtomography to studies of bones and teeth. *Journal of X-ray Science and Technology,* 4**,** 102-117.
ELLIOTT, J., BOLLET-QUIVOGNE, F., ANDERSON, P., DOWKER, S., WILSON, R. & DAVIS, G. 2005. Acidic demineralization of apatites studied by scanning X-ray microradiography and microtomography. *Mineralogical Magazine,* 69**,** 643-652.
ELLIOTT, J. & DOVER, S. 1982. X-ray microtomography. *Journal of microscopy,* 126**,** 211-213.
ELLIOTT, J., HOLCOMB, D. & YOUNG, R. 1985. Infrared determination of the degree of substitution of hydroxyl by carbonate ions in human dental enamel. *Calcified tissue international,* 37**,** 372-375.
ELLIOTT, J., WONG, F., ANDERSON, P., DAVIS, G. & DOWKER, S. 1998. Determination of mineral concentration in dental enamel from X-ray attenuation measurements. *Connective tissue research,* 38**,** 61-72.
ELLIOTT, J. C. 1964. *The crystallographic structure of dental enamel and related apatites.* PhD Thesis, University of London, London, UK.
ELLIOTT, J. C. 1994. *Structure and chemistry of the apatites and other calcium orthophosphates*, Elsevier, Amsterdam, The Netherlands.
ELLIOTT, J. C. 1997. Structure, crystal chemistry and density of enamel apatites. *Dental Enamel (Ciba Foundation Symposium).* 1997/01/01 ed.: John Wiley & Sons Ltd., West Sussex, UK.
ELLIOTT, J. C., MACKIE, P. & YOUNG, R. 1973. Monoclinic hydroxyapatite. *Science,* 180**,** 1055-1057.
ENGFELDT, B. & HAMMARLUND-ESSLER, E. 1956. Studies on mineralized denial tissues.: IX. A microradiographic study of the mineralization of developing enamel. *Acta Odontologica Scandinavica,* 14**,** 273-289.
EVERSHED, A. N., MILLS, D. & DAVIS, G. Multi-species beam hardening calibration device for X-ray microtomography. SPIE Optical Engineering+ Applications, 2012. International Society for Optics and Photonics, 85061N-85061N-12.
FANG, P.-A., CONWAY, J. F., MARGOLIS, H. C., SIMMER, J. P. & BENIASH, E. 2011. Hierarchical self-assembly of amelogenin and the regulation of biomineralization at the nanoscale. *Proceedings of the National Academy of Sciences,* 108**,** 14097-14102.

FEARNE, J., ANDERSON, P. & DAVIS, G. R. 2004. 3D X-ray microscopic study of the extent of variations in enamel density in first permanent molars with idiopathic enamel hypomineralisation. *British Dental Journal,* 196**,** 634-638.
FEARNE, J., ELLIOTT, J., WONG, F., DAVIS, G., BOYDE, A. & JONES, S. 1994. Deciduous enamel defects in low-birth-weight children: correlated X-ray microtomographic and backscattered electron imaging study of hypoplasia and hypomineralization. *Anatomy and embryology,* 189**,** 375-381.
FELDKAMP, L., DAVIS, L. & KRESS, J. 1984. Practical cone-beam algorithm. *Optical Society of America,* 1**,** 612-619.
FELDKAMP, L. A., GOLDSTEIN, S. A., PARFITT, M. A., JESION, G. & KLEEREKOPER, M. 1989. The direct examination of three-dimensional bone architecture in vitro by computed tomography. *Journal of bone and mineral research,* 4**,** 3-11.
FINCHAM, A., MORADIAN-OLDAK, J., SIMMER, J., SARTE, P., LAU, E., DIEKWISCH, T. & SLAVKIN, H. 1994. Self-assembly of a recombinant amelogenin protein generates supramolecular structures. *Journal of structural biology,* 112**,** 103-109.
FINCHAM, A. G., BESSEM, C. C., BRINGAS, P., JR., HU, Y. Y., SNEAD, M. L. & SLAVKIN, H. C. 1989. Amelogenesis in vitro: a model for studies of epithelial postsecretory processing during tissue-specific extracellular matrix biomineralization. *Differentiation,* 41**,** 62-71.
FINCHAM, A. G., LAU, E. C., SIMMER, J. & ZEICHNERDAVID, M. 1992. Amelogenin Biochemistry - Form and Function. *Chemistry and Biology of Mineralized Tissues (Edited by Slavkin, H. and Price, P.).* Elsevier, Amsterdam, The Netherlands.
FINCHAM, A. G., MORADIAN-OLDAK, J. & SIMMER, J. P. 1999. The structural biology of the developing dental enamel matrix. *Journal of Structural Biology,* 126**,** 270-299.
FINCHAM, A. G., MORADIANOLDAK, J., DIEKWISCH, T. G. H., LYARUU, D. M., WRIGHT, J. T., BRINGAS, P. & SLAVKIN, H. C. 1995. Evidence for amelogenin nanospheres as functional components of secretory-stage enamel matrix. *Journal of Structural Biology,* 115**,** 50-59.
FINCHAM, A. G. & SIMMER, J. P. 1997. Amelogenin proteins of developing dental enamel. *Dentl enamel (Ciba Foundation Symposium).* John Wiley & Sons Ltd., West Sussex, UK.
FINKE, M., JANDT, K. D. & PARKER, D. M. 2000. The early stages of native enamel dissolution studied with atomic force microscopy. *Journal of Colloid and Interface Science,* 232**,** 156-164.
FRANK, R., CAPITANT, M. & GONI, J. 1966. Electron probe studies of human enamel. *Journal of Dental Research,* 45**,** 672-682.
FRANK, R. M. 1979. Tooth enamel: current state of the art. *Journal of dental research,* 58**,** 684-694.
FRAZIER, P. D. 1968. Adult human enamel: an electron microscopic study of crystallite size and morphology. *Journal of ultrastructure research,* 22**,** 1-11.
FREILICH, M., SHAFER, D., WEI, M., KOMPALLI, R., ADAMS, D. & KUHN, L. 2009. Implant system for guiding a new layer of bone. Computed microtomography and histomorphometric analysis in the rabbit mandible. *Clinical oral implants research,* 20**,** 201-207.
FRIDDLE, R. W., BATTLE, K., TRUBETSKOY, V., TAO, J., SALTER, E. A., MORADIAN-OLDAK, J., DE YOREO, J. J. & WIERZBICKI, A. 2011. Single-Molecule Determination of the Face-Specific Adsorption of Amelogenin's C-

Terminus on Hydroxyapatite. *Angewandte Chemie International Edition,* 50**,** 7541-7545.
FUJIMOTO, J. G., PITRIS, C., BOPPART, S. A. & BREZINSKI, M. E. 2000. Optical coherence tomography: an emerging technology for biomedical imaging and optical biopsy. *Neoplasia,* 2**,** 9-25.
FUKUMOTO, S., KIBA, T., HALL, B., IEHARA, N., NAKAMURA, T., LONGENECKER, G., KREBSBACH, P. H., NANCI, A., KULKARNI, A. B. & YAMADA, Y. 2004. Ameloblastin is a cell adhesion molecule required for maintaining the differentiation state of ameloblasts. *The Journal of Cell Biology,* 167**,** 973-983.
GAISER, S., DEYHLE, H., BUNK, O., WHITE, S. N. & MÜLLER, B. 2012. Understanding nano-anatomy of healthy and carious human teeth: a prerequisite for nanodentistry. *Biointerphases,* 7**,** 4.
GAO, X. J., ELLIOTT, J. C., ANDERSON, P. & DAVIS, G. R. 1993. Scanning microradiographic and microtomographic studies of remineralisation of subsurface enamel lesions. *Journal of the Chemical Society,* 89**,** 2907-2912.
GARNETT, J. & DIEPPE, P. 1990. The effects of serum and human albumin on calcium hydroxyapatite crystal growth. *Biochemical Journal,* 266**,** 863.
GAROT, E., ROUAS, P., D'INCAU, E., LENOIR, N., MANTON, D. & COUTURE-VESCHAMBRE, C. 2016. Mineral density of hypomineralised and sound enamel. *Bulletin du Groupement International pour la Recherche Scientifique en Stomatologie et Odontologie,* 53**,** e33-e36.
GIBSON, C. W., GOLUB, E., DING, W., SHIMOKAWA, H., YOUNG, M., TERMINE, J. & ROSENBLOOM, J. 1991. Identification of the leucine-rich amelogenin peptide (LRAP) as the translation product of an alternatively spliced transcript. *Biochemical and biophysical research communications,* 174**,** 1306-1312.
GLAS, J.-E. 1960. Studies on the ultrastructure of dental enamel-I: Size and shape of the apatite crystallites as deduced from X-ray diffraction data. *Journal of ultrastructure research,* 3**,** 334-344.
GLAS, J.-E. 1962. Studies on the ultrastructure of dental enamel-II: The orientation of the apatite crystallites as deduced from X-ray diffraction. *Archives of oral biology,* 7**,** 91-104.
GLIMCHER, M. J., DANIEL, E. J., TRAVIS, D. F. & KAMHI, S. 1965. Electron optical and X-ray diffraction studies of the organization of the inorganic crystals in embryonic bovine enamel. *Journal of ultrastructure research,* 12**,** 1-77.
GOLDBERG, M. & SEPTIER, D. 2002. Phospholipids in amelogenesis and dentinogenesis. *Critical Reviews in Oral Biology & Medicine,* 13**,** 276-290.
GOLDBERG, M., SEPTIER, D., LECOLLE, S., CHARDIN, H., QUINTANA, M. A., ACEVEDO, A. C., GAFNI, G., DILLOUYA, D., VERMELIN, L., THONEMANN, B., SCHMALZ, G., BISSILAMAPAHOU, P. & CARREAU, J. P. 1995. Dental mineralization. *International Journal of Developmental Biology,* 39**,** 93-110.
GOLDBERG, M., SEPTIER, D., RAPOPORT, O., IOZZO, R., YOUNG, M. & AMEYE, L. 2005. Targeted disruption of two small leucine-rich proteoglycans, biglycan and decorin, excerpts divergent effects on enamel and dentin formation. *Calcified tissue international,* 77**,** 297-310.
GOLDMAN, L. W. 2007. Principles of CT and CT technology. *Journal of Nuclear Medicine Technology,* 35**,** 115-128.
GÖTZ, H., DUSCHNER, H., WHITE, D. J. & KLUKOWSKA, M. A. 2007. Effects of elevated hydrogen peroxide 'strip'bleaching on surface and subsurface enamel including subsurface histomorphology, micro-chemical composition and fluorescence changes. *Journal of dentistry,* 35**,** 457-466.

GOWER, L. B. 2008. Biomimetic model systems for investigating the amorphous precursor pathway and its role in biomineralization. *Chemical reviews,* 108**,** 4551-4627.
GRANGEAT, P. 2009. *Tomography*, ISTE Ltd. and John Wiley & Sons Inc., London, UK.
GRYNPAS, M. D. & OMELON, S. 2007. Transient precursor strategy or very small biological apatite crystals? *Bone,* 41**,** 162-164.
GWINNETT, A. 1966. The ultrastructure of the "prismless" enamel of deciduous teeth. *Archives of oral biology,* 11**,** 1109-1115.
GWINNETT, A. 1967. The ultrastructure of the "prismless" enamel of permanent human teeth. *Archives of Oral Biology,* 12**,** 381-387.
HABELITZ, S. 2015. Materials engineering by Ameloblasts. *Journal of dental research,* 94**,** 759-767.
HADJIMARKOS, D. & BONHORST, C. W. 1959. The selenium content of human teeth. *Oral Surgery, Oral Medicine, Oral Pathology,* 12**,** 113-116.
HALS, E. 1953. Fluorescence microscopy of developing and adult teeth, supplemented by investigations with ordinary, polarizing and phase-contrast microscope. *Odontologisk Tidskrift,* 61**,** 1-130.
HAMBA, H., NIKAIDO, T., SADR, A., NAKASHIMA, S. & TAGAMI, J. 2012. Enamel lesion parameter correlations between polychromatic micro-CT and TMR. *Journal of dental research,* 91**,** 586-591.
HAMMERSLEY, A. 1997. FIT2D: an introduction and overview. *European Synchrotron Radiation Facility Internal Report ESRF97HA02T,* 68**,** 58.
HARDWICK, J. & MARTIN, C. 1967. A pilot study using mass spectrometry for the estimation of the trace element content of dental tissues. *Helvetica odontologica acta,* 11**,** 62.
HE, B. B. 2009. *Two-dimensional X-ray diffraction*, John Wiley & Sons.
HE, B. B. & SMITH, K. L. 1997. Strain and stress measurements with a two-dimensional detector. *Advances in X-ray Analysis,* 41**,** 501-508.
HE, X., WU, S., MARTINEZ-AVILA, O., CHENG, Y. & HABELITZ, S. 2011. Self-aligning amelogenin nanoribbons in oil–water system. *Journal of structural biology,* 174**,** 203-212.
HEINZ, A., LOWENSTAM; STEPHEN, WEINER 1989. *On Biomineralization*, Oxford University Press, New York, USA.
HEMAE, K. M. 1967. Masticatory function in the mammals. *Journal of dental research,* 46**,** 883-893.
HEMONNOT, C. Y. & KÖSTER, S. 2017. Imaging of Biological Materials and Cells by X-Ray Scattering and Diffraction. *American Chemical Society Nano,* 11**,** 8542-8559.
HENDRICKS, S. & HILL, W. 1950. The nature of bone and phosphate rock. *Proceedings of the National Academy of Sciences,* 36**,** 731-737.
HENDRIKSZ, C. J., AL-JAWAD, M., BERGER, K. I., HAWLEY, S. M., LAWRENCE, R., MC ARDLE, C., SUMMERS, C. G., WRIGHT, E. & BRAUNLIN, E. 2013. Clinical overview and treatment options for non-skeletal manifestations of mucopolysaccharidosis type IVA. *Journal of Inherited Metabolic Disease,* 36**,** 309-322.
HILLER, C. R., ROBINSON, C. & WEATHERELL, J. A. 1975. Variations in the composition of developing rat incisor enamel. *Calcified Tissue International,* 18**,** 1-12.
HIRAI, G. 1971. Relative solubility of prism components as observed with the scanning electron microscope. *Tooth enamel II (Edited by Fearhead R. W. and Stack M. V.)* John Wright, Bristol, UK.

HIROTA, F. 1982. Prism arrangement in human cusp enamel deduced by X-ray diffraction. *Archives of oral biology,* 27**,** 931-937.
HIROTA, F. 1986. An explanation for the" two fiber axes" problem in human enamel by X-ray diffraction. *Journal of dental research,* 65**,** 978-981.
HIROTA, F. 1989. X-ray crystallographic studies as to the calcification in the Hunter-Schreger bands of human enamel. *Japanese Journal of Oral Biology,* 31**,** 385-391.
HOFMANN, A. 2004. *The physics of synchrotron radiation*, Cambridge University Press, New York, USA.
HOLCROFT, J. & GANSS, B. 2011. Identification of Amelotin-and ODAM-interacting enamel matrix proteins using the yeast two-hybrid system. *European journal of oral sciences,* 119**,** 301-306.
HOLLISTER, S. J., LIN, C., SAITO, E., SCHEK, R., TABOAS, J., WILLIAMS, J., PARTEE, B., FLANAGAN, C., DIGGS, A. & WILKE, E. 2005. Engineering craniofacial scaffolds. *Orthodontics & craniofacial research,* 8**,** 162-173.
HOPPE, K. A., KOCH, P. L. & FURUTANI, T. 2003. Assessing the preservation of biogenic strontium in fossil bones and tooth enamel. *International Journal of Osteoarchaeology,* 13**,** 20-28.
HOUNSFIELD, G. N. 1973. Computerized transverse axial scanning (tomography): Part 1. Description of system. *British Journal of Radiology,* 46**,** 1016-1022.
HU, C.-C., FUKAE, M., UCHIDA, T., QIAN, Q., ZHANG, C. H., RYU, O. H., TANABE, T., YAMAKOSHI, Y., MURAKAMI, C., DOHI, N., SHIMIZU, M. & SIMMER, J. P. 1997. Cloning and Characterization of Porcine Enamelin mRNAs. *Journal of Dental Research,* 76**,** 1720-1729.
HU, J. C.-C., HU, Y., SMITH, C. E., MCKEE, M. D., WRIGHT, J. T., YAMAKOSHI, Y., PAPAGERAKIS, P., HUNTER, G. K., FENG, J. Q. & YAMAKOSHI, F. 2008. Enamel defects and ameloblast-specific expression in Enam knock-out/lacz knock-in mice. *Journal of Biological Chemistry,* 283**,** 10858-10871.
HU, J. C. C., SUN, X., ZHANG, C., LIU, S., BARTLETT, J. D. & SIMMER, J. P. 2002. Enamelysin and kallikrein-4 mRNA expression in developing mouse molars. *European journal of oral sciences,* 110**,** 307-315.
HUANG, T. T., JONES, A. S., HE, L. H., DARENDELILER, M. A. & SWAIN, M. V. 2007. Characterisation of enamel white spot lesions using X-ray micro-tomography. *Journal of dentistry,* 35**,** 737-743.
HUBBARD, M. J. 2000. Calcium transport across the dental enamel epithelium. *Critical Reviews in Oral Biology & Medicine,* 11**,** 437-466.
HULL, A. 1919. A new method of chemical analysis. *Journal of the American Chemical Society,* 41**,** 1168-1175.
IWASAKI, K., BAJENOVA, E., SOMOGYI-GANSS, E., MILLER, M., NGUYEN, V., NOURKEYHANI, H., GAO, Y., WENDEL, M. & GANSS, B. 2005. Amelotin—a novel secreted, ameloblast-specific protein. *Journal of dental research,* 84**,** 1127-1132.
JODAIKIN, A., WEINER, S. & TRAUB, W. 1984. Enamel rod relations in the developing rat incisor. *Journal of ultrastructure research,* 89**,** 324-332.
JOHNSON, Q. C., KINNEY, J. H., BONSE, U., NICHOLS, M. C., NUSSHARDT, R. & BRASE, J. M. Micro-tomography using synchrotron radiation. MRS Proceedings, 1986. Cambridge Univ Press, 203.
JONGEBLOED, W., MOLENAAR, I. & ARENDS, J. 1975. Morphology and size-distribution of sound and acid-treated enamel crystallites. *Calcified tissue research,* 19**,** 109-123.

JOSEPHSEN, K. & FEJERSKOV, O. 1977. Ameloblast modulation in the maturation zone of the rat incisor enamel organ. A light and electron microscopic study. *Journal of anatomy,* 124**,** 45.
JOSEPHSEN, K., TAKANO, Y., FRISCHE, S., PRAETORIUS, J., NIELSEN, S., AOBA, T. & FEJERSKOV, O. 2010. Ion transporters in secretory and cyclically modulating ameloblasts: a new hypothesis for cellular control of preeruptive enamel maturation. *American Journal of Physiology-Cell Physiology,* 299**,** C1299-C1307.
KALLENBACH, E. 1973. The fine structure of Tomes' process of rat incisor ameloblasts and its relationship to the elaboration of enamel. *Tissue and Cell,* 5**,** 501-524.
KALLENBACH, E. 1974. Fine structure of rat incisor ameloblasts in transition between enamel secretion and maturation stages. *Tissue and Cell,* 6**,** 173-190.
KAY, M. I., YOUNG, R. & POSNER, A. 1964. Crystal structure of hydroxyapatite. *Nature,* 204**,** 1050-1052.
KEREBEL, B., DACULSI, G. & KEREBEL, L. 1979. Ultrastructural studies of enamel crystallites. *Journal of dental research,* 58**,** 844-851.
KHAN, M. A., ADDISON, O., JAMES, A., HENDRIKSZ, C. J. & AL-JAWAD, M. 2016. Synchrotron X-ray Diffraction And Scanning Electron Microscopy To Understand Enamel Affected By Metabolic Disorder Mucopolysaccharidosis. *Micron,* 83**,** 48-53.
KIKUCHI, T. 1990. Single crystal orientation measurement by X-ray methods. *The Rigaku Journal,* 7**,** 27-35.
KIM, I., PAIK, K. S. & LEE, S. P. 2007. Quantitative evaluation of the accuracy of micro-computed tomography in tooth measurement. *Clinical Anatomy,* 20**,** 27-34.
KO, A. C.-T., HEWKO, M., SOWA, M. G., DONG, C. C. & CLEGHORN, B. 2008. Early dental caries detection using a fibre-optic coupled polarization-resolved Raman spectroscopic system. *Optics express,* 16**,** 6274-6284.
KODAKA, T., DEBARI, K., YAMADA, M. & KUROIWA, M. 1992. Correlation between microhardness and mineral content in sound human enamel. *Caries research,* 26**,** 139-141.
KOENIGSWALD, W. V., RENSBERGER, J. & PRETZSCHNER, H. 1987. Changes in the tooth enamel of early Paleocene mammals allowing increased diet diversity. *Nature,* 328**,** 150-152.
KRINSLEY, D. H., PYE, K., BOGGS JR, S. & TOVEY, N. K. 2005. *Backscattered scanning electron microscopy and image analysis of sediments and sedimentary rocks*, Cambridge University Press, New York, USA.
KWAK, S., LITMAN, A., MARGOLIS, H., YAMAKOSHI, Y. & SIMMER, J. 2017. Biomimetic Enamel Regeneration Mediated by Leucine-Rich Amelogenin Peptide. *Journal of dental research,* 96**,** 524-530.
LACRUZ, R., SMITH, C., KURTZ, I., HUBBARD, M. & PAINE, M. 2013a. New paradigms on the transport functions of maturation-stage ameloblasts. *Journal of dental research,* 92**,** 122-129.
LACRUZ, R. S. & BROMAGE, T. G. 2006. Appositional enamel growth in molars of South African fossil hominids. *Journal of Anatomy,* 209**,** 13-20.
LACRUZ, R. S., BROOKES, S. J., WEN, X., JIMENEZ, J. M., VIKMAN, S., HU, P., WHITE, S. N., LYNGSTADAAS, S. P., OKAMOTO, C. T. & SMITH, C. E. 2013b. Adaptor protein complex 2–mediated, clathrin-dependent endocytosis, and related gene activities, are a prominent feature during maturation stage amelogenesis. *Journal of Bone and Mineral Research,* 28**,** 672-687.
LACRUZ, R. S., HABELITZ, S., WRIGHT, J. T. & PAINE, M. L. 2017. Dental Enamel Formation and Implications for Oral Health and Disease. *Physiological Reviews,* 97**,** 939-993.

LACRUZ, R. S., HACIA, J. G., BROMAGE, T. G., BOYDE, A., LEI, Y., XU, Y., MILLER, J. D., PAINE, M. L. & SNEAD, M. L. 2012a. The circadian clock modulates enamel development. *Journal of biological rhythms,* 27**,** 237-245.

LACRUZ, R. S., NANCI, A., KURTZ, I., WRIGHT, J. T. & PAINE, M. L. 2010. Regulation of pH during amelogenesis. *Calcified tissue international,* 86**,** 91-103.

LACRUZ, R. S., SMITH, C. E., BRINGAS, P., CHEN, Y. B., SMITH, S. M., SNEAD, M. L., KURTZ, I., HACIA, J. G., HUBBARD, M. J. & PAINE, M. L. 2012b. Identification of novel candidate genes involved in mineralization of dental enamel by genome-wide transcript profiling. *Journal of cellular physiology,* 227**,** 2264-2275.

LANDIS, E. N. & KEANE, D. T. 2010. X-ray microtomography. *Materials characterization,* 61**,** 1305-1316.

LANDIS, W. J., BURKE, G. Y., NEURINGER, J. R., PAINE, M. C., NANCI, A., BAI, P. & WARSHAWSKY, H. 1988. Earliest enamel deposits of the rat incisor examined by electron microscopy, electron diffraction, and electron probe microanalysis. *The Anatomical Record,* 220**,** 233-238.

LE NORCY, E., KWAK, S.-Y., WIEDEMANN-BIDLACK, F., BENIASH, E., YAMAKOSHI, Y., SIMMER, J. & MARGOLIS, H. 2011. Leucine-rich amelogenin peptides regulate mineralization in vitro. *Journal of dental research,* 90**,** 1091-1097.

LEFEVRE, M. L. & MANLY, R. S. 1938. Moisture, Inorganic and Organic Contents of Enamel and Dentin from Carious Teeth. *The Journal of the American Dental Association and The Dental Cosmos,* 25**,** 233-242.

LEGEROS, R., TRAUTZ, O., KLEIN, E. & LEGEROS, J. 1969. Two types of carbonate substitution in the apatite structure. *Cellular and Molecular Life Sciences,* 25**,** 5-7.

LEGEROS, R. Z. 1981. Apatites in biological systems. *Progress in crystal growth and characterization,* 4**,** 1-45.

LI, C. 2018. *Measurement and understanding the residual stress distribution as a function of depth in atmosphere plasma sprayed thermal barrier coatings.* University of Manchester.

LI, Z., MAISOON, A.-J., SIDDIQUI, S. & PASTERIS, J. D. 2015. A mineralogical study in contrasts: highly mineralized whale rostrum and human enamel. *Scientific reports,* 5**,** 1-10.

LIN, C. P., DOUGLAS, W. H. & ERLANDSEN, S. L. 1993. Scanning electron microscopy of type I collagen at the dentin-enamel junction of human teeth. *Journal of Histochemistry & Cytochemistry,* 41**,** 381-388.

LITTLE, M. & BRUDEVOLD, F. 1958. A study of the inorganic carbon dioxide in intact human enamel. *Journal of dental research,* 37**,** 991-1000.

LLANO, E., PENDÁS, A. M., KNÄUPER, V., SORSA, T., SALO, T., SALIDO, E., MURPHY, G., SIMMER, J. P., BARTLETT, J. D. & LÓPEZ-OTÍN, C. 1997. Identification and structural and functional characterization of human enamelysin (MMP-20). *Biochemistry,* 36**,** 15101-15108.

LLOYD, G. E. 1987. Atomic number and crystallographic contrast images with the SEM: a review of backscattered electron techniques. *Mineralogical Magazine,* 51**,** 3-19.

LO, E., ZHI, Q. & ITTHAGARUN, A. 2010. Comparing two quantitative methods for studying remineralization of artificial caries. *Journal of dentistry,* 38**,** 352-359.

LOW, I. M. 2004. Depth-Profiling of Crystal Structure, Texture, and Microhardness in a Functionally Graded Tooth Enamel. *Journal of the American Ceramic Society,* 87**,** 2125-2131.

LOWENSTAM, H. & WEINER, S. 1985. Transformation of amorphous calcium phosphate to crystalline dahllite in the radular teeth of chitons. *Science,* 227**,** 51-54.

LU, Y., PAPAGERAKIS, P., YAMAKOSHI, Y., HU, J. C.-C., BARTLETT, J. D. & SIMMER, J. P. 2008. Functions of KLK4 and MMP-20 in dental enamel formation. *Biological chemistry,* 389**,** 695-700.

LYMAN, C. E., NEWBURY, D. E., GOLDSTEIN, J., WILLIAMS, D. B., ROMIG JR, A. D., ARMSTRONG, J., ECHLIN, P., FIORI, C., JOY, D. C. & LIFSHIN, E. 1990. *Scanning electron microscopy, X-ray microanalysis, and analytical electron microscopy: a laboratory workbook*, Plenum Press, New York, USA.

LYNCH, C. D., O'SULLIVAN, V. R., DOCKERY, P., MCGILLYCUDDY, C. T. & SLOAN, A. J. 2010. Hunter-Schreger Band patterns in human tooth enamel. *Journal of Anatomy,* 217**,** 106-115.

LYON, D. & DARLING, A. 1957. Orientation of the crystallites in human dental enamel. *British dental Journal,* 102**,** 483-488.

MA, G. & LIU, X. Y. 2009. Hydroxyapatite: hexagonal or monoclinic? *Crystal Growth and Design,* 9**,** 2991-2994.

MAAS, M. C. & DUMONT, E. R. 1999. Built to last: the structure, function, and evolution of primate dental enamel. *Evolutionary Anthropology Issues News and Reviews,* 8**,** 133-152.

MACHO, G. A., JIANG, Y. & SPEARS, I. R. 2003. Enamel microstructure—a truly three-dimensional structure. *Journal of Human Evolution,* 45**,** 81-90.

MAGNE, P. 2007. Efficient 3D finite element analysis of dental restorative procedures using micro-CT data. *Dental Materials,* 23**,** 539-548.

MAHONEY, E. K., ROHANIZADEH, R., ISMAIL, F., KILPATRICK, N. & SWAIN, M. 2004. Mechanical properties and microstructure of hypomineralised enamel of permanent teeth. *Biomaterials,* 25**,** 5091-5100.

MAHONEY, P. 2012. Incremental enamel development in modern human deciduous anterior teeth. *American journal of physical anthropology,* 147**,** 637-651.

MANN, S. 2001. *Biomineralization: Principles and Concepts in Bioinorganic Materials Chemistry* Oxford University Press, New York, USA.

MARGARITONDO, G. 2001. The essential features of synchrotron radiation: an elementary approach. *Journal of alloys and compounds,* 328**,** 35-41.

MARGOLIS, H., BENIASH, E. & FOWLER, C. 2006. Role of macromolecular assembly of enamel matrix proteins in enamel formation. *Journal of dental research,* 85**,** 775-793.

MARTINEZ-AVILA, O., WU, S., KIM, S. J., CHENG, Y., KHAN, F., SAMUDRALA, R., SALI, A., HORST, J. A. & HABELITZ, S. 2012. Self-assembly of filamentous amelogenin requires calcium and phosphate: from dimers via nanoribbons to fibrils. *Biomacromolecules,* 13**,** 3494-3502.

MARTINEZ-AVILA, O. M., WU, S., CHENG, Y., LEE, R., KHAN, F. & HABELITZ, S. 2011. Self-assembly of amelogenin proteins at the water–oil interface. *European journal of oral sciences,* 119**,** 75-82.

MECKEL, A., GRIEBSTEIN, W. & NEAL, R. 1965a. Structure of mature human dental enamel as observed by electron microscopy. *Archives of oral biology,* 10**,** 775-783.

MECKEL, A., GRIEBSTEIN, W. & NEAL, R. 1965b. Ultrastructure of fully calcified human dental enamel. *Tooth Enamel (Edited by Stack M.V. and Fearnhead R.W.)* John Wright & Sons, Bristol, UK.

MÉHEUST, Y., KNUDSEN, K. D. & FOSSUM, J. O. 2006. Inferring orientation distributions in anisotropic powders of nano-layered crystallites from a single two-dimensional WAXS image. *Journal of applied crystallography,* 39**,** 661-670.

MEREDITH, N., SHERRIFF, M., SETCHELL, D. J. & SWANSON, S. A. V. 1996. Measurement of the microhardness and young's modulus of human enamel and dentine using an indentation technique. *Archives of Oral Biology,* 41**,** 539-545.

MILLER, W. H. 1839. *A treatise on crystallography*, The Pitt Press for J. & J.J. Deighton, Cambridge, UK.
MISHRA, S., THOMAS, H. F., FEARNE, J. M., BOYDE, A. & ANDERSON, P. 2009. Comparison of demineralisation rates in pre-and postnatal enamel and at the neonatal line. *Archives of oral biology,* 54**,** 101-106.
MORADIAN-OLDAK, J. 2001. Amelogenins: assembly, processing and control of crystal morphology. *Matrix Biology,* 20**,** 293-305.
MORADIAN-OLDAK, J. 2012. Protein-mediated enamel mineralization. *Frontiers in bioscience,* 17**,** 1996-2023.
MORADIAN-OLDAK, J., BOUROPOULOS, N., WANG, L. & GHARAKHANIAN, N. 2002. Analysis of self-assembly and apatite binding properties of amelogenin proteins lacking the hydrophilic C-terminal. *Matrix Biology,* 21**,** 197-205.
MORADIAN-OLDAK, J., LEUNG, W. & FINCHAM, A. G. 1998. Temperature and pH-Dependent Supramolecular Self-Assembly of Amelogenin Molecules: A Dynamic Light-Scattering Analysis. *Journal of Structural Biology,* 122**,** 320-327.
MORADIAN-OLDAK, J., PAINE, M., LEI, Y., FINCHAM, A. & SNEAD, M. 2000. Self-assembly properties of recombinant engineered amelogenin proteins analyzed by dynamic light scattering and atomic force microscopy. *Journal of structural biology,* 131**,** 27-37.
MORADIAN-OLDAK, J. & PAINE, M. L. 2008. Mammalian enamel formation. *Biomineralization: From Nature to Application (Edited by Sigel A., Sigel H. and Sigel R.K.O.).* Wiley & Sons Ltd., West Sussex, UK.
MORADIAN-OLDAK, J., SIMMER, J., LAU, E., SARTE, P., SLAVKIN, H. & FINCHAM, A. 1994. Detection of monodisperse aggregates of a recombinant amelogenin by dynamic light scattering. *Biopolymers,* 34**,** 1339-1347.
MORENO, E. & AOBA, T. 1987. Calcium binding in enamel fluid and driving force for enamel mineralization in the secretory stage of amelogenesis. *Advances in dental research,* 1**,** 245-251.
MURA-GALELLI, M., NARUSAWA, H., SHIMADA, T., IIJIMA, M. & AOBA, T. 1992. Effects of fluoride on precipitation and hydrolysis of octacalcium phosphate in an experimental model simulating enamel mineralization during amelogenesis. *Cells and Materials,* 2**,** 221-230.
MYOUNG, S., LEE, J., CONSTANTINO, P., LUCAS, P., CHAI, H. & LAWN, B. 2009. Morphology and fracture of enamel. *Journal of biomechanics,* 42**,** 1947-1951.
NAKATA, K., NIKAIDO, T., NAKASHIMA, S., NANGO, N. & TAGAMI, J. 2012. An approach to normalizing micro-CT depth profiles of mineral density for monitoring enamel remineralization progress. *Dental Materials Journal,* 31**,** 533-540.
NANCI, A. 2012. *Ten Cate's oral histology: development, structure, and function*, Elsevier Mosby, Missouri, USA.
NAZARI, A., SADR, A., SAGHIRI, M. A., CAMPILLO-FUNOLLET, M., HAMBA, H., SHIMADA, Y., TAGAMI, J. & SUMI, Y. 2013. Non-destructive characterization of voids in six flowable composites using swept-source optical coherence tomography. *Dental Materials,* 29**,** 278-286.
NEUMAN, W. 1980. Bone material and calcification mechanisms. *Fundamental and clinical bone physiology.* Lippincott Williams & Wilkins, Philadelphia, USA.
NEVES, A. D. A., COUTINHO, E., VIVAN CARDOSO, M., JAECQUES, S. V. & VAN MEERBEEK, B. 2010. Micro-CT based quantitative evaluation of caries excavation. *Dental materials : official publication of the Academy of Dental Materials,* 26**,** 579-88.

NG, S., FERGUSON, M., PAYNE, P. & SLATER, P. 1988. Ultrasonic studies of unblemished and artificially demineralized enamel in extracted human teeth: a new method for detecting early caries. *Journal of dentistry,* 16**,** 201-209.
NISHIO, C., WAZEN, R., MOFFATT, P. & NANCI, A. 2013. Expression of odontogenic ameloblast-associated and amelotin proteins in the junctional epithelium. *Periodontology 2000,* 63**,** 59-66.
NIXON, G., SMITH, H. & LIVINGSTON, H. Trace elements in human tooth enamel. Nucl. Activ. Tech. Life Sci., Proc. Symp., Amsterdam, 1967. 455-62.
NORTHROP, R. B. 2001. *Noninvasive instrumentation and measurement in medical diagnosis*, CRC Press, Florida, USA.
OLANDER, B. 1994. Centre of Rotation Determination Using Projection Data in X-ray Micro Computed Tomography. Linköping University, Sweden.
OLEJNICZAK, A. J. & GRINE, F. E. 2006. Assessment of the accuracy of dental enamel thickness measurements using microfocal X-ray computed tomography. *The Anatomical Record Part A: Discoveries in Molecular, Cellular, and Evolutionary Biology,* 288**,** 263-275.
OSBORN, J. 1968a. Directions and interrelationship of prisms in cuspal and cervical enamel of human teeth. *Journal of dental research,* 47**,** 395-402.
OSBORN, J. 1968b. Evaluation of previous assessments of prism directions in human enamel. *Journal of dental research,* 47**,** 217-222.
OSBORN, J. 1970. The mechanism of ameloblast movement: a hypothesis. *Calcified tissue research,* 5**,** 344-359.
OSBORN, J. 1990. A 3-dimensional model to describe the relation between prism directions, parazones and diazones, and the Hunter-Schreger bands in human tooth enamel. *Archives of oral biology,* 35**,** 869-878.
PAINE, M. L. & SNEAD, M. L. 1997. Protein interactions during assembly of the enamel organic extracellular matrix. *Journal of Bone and Mineral Research,* 12**,** 221-227.
PALMER, L. C., NEWCOMB, C. J., KALTZ, S. R., SPOERKE, E. D. & STUPP, S. I. 2008. Biomimetic systems for hydroxyapatite mineralization inspired by bone and enamel. *Chemical reviews,* 108**,** 4754-4783.
PARK, Y.-S., BAE, K.-H., CHANG, J. & SHON, W.-J. 2011. Theory of X-ray microcomputed tomography in dental research: application for the caries research. *Journal of Korean Academy of Conservative Dentistry,* 36**,** 98-107.
PAULUS, M. J., GLEASON, S. S., KENNEL, S. J., HUNSICKER, P. R. & JOHNSON, D. K. 2000. High resolution X-ray computed tomography: an emerging tool for small animal cancer research. *Neoplasia,* 2**,** 62-70.
PEARCE, E. & NELSON, D. 1989. Microstructural features of carious human enamel imaged with back-scattered electrons. *Journal of dental research,* 68**,** 113-118.
PENEL, G., LEROY, G., REY, C. & BRES, E. 1998. MicroRaman Spectral Study of the PO4 and CO3 Vibrational Modes in Synthetic and Biological Apatites. *Calcified Tissue International,* 63**,** 475-481.
PERETZ, B., NEVIS, N. & SMITH, P. 1997. Morphometric variables of developing primary maxillary first molar crowns in humans. *Archives of oral biology,* 42**,** 423-427.
PIEZ, K. 1960. The nature of the protein matrix of human enamel. *Journal of Dental Research,* 39**,** 712.
PIEZ, K. A. 1963. The amino acid chemistry of some calcified tissues. *Annals of the New York Academy of Sciences,* 109**,** 256-268.
POOLE, D. & BROOKS, A. 1961. The arrangement of crystallites in enamel prisms. *Archives of oral biology,* 5**,** 14-26.

POTTS, P. J. 2012. *A handbook of silicate rock analysis*, Springer Science & Business Media, Berlin, Germany.
PROUT, R., ODUTUGA, A. & TRING, F. 1973. Lipid analysis of rat enamel and dentine. *Archives of oral biology,* 18**,** 373-380.
QI, C. & WANG, Y. 2009. Feature-based crystal construction in computer-aided nano-design. *Computer-Aided Design,* 41**,** 792-800.
QUIGLEY, M. B. 1959. Electron microscopy of developing enamel matrix in the Syrian hamster. *Journal of dental research,* 38**,** 180-187.
RASHID, S., LEE, S. Y. & HASAN, M. K. 2012. An improved method for the removal of ring artifacts in high resolution CT imaging. *EURASIP Journal on Advances in Signal Processing,* 2012**,** 1-18.
RAUE, L., GERSDORFF, N., RODIGER, M. & KLEIN, H. 2012. New insights in prism orientation within human enamel. *Archives of Oral Biology,* 57**,** 271-276.
RAUE, L., HARTMANN, C. D., RÖDIGER, M., BÜRGERS, R. & GERSDORFF, N. 2014. Anisotropic local physical properties of human dental enamel in comparison to properties of some common dental filling materials. *Acta Odontologica Scandinavica,* 72**,** 591-596.
RAUE, L. & KLEIN, H. 2010. Location depending textures of the human dental enamel. *Solid State Phenomena,* 160**,** 281-286.
RAUE, L. & KLEIN, H. 2011. Calculation of anisotropic properties of dental enamel from synchrotron data. *Journal of synchrotron radiation,* 18**,** 550-556.
RAVINDRANATH, R. M., DEVARAJAN, A. & BRINGAS, P. 2007. Enamel formation in vitro in mouse molar explants exposed to amelogenin polypeptides: ATMP and LRAP on enamel development. *archives of oral biology,* 52**,** 1161-1171.
RAZEGHI, M. 2009. *Fundamentals of solid state engineering*, Springer, Illinois, USA.
REID, D. J., BEYNON, A. D. & ROZZI, F. V. R. 1998. Histological reconstruction of dental development in four individuals from a medieval site in Picardie, France. *Journal of Human Evolution,* 35**,** 463-477.
REIMERS, W., PYZALLA, A. R., SCHREYER, A. & CLEMENS, H. 2008. *Neutrons and synchrotron radiation in engineering materials science*.
REITH, E. J. & BOYDE, A. 1981. The arrangement of ameloblasts on the surface of maturing enamel of the rat incisor tooth. *Journal of anatomy,* 133**,** 381-388.
RETIEF, D., CLEATON-JONES, P., TURKSTRA, J. & DE WET, W. 1971. The quantitative analysis of sixteen elements in normal human enamel and dentine by neutron activation analysis and high-resolution gamma-spectrometry. *Archives of oral biology,* 16**,** 1257-1267.
REY, C., RENUGOPALAKRISHNAN, V., SHIMIZU, M., COLLINS, B. & GLIMCHER, M. J. 1991. A resolution-enhanced Fourier transform infrared spectroscopic study of the environment of the CO3 2− ion in the mineral phase of enamel during its formation and maturation. *Calcified Tissue International,* 49**,** 259-268.
REYES-GASGA, J., MARTÍNEZ-PIÑEIRO, E. L., RODRÍGUEZ-ÁLVAREZ, G., TIZNADO-OROZCO, G. E., GARCÍA-GARCÍA, R. & BRÈS, E. F. 2013. XRD and FTIR crystallinity indices in sound human tooth enamel and synthetic hydroxyapatite. *Materials Science and Engineering: C,* 33**,** 4568-4574.
REYES-GASGA, J., MARTÍNEZ-PIÑEIRO, E. & BRES, E. 2012. Crystallographic structure of human tooth enamel by electron microscopy and x-ray diffraction: hexagonal or monoclinic? *Journal of microscopy,* 248**,** 102-109.
RHODES, J., FORD, T., LYNCH, J., LIEPINS, P. & CURTIS, R. 1999. Micro-computed tomography: a new tool for experimental endodontology. *International Endodontic Journal,* 32**,** 165-170.

RISNES, S. 1998. Growth tracks in dental enamel. *Journal of Human Evolution,* 35**,** 331-350.
ROBINSON, C. 2014. Enamel maturation: a brief background with implications for some enamel dysplasias. *Frontiers in physiology,* 5.
ROBINSON, C., BROOKES, S. J., BONASS, W. A., SHORE, R. C. & KIRKHAM, J. 1997. Enamel maturation. *Dental Enamel (Ciba Foundation Symposium)*. John Wiley & Sons Ltd., West Sussex, UK.
ROBINSON, C., BROOKES, S. J., SHORE, R. C. & KIRKHAM, J. 1998. The developing enamel matrix: nature and function. *European journal of oral sciences,* 106**,** 282-291.
ROBINSON, C., CONNELL, S., KIRKHAM, J., SHORE, R. & SMITH, A. 2004. Dental enamel - a biological ceramic: regular substructures in enamel hydroxyapatite crystals revealed by atomic force microscopy. *Journal of Materials Chemistry,* 14**,** 2242-2248.
ROBINSON, C., KIRKHAM, J., BROOKES, S. & SHORE, R. 1992. The role of albumin in developing rodent dental enamel: a possible explanation for white spot hypoplasia. *Journal of dental research,* 71**,** 1270-1274.
ROBINSON, C., KIRKHAM, J., BROOKES, S. J., BONASS, W. A. & SHORE, R. C. 1995a. The chemistry of enamel development. *International Journal of Developmental Biology,* 39**,** 145-152.
ROBINSON, C., KIRKHAM, J., BROOKES, S. J. & SHORE, R. C. 1995b. Chemistry of mature enamel. *Dental Enamel: Formation to Destruction (Edited by Robinson C., Kirkham J. and Shore R.C.).* First Edition ed.: CRC Press, New York, USA.
ROBINSON, C., SHORE, R., BROOKES, S., STRAFFORD, S., WOOD, S. & KIRKHAM, J. 2000. The chemistry of enamel caries. *Critical Reviews in Oral Biology & Medicine,* 11**,** 481-495.
ROBINSON, C., WEATHERELL, J. & HALLSWORTH, A. 1971. Variation in composition of dental enamel within thin ground tooth sections. *Caries research,* 5**,** 44-57.
ROBINSON, C., WEATHERELL, J. & HALLSWORTH, A. 1983. Alterations in the composition of permanent human enamel during carious attack. *Demineralisation and remineralisation of the teeth.* IRL Press, Oxford, UK.
RÖNNHOLM, E. 1962a. The amelogenesis of human teeth as revealed by electron microscopy: II. The development of the enamel crystallites. *Journal of Ultrastructure Research,* 6**,** 249-303.
RÖNNHOLM, E. 1962b. An electron microscopic study of the amelogenesis in human teeth: I. The fine structure of the ameloblasts. *Journal of Ultrastructure Research,* 6**,** 229-248.
ROZZI, F. R. 1998. Introduction: Enamel structure and development and its application in hominid evolution and taxonomy. *Journal of human evolution,* 35**,** 327-330.
RYU, O., FINCHAM, A., HU, C.-C., ZHANG, C., QIAN, Q., BARTLETT, J. & SIMMER, J. 1999. Characterization of recombinant pig enamelysin activity and cleavage of recombinant pig and mouse amelogenins. *Journal of dental research,* 78**,** 743-750.
SAGHIRI, M. A., ASGAR, K., LOTFI, M., KARAMIFAR, K., SAGHIRI, A. M., NEELAKANTAN, P., GUTMANN, J. L. & SHEIBANINIA, A. 2012. Back-scattered and secondary electron images of scanning electron microscopy in dentistry: a new method for surface analysis. *Acta Odontologica Scandinavica,* 70**,** 603-609.
SALIDO, E. C., YEN, P. H., KOPRIVNIKAR, K., YU, L. C. & SHAPIRO, L. J. 1992. The human enamel protein gene amelogenin is expressed from both the X and the Y chromosomes. *The American Journal of Human Genetics,* 50**,** 303-316.
SANII, B., MARTINEZ-AVILA, O., SIMPLICIANO, C., ZUCKERMANN, R. & HABELITZ, S. 2014. Matching 4.7-Å XRD Spacing in Amelogenin Nanoribbons and Enamel Matrix. *Journal of dental research,* 93**,** 918-922.

SASAKI, S., TAKAGI, T. & SUZUKI, M. 1991. Cyclical changes in pH in bovine developing enamel as sequential bands. *Archives of oral biology,* 36**,** 227-231.
SASAKI, T. & HIGASHI, S. 1983. Scanning and transmission electron microscopy of developing enamel surfaces in the kitten tooth germs. *Journal of electron microscopy,* 32**,** 163-171.
SAWHNEY, K., DOLBNYA, I., SCOTT, S., TIWARI, M., PREECE, G., ALCOCK, S. & MALANDAIN, A. A double multilayer monochromator for the B16 Test beamline at the Diamond Light Source. Proceedings SPIE Optical Engineering+ Applications, 2011. 8139081-8139088.
SCHICHO, K., KASTNER, J., KLINGESBERGER, R., SEEMANN, R., ENISLIDIS, G., UNDT, G., WANSCHITZ, F., FIGL, M., WAGNER, A. & EWERS, R. 2007. Surface area analysis of dental implants using micro-computed tomography. *Clinical oral implants research,* 18**,** 459-464.
SCHMITZ, J., TEEPE, J., HU, Y., SMITH, C., FAJARDO, R. & CHUN, Y.-H. 2014. Estimating mineral changes in enamel formation by ashing/BSE and microCT. *Journal of dental research,* 93**,** 256-262.
SCHOUR, I. 1936. The Neonatal Line in the Enamel and Dentin of the Human Deciduous Teeth and First Permanent Molar. *The Journal of the American Dental Association,* 23**,** 1946-1955.
SCHOUR, I. & MASSLER, M. 1940a. Studies in tooth development: the growth pattern of human teeth. *The Journal of the American Dental Association,* 27**,** 1778-1793.
SCHOUR, I. & MASSLER, M. 1940b. Studies in tooth development: the growth pattern of human teeth part II. *The Journal of the American Dental Association,* 27**,** 1918-1931.
SCHWASS, D. R., SWAIN, M. V., PURTON, D. G. & LEICHTER, J. W. 2009. A System of Calibrating Microtomography for Use in Caries Research. *Caries Research,* 43**,** 314-321.
SCOTT, D. B., USSING, M. J., SOGNNAES, R. F. & WYCKOFF, R. W. 1952. Electron microscopy of mature human enamel. *Journal of dental research,* 31**,** 74-84.
SEIBERT, J. A. 2004. X-ray imaging physics for nuclear medicine technologists. Part 1: Basic principles of x-ray production. *Journal of nuclear medicine technology,* 32**,** 139-147.
SEREDIN, P., KASHKAROV, V., LUKIN, A., IPPOLITOV, Y., JULIAN, R. & DOYLE, S. 2013. Local study of fissure caries by Fourier transform infrared microscopy and X-ray diffraction using synchrotron radiation. *Journal of synchrotron radiation,* 20**,** 705-710.
SHAHMORADI, M. & SWAIN, M. V. 2016. Quantitative characterization and micro-CT mineral mapping of natural fissural enamel lesions. *Journal of dentistry,* 46**,** 23-29.
SHAPIRO, I., WUTHIER, R. & IRVING, J. 1966. A study of the phospholipids of bovine dental tissues—I: Enamel matrix and dentine. *Archives of oral biology,* 11**,** 501-512.
SHELLIS, R. 1984. Relationship between human enamel structure and the formation of caries-like lesions in vitro. *Archives of Oral Biology,* 29**,** 975-981.
SHELLIS, R., FINKE, M., EISENBURGER, M., PARKER, D. & ADDY, M. 2005. Relationship between enamel erosion and liquid flow rate. *European journal of oral sciences,* 113**,** 232-238.
SHORE, R. C., ROBINSON, C., KIRKHAM, J. & BROOKES, S. J. 1995a. Structure of developing enamel. *Dental Enamel: Formation to Destruction (Edited by Robinson C., Kirkham J. and Shore R.C.).* CRC Press, New York, USA.
SHORE, R. C., ROBINSON, C., KIRKHAM, J. & BROOKES, S. J. 1995b. Structure of mature enamel *Dental Enamel: Formation to Destruction (Edited by Robinson C., Kirkham J. and Shore R.C.).* CRC Press, New York, USA.

SIDDIQUI, S. & AL-JAWAD, M. 2016. Enamelin Directs Crystallite Organization at the Enamel-Dentine Junction. *Journal of dental research*, 0022034516632745.
SIDDIQUI, S., ANDERSON, P. & AL-JAWAD, M. 2014. Recovery of Crystallographic Texture in Remineralized Dental Enamel. *PLOS ONE,* 9, 1-9.
SIGEL, A., SIGEL, H. & SIGEL, R. K. 2008. *Biomineralization: from nature to application*, John Wiley & Sons Ltd., West Sussex, UK.
SIMMER, J. & FINCHAM, A. 1995. Molecular mechanisms of dental enamel formation. *Critical Reviews in Oral Biology & Medicine,* 6, 84-108.
SIMMER, J. P. & HU, J. 2001. Dental enamel formation and its impact on clinical dentistry. *Journal of Dental Education,* 65, 896-905.
SIMMER, J. P. & HU, J. C.-C. 2002. Expression, structure, and function of enamel proteinases. *Connective tissue research,* 43, 441-449.
SIMMER, J. P., RICHARDSON, A. S., HU, Y.-Y., SMITH, C. E. & HU, J. C.-C. 2012. A post-classical theory of enamel biomineralization...and why we need one. *International journal of oral science,* 4, 129-134.
SIMMONS, L. M., AL-JAWAD, M., KILCOYNE, S. H. & WOOD, D. J. 2011. Distribution of enamel crystallite orientation through an entire tooth crown studied using synchrotron X-ray diffraction. *European Journal of Oral Sciences,* 119, 19-24.
SIMMONS, L. M., MONTGOMERY, J., BEAUMONT, J., DAVIS, G. R. & AL-JAWAD, M. 2013. Mapping the spatial and temporal progression of human dental enamel biomineralization using synchrotron X-ray diffraction. *Archives of Oral Biology,* 58, 1726-34.
SKOBE, Z. 2006. SEM evidence that one ameloblast secretes one keyhole-shaped enamel rod in monkey teeth. *European journal of oral sciences,* 114, 338-342.
SKOBE, Z. & STERN, S. 1980. The pathway of enamel rods at the base of cusps of human teeth. *Journal of dental research,* 59, 1026-1032.
SMITH, C. 1979. Ameloblasts: secretory and resorptive functions. *Journal of dental research,* 58, 695-707.
SMITH, C., POMPURA, J., BORENSTEIN, S., FAZEL, A. & NANCI, A. 1989. Degradation and loss of matrix proteins from developing enamel. *The Anatomical Record,* 224, 292-316.
SMITH, C. & WARSHAWSKY, H. 1977. Quantitative analysis of cell turnover in the enamel organ of the rat incisor. Evidence for ameloblast death immediately after enamel matrix secretion. *The Anatomical Record,* 187, 63-97.
SMITH, C. E. 1998. Cellular and chemical events during enamel maturation. *Critical Reviews in Oral Biology & Medicine,* 9, 128-161.
SMITH, C. E., HU, Y., HU, J. C. C. & SIMMER, J. P. 2016. Ultrastructure of early amelogenesis in wild-type, Amelx-/-, and Enam-/-mice: enamel ribbon initiation on dentin mineral and ribbon orientation by ameloblasts. *Molecular Genetics & Genomic Medicine,* 4, 662-683.
SMITH, C. E. & NANCI, A. 1995. Overview of morphological-changes in enamel organ cells associated with major events in amelogenesis. *International Journal of Developmental Biology,* 39, 153-161.
SMITH, T. M. 2008. Incremental dental development: methods and applications in hominoid evolutionary studies. *Journal of Human Evolution,* 54, 205-224.
SMITH, T. M., OLEJNICZAK, A. J., MARTIN, L. B. & REID, D. J. 2005. Variation in hominoid molar enamel thickness. *Journal of Human Evolution,* 48, 575-592.
SMITH, T. M. & TAFFOREAU, P. 2008. New visions of dental tissue research: tooth development, chemistry, and structure. *Evolutionary Anthropology: Issues, News, and Reviews,* 17, 213-226.

SNEAD, M. L., LAU, E. C., ZEICHNERDAVID, M., FINCHAM, A. G., WOO, S. L. C. & SLAVKIN, H. C. 1985. DNA-sequence for cloned cDNA for murine amelogenin reveal the amino-acid sequence for enamel-specific protein. *Biochemical and Biophysical Research Communications,* 129**,** 812-818.
SOMOGYI-GANSS, E., NAKAYAMA, Y., IWASAKI, K., NAKANO, Y., STOLF, D., MCKEE, M. D. & GANSS, B. 2012. Comparative temporospatial expression profiling of murine amelotin protein during amelogenesis. *Cells Tissues Organs,* 195**,** 535-549.
SPEARS, I. R. & MACHO, G. A. 1998. Biomechanical behaviour of modern human molars: implications for interpreting the fossil record. *American Journal of Physical Anthropology,* 106**,** 467-482.
STACK, M. 1967. Chemical organization of the organic matrix of enamel. *Structural and chemical organization of teeth,* 2**,** 317-346.
STAHL, J., NAKANO, Y., KIM, S.-O., GIBSON, C. W., LE, T. & DENBESTEN, P. 2013. Leucine rich amelogenin peptide alters ameloblast differentiation in vivo. *Matrix Biology,* 32**,** 432-442.
STAINES, M., ROBINSON, W. & HOOD, J. 1981. Spherical indentation of tooth enamel. *Journal of materials science,* 16**,** 2551-2556.
STARON, P., SCHREYER, A., CLEMENS, H. & MAYER, S. 2017. *Neutrons and Synchrotron Radiation in Engineering Materials Science: From Fundamentals to Applications*, Wiley-VCH Verlag GmbH & Co. KGaA, Weinheim, Germany.
STAUBER, M. & MÜLLER, R. 2008. Micro-computed tomography: a method for the non-destructive evaluation of the three-dimensional structure of biological specimens. *Osteoporosis: Methods and Protocols***,** 273-292.
STAVRIANOS, C., PAPADOPOULOS, C., VASILIADIS, L., DAGKALIS, P., STAVRIANOU, I. & PETALOTIS, N. 2010. Enamel structure and forensic use. *Research Journal of Biological Sciences,* 5**,** 650-655.
STENSTRÖM, M. 2001. *Computerised Microtomography: Non-invasive imaging and analysis of biological samples, with special reference to monitoring development of osteoporosis in small animals.* Medical Dissertations, Linköping University, Sweden.
STOCK, S. 1999. X-ray microtomography of materials. *International Materials Reviews,* 44**,** 141-164.
STOCK, S. 2008. Recent advances in X-ray microtomography applied to materials. *International Materials Reviews,* 53**,** 129-181.
STRAWICH, E. & GLIMCHER, M. J. 1990. Tooth 'enamelins' identified mainly as serum proteins. *The FEBS Journal,* 191**,** 47-56.
STRAWICH, E., SEYER, J. & GLIMCHER, M. J. 1993. Note on Tooth Enamelins Immuno-Identification of Two Non-Amelogenin Proteins of Developing Bovine Enamel Isolated by Affinity Chromatography. *Connective tissue research,* 29**,** 163-169.
SUGA, S. Electron microprobe analysis and microradiography of the carious lesions of enamel. Pro-ceedings OJ the First Pan-Pacific Congress on Denral Researrh, 1970.
SUGA, S. 1989. Enamel hypomineralization viewed from the pattern of progressive mineralization of human and monkey developing enamel. *Advances in dental research,* 3**,** 188-198.
SUI, T., LUNT, A. J., BAIMPAS, N., SANDHOLZER, M. A., HU, J., DOLBNYA, I. P., LANDINI, G. & KORSUNSKY, A. M. 2014a. Hierarchical modelling of in situ elastic deformation of human enamel based on photoelastic and diffraction analysis of stresses and strains. *Acta Biomater,* 10**,** 343-54.
SUI, T., SANDHOLZER, M. A., LE BOURHIS, E., BAIMPAS, N., LANDINI, G. & KORSUNSKY, A. M. 2014b. Structure-mechanical function relations at nano-scale in

heat-affected human dental tissue. *Journal of the Mechanical Behavior of Biomedical Materials,* 32**,** 113-124.
SUVOROVA, E., BUFFAT, P., LAYROLLE, P., BOULER, J. & DACOLSI, G. 2001. Electron diffraction and high resolution transmission electron microscopy in the characterization of calcium phosphate precipitation from aqueous solutions under biomineralization conditions. *European Cells and Materials,* 1**,** 27-42.
SWAIN, M. V. & XUE, J. 2009. State of the art of micro-CT applications in dental research. *International journal of oral science,* 1**,** 177.
TARASEVICH, B. J., HOWARD, C. J., LARSON, J. L., SNEAD, M. L., SIMMER, J. P., PAINE, M. & SHAW, W. J. 2007. The nucleation and growth of calcium phosphate by amelogenin. *Journal of crystal growth,* 304**,** 407-415.
TERMINE, J., BELCOURT, A., CHRISTNER, P., CONN, K. & NYLEN, M. 1980. Properties of dissociatively extracted fetal tooth matrix proteins. I. Principal molecular species in developing bovine enamel. *Journal of Biological Chemistry,* 255**,** 9760-9768.
THEWLIS, J. 1936. X-Ray Examination of Tooth Structure. *Nature,* 137.
THEWLIS, J. 1940. The Structure of Teeth as Shown by X-ray Examination. *Special Report Series. Medical Research Council***,** 82.
TOBY, B. H. & VON DREELE, R. B. 2013. GSAS-II: the genesis of a modern open-source all purpose crystallography software package. *Journal of Applied Crystallography,* 46**,** 544-549.
TRAUTZ, O. R. 1955. X-Ray diffraction of biological and synthetic apatites *Annals of the New York Academy of Sciences,* 60**,** 696-712.
TRAUTZ, O. R., KLEIN, E., FESSENDEN, E. & ADDELSTON, H. K. 1953. The interpretation of the X-ray diffractograms obtained from human dental enamel. *Journal of dental research,* 32**,** 420-431.
TUCKER, A. & SHARPE, P. 2004. The cutting-edge of mammalian development; How the embryo makes teeth. *Nature Reviews Genetics,* 5**,** 499-508.
USKOKOVIĆ, V. 2013. Biomineralization and Biomimicry of Tooth Enamel. *Non-Metallic Biomaterials for Tooth Repair and Replacement (Edited by Vallittu P.).* Woodhead Publishing Ltd., Cambridge, UK.
VARGA, G., KERÉMI, B., BORI, E. & FÖLDES, A. 2015. Function and repair of dental enamel–Potential role of epithelial transport processes of ameloblasts. *Pancreatology,* 15**,** S55-S60.
VEIS, A. 2003. Mineralization in organic matrix frameworks. *Reviews in mineralogy and geochemistry,* 54**,** 249-289.
VERDONSCHOT, N., FENNIS, W. M., KUIJS, R. H., STOLK, J., KREULEN, C. M. & CREUGERS, N. H. 2001. Generation of 3-D finite element models of restored human teeth using micro-CT techniques. *The International Journal of Prosthodontics,* 14**,** 310-315.
VIDELA, A., LIN, C. & MILLER, J. 2007. 3D characterization of individual multiphase particles in packed particle beds by X-ray microtomography (XMT). *International Journal of Mineral Processing,* 84**,** 321-326.
VON DREELE, R. 1997. Quantitative texture analysis by Rietveld refinement. *Journal of Applied Crystallography,* 30**,** 517-525.
WALLWORK, M. L., KIRKHAM, J., ZHANG, J., SMITH, D. A., BROOKES, S. J., SHORE, R. C., WOOD, S. R., RYU, O. & ROBINSON, C. 2001. Binding of matrix proteins to developing enamel crystals: an atomic force microscopy study. *Langmuir,* 17**,** 2508-2513.

WANG, H., TANNUKIT, S., ZHU, D., SNEAD, M. L. & PAINE, M. L. 2005. Enamel matrix protein interactions. *Journal of Bone and Mineral Research,* 20**,** 1032-1040.
WANG, R. & WEINER, S. 1997. Strain–structure relations in human teeth using Moiré fringes. *Journal of biomechanics,* 31**,** 135-141.
WANG, S., CHOI, M., RICHARDSON, A., REID, B., SEYMEN, F., YILDIRIM, M., TUNA, E., GENCAY, K., SIMMER, J. & HU, J. 2014. STIM1 and SLC24A4 are critical for enamel maturation. *Journal of dental research,* 93**,** 94S-100S.
WARSHAWSKY, H. 1985. Ultrastructural studies on amelogenesis. *The Chemistry and Biology of Mineralized Tissues,* 33.
WARSHAWSKY, H., JOSEPHSEN, K., THYLSTRUP, A. & FEJERSKOV, O. 1981. The development of enamel structure in rat incisors as compared to the teeth of monkey and man. *The Anatomical Record,* 200**,** 371-399.
WARSHAWSKY, H. & SMITH, C. 1974. Morphological classification of rat incisor ameloblasts. *The Anatomical Record,* 179**,** 423-445.
WATSON, M. L. & AVERY, J. K. 1954. The development of the hamster lower incisor as observed by electron microscopy. *American Journal of Anatomy,* 95**,** 109-161.
WATT, I. M. 1997. *The principles and practice of electron microscopy*, Cambridge University Press, New York, USA.
WAZEN, R., MOFFATT, P., PONCE, K., KURODA, S., NISHIO, C. & NANCI, A. 2014. Inactivation of the Odontogenic ameloblast-associated gene affects the integrity of the junctional epithelium and gingival healing. *European cells & materials,* 30**,** 187-199.
WEATHERELL, J., ROBINSON, C. & HALLSWORTH, A. 1974. Variations in the chemical composition of human enamel. *Journal of Dental Research,* 53**,** 180-192.
WEATHERELL, J., WEIDMANN, S. & HAMM, S. M. 1967. Density patterns in enamel. *Caries research,* 1**,** 42-51.
WEIDMANN, S., WEATHERELL, J. & HAMM, S. M. 1967. Variations of enamel density in sections of human teeth. *Archives of oral biology,* 12**,** 85-97.
WEINMANN, J. P., WESSINGER, G. D. & REED, G. 1942. Correlation of chemical and histological investigations on developing enamel. *Journal of Dental Research,* 21**,** 171-182.
WENK, H. & VAN HOUTTE, P. 2004. Texture and anisotropy. *Reports on Progress in Physics,* 67**,** 1367.
WHAITES, E. & CAWSON, R. A. 2007. *Essentials of Dental Radiography and Radiology*, Elsevier, Churchill Livingstone, London, UK.
WILLEMS, G., CELIS, J.-P., LAMBRECHTS, P., BRAEM, M. & VANHERLE, G. 1993. Hardness and Young's modulus determined by nanoindentation technique of filler particles of dental restorative materials compared with human enamel. *Journal of Biomedical Materials Research Part A,* 27**,** 747-755.
WILLMOTT, N., WONG, F. & DAVIS, G. 2007. An X-ray microtomography study on the mineral concentration of carious dentine removed during cavity preparation in deciduous molars. *Caries research,* 41**,** 129-134.
WILLMOTT, P. 2011. *An introduction to synchrotron radiation: techniques and applications*, John Wiley & Sons Ltd., West Sussex, UK.
WILSON, P. & BEYNON, A. 1989. Mineralization differences between human deciduous and permanent enamel measured by quantitative microradiography. *Archives of Oral Biology,* 34**,** 85-88.
WILSON, R. M., ELLIOTT, J. C. & DOWKER, S. E. P. 1999. Rietveld refinement of the crystallographic structure of human dental enamel apatites. *American Mineralogist,* 84**,** 1406-1414.

WONG, F., ANDERSON, P., FAN, H. & DAVIS, G. 2004. X-ray microtomographic study of mineral concentration distribution in deciduous enamel. *Archives of Oral Biology,* 49**,** 937-944.
WONG, F. S. L., WILLMOTT, N. S. & DAVIS, G. R. 2006. Dentinal carious lesion in three dimensions. *International Journal of Paediatric Dentistry,* 16**,** 419-423.
XUE, J., LI, W. & SWAIN, M. V. 2009. In vitro demineralization of human enamel natural and abraded surfaces: a micromechanical and SEM investigation. *Journal of dentistry,* 37**,** 264-272.
XUE, J., ZHANG, L. L., ZOU, L., LIAO, Y. M., LI, J. Y., XIAO, L. Y. & LI, W. 2008. High-resolution X-ray microdiffraction analysis of natural teeth. *Journal of Synchrotron Radiation,* 15**,** 235-238.
YAGI, N., OHTA, N., MATSUO, T., TANAKA, T., TERADA, Y., KAMASAKA, H. & KOMETANI, T. A Microbeam Small-Angle X-ray Scattering Study on Enamel Crystallites in Subsurface Lesion. Journal of Physics: Conference Series, 2010. IOP Publishing.
YAGI, N., OHTA, N., MATSUO, T., TANAKA, T., TERADA, Y., KAMASAKA, H., TO-O, K., KOMETANI, T. & KURIKI, T. 2009. Evaluation of enamel crystallites in subsurface lesion by microbeam X-ray diffraction. *Journal of synchrotron radiation,* 16**,** 398-404.
YAMAKOSHI, Y., TANABE, T., FUKAE, M. & SHIMIZU, M. 1994. Porcine amelogenins. *Calcified Tissue International,* 54**,** 69-75.
YAMAKOSHI, Y., TANABE, T., OIDA, S., HU, C. C., SIMMER, J. P. & FUKAE, M. 2001. Calcium binding of enamel proteins and their derivatives with emphasis on the calcium-binding domain of porcine sheathlin. *Archives of Oral Biology,* 46**,** 1005-1014.
YIN, K., HACIA, J. G., ZHONG, Z. & PAINE, M. L. 2014. Genome-wide analysis of miRNA and mRNA transcriptomes during amelogenesis. *BMC genomics,* 15**,** 998.
YOUNG, R. & MACKIE, P. 1980. Crystallography of human tooth enamel: initial structure refinement. *Materials Research Bulletin,* 15**,** 17-29.
ZEYGERSON, T., SMITH, P. & HAYDENBLIT, R. 2000. Intercusp differences in enamel prism patterns in early and late stages of human tooth development. *Archives of oral biology,* 45**,** 1091-1099.
ZHU, Y., ZHAO, M., LI, H. & ZHANG, P. 2013. Micro-CT artifacts reduction based on detector random shifting and fast data inpainting. *Medical physics,* 40**,** 031114.
ZOU, D., TIE, Z., LU, C., QIN, M., LU, X., WANG, M., WANG, W. & CHEN, P. 2010. Effects of hydrophobicity and anions on self-assembly of the peptide EMK16-II. *Biopolymers,* 93**,** 318-329.
ZOU, W., HUNTER, N. & SWAIN, M. V. 2011. Application of Polychromatic μCT for Mineral Density Determination. *Journal of Dental Research,* 90**,** 18-30.